PROCEEDINGS OF SPIE

# *Photonics in the Transportation Industry: Auto to Aerospace II*

**Alex A. Kazemi**
**Bernard C. Kress**
*Editors*

**13–14 April 2009**
**Orlando, Florida, United States**

*Sponsored and Published by*
SPIE

**Volume 7314**

Proceedings of SPIE, 0277-786X, v. 7314

The papers included in this volume were part of the technical conference cited on the cover and title page. Papers were selected and subject to review by the editors and conference program committee. Some conference presentations may not be available for publication. The papers published in these proceedings reflect the work and thoughts of the authors and are published herein as submitted. The publisher is not responsible for the validity of the information or for any outcomes resulting from reliance thereon.

Please use the following format to cite material from this book:
Author(s), "Title of Paper," in *Photonics in the Transportation Industry: Auto to Aerospace II*, edited by Alex A. Kazemi, Bernard C. Kress, Proceedings of SPIE Vol. 7314 (SPIE, Bellingham, WA, 2009) Article CID Number.

ISSN 0277-786X
ISBN 9780819475800

Published by
**SPIE**
P.O. Box 10, Bellingham, Washington 98227-0010 USA
Telephone +1 360 676 3290 (Pacific Time) · Fax +1 360 647 1445
SPIE.org



Printed in the United States of America.

Publication of record for individual papers is online in the SPIE Digital Library.

SPIE Digital Library

SPIEDigitalLibrary.org

---

**Paper Numbering:** Proceedings of SPIE follow an e-First publication model, with papers published first online and then in print and on CD-ROM. Papers are published as they are submitted and meet publication criteria. A unique, consistent, permanent citation identifier (CID) number is assigned to each article at the time of the first publication. Utilization of CIDs allows articles to be fully citable as soon they are published online, and connects the same identifier to all online, print, and electronic versions of the publication. SPIE uses a six-digit CID article numbering system in which:

- The first four digits correspond to the SPIE volume number.
- The last two digits indicate publication order within the volume using a Base 36 numbering system employing both numerals and letters. These two-number sets start with 00, 01, 02, 03, 04, 05, 06, 07, 08, 09, 0A, 0B … 0Z, followed by 10-1Z, 20-2Z, etc.

The CID number appears on each page of the manuscript. The complete citation is used on the first page, and an abbreviated version on subsequent pages. Numbers in the index correspond to the last two digits of the six-digit CID number.

# Contents

# Conference Committee

*Symposium Chair*

**Ray O. Johnson,** Lockheed Martin Corporation (United States)

*Symposium Cochair*

**Michael T. Eismann,** Air Force Research Laboratory (United States)

*Conference Chairs*

**Alex A. Kazemi,** The Boeing Company (United States)
**Bernard C. Kress,** Université Louis Pasteur (France)

*Program Committee*

**Frank Abdi,** AlphaSTAR Corporation (United States)
**Ayman Abouraddy,** CREOL, The College of Optics and Photonics, University of Central Florida (United States)
**Hamid Aghvami,** King's College London (United Kingdom)
**Thomas D. P. Allsop,** Aston University (United Kingdom)
**Pierre Ambs,** Université de Haute Alsace (France)
**Ayoub Chakari,** Université Louis Pasteur (France)
**Eric Y. Chan,** The Boeing Company (United States)
**Catherine Ciardiello,** OFS (United States)
**Marc Comet,** Institut Franco-Allemand de Recherches de Saint-Louis (France)
**Brian Culshaw,** University of Strathclyde (United Kingdom)
**Dan S. Curticapean,** Fachhochschule Offenburg (Germany)
**Mahendra S. Dassanayake,** Ford Company (United States)
**Richard M. De La Rue,** University of Glasgow (United Kingdom)
**Thomas Dietsch,** BMW AG (Germany)
**Basil Garabet,** EM4, Inc. (United States)
**Harold Hager,** The Boeing Company (United States)
**Beth C. Haskell,** PerkinElmer Optoelectronics (United States)
**Kenneth M. Hays,** The Boeing Company (United States)
**Zuyuan He,** The University of Tokyo (Japan)
**Vic Hejmadi,** Universal Semiconductor, Inc. (United States)
**Richard T. Howard,** NASA Marshall Space Flight Center (United States)
**Jeffrey H. Hunt,** The Boeing Company (United States)
**Nicolas Javahiraly,** Université Louis Pasteur (France)
**Lothar U. Kempen,** Intelligent Optical Systems, Inc. (United States)
**Peter Kiesel,** Palo Alto Research Center, Inc. (United States)
**Georg Kodl,** LEONI AG (Germany)

**David A. Krohn,** Light Wave Venture Consulting, LLC (United States)
**Jack Latchinian,** Zygo Corporation (United States)
**Patrick P. Meyrueis,** Université Louis Pasteur (France)
**Jean-Pierre Moeglin,** Institut Franco-Allemand de Recherches de Saint-Louis (France)
**Mohammad Mojahedi,** University of Toronto (Canada)
**Herbert O. Moser,** National University of Singapore (Singapore)
**Nezih Mrad,** Defence Research and Development Canada (Canada)
**Juock S. Namkung,** Naval Air Warfare Center (United States)
**Allen S. Panahi,** Accro USA LLC (United States)
**Saeed Rehman,** FiberLogix Ltd. (United Kingdom)
**Ahmad Safaai-Jazi,** Virginia Polytechnic Institute and State University (United States)
**Stephen Sagan,** BAE Systems (United States)
**Martin Schell,** Fraunhofer-Institut für Nachrichtentechnik-Heinrich-Herz (Germany)
**Michel Sirieix,** Sagem Defense Securite (France)
**Massood Tabib-Azar,** Case Western Reserve University (United States)
**Simon Thibault,** ImmerVision (Canada)
**Tuan Vo-Dinh,** Duke University (United States)

*Session Chairs*

1 Sensors in Transportation/Aerospace Applications I
**Alex A. Kazemi,** The Boeing Company (United States)

2 Sensors in Transportation/Aerospace Applications II
**Tuan Vo-Dinh,** Duke University (United States)

3 Sensors in Transportation/Aerospace Applications III
**Bernard C. Kress,** Université Louis Pasteur (France)

4 Micro/Nanophotonics in Transportation
**Saeed Rehman,** FibertroniX (United Kingdom)

5 Photonics in Data Transmission for Transportation
**Eric Y. Chan,** The Boeing Company (United States)

# Introduction

The field of fiber optic sensors has undergone a remarkable change over the past three decades. Today a great proportion of the world's communications are carried by fiber optic cables. The fiber optic technology has revolutionized the telecommunication market and is rapidly becoming a major player in such areas as telephone, cable TV, and local-area network (LAN). It has spread into every situation in which information is being transmitted.

Over the years, I have been greatly impressed by the tremendous progress in photonics in transportation industry. The technology has gone through a quantum leap. More information, intelligence, and data are transferred from one point to another, more quickly and precisely than ever thought possible, thanks to the miracle of optical fibers. I find myself among pioneers and the thrill of technical achievement can be just as tangible to those of us involved with engineering, technology, and science as the thrill of lifetime accomplishment.

As fiber optic algorithms and equations are developed and proven, fiber optics shall become as common as wire, easy to construct to precise tolerances, and accurate and perfect in operation. At the same time fiber optic sensor technology and photonics in transportation industry have developed in parallel with fiber optic and other optoelectronics industries such as lasers, which dominate the compact disk, DVD, laser printer, and scanner industry with the most promising uses for lasers and communications over fiber optic cables. In recent years, the fiber optic sensor greatly benefitted from the low-cost telecommunications industries. Due to this synergy, an enormous amount of new technologies have been introduced in the form of smart sensors, biomedical sensors, pressure, temperature and liquid level, to name a few.

This book contains a series of papers which contains state-of-the art fiber optic sensor technologies for photonics in transportation industries such as emerging technologies for cryogenic hydrogen leak detection systems for space applications to a new generation of fiber optic sensor using holography for detection of motion and vibration in automobile bumper shock, and finally a 360-degree vision system for transportation.

On behalf of SPIE and myself, I would like to thank the individual authors for their valuable contributions. Their support is truly appreciated.

Dedicated to my wife, **Mary**, mother **Touran** and late father **Kamal** for their inspiration and support throughout my life.

**Alex A. Kazemi**

# Resonator Fiber Optic Gyroscope with Digital Serrodyne Scheme Using a Digital Controller

Xijing Wang, Zuyuan He, and Kazuo Hotate

Department of Electrical Engineering and Information Systems, The University of Tokyo,
7-3-1 Hongo, Bunkyo-ku, Tokyo 113-8656, Japan
E-mail: {wangxj, ka, hotate}@sagnac.t.u-tokyo.ac.jp

## ABSTRACT

To get rid of the complex analogue control loops that are traditionally used in resonator fiber optic gyroscope (R-FOG) and to meet the requirements of high accuracy as well as small-size and light-weight in Inertial Navigation Systems (INSs), a digital controller is developed and demonstrated experimentally to control the R-FOG with the digital serrodyne modulation. The digital controller is designed to implement the function of tracking the laser diode frequency drift and to compensate for the imperfect 2π modulation voltage of the phase modulator for the serrodyne modulation. To acquire the resonant frequency, the digital serrodyne modulation with symmetric frequency shift is adopted as a counter-measure for Rayleigh backscattering noise. The optimal serrodyne modulation generated frequency shift is decided to be in the range of 100~120 kHz according to the numerical calculation. The successful demonstration of the open loop operation with the digital controller is deemed as the basis for the digitalized closed-loop experiment in future.

**Keywords:** ring resonator fiber optic gyro, digitalized control, 2π voltage control, rotation detection

## 1. INTRODUCTION

The Fiber Optic Gyroscope (FOG) is used to detect the rotation with respect to an inertial frame [1, 2]. Its working principle is based on the so called *Sagnac* Effect. One type of the FOGs, the Ring Resonator Fiber Optic Gyroscope (R-FOG), works as a multipass ring resonator, with sharp peaks/dips at the resonant frequency. Based on observing the difference in resonance frequencies between clockwise (CW) and counter clockwise (CCW) lightwaves, a R-FOG is expected to realize high grade rotation sensor satisfying the inertial navigation systems (INSs) requirement ($10^{-7}$rad/s) with an optical fiber loop as short as only 5~10 meters [1]. Its counterpart or the interferometric fiber optic gyro (I-FOG), on the contrary, requires a fiber sensing loop as long as 1 km [2] to achieve the same sensitivity. The reduced length of fiber loop in R-FOG cuts down the bias drift a lot due to time-variant temperature distribution in the sensing coil [3]. Besides, a short sensing coil is also favorable for reducing the size and weight of the gyro, which is crucial for applications such as INS [4].

Traditionally, the R-FOG is controlled by complex analogue feedback loops. With the development of digital signal processing techniques, it is possible to design digitalized controllers with lighter weight and higher accuracy. In this paper, we focus on the development and application of a digital controller to the R-FOG.

## 2. DIGITAL SERRODYNE MODULATION TECHNIQUE IN R-FOG

### 2.1 Rotation Detection with Hybrid Digital Serrodyne Modulation

The resonator fiber-optic gyroscope is composed of a high finesse ring resonator as shown in Fig. 1. When R-FOG rotates, the resonant frequency difference between the CW and CCW side can be written as

$$\Delta f = \frac{D}{n\lambda}\Omega, \tag{1}$$

where $\Delta f$, $D$, $n$, $\lambda$, $\Omega$ are the resonant frequency difference, the diameter of the fiber coil, the refractive index of the light path, wavelength, and the rotation speed, respectively.

To detect rotation, resonant frequencies for both the CW and CCW side are required. A conventional method to detect the resonant frequency, as so-called serrodyne modulation, is to linearly modulate the phase of the lightwave in a

Photonics in the Transportation Industry: Auto to Aerospace II, edited by Alex A. Kazemi, Bernard C. Kress
Proc. of SPIE Vol. 7314, 731402 · © 2009 SPIE · CCC code: 0277-786X/09/$18 · doi: 10.1117/12.818471

sawtooth waveform with 2π-amplitude to shift the frequency of the lightwave [5]. The digital serrodyne scheme, on the contrary, modulates the phase of the input lightwave with a stepwised sawtooth waveform [6-8] whose amplitude is 2π. It has been approved that the modulation shifts the central frequency of the input lightwave with a constant amount as the same as the analogue serrodyne modulation, so long if the step duration τ equals to one turn transmission time in the ring resonator [6]. Compared with generating an accurate analogue waveform, it is much easier to produce a stepwise waveform with constant modulation amplitude and slope throughout the period.

Furthermore, the digital serrodyne waveform can be modified into a hybrid digital serrodyne modulation, which changes the slope of the digital serrodyne waveform periodically, as shown in Fig. 2 [7]. Fig 3(a) and 3(b) depict the resonator output of R-FOG when the resonant frequency is equal and away from the resonant frequency. The hybrid digital serrodyne modulation shifts light frequency by $+\Delta f_j$ (j=CW, CCW) in the first half and $-\Delta f_j$ in the second half, with a repetition frequency of $f_{rp,j}$ (j=CW, CCW) as in Fig. 2. This modulation waveform can be used in resonant frequency detection [7]. Denote the central frequency of input lightwave to be $f_0$. If $f_0$ equals to the resonant frequency, the output of R-FOG with the phase modulation is a DC signal as shown in Fig. 3(a). Otherwise, the output becomes a square waveform with the same frequency of $f_{rp,j}$ and amplitude of $I_2$-$I_1$ as shown in Fig. 3(b). Therefore, it is possible to judge if the lightwave central frequency is equal to the resonant frequency or not by synchronously detecting $f_{rp,j}$ component in the output.

## 2.2 Noisee Reduction with Digital Serrodyne Scheme

R-FOG usually encounters with Rayleigh backscattering noise [9]. Counter- measures are necessary to achieve high grade R-FOG. The counter-measures against these noises can be introduced by the digital hybrid serrodyne modulation as stated in [6, 7]. The Rayleigh backscattering occurred inside the ring resonator reaches the detector with the signal lightwave. Thus, the total power detected is expressed as

$$\overline{E(t)E^*(t)} = \overline{|E_s(t)|}^2 + 2\,\mathrm{Re}\{\overline{E_s(t)E_n^*(t)}\} + \overline{|E_n(t)|}^2, \tag{2}$$

where $E_s(t)$ and $E_n(t)$ stand for the electric field of signal lightwave and the Rayleigh backscattering noise, respectively. In Eq. (2), the second and the third are the noise components, representing the power of the interference between the signal lightwave and the Rayleigh backscattering, and the power of the Rayleigh backscattering itself. With different repetition frequencies between CW and CCW side ($f_{rp,CW}$ and $f_{rp,CCW}$), the hybrid digital serrodyne modulation moves the third noise term in Eq. (2) out of the detection band [7]. Moreover, the second term in Eq. (2) is also reduced by using the different frequency shift $\Delta f_j$ between the CW and the CCW lightwave [7]. Under this condition, the CW and the CCW lightwave frequencies are always different, so the second term in Eq. (2) does not exist in the gyro signal bandwidth [7].

One problem with the serrodyne phase modulation, as pointed out in [5], is the occurrence of pluses at the output of photodetector when the modulation waveform resets with an imperfect 2π voltage. It is also pointed out in [5] that a smaller-than-ideal modulation voltage causes a convex pulse and a larger-than-ideal modulation voltage causes a concave pulse in the output. If no counter-measure is taken against this problem, the performance of R-FOG will be degraded since the frequency of resetting pulse is the higher harmonic of the repeating frequency $f_{rp,j}$, at which the rotation signal is read out.

## 2.3 Central Frequency Shift without Rotation

By modifying the hybrid digital serrodyne modulation waveform as shown in Fig. 4, we can also introduce a central frequency shift to emulate the situation of quasi rotation [7]. If the central frequency of the CCW lightwave, for example, is locked to the resonant frequency, an additional central frequency shift $f_s$ should be introduced in the CW side to have the closed-loop operation, in which the resonant frequencies of the resonator are locked to the input lightwave frequencies both for the CW and the CCW lightwave under the rotation. What R-FOG takes for as the resonant frequency is the amount averaged in one period of the hybrid digital serrodyne modulation. When the gyro is at rest, the CW side has a resonant frequency of

$$f_r = [(f_0 - \Delta f_{CW}) + (f_0 + \Delta f_{CW})]/2 = f_0, \tag{3}$$

which is the same as that of the CCW side. Fig. 4(a) shows the case of up shifted central frequency. A linear waveform with positive slope $+f_s$, which is denoted as the dotted line in Fig. 4(a), is added to the original waveform throughout the whole period [7]. The resonant frequency now becomes

$$f_r = [(f_0 - \Delta f_{CW} + f_s) + (f_0 + \Delta f_{CW} + f_s)]/2 = f_0 + f_s. \tag{4}$$

It is ahead of the resonant frequency of CCW side by $f_s$. The same is true if a negative linear waveform is added to the original waveform to introduce the down shifted central frequency as shown in Fig. 4(b). This method to control the central frequency of the input lightwave to the resonator is to be used in an experiment of the quasi-rotation measurement later in this paper.

## 3. PARAMETER OPTIMIZING FOR THE FREQUENCY SHIFT IN THE HYBRID DIGITAL SERRODYNE WAVEFORM

The target of this mathematical model is to optimize the frequency shift $\Delta f_j$ in the hybrid digital serrodyne waveform. For simplicity, the modeling process based on the analogue serrodyne modulation scheme is considered, since the digital serrodyne has the same effect if the step duration $\tau$ equals to the one-turn transmission time [6].

Consider the optical setup shown in Fig. 1, the output electric fields of the CW and CCW sides are written as

$$E_j(t) = E_0 e^{j2\pi f_0 t}(e^{j\Delta\Phi_j(t)}\beta - \gamma\sum_{n=1}^{\infty}\delta^{n-1}e^{-jn2\pi f_0\tau}e^{j\Delta\Phi_j(t-n\tau)}), \tag{5}$$

where

$$\begin{aligned}\beta &= \lambda_{CT}\sqrt{1-\kappa_C}\\ \gamma &= \lambda_{CR}^2\kappa_C\lambda_L\\ \delta &= \lambda_L\lambda_{CT}\sqrt{1-\kappa_C}\end{aligned}, \tag{6}$$

and $E_0$ is the amplitude of the input electric filed, $\kappa_c$ the reflectivity of the coupler, $\lambda^2_{CT}$ the loss of the transmission port of the coupler, $\lambda^2_{CR}$ the loss of the transmission port of the coupler, $\lambda^2_L$ the fiber induced one turn transmission loss (splicing loss included). Therefore, $\beta$ and $\delta$ are the amplitude transmission coefficient of the coupler and the one turn amplitude transmission coefficient of the ring, respectively. The serrodyne modulation signal is

$$\Delta\Phi(t)_j = 2\pi\Delta f_j t. \tag{7}$$

The finesse of the ring resonator is defined as

$$F = \frac{\pi\sqrt{\delta}}{1-\delta}. \tag{8}$$

The $f_{rp,j}$ component in the detector output is calculated as

$$I_{out,f_{rp,j}} = \frac{2E_0^2}{\pi}\left[\frac{2\beta\gamma\cos 2\pi(f_0+\Delta f_j)\tau+\gamma^2}{(1-\delta)^2+4\delta\sin^2\pi(f_0+\Delta f_j)\tau} - \frac{2\beta\gamma\cos 2\pi(f_0-\Delta f_j)\tau+\gamma^2}{(1-\delta)^2+4\delta\sin^2\pi(f_0-\Delta f_j)\tau}\right]. \tag{9}$$

The shot noise determined sensitivity is used as a scale to optimize the serrodyne frequency. This limit is reached if the rotation induced current is equal to the shot noise induced current. The minimum detectable phase difference is calculated as

$$\Omega_{SN} = \frac{n\lambda}{D}\left(\beta - \frac{\gamma}{1-\delta}\right)\sqrt{\frac{2Bhf}{\eta}}\frac{(1-2\delta\cos\pi\Delta f_j\tau+\delta^2)^2}{16\sqrt{P}\beta\gamma\tau(1+2\delta\gamma^2+\gamma^2)\sin\pi\Delta f_j\tau}, \tag{10}$$

where $e$, $\eta$, $h$, $B$, $P$ are the electricity of one electron, quantum efficiency of the photo detector, Prank constant, bandwidth of the signal processing circuit, and input power, respectively.

Fig. 5 shows the shot noise determined sensitivity as a function of the frequency shift $\Delta f_j$ of the hybrid serrodyne modulation. Simulation parameters are decided considering the experimental setup shown below: resonator length $L=10.7$ m; coupler transmission port loss $-20\log\lambda_{CT}=0.4$ dB; coupler reflection port loss $-20\log\lambda_{CR}=0.3$ dB; one-turn fiber transmission loss including splicing loss $-20\log\lambda_L=0.05$ dB; coupler reflectivity $\kappa_C=0.01$; input power $P=10$ mW; resonator diameter $D=10$ cm; signal processing bandwidth $B=0.5$ Hz; photo detector quantum efficiency $\eta=0.6$; fiber refractive index $n=1.46$. From the numerical simulation result as shown in Fig. 5, it can be concluded that the optimized amount of frequency shift of the hybrid serrodyne modulation is in the range of 100~120 kHz, where the shot noise is below the INS requirement.

## 4. EXPERIMENT

### 4.1 Experiment Setup

The experimental setup scheme is depicted in Fig. 6. The demodulation scheme is composed of three feedback loops and one output circuit, all of which are built with the PXI real time system (National Instrument (NI)). The loop No. 1 and the loop No. 4 are used to control the amplitude of the hybrid digital serrodyne waveform for CW and CCW lightwaves, respectively. In these two loops, the A/D converters sample the $\Delta f_j$ component outputs from the lock-in amplifiers (LIA1 and LIA4), and send the values to proportional and integration (PI) modules. The PI modules use these values as the error signals and calculate the corresponding feedback. The feedback signals are in the form of digital gain and are sent out to the function generators (FG2 and FG1) (NI, PXI 5422), to amplify or attenuate signals before they are generated as analogue voltages. The digital processing procedure avoids the traditional analogue amplification setting at the FGs, which takes up space and time. Next, with the resonant frequency of the CCW side locked to the frequency of the laser diode (LD) through the loop No. 3, the resonant frequency difference between CCW and CW side is regarded as the rotation output. In the loop No. 3, the feedback signal is converted to analogue voltage through the D/A converter to modify the bias current of the LD to cancel the slow drift of the laser frequency. Besides, an additional analogue signal is fed back to the piezoelectric transducer (PZT) to track high frequency drifts. This function can also be integrated into the digital processor if a digital processor with faster processing speed, such as a FPGA, is used. This experimental setup is an open-loop scheme, in which the difference between A/D No. 2 and No. 3 is regarded as the gyro rotation output and sent to the computer. As stated in [7], the gyro rotation output can also be used to control the central frequency of the hybrid digital serrodyne modulation, when a closed loop scheme is adopted.

### 4.2 Hybrid Digital Serrodyne Waveform Design

The digital serrodyne waveform parameters are carefully designed according to the experimental condition. The LD is first scanned with a sawtooth waveform to measure the resonant curve. The finesse and the fiber length are retrieved to be 59 and 10.7 m, respectively. As stated in [6], the step duration $\tau$ of the digital serrodyne waveform should be equal to the one turn transmission time. Therefore, the sampling rate of the function generator should be set to that of one free spectral range (FSR), which is 19.24 M samples/s in this case.

Moreover, according to Fig. 2, the amount of frequency shift $\Delta f_j$ in hybrid digital serrodyne modulation is related to the sampling rate of FG by

$$\Delta f_j = \frac{f_{FG}}{n_{s,j}}, \tag{11}$$

where $n_{s,j}$ and $f_{FG}$ stand for the number of steps the digital serrodyne modulation composed of before resetting, and the sampling rate of the FG. Besides, if there are $n_{rp,j}$ (j=CW, CCW) serrodyne periods in each half, the repetition frequency becomes

$$f_{rp,j} = \frac{f_{FG}}{2n_{s,j}n_{rp,j}}. \tag{12}$$

According to the numerical simulation given in Section II-C, the system has the best performance when the frequency shift $\Delta f_j$ is in the range of 100~120 kHz. To get rid of the influences of the backscattered light, not only the frequency shift $\Delta f_{CW}$ and $\Delta f_{CCW}$ should be different but also their higher harmonics should not cover each other [7]. In other words, the generated waveforms should not overlap with one another as long as possible. This can be satisfied if $n_{s,j}$ is chosen to be a prime number. However, according to the manual of NI PXI Function Generator 5422, the number of samples that each waveform contains should be an integer time of 4. Thus, we choose 4 times a smaller prime number as the sampling points in one serrodyne waveform. Taking the above requirements into considerations, $n_{s,CCW}$ and $n_{s,CW}$ are set to 4×47=188 and 4×43=172, respectively. According to Eq. (11), this corresponds to a frequency shift of 102.3 kHz in the CCW side and 111.9 kHz in the CW side, respectively. When designing the repetition frequency, two points are considered: (1) the first half is symmetric to the second half; (2) the number of serrodyne periods in each half $n_{rp,j}$ is also a prime number. In this experiment, we choose $n_{rp,CCW}$=5, $n_{rp,CW}$=7. According to Eq. (12), this equals to $f_{rp,CCW}$=10.23 kHz and $f_{rp,CW}$=7.99 kHz. Figure 7 shows the hybrid digital serrodyne waveform designed for the CCW side.

### 4.3 Adaptive Compensation 2π Voltage of the Phase Modulator

To synchronously detect the imperfect 2π voltage from the LIA output, synchronization signals with frequency of $\Delta f_{CCW}$ and $\Delta f_{CW}$ are required. At first, we supplied the LIA with a signal that is generated by low pass filtering the hybrid digital serrodyne modulation signal. However, it was found that the LIA met with the "UNLOCK" problem due to the phase

shift in the middle point of the waveform. This was solved by using the so-called "Marker Event" technique available in NI PXI 5422 function generator. With a marker event, the state of trigger lines will change synchronously with the generation of a specific sample. In Fig. 7, the synchronization signal is also shown as well as the generated hybrid digital serrodyne modulation waveform.

To demonstrate the idea that the imperfect modulation amplitude produces different transient tails according to the amplitude levels, two input voltages are arbitrarily selected: 3.4 V and 6.3 V. The loop No. 3 is on to track the LD frequency. The output is obtained directly from the photodetector at the CCW side, which is shown in Fig. 8. According to later experimental results, 3.4 V is smaller than the ideal $2\pi$ voltage of the phase modulator while 6.3 V is too large. The results fit well with the previous explanation in II-A that small voltage produces a convex tail while large voltage generates a concave tail [5]. Next, the synchronous detection with different input voltages is examined. The voltage is increased from 5.4 V to 6.0 V by 0.05 V per step. LIA1 and LIA4 are synchronized to the serrodyne frequencies $\Delta f_{CW}$ and $\Delta f_{CCW}$, respectively. The result of CCW side is displayed in Fig. 9. This graph indicates that the synchronous detection with the serrodyne frequency is linearly related to the amplitude of modulation waveform, which makes the PI feedback possible. Fig. 10 records LIA4 output before and after the feedback loop is turned on when the output is sampled at a rate of 15.1 kHz. From this figure we can conclude that the digital processor finally found the appropriate $2\pi$ voltage of the phase modulator that brought the LIA output to 0V.

Finally, we checked the photodetector output when the modulation amplitude is set to the appropriate value, which is 5.68V in this experiment. By comparing Fig. 11 with Fig. 8, it can be concluded that this scheme is effective in reducing the imperfect $2\pi$ voltage induced noise.

### 4.4 Quasi-Rotation Measurement

Central frequency shifts are generated to the CW side hybrid digital serrodyne waveform by adding a positive slope waveform for +0.65 kHz and a negative slope waveform for -0.65 kHz, as shown in Fig. 4. They are realized by adding or subtracting 2 Least Significant Bits (LSBs) from each step of the original waveform, whose step height is 340 LSBs. Three waveforms, original, up shifted, and down shifted, are generated by only one function generator in a sequential order. The quasi-rotation measurement was performed, and the result is shown in Fig. 12. This is obtained by subtracting the digitalized voltage output of LIA2 from that of LIA3. The result of $0.8^{o}$/s fits well with the 0.65 kHz frequency shift, as according to Eq. (1).

## 5. CONCLUSION

We have experimentally demonstrate the quasi-rotation measurement of the R-FOG, where a digital controller is newly developed to track the laser diode central frequency drift and to compensate the $2\pi$ voltage of the phase modulator based on the reset pulse amplitude of digital serrodyne modulation. The digital processor is designed with much higher flexibility and simplicity compared with traditional analogue circuits. By incorporating modules with higher processing power, we are expecting to build an R-FOG that is totally digitalized.

## REFERENCES


1. K. Hotate, "Fiber-optic gyros," in *Optical Fiber Sensors*, *Applications, Analysis, and Future Trends,* vol. 4, ch. 11, J. Dakin and B. Culshaw, Ed., Artech house, 1997.
2. H. Lefevre, *The Fiber-optic Gyro*, Artech House, 1993.
3. D. M. Shupe, "Thermally induced nonreciprocity in the fiber-optic interferometer," *Appl. Opt.*, vol. 19, no. 5, pp. 654-655, 1980.
4. K. Sakuma, "Fiber optic gyro production at JAE," in *Proc. SPIE*, vol. 1585, pp. 8-16, 1991.
5. L. K. Strandjord and G. A. Sanders, "Effect of imperfect serrodyne phase modulation in resonator fiber-optic gyroscopes," in *Proc. SPIE*, vol. 2292, pp. 272-282, 1994.
6. K. Hotate and M. Harumoto, "Resonator fiber optic gyro using digital serrodyne modulation," *J. Lightwave Technol.*, vol. 15, no. 3, pp. 466-472, 1997.
7. K. Hotate and G. Hayashi, "Resonator fiber optic gyro using digital serrodyne modulation -method to reduce the noise induced by the backscattering and closed-loop operation using digital signal processing-," in *Proc. 13th International Conference on Optical Fiber Sensors*, Tu4-1, pp. 104-107, 1999.

8. M. Inai and K. Hotate, “Resonator fiber optic gyro using digital serrodyne modulation -experimental result of system to adjust the imperfect serrodyne waveform amplitude,” *Optics Japan*, 9aA6, pp. 238-239, 2003.
9. K. Iwatsuki, K. Hotate and M. Higashiguchi, “Effect of Rayleigh backscattering in an optical passive ring-resonator gyro,” *Appl. Opt.*, vol. 23, no. 21, pp. 3916-3924, 1984.

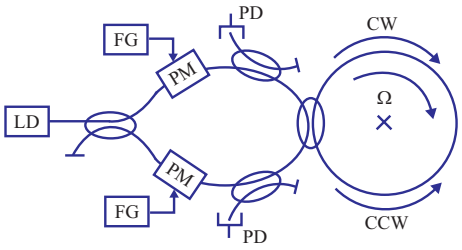


Fig. 1. Basic configuration of R-FOG. LD: laser diode; PM: phase modulator; FG: function generator; PD: photodetector.

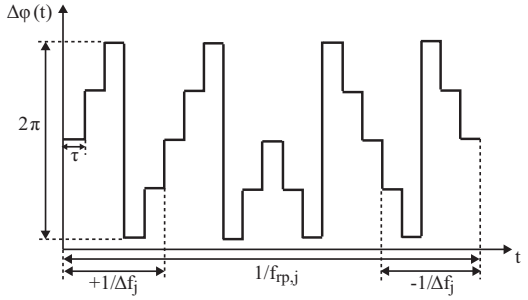


Fig. 2. Hybrid digital serrodyne waveform designed to acquire the resonant frequency.

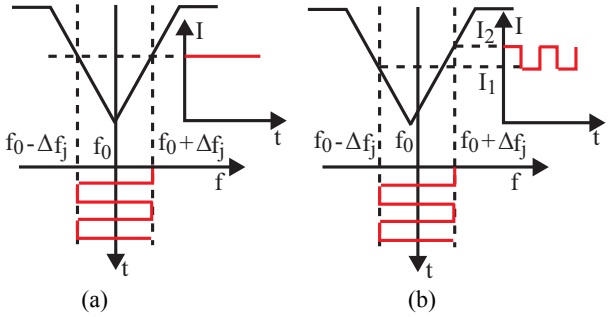


Fig. 3 (a) Resonator output when light frequency is equal to the resonant frequency; (b) resonator output when light frequency is away from the resonant frequency.

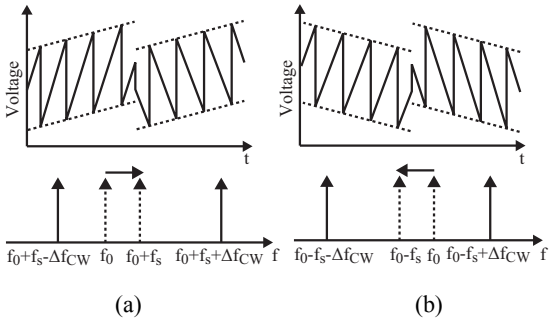


Fig. 4. Central frequency shift by modifying the hybrid digital serrodyne modulation waveform. (a) Central frequency shifted by “+$f_s$”; (b) Central frequency shifted by “-$f_s$”.

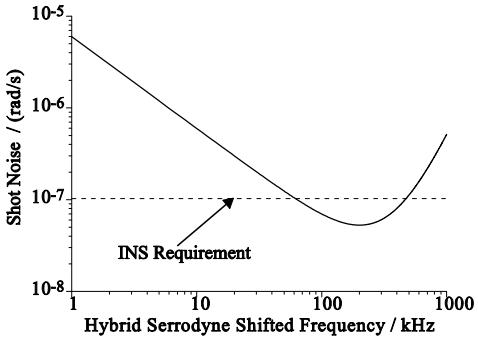


Fig. 5 Shot noise determined detection sensitivity.

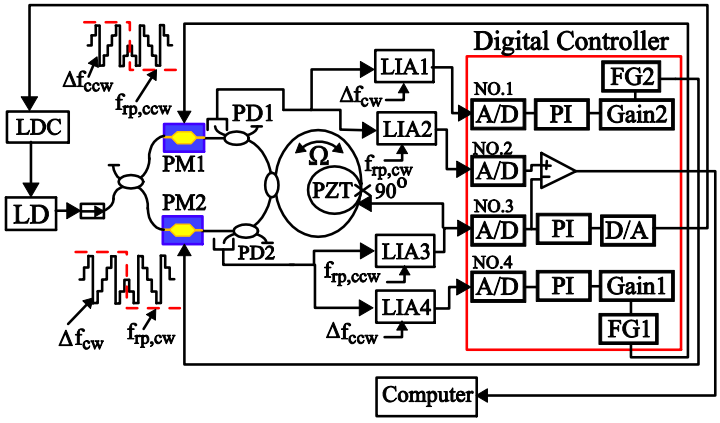


Fig. 6 Experimental setup scheme with the digital processor. LD: laser diode; LDC: laser diode controller; ISO: isolator; PM: phase modulator; FG: function generator; PD: photodetector; LIA: lock-in amplifier, PZT: piezoelectric transducer.

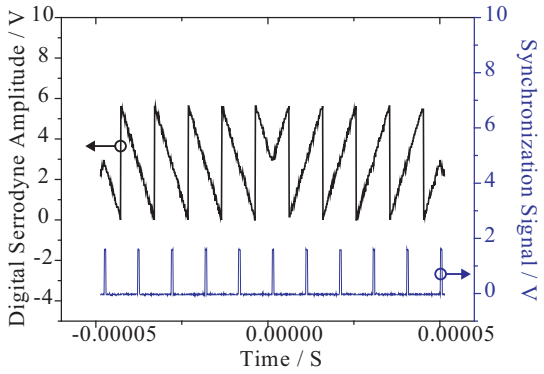


Fig.7 Generated hybrid digital serrodyne modulation waveform and the synchronization signal.

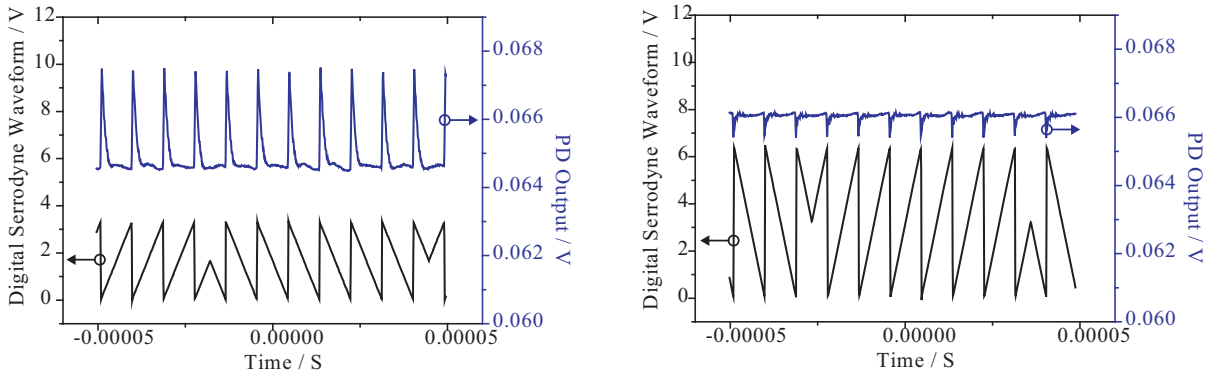


Fig. 8 CCW side photodetector output showing transient behavior of hybrid digital serrodyne modulation with different amplitude: (a) 3.4V, (b) 6.3V.

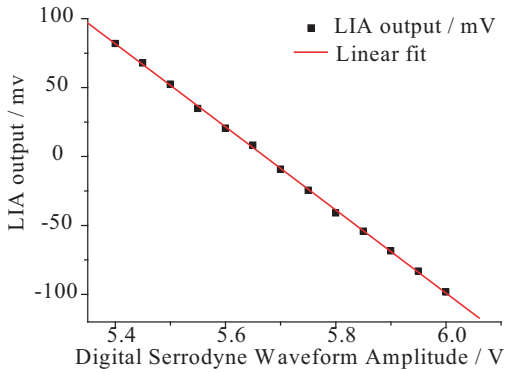


Fig. 9 LIA4 output as a function of modulation amplitude.

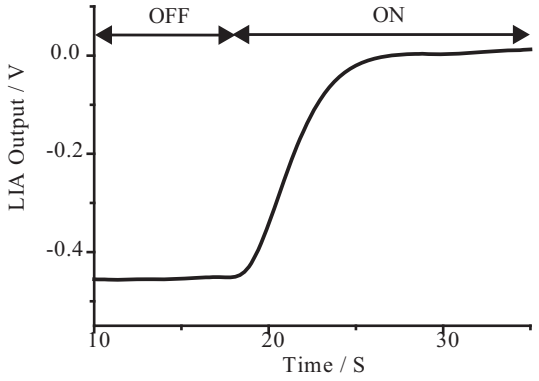


Fig. 10 LIA4 output before and after the 2π voltage feedback loop is on.

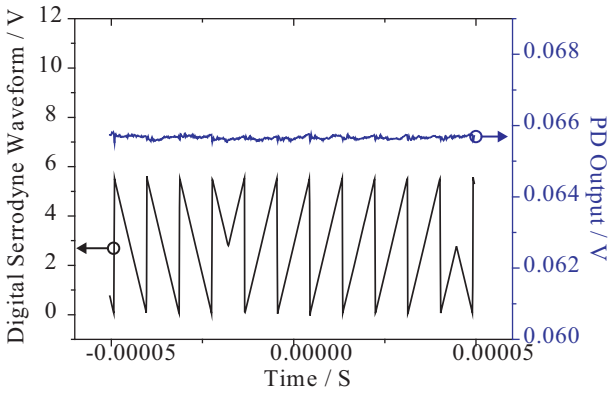


Fig. 11 CCW side photodetector output when the 2π voltage of the phase modulator is adjusted.

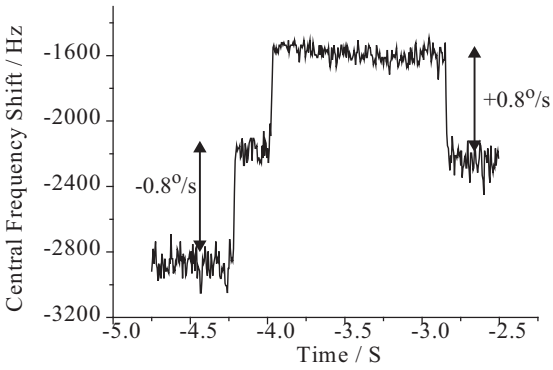


Fig. 12 Quasi-rotation measurement result.

# Wireless-Zigbee Strain Gage Sensor System for Structural Health Monitoring

**Hiroshi Ide[1], Frank Abdi[1], Rashid Miraj[3], Chau Dang[1], Tatsuya Takahashi[1], Bruce Sauer[2]**

[1]Alpha STAR Electronics, Long beach, CA, USA
[2]OCM Test Laboratories Inc., 3883 East Eagle Dr., Anaheim, CA, USA
[3] University of California at Irvine (UCI), Department of Civil and Environmental Engineering, Irvine, CA, USA

## ABSTRACT

A compact cell phone size radio frequency (ZigBee) wireless strain measurement sensor system to measure the structural strain deformation was developed. The developed system provides an accurate strain measurement data stream to the Internet for further Diagnostic and Prognostic (DPS) correlation. Existing methods of structural measurement by strain sensors (gauges) do not completely satisfy problems posed by continuous structural health monitoring. The need for efficient health monitoring methods with real-time requirements to bidirectional data flow from sensors and to a commanding device is becoming critical for keeping our daily life safety. The use of full-field strain measurement techniques could reduce costly experimental programs through better understanding of material behavior. Wireless sensor-network technology is a monitoring method that is estimated to grow rapidly providing potential for cost savings over traditional wired sensors. The many of currently available wireless monitoring methods have: the proactive and constant data rate character of the data streams rather than traditional reactive, event-driven data delivery; mostly static node placement on structures with limited number of nodes. Alpha STAR Electronics' wireless sensor network system, ASWN, addresses some of these deficiencies, making the system easier to operate. The ASWN strain measurement system utilizes off-the-shelf sensors, namely strain gauges, with an analog-to-digital converter/amplifier and ZigBee radio chips to keep cost lower. Strain data is captured by the sensor, converted to digital form and delivered to the ZigBee radio chip, which in turn broadcasts the information using wireless protocols to a Personal Data Assistant (PDA) or Laptop/Desktop computers. From here, data is forwarded to remote computers for higher-level analysis and feedback using traditional cellular and satellite communication or the Ethernet infrastructure. This system offers a compact size, lower cost, and temperature insensitivity for critical structural applications, which require immediate monitoring and feedback.

*Keywords*: ***Wireless strain sensor, Infrastructure, Wheatstone Bridge, Structure Health Monitoring, Static node, Mobile node, Mesh Network, ZigBee***

## 1. INTRODUCTION

Normally a simple structural fault can lead to serious damage. Therefore, detecting the fault quickly and issuing appropriate warnings to prevent disasters are critical but it generates wide-ranging technical challenges. Real-time monitoring of full field strain measurement over a large area has been utilized by many researchers. Development of a practical optical fiber system for health monitoring composite structures using light weight instrument technology Bragg grating optical sensors (FBG's) have shown great promises, but are time consuming (the handling of the optical fiber) during the manufacturing process, expensive to implement, unreliable due to breakage of fiber connectors, and hard to repair [1].

Traditionally, structural deformation detectors need to monitor the structure in a certain way and can be time consuming as well as costly. The most crucial deficiency of such systems is their lack of communication methods for notification of structural abnormality quickly. This is where a wireless monitoring device can be used and information can be transmitted to off-site locations effectively.

Photonics in the Transportation Industry: Auto to Aerospace II, edited by Alex A. Kazemi, Bernard C. Kress
Proc. of SPIE Vol. 7314, 731403 · © 2009 SPIE · CCC code: 0277-786X/09/$18 · doi: 10.1117/12.819358

There are many wireless detection/communication methods already in the market. One is real-time structural deformation and temperature monitoring system using the off-the-shelf strain gauges. These detecting systems, combined with a wireless communication method such as Wi-Fi or ZigBee based mesh network and a global positioning (GPS) have become more popular. The current systems come with batteries and their monitoring, processing and/or communicating capabilities are still limited [2].

In order to overcome these problems a better structural deformation detection system of Alpha STAR wireless sensor network (ASWN) has been introduced. The system detects deformation effectively and efficiently in real-time at early stages of damage. Each sensor module in the system is small in size but has a radio and is battery-operated for autonomous monitoring. Many sensor modules can be scattered throughout a structure to monitor its environmental conditions, deformation, storing the results in buffers until wireless transmission begins. The sensor modules, repeaters and a coordinator can form wireless MESH networks. Once sensors detect deformation abnormality, the condition is reported to the engineering center directly or is analyzed at each sensor location and result reported to the center via hops within the MESH and to the existing Ethernet network infrastructure, i.e., Internet.

The sensor module can be designed so that each sensor node will have its own processor to pre-process the data before it is sent wirelessly. Thus the system works more efficiently by reducing the radio transmission period. System efficiency can be enhanced by using the intelligent wireless MESH method with reliable and robust networking characteristics (i.e., "self configuring" and "self healing") specifically tuned to this system. If one path fails because of obstructions in the signal path, a defective node, or multipath attenuation, the signal can find one or more alternative routes.

The significance of this development is integration of two existing technologies; the structure strain sensor [2-3] with the IEEE 802.15.4 (ZigBee) [4] based flexible wireless protocol and structure safety judgment tool/analysis based on most updated FEM system, GENOA [11]. GENOA uses leading edge technology from the fields of composites, conventional structures and efficient computing sciences to deliver unequaled ultra-rapid performance and analytical capability directly into the hands of today's engineers. Especially, GENOA's multi-scale (Micro-macro mechanics) progressive failure analysis, a durability/reliability life prediction tool is designed to improve the limitation of commercial FE tools in composite. Genoa utilizes a mechanistic failure theory utilizing critical intrinsic properties of the polymeric matrix and the fiber reinforcement materials to asses the onset of damage initiation, damage progression and the ultimate residual strength. The wireless technology allows users to select type of analysis required. Many sensor modules are scattered throughout an entire specimen to monitor the structural conditions as seen in Figure 1. The individual strain gage signals will be transmitted to a PC where GENOA resides. Once GENOA picks these signals, it will convert them into usable strain/stress parameters to be processed and analyzed further. Since each signal is associated with specific geometry information and time, streaming the data will provide dynamic information to be used within GENOA. Full-field stress/strain distributions can then be extracted using GENOA's unique nonlinear analysis techniques, thus the data is properly diagnosed and appropriate prognoses will be issued for quick actions to follow.

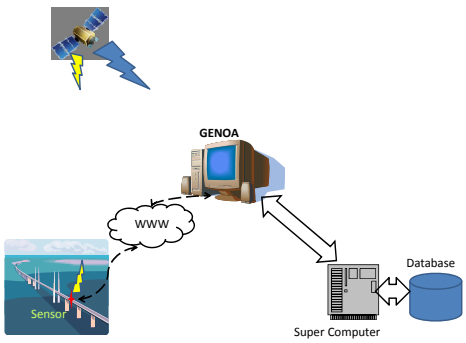


Figure 1. ASWN and GENOA integration concept

In this paper, we will discuss ASWN aspect in details even GENOA is one of key mechanism and it is a vital form of system decision making. The ASWN's hardware includes off-the-shelf strain gauges, electronics components, and controller as show in Figures 2a and 2b. The system controller and the protocol/driver have been written by Alpha STAR Electronics.

a) b)

Figure 2. ASWN System: a) PCB design, b) Connection

## 2.0 SYSTEM DESCRIPTION

For the normal STAR topology, the system conform the following configuration (see Figure 3).

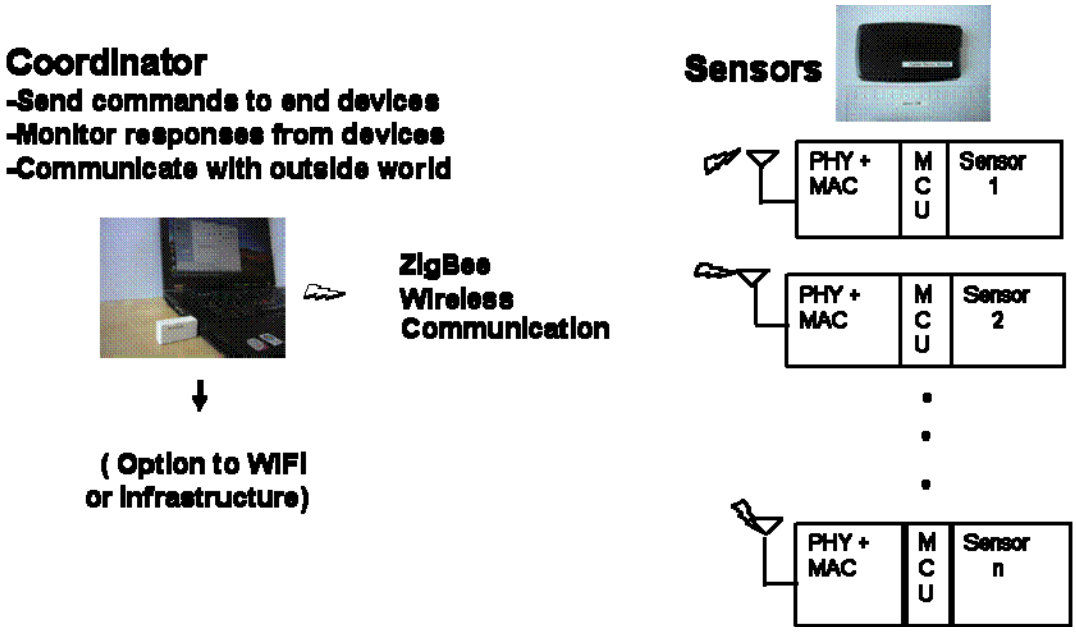


Figure 3. ASWN's STAR topology with each cluster

The ASWN characteristic and its preliminary specification support:

1. Low cost
2. Small & light configuration
3. Low power consumption & simple solution for PC applications
4. Easy to install

Table 1. Preliminary ASWN sensor spec

| Item | Specification |
|---|---|
| RF type | IEEE 802.15.4, ZigBee standard |
| Range | 15 m typical (50 m LOS) |
| Data Rate | 40 Kbps (100 Kbps max) |
| Max sensor nodes | 16 (soon 100) |
| Power Consumption | 20 mA typical Tx (transmission) and Rx (receiving)<br>1μA in deep sleep, |
| Rx Sensitivity | -94 dBm |
| Box Dimension (L x W x T in mm) | 50.8 x 25.4 x 12.7 |
| Weight (in g) | 30 |

**2.1 Development**

In general, the resistor change at the strain sensor is proportional to the strain change (Eq. 1).

$$\Delta r/R = GF \times \Delta l/L, \quad (1)$$

where $\Delta r$ is resistor value change, R is the original sensor resistor value, GF is a gauge factor (material dependant), $\Delta l$ is change in length of the structure and L is the original length of subject material. Because strain, $\varepsilon$, is defined as $\Delta l/L$ and GF is a known number of 1.5-1.7 (normally 2 is used), Equation 1 can be expressed as

$$\varepsilon = \Delta r/R \div GF. \quad (2)$$

Eq. (2) shows the output electronics signal can be forwarded to the module's main circuit for the analog to digital conversion (ADC). The processed digital signal is converted to a certain interface signal format, i.e., serial peripheral interface (SPI) to be transmitted by the ZigBee's PHY chip.

The sensor module consists of the sensor daughter ADC board, ACAM PS021 [7], ZigBee chips, MCU and a flash memory as shown in Figure 4. The module will be battery operated with enough memory space to hold firmware. The capacity size of EEPROM and MCU will determine ability to process the data locally. At this phase, they are considered optional and we use MCU and memory within the ZigBee chip.

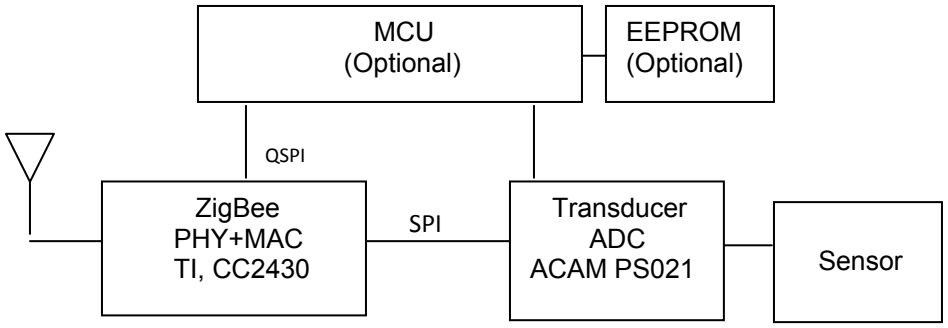


Figure 4. ZigBee Strain Sensor Module Schematic

Because of the data sampling accuracy, provision of the SPI interface, and auto temperature calibrated mechanism, ACAM's PS021 ADC chip [7] is used. PS021 charges the capacitor to the specified voltage and once it is fully charged, it discharges to the sensor resistor (described above). The discharge time is monitored precisely so that slight change in R of the structure will become delay in the discharge. The charge/discharge will be repeated 8 times per digitization sampling cycle. PS021 takes total of 50,000 cycles of sampling to make sure same result should be obtained and each cycle should be 18~22 bits accuracy. PS021's sampling rate is 15 ps (pico second or 15 x $10^{-12}$

second) where normal capacitor discharges about 2~100 μ s (micro second or 50 x $10^{-6}$ second) and the time delay is in normally expressed in ns (nano second) unit. Apparent strain by temperature change shows much slower than this sampling rate, PS021 can pick up slight changes and it is considered plenty accurate.

### 2.2 Sensor Module Firmware

Firmware for ZigBee physical layer (PHY), media access control layer (MAC) and sensor interface to be loaded in the MCU buffer are developed. The firmware has two roles. One is administrating and controlling the sensor circuit and the other is controlling ZigBee chips. Logic of sensor data gathering timing and the method, the transducer interface, ZigBee chip interface, decision to store or send and other commands for sensor circuit were identified and defined. The basic firmware development determines the system efficiency including the driver performance. The software structure is designed so that many PHY and MAC parameters can be operated from the driver. This will enable system expandability and additional capability such as autonomous detection of structure abnormality without rewriting the entire driver/firmware.

The current stack and the driver architecture include the basic handling of the sensor application layer as shown in Figure 5. The sensor interface layer is independent so that other type of sensors can be integrated into the system easily.

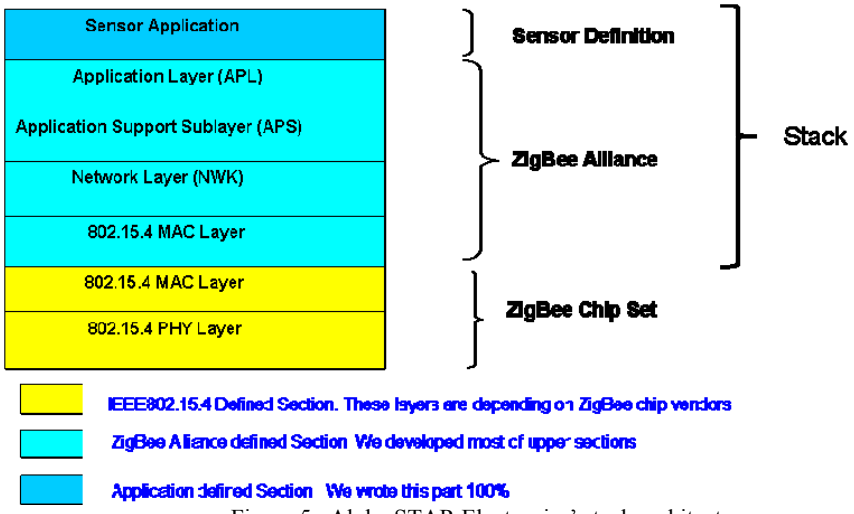


Figure 5. Alpha STAR Electronics' stack architecture

### 2.3 System Validation Test and Debugging

Strain gauge terminal connections on the sensor module are shown in Figures 6 and 7. This setup reads two values of strain values for either a 2-full bridge configuration or a 2-half bridge configuration.

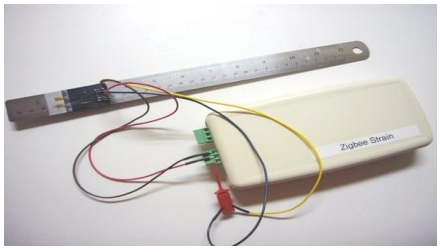

Figure 6. Test setup.

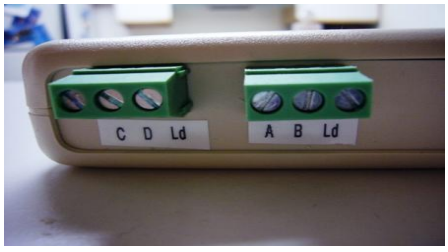


Figure 7. Strain gauge connectors

The wiring diagrams for these cases are shown in Figures 8 and 9.

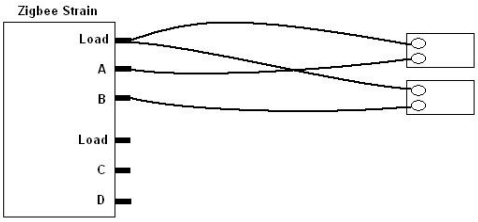


Figure 8. ½ Bridge wiring configuration

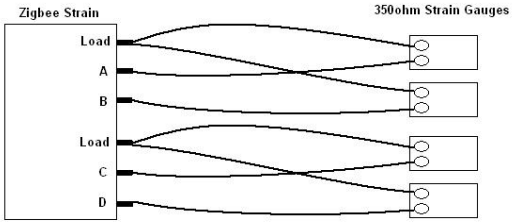


Figure 9. Full Bridge Strain Gauge Connection

In order to verify the accuracy (sensitivity as a system) of ASWN unit, it was compared with the reference system at the University of California, Irvine, UCI civil engineering lab, NI PXI 1042/Q Data Acquisition System ("NI PXI 1042/Q") by measuring bending strain of a metal coupon simultaneously. The coupon, a steel metal strip (10 x 2 x 1/8 inch), is pulled by a mechanical puller, Tinius Olsen Universal Testing Machine shown Figure 10.

a) Sample strip is pulled by the puller.

b) Puller machine in relative to the data acquisition system. (see ASWN system – PDA – at the right end)

Figure 10. Test Validation of Zigbee Wireless Strain Sensor

### 2.3.1 Test preparation

Two sets of 120 ohm with gage factor of 2.075 strain gauges are pasted on the steel metal strip, front and back, for the half bridge configuration as shown in Figures 11 and 12. Two gauges are mounted on each side at same distance from the center, so two systems can measure the same load simultaneously. The same strain gauges are used for both NI PXI system as well as ASWN system.

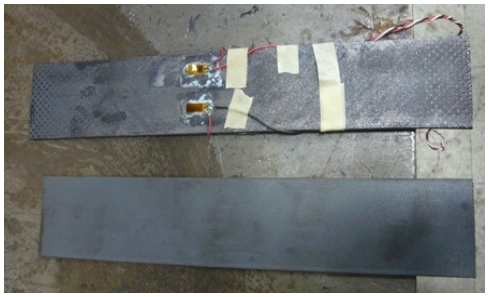

Figure 11. Location of strain gauges (up) and original coupon (bottom)

Figure 12. Strain gauges are mounted on the sample strip. Two more gauges are glued to the other side of strip, too.

### 2.3.2 Test Setup

A simple setup schematic is shown in Figure 13.

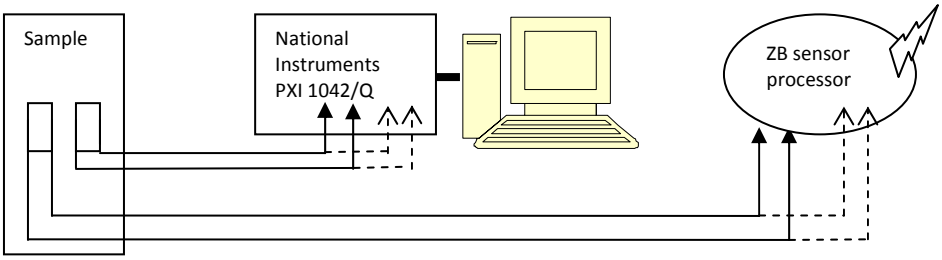


Figure 13. ASWN test setup illustration

The length of wire between the strain gauges and the NI PXI 1042/Q processor and the ZigBee sensor processor is about 3 feet (NI PXI 1042/Q and ZB sensor processor are located at the same location). Therefore, noise received by these wires can be considered minimum. The NI PXI 1042/Q reference Wheatstone bridge measuring equipment and Zigbee wireless sensor system are seen in Figure 14.

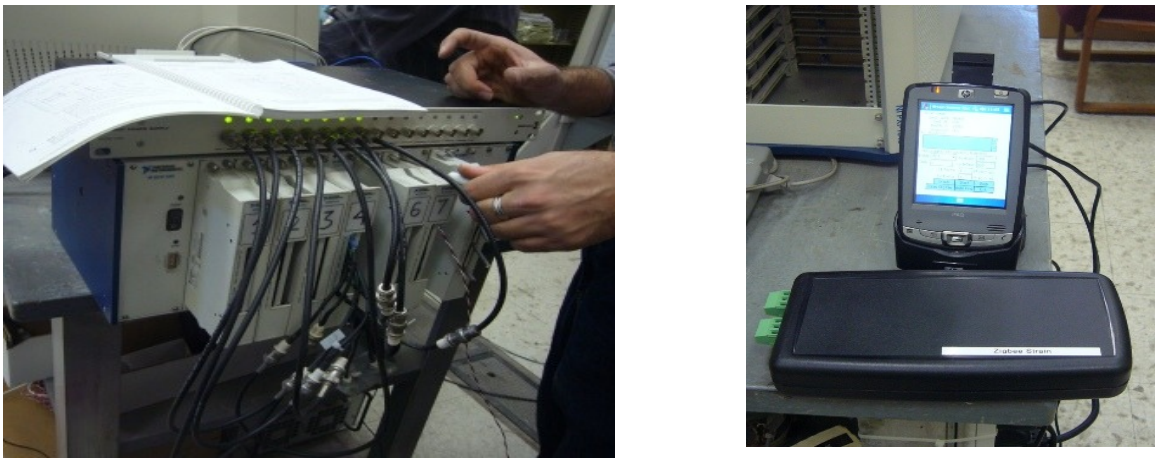

Figure 14. NI PXI 1042/Q (left) and Zigbee sensor and PDA (right); note the complexity of wiring for the reference system.

### 2.3.3 Test Environment

The test was conducted in a room size of 17' by 25' with cemented walls and floor as seen in Figure 15. The thickness of wall and floor is unknown. There are many equipment and metallic obstacles in the lab. It is considered a typical university lab environment. The Zigbee host PDA, however, was able to receive measurement data anywhere in the room without losing the sensitivity and signal strength.

Figure 15. Test lab with equipment

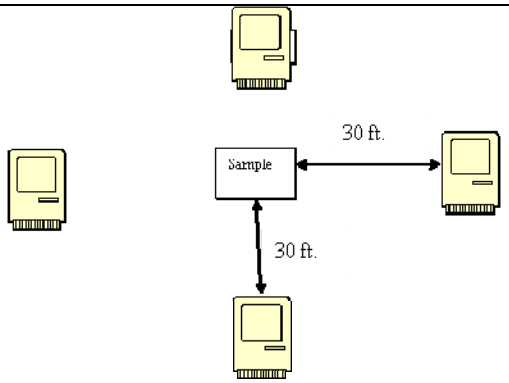


Figure 16. Wireless range test

# 3.0 RESULTS

## 3.1 Metal Coupon Test

The experiment for a metal coupon (see Figure 11) started to measure the strain at 8 Hz, and the load is gradually applied to the coupon, from 0 to 8,000 lbs, then back to 0 lb. The result is shown in Figure 17. The data sampling rates for the NI PXI1042/Q (the reference) and the ZigBee wireless processor's data sampling rate are both set to 8 samples per second. It takes approximately 30 seconds to become stabilizing and become ready to measure.

Time zero represents after calibration period is finished for both systems. There are many factors that can cause differences in the two systems. But we observed similar curves for the reference system and the Zigbee Strain sensor unit. Figure 14 shows Zigbee system has less noise than the reference system. The strained coupon and the original coupon are compared side-by-side at Figure 11. It clearly shows the top coupon has been stressed.

In order to see wireless sensor's reaction for an abnormal case, we installed the strain gauges near the center of the coupon where breakage is expected to occur. The loading condition is the same as previous case except loading is done more gradually. The result is shown in Figure 20.

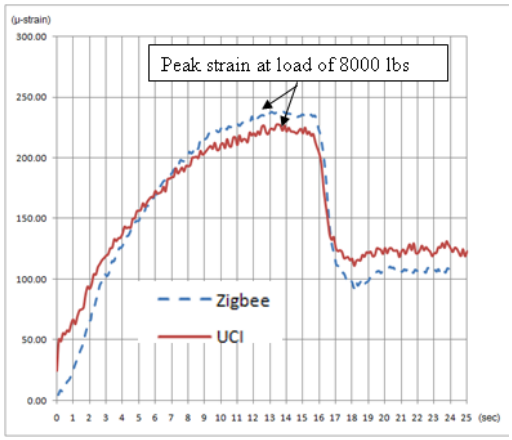


Figure 17. Test result and comparison with experiment

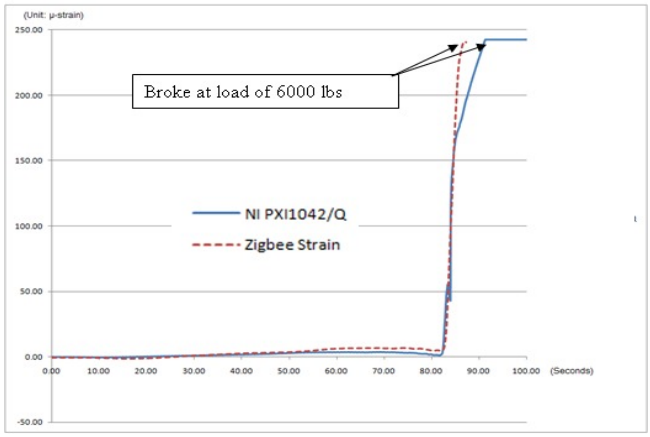


Figure 18. Wireless sensor reaction at the breakage point.

In Figure 17 we observed peak strain of 242.47 μ-strain from the reference system and 240.79 μ-strain from the Zigbee Strain sensor unit. Again, Zigbee wireless system tracks well on the reference system even the condition is not normal (near the fracture point).

## 3.2 Composite Coupon Test

We have repeated the similar tests with using composite coupons. The composite material is typical carbon fiber composite ePlate MH1020 by Mitsubishi Plastic (http://www.yes-mpi.com/tanso/eplate.html) as shown in Figure 19a.

The composite material is fabricated to a dog-bone shape so that it will be forced to fracture in the neck down area. The test coupon size is 10 x 1 x 0.095 in (neck section is about 60%, or 0.615") and the same train gauges as metal case are installed both sides of composite coupon as shown in Figure 19b. Strain gauges cannot be installed side-by-side due to narrow area; they had to be installed head on fashion about the same area (not exactly the ideal situation).

Due to composite materials surface characteristic is different from metals, strain gauges' epoxy bonding force is also expected to be different, and thus installation of strain gauges on the composite surface took significant care and time. Even with cautious preparations and installation bonding became an issue when load was begin to apply. The test coupon is installed to the puller like previous metal coupon and it is shown in Figure 19c.

a) Composite material used in the test.

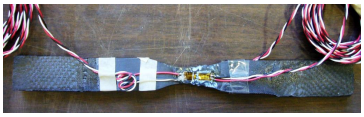

b) Composite coupon with strain gauges

c) composite coupon in the puller

Figure 19. Material and Test Set up

The actual test was performed after several trials of pulling making sure the composite fractures at the expected area since earlier tests showed sample fractured crimped points. Also, loading was applied even gradually (twice slower than metal cases) making sure the strain gauges do not peel off. These trials carefully performed to see strain gauge's bonding condition as well as hearing cracking sound so that to study the loading process. One of controlled tests result for up to 2000 lbs of load is shown in Figure 20.

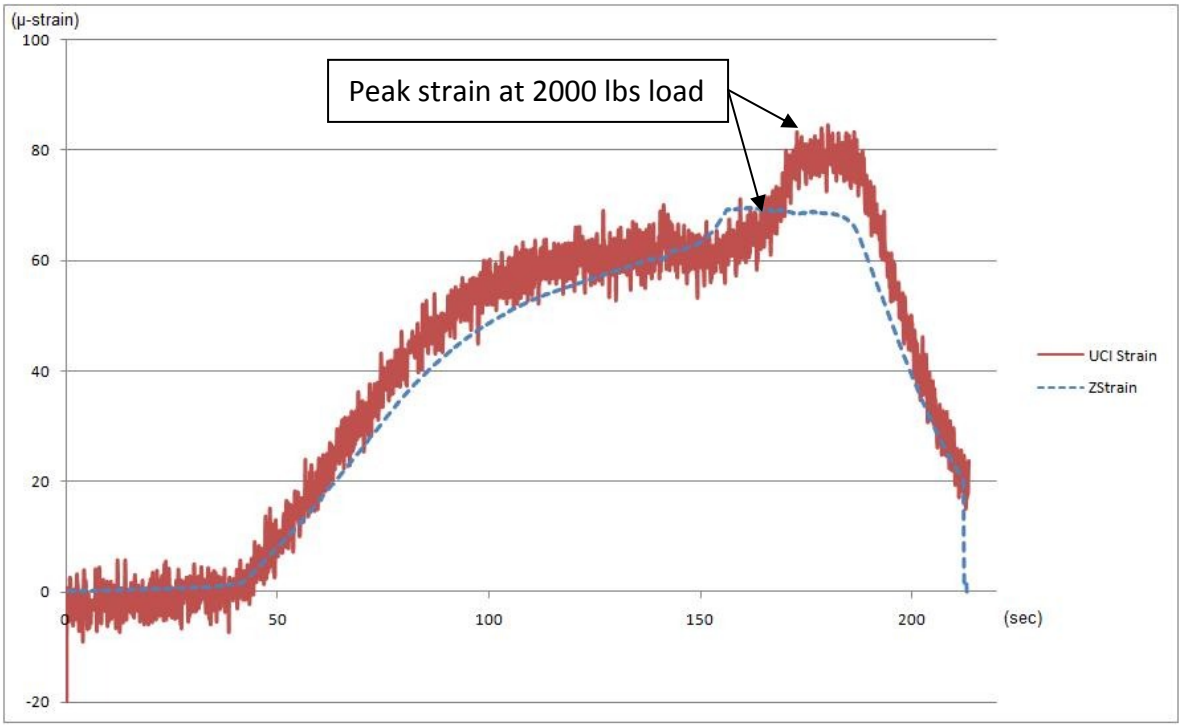


Figure 20. Strain vs. Load for a composite coupon

Figure 20 shows general trend of composite internal energy build up to the predetermined safety loading of 2000 lbs where strain gauges tend to peel off around this loading from previous trials. The strain rate difference near the peak load is due to strain gauge's bonding characteristic. If strain gauges are bonded in the fracture surface side, it will show earlier strain drop while the other surface still may be experiencing load holding.

Finally, we have prepared the composite coupon fracture test. Unfortunately, strain gauges for the reference (UCI equipment) did not work and only ZigBee wireless data are available. Therefore, no comparison was performed. The result is shown in Figure 21. This time the applied load was increased continuously to 9000 lbs for about 170 sec when crack sound was heard. After reaching to the max load, the load was kept without increasing until complete fracture occurred. This figure shows typical composite characteristic of holding partial load even after showing internal fracture 1$^{st}$ time (after 170 sec up to about 240 sec). The structure finally gave out at around 250 sec. Metal fracture would drop the strain rather suddenly as shown in Figure 17 above. Although, there is no direct comparison available for this test wireless system seems to pick up key element for the structure deformation assessing from Figures 17, 18 and 20.

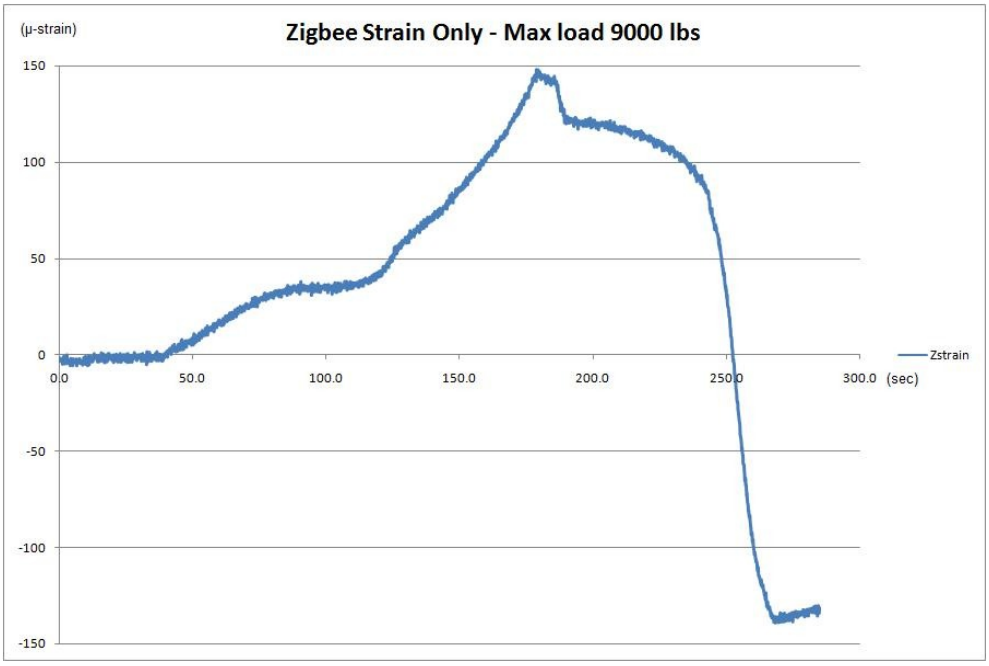

Figure 21. ZigBee strain sensor vs. load result for a composite coupon

The fractured composite coupon is shown in Figure 22.

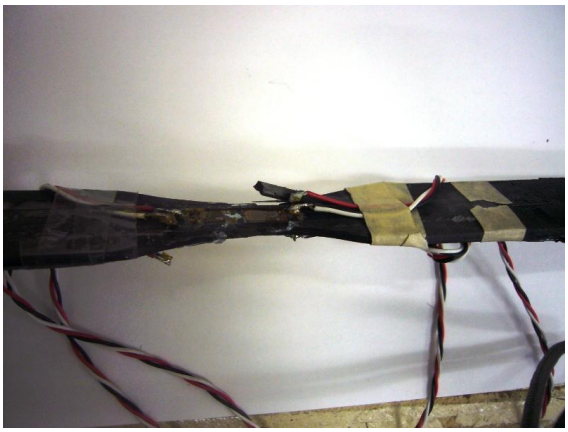
Figure 22. Fractured composite coupon

## CONCLUSIONS

It has been shown that the ZigBee wireless system works well in both metal and composite structural samples for strain experiments. Also, the system has shown that the wireless data sample rate may be sufficient enough to pick up important structural features. Preparations, especially for strain gauges installation, to composite materials continue to be a serious issue since the test results depend highly on the gauge's bonding condition.
Changing the sample data rate, power management (for radio transmission) and use of ease will be added as improved version and we will be performing similar test for composite materials next.

A wireless sensor system to measure the structural strain deformation was developed. Although system-level power consumption and very large scale dataset transmissions (within the Internet) were not tested, the basic data process and

wireless operation worked well. In fact, it has been proven that the ASWM is accurate enough for strain measurement using existing technologies, as-is and/or modified. Thus, the system can be expanded to a larger extent economically. With the inclusion of efficient MESH protocol, we intend to improve wireless communication significantly.

Normally, structure deformation monitoring requires multiple sensors, gathering data from those sensors quickly, processing the information stream, and sending the results to remote locations for engineering evaluation. All these processes must be done quickly and accurately. Therefore, the system cost can be prohibitively high. ASWN can be one of quick solutions to that problem.

## 5.0 ACKNOWLEDGEMENTS

The author wishes to acknowledge Mr. A NASR, and Professor A. Mosallam of University of California at Irvine (UCI) for thier technical support in test and validation. The authors wish to thank the U. S Army AMSTA-TR-E/BRDG (Contract No. W56HZV-04-C-0022) for supporting this SBIR effort.

## 6.0 REFERENCES

[1] Volanthen, M., Diamanti, K., "Development of a Practical Optical Fibre System for Health Monitoring Composite Structures," AIAA-2006-2213, Newport, RI, (2006).
[2] Ide H., Abdi F., Dang C., Takahashi T., Sauer B., "Development Of A Wireless Strain Sensor System For Structural Health Monitoring," American Society Of Civil Engineers International Committee, Los Angeles Section, 5th International Engineering and Construction Conference (IECC'5), (2008).
[3] Measuring strain with strain gauges, National Instruments, http://zone.ni.com/devzone/cda/tut/p/id/3642 (2008).
[4] The strain gage, Omega, http://www.omega.com/literature/transactions/volume3/strain.html (1997).
[5] IEEE Computer Society, "802.15.4, Wireless Medium Access Control and Physical Layer Specifications for Low-Rate Wireless Persona Area networks," IEEE standard 802.15.4 (2003).
[6] ZigBee Alliance Board of Directors, "ZigBee Specification," ZigBee Alliance Doc # 053474r06, ver 1.0, (2005).
[7] SDIO-ZigBee Programmer's Guide, Product Manual, www.embeddedworks.net/cguys/ (2005).
[8] PS021 strain gauge transducer by ACAM, http://www.acam-usa.com/Content/English/ps021/ps021_1.html
[9] Texas Instruments data sheet for CC2420, http://focus.ti.com/lit/ds/symlink/cc2420.pdf (2007).
[10] ATMEL Atmega128 data sheet, (2008).
[11] http://www.engr.sjsu.edu/bjfurman/courses/ME106/ME106pdf/intro-atmel.pdf
[12] http://www.ascgenoa.com

# Design, study and achievement of a fiber optic amplitude modulation sensor for angular position detection: Application to an automotive steering system

Nicolas Javahiraly, Cédric Perrotton, Ayoub Chakari and Patrick Meyrueis

Photonic Systems Laboratory, Louis Pasteur University,
Bvd Sébastien Brant, 67400 Illkirch, Strasbourg, France

## ABSTRACT

The reliable, accurate and low cost measurement of angular position is an important challenge for numerous industries such as aerospace or automotive industries. We propose a new optical fiber angular position sensor connected to an automotive power steering column. This sensor allows the measurement of the angular position of a car steering wheel over a large range (± 3 turns of wheel). The wheel rotation induces micro-bending in the transducer part of the optical fiber sensing system. This system operates as an amplitude modulation sensor based on mode coupling in the transducing fiber in the case when all the modes are equally excited. We study the sensor's response both theoretically and experimentally with a multimode step index optical fiber [Rf (fiber radius) = 300µm; $r_c$ (core radius) = 50µm; $n_c$ (core index) = 1,457; N.A. = 0, 22 and the wavelength is 632, 8 nm at the ambient Temperature (20°C)]. This sensor has been tested between (-3x360) and (+3x360) degrees with 0,147 sensitivity. We show that the sensitivity can be controlled as a function of the sensor's length and the study of the sensor's output power as a function of the angular position has been achieved. We compare modeling and experimental validation and we conclude by a perspective of what could be soon an industrial sensor.

Keywords: Sensor, fiber optic, amplitude modulation, micro-bending.

## 1. INTRODUCTION

Numerous areas of research in the aerospace and automotive industry try to solve problems through answers to similar constraints. The reliable, accurate and low cost measurement of an angular position is an important challenge for numerous industries, such as the aerospace or automotive industries.
Several techniques have been proposed and tested to determine the angular position data such as magnetic techniques [1-2]. Lots of studies are being performed using capacitive techniques [3-4] with limited industrial applications. There has also been work using a conductive rotor blades fixed to a non conductive shaft. The angular position data can currently be determined by several optical techniques such as interferometry methods [5]. Some optical techniques using fiber optic have been achieved. For these angular position sensors, the principle is based on light modulation when a constraint is applied to the fiber, constraint which modifies the light properties like polarization or frequency… [6].

We propose a new optical fiber angular position sensor connected to an automotive power steering column. This sensor operates as an amplitude modulation sensor based on modes coupling in the transducing fiber in the case when all the modes are equally excited.

## 2. PRINCIPLE OF THE ANGULAR POSITION SENSOR

The principle is based on the light modification passing through an optical fiber to which a perturbation is applied.

Photonics in the Transportation Industry: Auto to Aerospace II, edited by Alex A. Kazemi, Bernard C. Kress
Proc. of SPIE Vol. 7314, 731405 · © 2009 SPIE · CCC code: 0277-786X/09/$18 · doi: 10.1117/12.819936

We employ global detection to obtain the propagation losses due to the coupling between the guided modes and the radiated modes. The determination of the coupling is defined by the ratio of the mode's order m and the group mode number M.
The propagation constant as a function of the normalized order m/M of a modes group is defined by:

$$\beta = kn_c\left[1-2\Delta\left(\frac{m}{M}\right)^{\frac{2\alpha}{\alpha+2}}\right]^{\frac{1}{2}} \qquad \text{and} \qquad \Delta = \frac{n_c^2-n_g^2}{2n_c^2} = \frac{AN^2}{2n_c^2}$$

Where $n_c$ is the core index of the fiber, $n_g$ the clouding index and NA is the Numerical Aperture.

The modes are solutions to the propagation general equations and can be coupled to one another due to fiber irregularities.
The space between two modes is:

$$\Delta\beta = \beta_m - \beta_{m-1} = -2\frac{\sqrt{\Delta}}{r_c}\left(\frac{\alpha}{\alpha+2}\right)^{1/2}\left(\frac{m}{M}\right)^{\frac{\alpha-2}{\alpha+2}}$$

Two modes will be coupled by a perturbation if their propagation constants are separated by a spatial frequency in the perturbation spectra.
A $\Lambda$ wavelength sinusoidal perturbation induces a mode coupling for which the propagation constants are separated by a $2\pi/\Lambda$ spatial frequency.
So to optimize the light attenuation measures in the fiber, we can increase the total losses by inducing a maximum coupling between the guided and the radiated modes by the application of a constraint with an appropriated periodicity.
The phenomenon is effective when the spatial period corresponds to the modes coupling period.
We apply a $\Lambda$ microbending period to the fiber. It exists a $\Lambda$ for which the modes coupling is maximum.

$$\Delta\beta = \beta_m - \beta_{m+1} = \pm\frac{2\pi}{\Lambda}$$

For a step index fiber ($\alpha=\infty$), we have:

$$\Delta\beta \Rightarrow \frac{2\sqrt{\Delta}}{r_c}\left(\frac{m}{M}\right) = \frac{2\pi}{\Lambda}$$

For a multimode step index optical fiber, we have:

$$\frac{m}{M} = \frac{\sqrt{2}\pi.r_c.n_c}{NA.\Lambda}$$

Where $r_c$ is the core radius, $n_c$ is the core index; NA is the Numerical Aperture and $\Lambda$ the perturbation wavelength.
It is necessary, in our case, to define the perturbation wavelength when torsion is applied to the fiber as:

$$\Lambda = 2r + 2r_f$$

where r is the curve radius and $r_f$ the fiber radius.

To understand the principle of our sensor, it is necessary to describe the microbending system.
The microbending system, which function is to hollow a total excitation of the modes during the perturbation, is necessary in order to detect the angular position of the wheel, based on the torsion fiber.

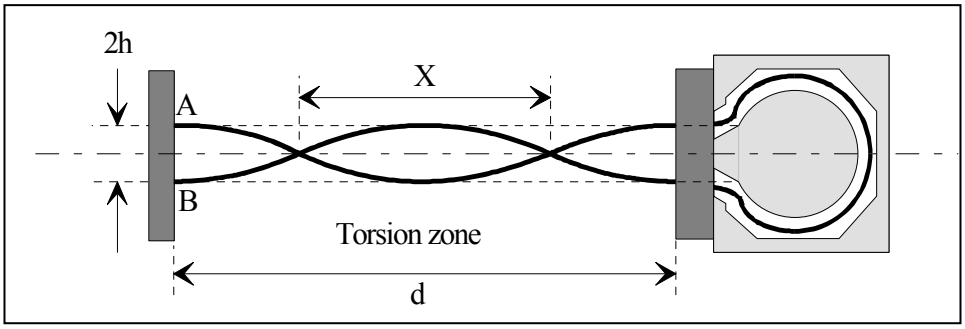


*Figure 1: The torsion zone*

The perturbation wavelength can be written as follow:

$$\Lambda(\theta) = \frac{h}{2} + 2.\frac{\pi^2.d^2}{h}.\frac{1}{\theta^2} + 2.r_f$$

where θ is the rotation angle, $\Lambda$ the perturbation wavelength, $r_f$ the fiber total radius curve, h is the torsion amplitude and d the length of the fiber torsion zone.
The output intensity is given by:

$$I_L = K.\frac{m}{M}(\theta)$$

## 3. THE EXPERIMENT ARRANGEMENT

### 3.1. Microbending system.

The principle is to study the amplitude response of a step index multimode fiber in order to determine the losses introduced by the microbending.

A λ wavelength is emitted by a LED and injected in the step index multimode fiber. The fiber optic passes through the microbending system composed by two periodical arrangements of metallic cylinders. These cylinders have got a Λ period arrangement and are Λ/2 shifted. These micro curves will modulate the light signal detected at the output system by an optical detector.

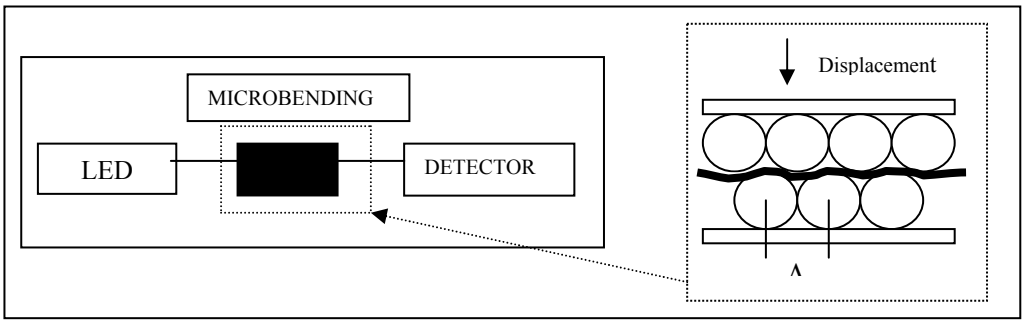


*Figure 2: The microbending system*

When a pressure is applied to the fiber, it introduces modes coupling between the guided modes and the radiated modes. So, our purpose is to find the right displacement in order to have a maximum coupling between the guided modes and the radiated modes.

### 3.2. The experimental arrangement

The experimental setup is presented in figure 3. The source is a diode laser emitting at 632,8nm. The beam is injected in the multimode step index optical fiber ($r_f$=300µm; $r_c$=50µm; $n_c$=1,457; N.A. = 0, 22).
A Microbending system (MB) is attached to the fiber before it enters the sensitive part of the sensor, which has a variable length d.
This system has been developed to allow a rotation and an automated torsion of the fiber operated by a control command.
The rotation of the mobile part induces torsion in the sensitive part of the sensor, which modulates the signal.

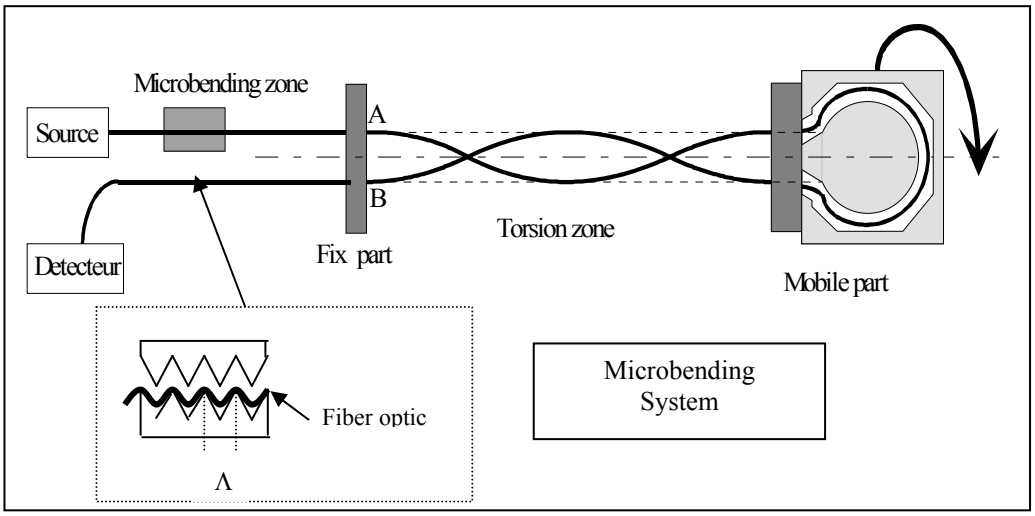


*Figure 3: the experimental setup*

### 3.3 Adaptation to the steering system

The adaptation of our sensor to the steering system is described in figure 4. When a rotation is applied to the wheel (1), the shaft (2) will turn with the same angle due to a system of gear wheels (3).

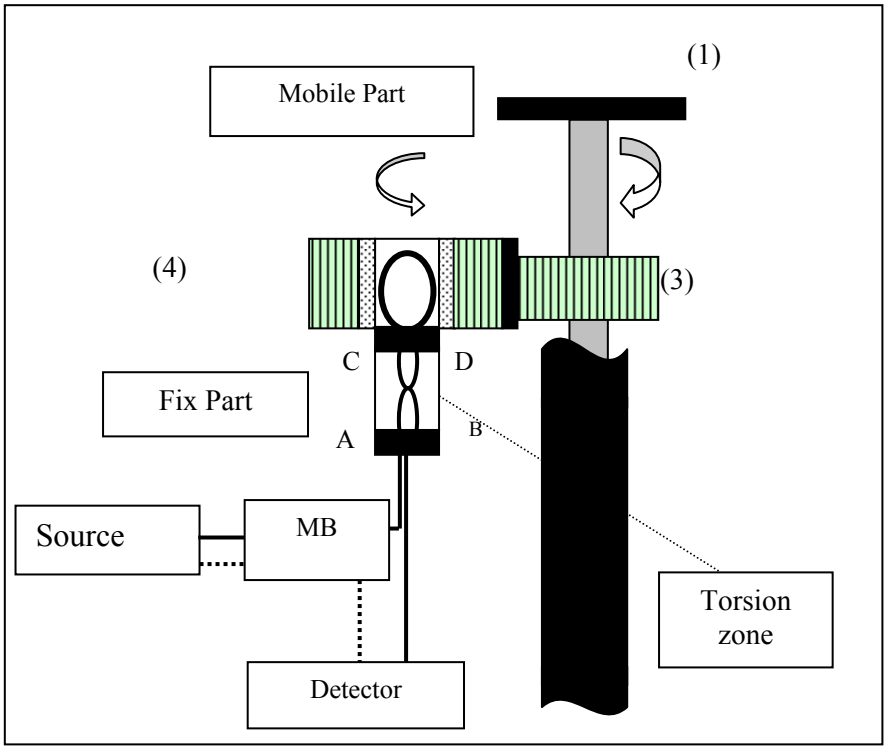


*Figure 4: Application to the steering system*

The loop (4) (to which the fiber is linked) is mobile and induces torsion to the fiber in the torsion zone. The length of the sensitive part (ABCD) depends on how many turns are required and can be adjusted.

## 4. RESULTS

### 4.1. Microbending

After the description of the microbending system, we present the results obtained for two types of fiber using different perturbation wavelengths.

The first fiber, fiber 1 presents a 100µm core radius, a 1,456 core index, a 300µm fiber radius and a 0, 4 numerical aperture. The second fiber ($r_f$=150µm) presents a 50µm core radius and a 0, 22 numerical aperture. Figure 5 and 6 present the transmission rates as a function of the microbending system lateral displacement for different cylinders (of the microbending system) radius.

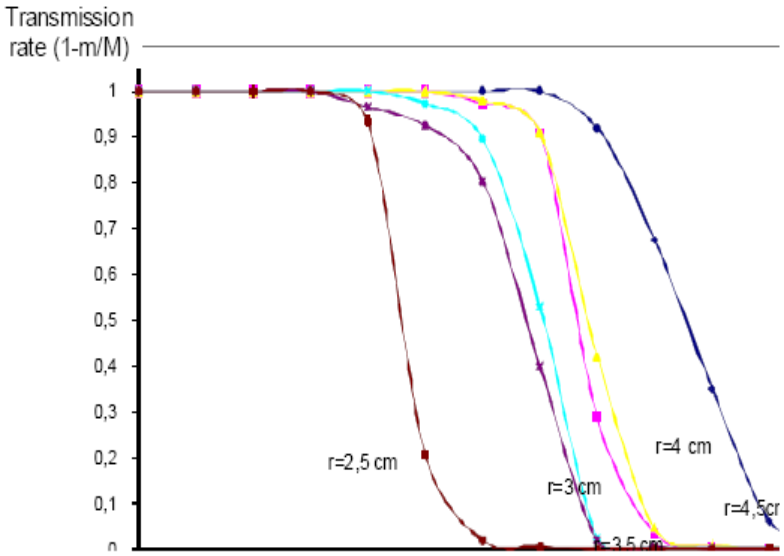


*Figure 5: Transmission rate as function of the displacement. Fiber 1.*

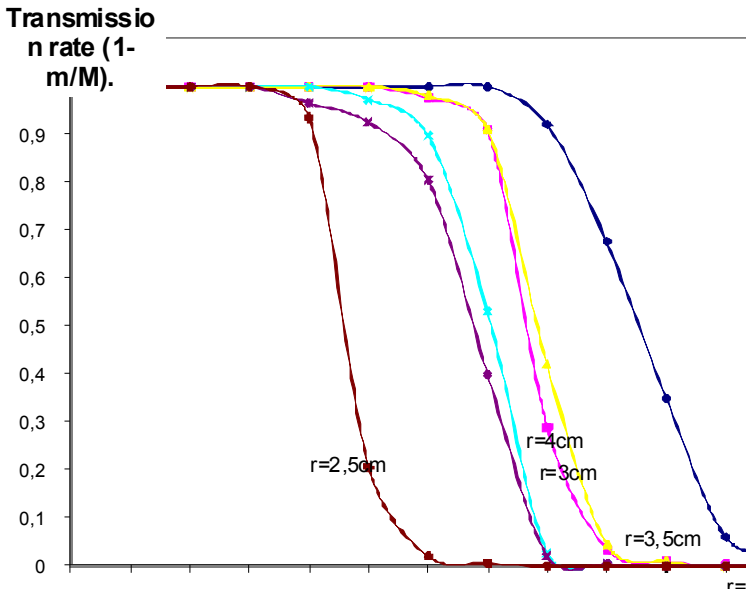


*Figure 6: Transmission rate as function of the displacement. Fiber 2.*

In both cases, the output power is constant up to a d limit. All fiber modes are not equally excited. So, in the case studied, the microbending is created by the torsion of the fiber itself in the torsion zone

### 4.2. Simulation of the sensor

The simulation of the sensor accounts for the results presented in the following figure.

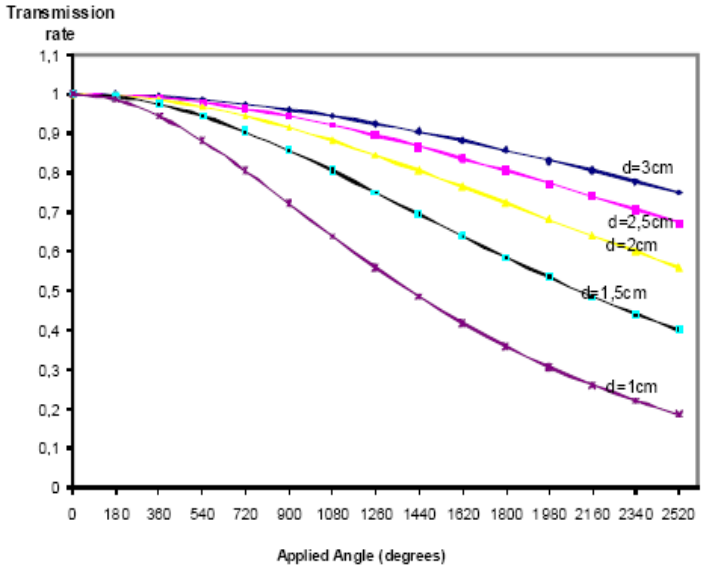


*Figure 7: Transmission rate as a function of the angle.*

The smaller the length of the sensitive part d, the greater the decrease in the transmission rates. Measurements can be made up to a large number of turns of the wheel (6-7 turns).

### 4.3. Experimental results

The transmission rate changes as a function of the number of loops for a fixed distance d.

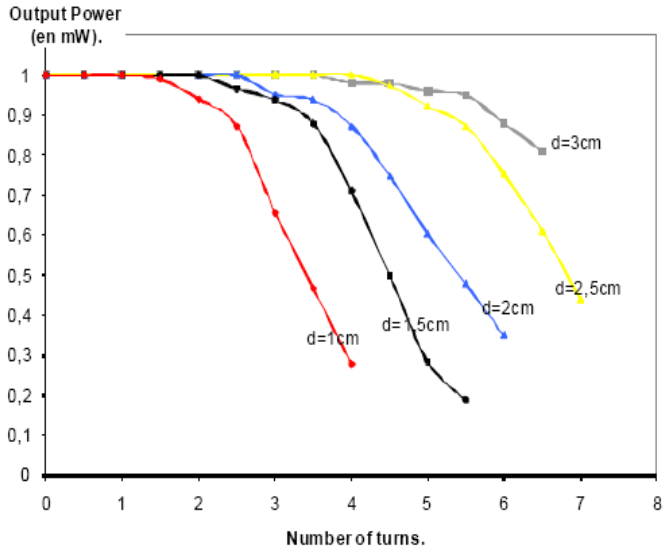


*Figure 8: Output power as function of the number of turns*

This sensor can only be used on the linear parts of these curves. The presence of the plateau can be explained by the fact that all the fiber modes are not equally excited. This can be overcome by applying the microbending system.

So the fiber itself is a microbending system when the torsion is applied to it but to have optimum excitation modes, we can add a "real" microbending system to eliminate this plateau and get to a maximum efficiency. Another way is to have a beam which Numerical Aperture equals or is superior to the fiber Numerical Aperture.

## 5. CONCLUSION

A new optical fiber angular position sensor connected to an automotive power steering column has been achieved.

This sensor is based on the coupling between the guided modes and the radiated modes of the fiber during the light transmission.

We used a multimode step index optical fiber ($r_f$ =300µm; rc=50µm; nc=1,457; N.A. =0, 22) as a transducer and we demonstrated that this sensor allows for the measurement of a car steering wheel angular position over a large range (± 3 turns of the wheel).

We showed too that the sensitivity could be controlled as a function of the sensor length. The comparison between the theoretical and the experimental results give us good perspectives of what could soon be an industrial sensor in the steering assistance.

## 6. REFERENCES


[1] Popovic R.S., "Not-plate-like Hall magnetic sensors and their applications", Sensors and Actuators A, Vol. A85, pp. 9-17 (2000).

[2] Zongsheng L., Yan C., Zhen J., Dehong H. and Xiaoli Z., "A study on the new two-dimensional Hall angular detector", Journal of Transduction Technology, Vol.14, pp. 14-17 (2001).

[3] Brasseur G., Fulmek P.L. and Smetana W., "Virtual rotor grounding of capacite angular position sensors", IEEE Transductions on Intrumentation and Measurement, Vol. 49, pp. 1108-1111 (2000).

[4] Cermak S.P., Brasseur G. and Fulmek P.L., "A planar capacitive sensor for angular measurement", IMTC 2001. Proceedings of the 18th IEEE Instrumentation and Measurement Technology Conference. Rediscovering Measurement in the Age of Informatics (Cat. No.01CH37188), Vol. 2, pp. 1393-1396, (2001).

[5] Santos J.C. and Cortes A.L., "A new electro-optical method for recovering white light interferometric signals", SBMO/IEEE MTT-S International Microwave and Optoelectronics Conference, Vol. 1, pp. 149-152 (1999).

[6] Mancier N., Chakari A., Meyrueis P. and Clement M., "Angular displacement fiber-optic sensor: theoretical and experimental study", App. Optics, Vol. 34, No. 28 (1995).

# Fiber Optic Emerging Technologies for Detection of Hydrogen in Space Applications

Alex A. Kazemi*
The Boeing Co., Integrated Defense Systems, Anaheim, CA 92806

## ABSTRACT

Hydrogen detection in space application is very challenging; public acceptance of hydrogen fuel would require the integration of a reliable hydrogen safety sensor. For detecting leakage of cryogenic fluids in spaceport facilities, launch vehicle industry and aerospace agencies are currently relying heavily on the bulky mass spectrometers, which fill one or more equipment racks, and weigh several hundred kilograms. Optical hydrogen sensors are intrinsically safe since they produce no arc or spark in an explosive environment caused by the leakage of hydrogen. Safety remains a top priority since leakage of hydrogen in air during production, storage, transfer and distribution creates an explosive atmosphere for concentrations between 4% (v/v) – the lower explosive limit (LEL) and 74.5% (v/v) – the upper explosive limit (UEL) at room temperature and pressure. Being a very small molecule, hydrogen is prone to leakage through seals and micro-cracks. This paper describes the development of fiber optic emerging technologies for detection of hydrogen in space applications. These systems consisted of Micro Mirror, Fiber Bragg grating, Evanescent Optical Fiber and Colorimetric Technology. The paper would discuss the sensor design and performance data under field deployment conditions.

**Key Words:** Fiber Optic Sensors, Hydrogen Cryogenic Detection, Leak Monitoring, Space Applications

## 1. INTRODUCTION

Lunch vehicles and other satellite users need launch services that are highly reliable, less complex, easier to test, and cost effective. Safety concern within ground support personnel and safety requirements to sense and monitor the concentration of hydrogen in the vicinity of the main engines and propellant tanks although makes the current baseline of launch vehicle quite safe, the number of sensing locations and the sensing methods are based on historical approaches and the baseline approach may limit launch abort decision data to a single sample and could result in unnecessary delay and abort.

Despite considerable effort to minimize occurrence of leak, several of Space Shuttle experienced delays as a result of repeated leak detection. The current baseline method employs remote analytical mass spectrometers systems fed by tubes. This results in delay between leak initiation and leak detection as well as being limited in sensing locations.

Commercial and military launch vehicles are designed to use cryogenic hydrogen as the main propellant, which is very volatile, extremely flammable, and highly explosive. Current detection system uses Teflon transfer tubes at small number of vehicle location through which gas samples are drawn and stream analyzed

* Corresponding author e-mail address: alex.kazemi@yahoo.com

Photonics in the Transportation Industry: Auto to Aerospace II, edited by Alex A. Kazemi, Bernard C. Kress
Proc. of SPIE Vol. 7314, 731406 · © 2009 SPIE · CCC code: 0277-786X/09/$18 · doi: 10.1117/12.820763

by a mass spectrometer. A concern with this approach is the high cost of the system. Also, the current system does not provide leak location and is not in real time. This system is very complex and cumbersome for production and ground support measurement personnel [1].

Liquid hydrogen is widely used as a propellant in launch vehicles. Since hydrogen is highly dangerous and prone to explosion, detection of hydrogen become critical for the safety and efficiency during launch operations. Several techniques such as catalytic bead sensors and solid state sensors are not very accurate beyond 1% (10,000 ppm) hydrogen concentration with nitrogen present. There is a need to monitor hydrogen ($H_2$) concentration in the vicinity of rocket fuel tanks to detect leaks, see Figure 1-1. Palladium (Pd) based gas sensor with various electrical and optical sensing schemes have been explored for past 40 years. The most commonly used detection system is a mass spectrometer [2].

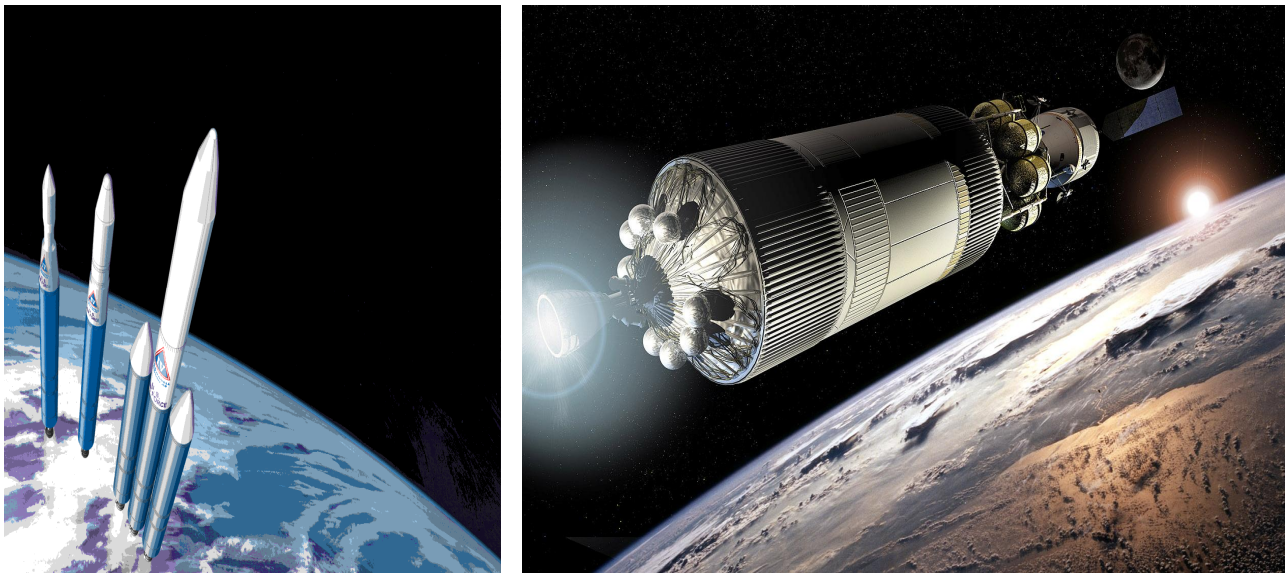

**Figure 1-1. Fiber optic hydrogen leak detection need for present and future launch vehicles.**

## 2. MICROMIRROR SENSOR TECHNOLOGY

The first optosensor for hydrogen was developed by Butler and Ginley. In their system an optical fiber coated with palladium was used as sensing mechanism. They recognized the changes in the elastic property of palladium during hydrogen absorption and desired a fiber optic hydrogen sensor. In their work, the sensor is an interferometer in which one of its arms (i.e. sensing structure) was coated with palladium film and the optical path length of the sensing arm changes as it is exposed to hydrogen. The change in the optical path length shifts the fringes at the output of the interferometer and hence it can be detected. Further investigation by Butler resulted in the development of micormirror sensor (see Figure 1-2.). The work report in this paper is the result of further development of micormirror sensor for temperature requirement at sub-zero and multiplexing of many sensors in an integrated read-out scheme based on optical switches and driver/receiver network [2].

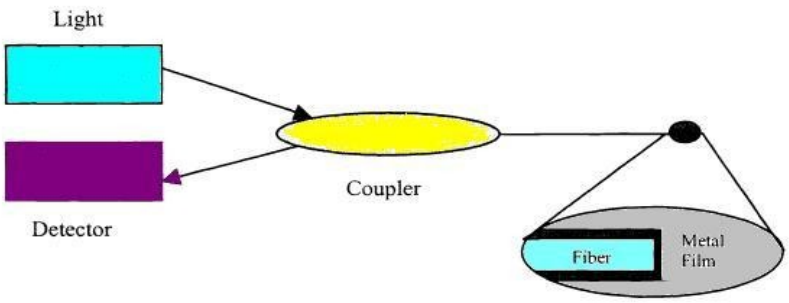


**Figure 1-2. Micormirror sensor schematic.**

### 2.1 Operation Principals of Micormirror Chemical Sensor

Hydrogen is an exceptional molecule in that it has no useful absorption in the near Infrared (NIR), where fiber absorptiometry is preferably performed because of the good transmittance of fibers for NIR light. In addition, no indicators are known that would respond to hydrogen by reversible color change, except for the poorly defined tungsten oxide. Consequently, other sensing approach had to be made. An optical fiber coated with palladium is one very important sensor that has been developed. In this sensor, palladium expands on exposure to hydrogen because of the formation of a palladium hydride (PdHx) having an expanded lattice constant. The expansion depends on the partial pressure of hydrogen and stretches the fiber in both the axial and radial direction. This result in a change in the effective optical path length of the fiber can be detected by Mach-Zender interferometry [2].

In the micro-mirror chemical sensor, an end of a multi-mode optical fiber is coated with a thin film of specially selected material (Pd) that acts as a chemical transducer through changes in its optical properties in response to certain chemicals. These optical changes alter the reflectivity from the end of the fiber. The overall reflectivity of coated optical fiber end depends on both its front surface reflectivity and its optical thickness. Response to different chemical species is achieved by selecting the coating material deposited on the fiber end. Palladium film is used for hydrogen detection. In our development, the fiber optic hydrogen micorsensor operates in 4 simple steps as shown in Figure 2.1-1:

1. Modulated LED source launches into sensor array.
2. Photodiode detectors synchronously measures reflected signal.
3. Reversible chemical interaction causing a change in reflectivity.
4. Reflectivity corrected to the local concentration of target chemical species is measured.

Also, in our system, an optical driver receiver launches a modulated LED source into an optically multiplexed sensor array and photodiode detectors synchronously measure the reflected signals, see Figures 2.1-2.

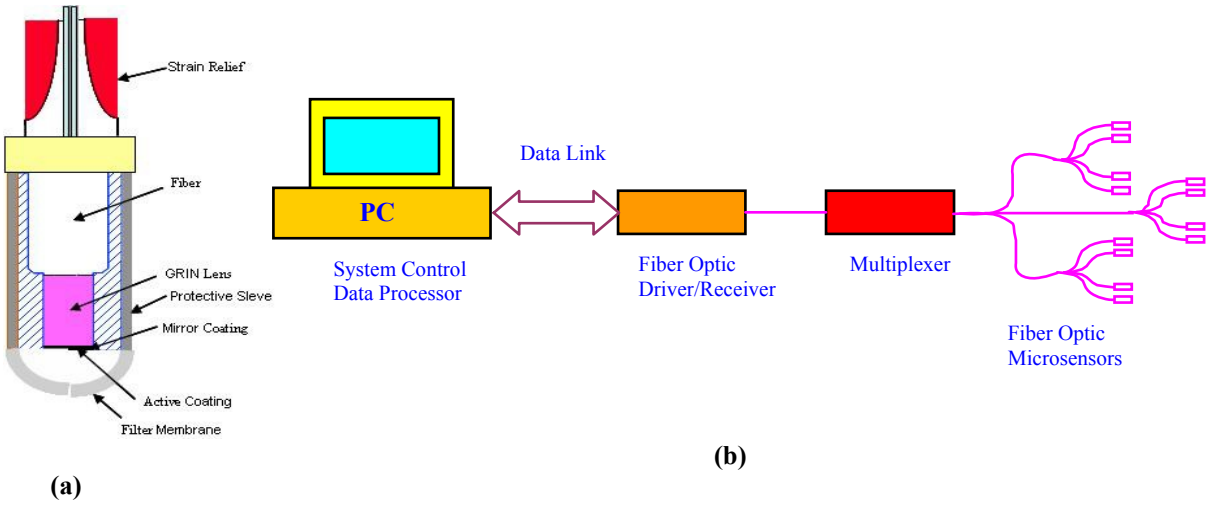


**Figure 2.1-1. Fiber optic micorsensor. (a) Sensor schematic. (b) Distribution network.**

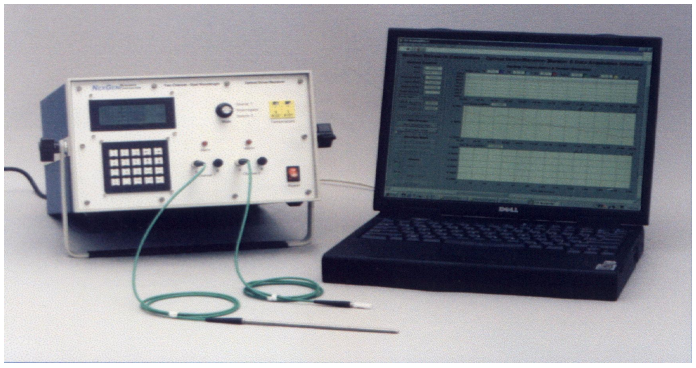

**Figure 2.1-2. Fiber Optic Sensor System with Optical Driver Receiver and PC.**

## 2.2 Field Demonstration on Stennis B-2 Test Stand

A field demonstration was performed at NASA/Stennis Cryogenic Test Lab and to simulate hydrogen leakage, sensors were exposed to concentrations of bottled 2% hydrogen in nitrogen.

The hydrogen sensor used in the demonstration responded immediately, with full response in about 3-5 seconds (See Figure 2.2-1a). When exposed to clear air, the sensor recovered in about one second. Sensor response was repeatable, with two successive exposures to 2% hydrogen in nitrogen shown in the graph. For temperature demonstration, a sensor was used and operated normally with good accuracy to the ice bath in which it was installed. This sensor was removed from the ice bath and exposed to the air on the bench in the field, and it responded up to the ambient temperature. When put back into the ice bath at the right side of the chart, it rapidly went back to the ice temperature (See Figure 2.2-1).

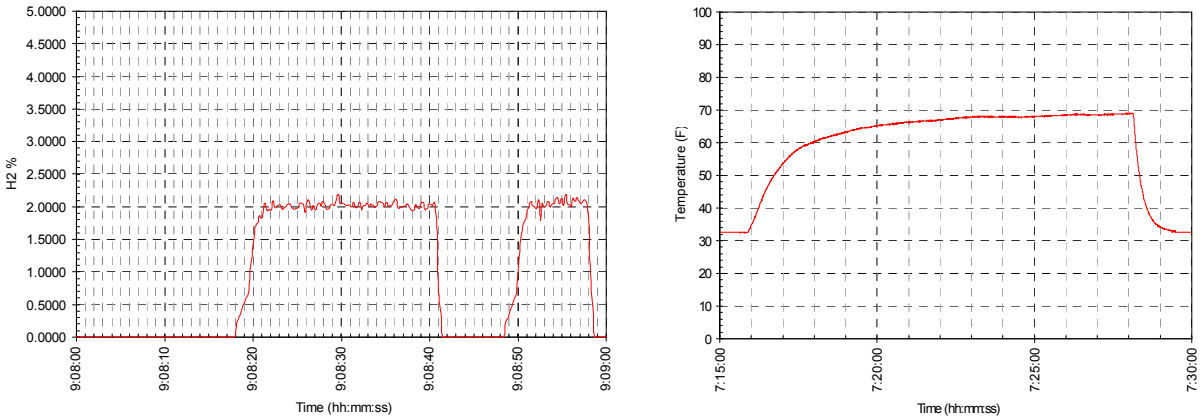


**Figure 2.2-1. (a) Hydrogen sensor responds to exposures of 2% hydrogen. (b) Temperature response to ice/air**

## 3. FIBER-OPTIC BRAGG GRATING SENSORS FOR HYDROGEN SENSING

We report a new type of optical hydrogen sensor with a fiber optic Bragg grating (FBG) coated with palladium. The sensing mechanism in this device is based on the mechanical stress that is induced in the palladium coating when it absorbs hydrogen. The stress in the palladium coating stretches and shifts the Bragg wavelength of the FBG. Using FBGs with different wavelengths many such hydrogen sensors can be multiplexed on a single optical fiber. Operation of two multiplexing sensors is demonstrated. Moreover, hydrogen and thermal sensitivities of the sensors were measured and calculated using a simple elastic model. Moreover, to quantify the amount of stress in the palladium film as a function of hydrogen concentration, a novel and very sensitive method was devised and used to detect deflections in a Pd-coated cantilever using an evanescent microwave probe. This stress was in the range of 5.26—8.59xl0$^7$ Pa for $H_2$ concentrations of 0.5—1 .4% at room temperature, which is about three times larger than that found in the bulk palladium for the same range of $H_2$ concentrations [3] .

### 3.1 Results and Discussion

Transmission spectra of a sensor as a function of hydrogen concentration are shown in figure 3.1-1-a. The Bragg wavelength of this sensor was 829.73 nm and it had a 35 μm cladding and a 560 nm Pd coating. From the figure, the Bragg wavelengths of the sensors were shifted to right when the sensor was exposed to a higher hydrogen concentration. The sensor showed a completely reversible response to cycles of hydrogen/nitrogen exposures at low hydrogen concentrations. However when exposed to hydrogen concentrations higher than 1.8%, the Pd coating peeled off and the sensor was destroyed. Figure 3-1-b shows the hydrogen sensitivity of the sensor. The Bragg wavelength increased almost linearly as a function of hydrogen concentrations in the range of 0.3—1 .8% H2 and decreased and became irreversible when it was exposed to hydrogen above 1 .8%. Optical pictures of the sensors after exposure to 1 .8% H2 revealed that the Pd coating peeled off. In the linear range of its operation, the sensor had 1.95x10$^2$ nm/1% H2 sensitivity.

Figure 3.1-2 shows the spectrum from an array of two sensors with the Bragg wavelengths at 829.73 nm and 846.65 nm. These sensors were joined together using a mechanical splicer. In figure 3-2, the top curve shows the transmission spectrum from the array of the two sensors in which only the second sensor was exposed to

hydrogen (1% in nitrogen ambient). The second sensor clearly responded to hydrogen, as indicate in the bottom curve in the figure which shows the difference between the spectrum with and without hydrogen.

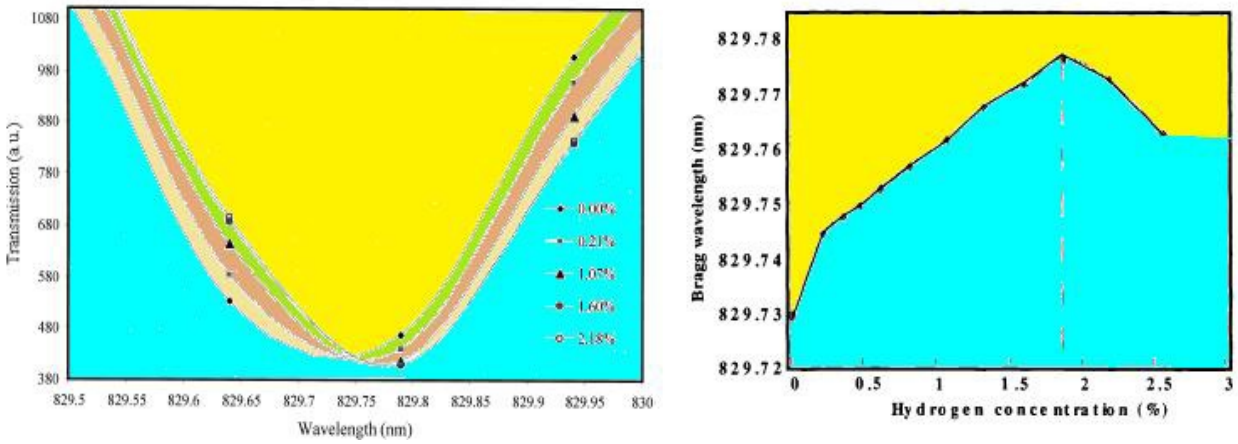


**Figure 3.1-1. (a) transmission spectrum of the FBG sensor as a function of hydrogen concentrations. The sensor was coated with a 0.56 pm thick Pd. (b) Bragg wavelengths of the FBG sensor as a function of hydrogen concentrations. After exposure to 1.8% H2 the sensor response was deteriorated and became irreversible.**

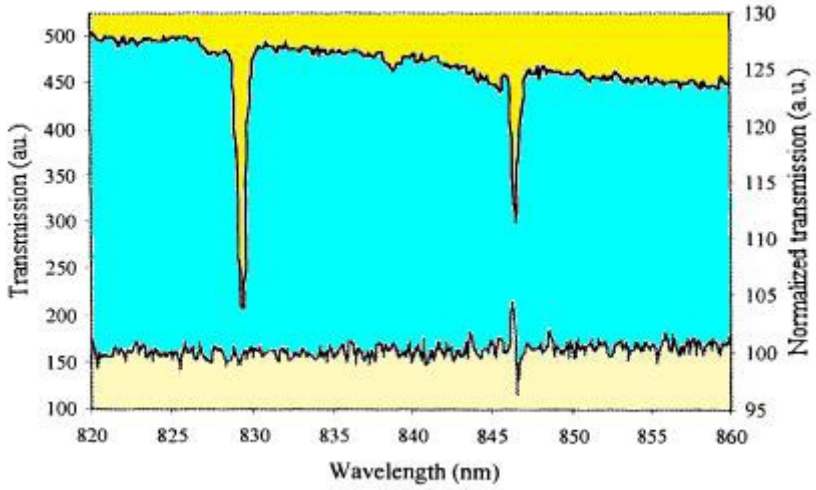


**Figure 3.1-2. Transmission spectrum of the two multiplexed FBG sensors (top) where only the second sensor was exposed to 1% H2. The bottom curve is the difference between the sensors spectra with and without (the reference spectrum) the hydrogen exposure.**

## 4. PALLADIUM COATED FIBER OPTIC EVANESCENT FIELD HYDROGEN SENSORS

A new types of hydrogen fiber optic sensors are reported. Our sensors consist of multimode optical fiber with a thin palladium film deposited on a suitable length of the fiber core, and operate through evanescent field interactions. Different sensor configurations are discussed and experimental results for different hydrogen concentration are presented. It is shown that these kind of sensors are suitable for detecting hydrogen concentrations form 0.5% to 3% with high sensitivity and fast time response .

### 4.1 The Palladium Film-Hydrogen Interaction

It has been known for many years that palladium has the property of absorbing hydrogen, up to hundreds of times its own weight. The mechanism of interaction and the process that takes place in the palladium film, when it absorbs hydrogen, have been widely discussed in the literature. However, it is convenient to briefly discuss here some of the fundamentals of such an interaction.

When Pd is exposed to hydrogen, $H_2$ molecules are converted to two $H_2$ atoms ($H_2 \longrightarrow 2H$) at the Pd surface with a very efficient dissociation rate. The hydrogen atoms then diffuse rapidly into Pd, converting it into palladium hydride, PdHx, (where x is the hydrogen content or the atomic ratio of H/Pd). The ratio H/Pd depends directly on the hydrogen partial pressure. It is also postulated that nearly 100% of hydrogen is dissociated upon arrival at the Pd surface. The palladium hydride film has different mechanical, electric, and optical properties than Pd. It also has two solid phases: α and β phases depending upon the Pd/H composition. The reversible α-phase is found at low hydrogen concentrations, typically from 0 to 3%, and the irreversible β-phase at higher concentrations. The hydrogen concentration at which the phase transition takes place depends on the Pd film thickness and temperature. It also introduces a hysteresis in the optical and mechanical parameters of the Pd film. Transitions from the α-phase to β-phase for a thin Pd film (100-1000Å) occurs at wider H2 concentration range than the transition in thicker films (>10 um) which occurs around 4% $H_2$. Most hydrogen sensor that use Pd as the sensing material operate in the α-phase, avoiding hysterisis [4].

It has been found that the Pd film reflectance decreases when the film is exposed on hydrogen. The changes in magnitude for the transmittance (or reflectance) depend directly, but not linearly, on the hydrogen partial pressure. Transmission and reflection data obtained simultaneously from Pd film may be used to determine fundamental optical parameters including reflectivity and absorption coefficients at a given hydrogen concentration, assuming that the film thickness is known. Note that the absorption coefficient is directly related to the extinction coefficient or the imaginary part of the refractive index. When a Pd film absorbs hydrogen it becomes less absorbing. This results in more or less light transmitted, or reflected by the Pd film which may be easily monitored with a light sensitive device. In contrast, the resistivity of the film, as well as the real part of its refractive index, increases. It is well known that the increment of the Pd film resistivity as a function of hydrogen absorption is exploited in electrical sensors.

### 4.2 Sensor Principal Configurations

Although the principle of evanescent field sensors has been widely discussed in the literature it is convenient to repeat here the main aspects for self-consistence. Evanescent field sensor have been mostly exploited for bio-chemical applications owing to the inherent advantages they offer over other techniques. However, evanescent field sensors have been little exploited for hydrogen sensing so far.

Typical bio-chemical evanescent field sensors make use of plastic-clad-silica (PCS) multimode fiber, D-shape single-mode fibers, or integrated optical devices. In such cases, the evanescent fields interact directly with chemical itself (monitoring absorption or index change), or the interaction is within an intermediate layer involving, for example absorption or fluorescence. An evanescent field, created when total internal reflection between two dielectric media occurs, is an electromagnetic field in the lower refractive index medium. In the case of optical fibers, the evanescent field decays exponentially away from the fiber core/cladding interface. The evanescent field can be expressed as:

$$E = E_0 \exp\left(\frac{-x}{d_p}\right) \quad \textbf{(1)}$$

where $E_0$ is the field amplitude at the boundary and $d_p$ is the penetration depth (l/e depth) into the lower index medium (the fiber cladding) given by :

and $k_0=2\pi\lambda_0$ being $\lambda_0$ the wavelength of the light used, and $n_1$ and $n_2$ are the reflective index of the fiber core and the cladding respective. See Figure 4.2-1.

$$d_p = \frac{1}{k_0\sqrt{n_2^{\,2}\sin_2\theta - n_1^{\,2}}} \quad \textbf{(2)}$$

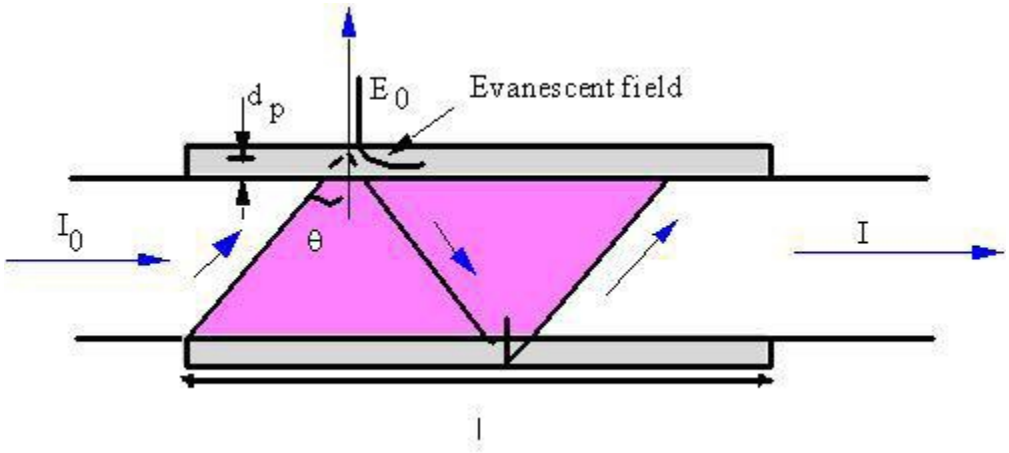


Figure 4.2-1. Schematic of evanescent fields and light propagation in an optical fiber. The gray zone of length I represent an absorbing thin film.

## 4.3 Experimental Results

Two detection systems, depicted in Figure 4.3-1, were employed to test the sensors. In Figure 4.3-1 a. a set up with conventional detection electronics is shown. It consists of a broadband light source, a chopper, a focusing system, a conventional detector, and a lock in amplifier. In turn, Figure 4.3-1 b. shows a set up with the schematic of a detection system designed and fabricated in our lab. The light source is this case was an infrared LED modulated at 500 Hz. The detector used was a single phototransistor whose electronic circuit is also shown. All the experimental data were recorded in a personal computer (PC) where they were later processed and analyzed.

Figure 4.3-2 shows the data obtained with a reflection-mode sensor. The core diameter was 60 μm, and the detection electronics was designed and assembled in our laboratory (Figure 4.3-1 b.). The sensor in this case had an interaction length of 1.5 cm, covered with a 200 Å thick Pd film. The mirror was made with a very thick Al thick film. The plot shown in Figure 5 was obtained when the sensor was exposed to 1% H2 concentration. The hydrogen flow was continuously turned on and off. Similar time response to that of the transmission-mode sensors was observed for the reflection-mode sensors. The signal to noise ratio was much larger when the sensor was deposited directly onto the arm of a 3-dB coupler. It was also found that this configuration is more robust and easier to handle. It is also more compact. This may be an important

advantage, fro instance, in places where sensor size is a concern. Also, remote sensing is more convenient with the last approach.

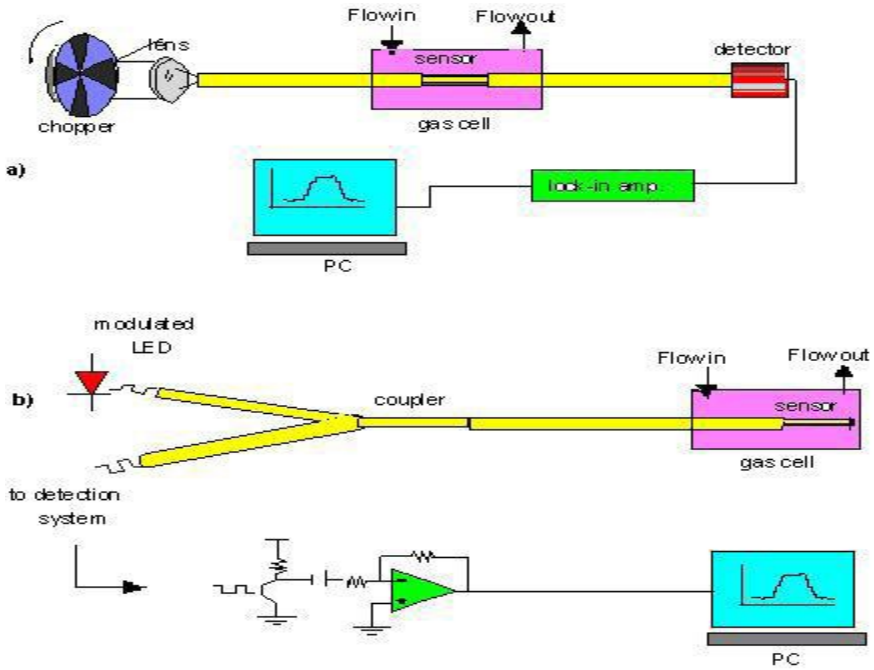


**Figure 4.3-1. Schematic of two experimental setups. a) depicts a set-up with conventional instruments and b) shows the electronic circuit that was employed in our detection.**

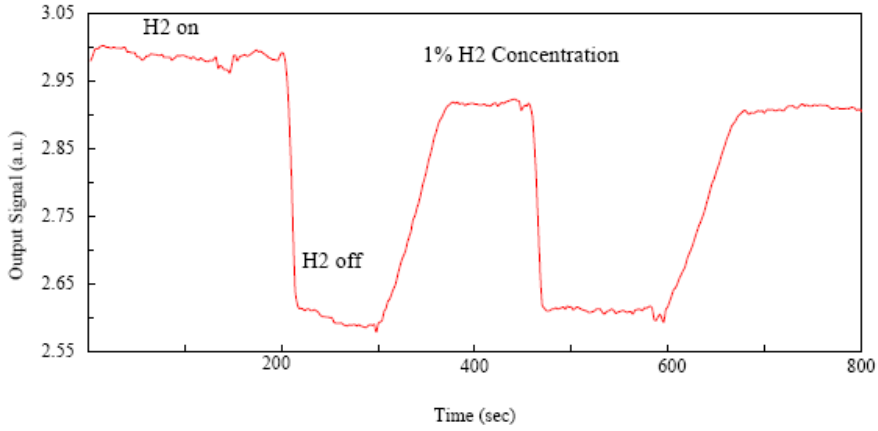


**Figure 4.3-2. Reflection-mode fiber optic evanescent field hydrogen sensor output as a function of time.**

## 5. COLORIMETRIC SENSOR TECHNOLOGY

We developed a Colorimetric technology and demonstrated successfully test of a multi-point fiber optic hydrogen sensor system during the static firing of an Evolved Expandable Launch Vehicle at NASA's Stennis Space Center. The system consisted of microsensors (optrodes) using hydrogen gas sensitive indicator incorporated onto an optically transparent porous substrate. The modular optoelectronics and

multiplexing network system was designed and assembled utilizing a multi-channel optoelectronic sensor readout unit that monitored the hydrogen and temperature response of the individual optrodes in real-time and communicated this information via a serial communication port to a remote laptop computer. The paper would discuss the sensor design and performance data under field deployment conditions.

### 5.1 Comparison of Fiber Optic System with Mass Spectrometer

Recent breakthrough in fiber optic chemical micro sensor technology and fiber optic micro sensor provides real-time continuous measurement of chemical species concentration at a vast number of remote locations including inaccessible areas and areas with hostile environments. These present a safety hazard to the inspector. This class of sensor relies on a reversible chemical interaction causing a change in reflectivity. The magnitude of the change in reflectivity is correlated to the magnitude of chemical interaction. The overall reflectivity of the coated optical optrodes depends on both its front-surface reflectivity and it optical thickness. Response to different chemical species is achieved by selecting the coating material deposited on the porous glass. Palladium and Tungsten Oxide is used for hydrogen detection. Consequently fiber optic based system is far superior to the current baseline with following distinct advantages [5]:

i. Leak Locations
ii. Leak Response
iii. Engine Leak Location
iv. Safety and Simplicity of Operation
v. Future Expandability
vi. Multiple Detection
vii. Extremely fast Multiplexing

The mass spectrometer uses remote system fed by tubes, this results in delays between leak initiation and leak sensing and being limited in leak locations. Very slow multiplexing. For mass spectrometer, the effective response time (transit time x tube no.) + sampling response time.

For fiber optic system, the effective response time = sensor response time. Figure 5.1-1 illustrates the difference between mass spectrometer Vs. fiber optic system.

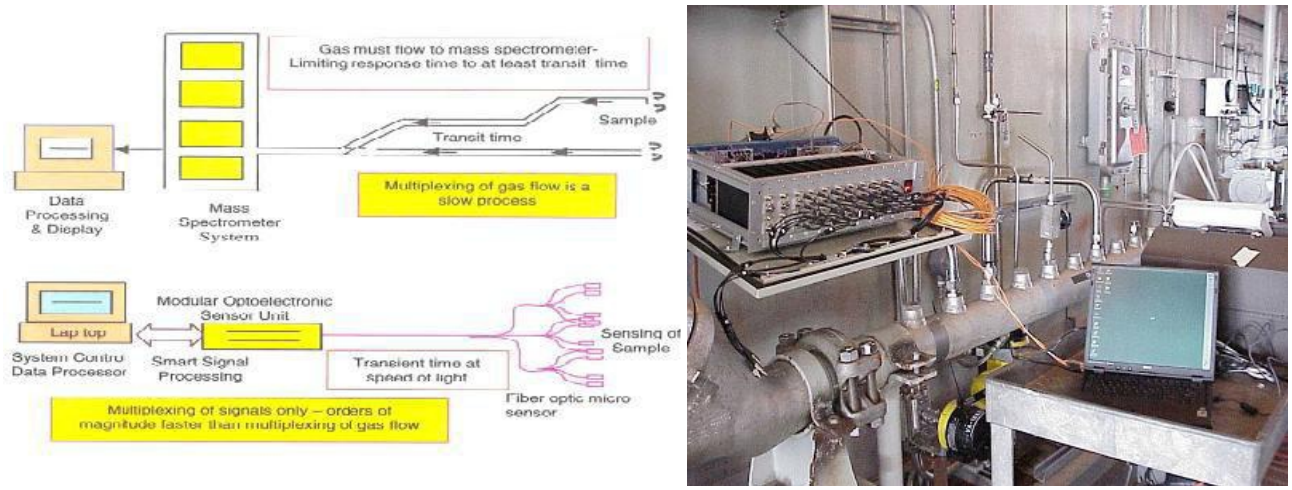


**Figure 5.1-1. Mass Spectrometer Vs. Fiber Optic Sensor System.**

### 5.2 System Concept

The Boeing Co. in collaboration with Intelligent Optical System have developed and tested the field deployable prototype of a 14-channel fiber optic hydrogen and oxygen sensor system for the early detection of cryogenic fuel leaks. This system was designed for use in the Boeing Company's EELV Delta IV program and was tested successfully during Delta CBC-hot fiber test in April 2001 at NASA Stennis Space Center. For the deployable unit, we had successfully designed and fabricated the sensors, the H2 optoelectronics boxes and multiplexing network system, see Figure 5.2-1 (a-d). The hydrogen sensor packaging consists of two optrodes; one doped with an indicator sensitive to hydrogen, and the other doped with an indicator sensitive to temperature. The sensor package is attached to a custom fiber optic ribbon cable, which is then connected to a fiber optic trunk communications cable (standard telecommunications-grade fiber) that connected to the optoelectronics module. Each board in the expandable module contains all the light sources, photodetectors, and associated electronics required for one sensor package. Performance data for the system is shown in Table 5.2-1.

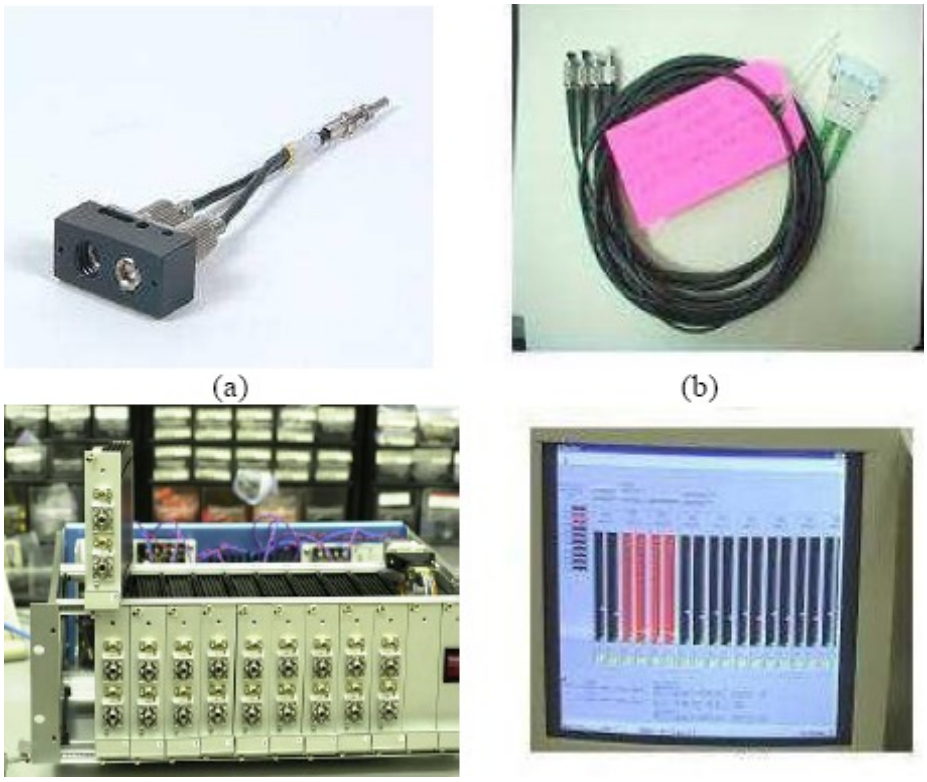


**Figure 5.2-1. Key Components of distributed sensing points system: (a) the sensor package; (b) the cable connects sensor package to the light source and detector; (c) multichannel optoelectronic system; (d) LabView-based display.**

**Table 5.2-1 Performance data of the fiber optic hydrogen detection system.**

| PARAMETER | HYDROGEN SENSOR |
|---|---|
| Range | 0.1 to 5% |
| Response Time (Immediate Response) | 1-5 Seconds |
| Response Time (to 90% of Full Scale) | 10 Seconds |
| Sensitivity (minimum detectable concentration) | 0.1% |
| Selectivity (Freedom from Interference) | 100% Nitrogen, 100% Oxygen |
| Temperature Range | -18º C to 60º C (0º F t0 140º F) |
| Half-Life of Sensor | 1 Year |
| False Alarm | 0 |
| Drift | 0.1% per day |

## 5.2 Characterization of Hydrogen Sensor

We fabricated hydrogen sensor optrodes, and optrodes for temperature compensation. The hydrogen optrodes were fabricated using a proprietary colorimetric indicator chemistry and the temperature optrodes used a ruthenium-based fluorescent indicator. To compensate for temperature, we fabricated temperature-sensitive optrodes using ruthenium indicator, however, these optrodes were further processed by coating them with an oxygen impermeable coating, which overcame the "oxygen quenching" phenomenon, and isolated the effect of temperature on the sensor performance. The indicator chemistries were immobilized on to porous glass using a solution based process. Figure 5.2-1 shows photograph for the fabricated hydrogen optrodes.


**Figure 5.2-1. Hydrogen optrodes fabricated in a porous glass rod.**

We tested the performance of the hydrogen optrode with an optoelectronic setup that uses a blue LED (440 nm to 520 nm bandwidth) to monitor the changes in the intensity of the reflected light from the optrode. In a routine test, we pressurized the experimental gas chamber with varying concentrations of hydrogen and nitrogen and measured the sensor's response (See Figure 6). This figure shows that the sensor responds readily to changes in the hydrogen environment in the range from 0% to 100% hydrogen. Furthermore, the figure shows that the sensor exhibits maximum sensitivity in the 0% to 5% hydrogen concentration range.

The next experiment was targeted at measuring the response time of the hydrogen sensor when changing the hydrogen concentration environment from 0% to 5%. In this experiment, the hydrogen/nitrogen gas mixture was delivered from the mass flow controllers at rate of 1 cc/min to a 500 cc/min within a gas cell that contained the sensors. As shown in Figure 6(a), the hydrogen optrode response to a 90% change in signal occurs in less than 15 seconds; the recovery time (the response to changing from 5% hydrogen to 0% hydrogen environment) is about 5 seconds. In this experiment, the response time of the optrode was

dependent on the time required to fill the test chamber at a flow rate of 1 cc/min. The following experiments were conducted to measure the reversibility and long term stability of the hydrogen optrode. Figure 6 (c) shows the reversible response of the optrode when changing the hydrogen environment back and forth from 0% to 5% hydrogen over 13-hour test run. This figure shows that the optrode response is completely reversible. Similarly, Figure 6 (d) shows the long term stability of the sensor when changing the hydrogen back and forth from 0% to 5% hydrogen over 3,600 minutes. In this figure, we observed an initial drift in the sensor response over first 1000 minutes of the run. This initial drift is believed to be caused by temperature effects; in this run temperature compensation was not in effect.

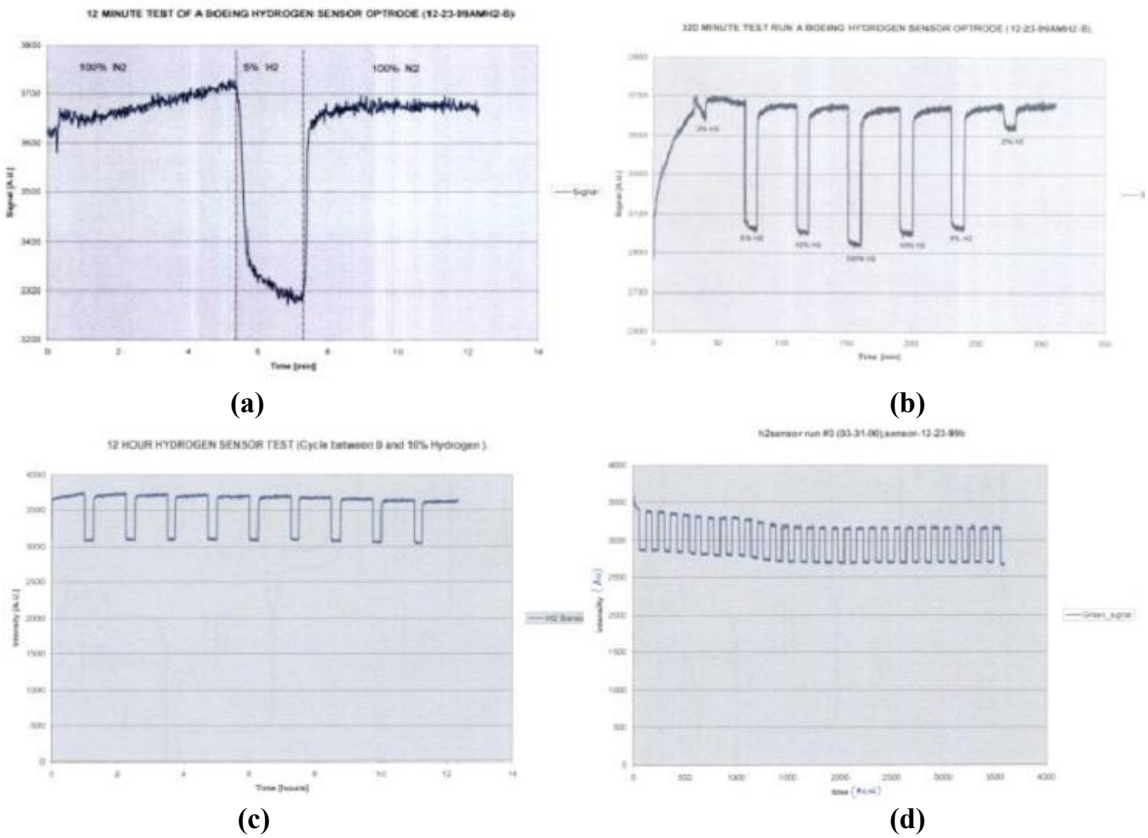


**Figure 5.2-2. Response of the hydrogen sensitive optrode: (a) Response to 90% of full scale; (b) Response in the range of 0% to 100%; (c) Reversibility of hydrogen optrode when varying the hydrogen environment from 0% to 5% hydrogen; (d) Long term response time to 3,600 minutes (note; drift in response from 0-1000 minutes is unaccounted for, but may be due to fluctuation in temperature inside the gas cell).**

### 5.3 Successful Demonstration of Fiber Optic Hydrogen Detection System on Delta IV Hot Fire Test at NASA/Stennis

New hydrogen sensing optrodes using Colorimetric technology with upgraded connecting cables were designed and developed before shipment to Stennis for The Boeing Company's Delta IV Common Booster Core (CBC) hot fire test at NASA/Stennis. Eight hydrogen sensors were installed, in pairs for redundancy, in the engine section (see Figure 5.3-1).

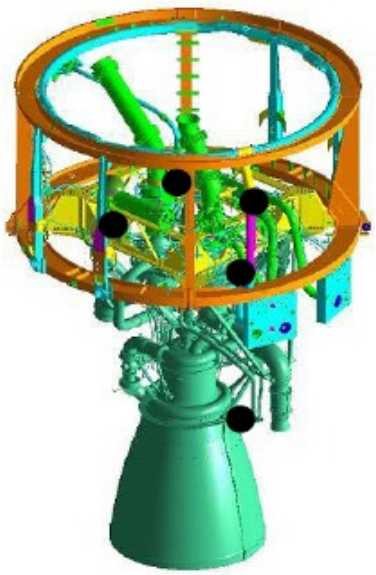

**Figure 5.3-1. Eight hydrogen sensors were installed, in pair for redundancy, inside engine section of Delta IV-CBC for hot fire test at NASA/Stennis Space Center.**

The final two sensors were placed on the engine fairing above the roll control nozzle (RCN) to sense hydrogen present prior to ignition (See Figure 10). The optrodes were tested, prior installation in the vehicle, by exposure to an atmosphere of 2% hydrogen in 98% nitrogen contained in a plastic bag placed over the optrode housing. Positive response were noted. The optrodes mounted outside the vehicle responded to the environment prior to main engine ignition.

On April 23, 2001, just prior ignition of CBC hot fire test, the RCN and engine torches were turned on to burn excessive hydrogen. Since, it was a wet day, the spark plug torch near RCN ignited 6 seconds late. Instantly, the hydrogen which is pumped to this torch, were not burned and we were able to detect it in 6 seconds and was recorded on laptop at NASA/Stennis test control center using Lab View graph (See Figure 5.3-2). This demonstration proved that our system was successful and able to detect hydrogen in open air environment.

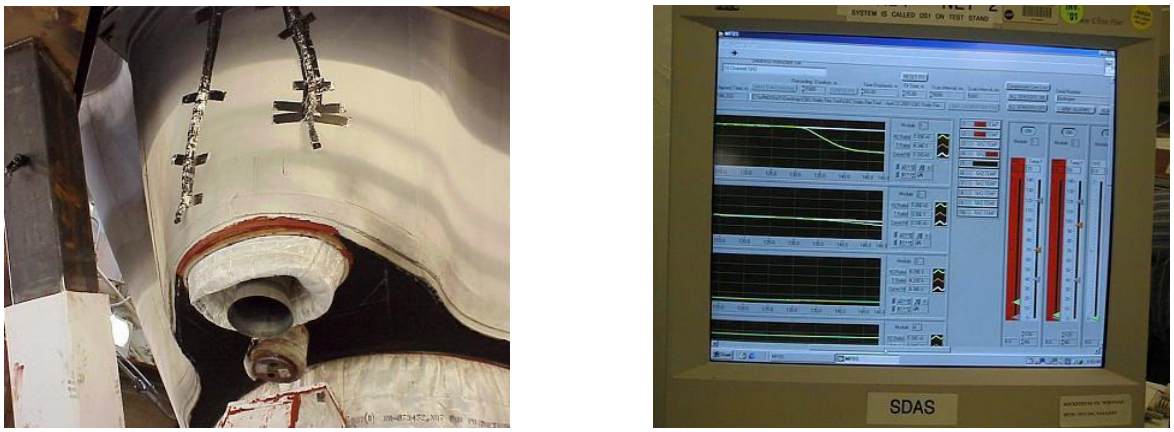


**(a)** **(b)**

**Figure 5. 3-2. Hydrogen Detection: (a) Hydrogen optrode mounted outside of Delta IV-CBC, engine just above RCN; (b) Response of hydrogen sensor placed outside of the vehicle.**

## 6. CONCLUSION

In Micromirror concept, a successful field demonstration of 20 sensors was performed at the EELV/Delta IV engine test stand at NASA-Stennis Space Center, with the sensors detecting hydrogen and responding to full scale within 5-15 seconds of exposure.

In fiber-optic Bragg grating sensors for hydrogen gas sensing, we have demonstrated a new type of hydrogen sensor that is based on the elastooptic in fiber Bragg grating coated with Pd. This type of sensors allows several sensors to be easily multiplexed on one single fiber using simple and low cost detection equipment. The sensor showed a linear sensitivity for 0.3— 1 .8% H2. Stress in the Pd film as a function of hydrogen concentrations was also measured. The film stress was found to be about three times higher than the bulk values.

In Pd-coated fiber optic evanescent field hydrogen sensor , it was observed that the amplitude of the sensor output signal decrease with consecutive exposures to hydrogen affecting the sensor sensitivity. This behavior has also been observed by other researchers in the past and is owing to the process that take place in the Pd film. Microblistering and micro-cracking are some of the causes.

In Colorimetric Technology, we have constructed and demonstrated successfully the world first multipoint fiber optic sensor system capable of the temperature-compensated detection of leak-level concentrations of the hydrogen on Delta IV program. We also established that porous glass optrodes doped with indicators are suitable for monitoring hydrogen gas concentrations, and are appropriate for use in engine section of launch vehicles. Thus, porous optrodes doped with colorimetric indicators meet the performance objective. This establishes the basis for an inexpensive optoelectronic device for hydrogen leak detection.

## 7. ACKNOWLEDGEMENT

I would like to acknowledge the Boeing Company for their support in the development of these technologies. I would also like to acknowledge the following individuals for their extensive contribution for the development of fiber optic hydrogen detection system: D. B. Larson, M. Wuestling, B. Sutapun, M. Tabib-Azar; J. Villartroro, R. M. Petrick, E. A. Mendoza, L. U. Kempen, E. Durets, and K. Goswami.

## 8. REFERENCES

[1]. A. A. Kazemi, "Fiber Optic Microsensor Technology for Detection of Hydrogen in Space Applications", SPIE, Vol. 7003, 2008.

[2]. A. A. Kazemi, J. W. Goepp, D. B. Larson, M. Wuestling, "Fiber optic microsensor hydrogen leak detection system on Aerospike X-33", SPIE Vol. 6958, 2008.

[3]. B. Sutapun, and M. Tabib-Azar, A. A. Kazemi, “Pd-Coated elastooptic fiber optic Bragg grating sensors for multiplexed hydrogen sensing”, Sensors and Actuators B*:* Volume 60, Issue 1, pp. 27-34, 1999.

[4]. J. Villartroro, R. M. Petrick, M. Tabib-Azar, A. A. Kazemi, “Pd-Coated Fiber Optic Evanescent Field Hydrogen Sensors”, Fiber Optic Sensor Technology and Applications IV, Proc. SPIE Vol. 6004, pp. 155-164, 2005.

[5]. A. A. Kazemi, “Fiber optic microsensor technology for detection of hydrogen in space applications”, SPIE, Vol. 7003, 2008.

# Fiber Optic Sensor Applications in Transportation Infrastructure Protection

David Krohn, Light Wave Venture LLC; Paul Nicholls, SensorTran Inc.

## Background

In a recent study [(1)] on transportation infrastructure, the results are very disturbing. It states that 83% of the United States transportation infrastructure in not capable of meeting the needs of the next 10 years. While other countries have been more aggressive in infrastructure development and monitoring, the United States is lagging behind.

There are a broad range of infrastructure sensing applications in transportation that are not being met. Many of these vital assets are aging or not adequately monitored with the potential for catastrophic failure. As examples, the bridge failure in Minneapolis, Minnesota was due to a structural failure. Fire safety problems, with recent life-loss fires, in road tunnels are challenging due to specific features of their infrastructure, nature of traffic using them and insufficient safety rules on vehicles. As a result, road tunnel fire safety issues are a concern.

NIST has recognized the need and is funding innovative research for the development of infrastructure monitoring and inspection technologies. Specifically, NIST through its Technology Innovation Program (TIP) will fund the development of a network of distributed, integrated sensor architectures that will monitor bridges, roadways, tunnels, dams and other critical infrastructure applications [(2)] Many of these applications can be facilitated by using fiber optic sensors.

This paper will specifically address monitoring bridges and tunnels using distributed fiber optic sensors to monitor strain, vibration, temperature and the associated benefits.

## Distributed Fiber Optic Sensing Technologies

Many of the monitoring protocols are based upon manual visual inspection which makes real time monitoring impossible. However, several photonics technologies have been used for structural health monitoring [(3)] with positive results. In the future, fully instrumented bridges and tunnels will require distributed sensing to provide real time structural integrity information. Distributed fiber optic sensing technologies include Bragg gratings, Raman scattering, Brillouin scattering and interferometric approaches.

In the Bragg grating approach, specific sensing points are introduced into the fiber, which is referred to as a quasi-distributed sensor since the entire fiber is not a sensor. Bragg grating sensors written into an optical fiber have periodic changes in refractive index which creates the grating effect. The wavelength of light corresponding to the grating pitch is reflected while all other wavelengths are transmitted. If the fiber is strained, the grating pitch changes that in turn changes the reflected Bragg wavelength as shown in figure 1. The spectral change corresponds to the level of strain. In essence, the Bragg grating sensor is spectrally modulated by strain and does not have the problems associated with intensity modulation. Bragg grating sensors have a resolution of 0.5 microstrain. However, in addition to strain, the grating can be modulated by temperature. Depending upon which parameter is to be measured, compensation will be required to discriminate between strain and temperature. A schematic representation of a quasi-distributed Bragg grating sensor is shown in figure 2.

Photonics in the Transportation Industry: Auto to Aerospace II, edited by Alex A. Kazemi, Bernard C. Kress
Proc. of SPIE Vol. 7314, 731407 · © 2009 SPIE · CCC code: 0277-786X/09/$18 · doi: 10.1117/12.820797

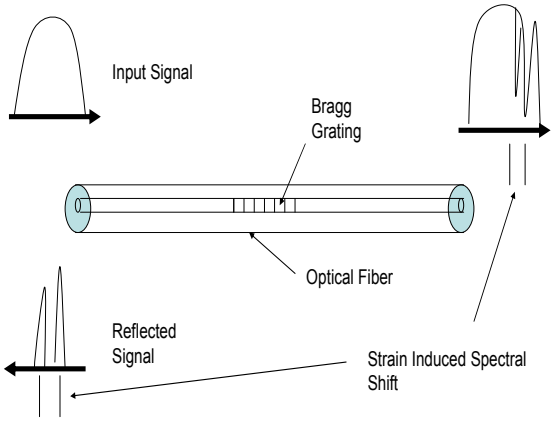


Figure 1 Bragg Grating Sensor Concepts [4]

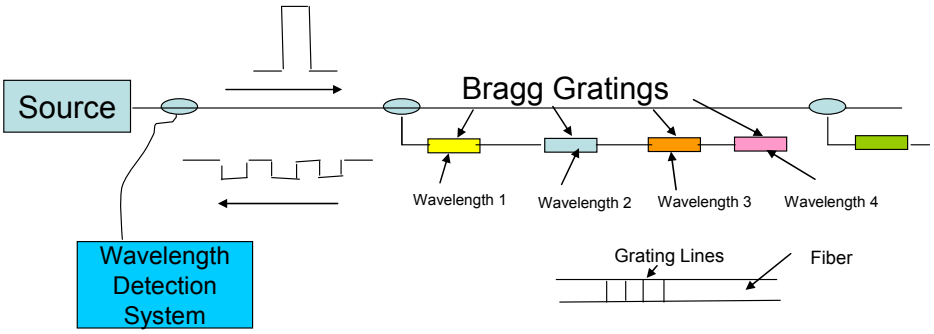


Figure 2 Quasi-Distributed Bragg Grating Sensors [5]

Distributed sensors use the full length of the fiber with the sensing function occurring anywhere along the fiber. A good example of such a sensing system is based on stimulated Brillouin scattering. Figure 3 shows the scattering process. Figure 4 illustrates how the scattering lines shift with both strain and temperature.

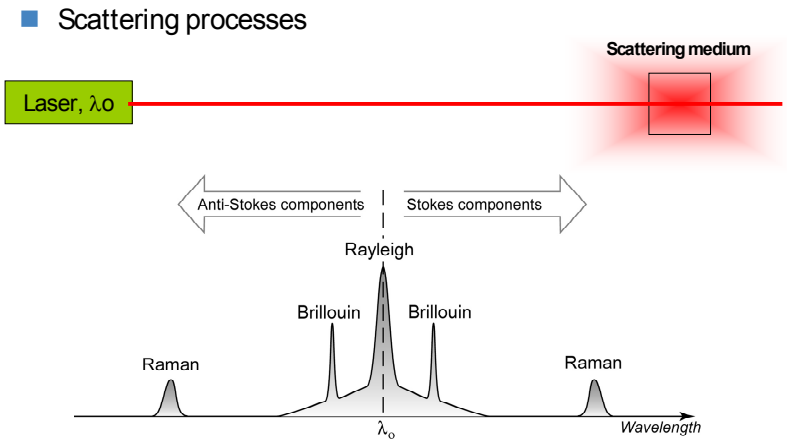


Figure 3 Scattering Processes [6]

- Scattering processes used for sensing applications
  - Raman scattered magnitude is temperature dependent
  - Brillouin lines are temperature and strain sensitive

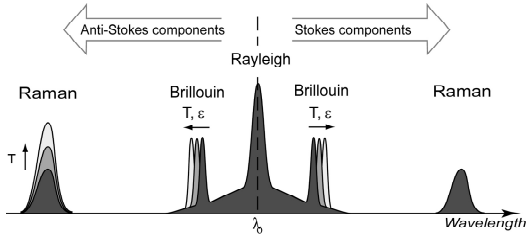


Figure 4 Scattering Processes Associated with Sensing Temperature and Strain [6]

As shown in figure 4, Raman scattering sensing systems only measure temperature and are independent of strain. The measurement range is up to 15 km with a 1 meter spatial resolution (up to 25km with a 1.5 meter resolution) of the location of the temperature perturbation.

Brillouin scattering based sensing systems have a measurement range of up to 30 km. The sensing point associated with a physical perturbation can be resolved to 1 meter on a 10 km length, but accuracy is reduced as distance increases. The strain resolution is 20 microstrain [3]. However, more advanced detection schemes can have a strain resolution of 0.1 microstrain [7]. While Brillouin scattering is an excellent strain sensor technology, the response time is about 1 second: and therefore, is not suitable for vibration measurements.

The Brillouin scattering wavelength shift is dependent upon temperature and strain. To function as a strain sensor it must be configured to discriminate between strain and temperature in a manner similar to the approach taken for Bragg grating sensors.

Interferometric sensors measure phase shift for detection with various schemes depicted in figure 5. This family of sensors can be quasi-distributed as shown in figures 5a and 5 b where the discrete sensing elements are separated by non-sensing fiber leads. In figure 5c the Bragg grating mirrors that define the sensing region create sensing elements that are continuous without a non-sensing region between sensors. As a result, the entire fiber is the sensing element. This is also the case for the distributed Rayleigh mirror configuration shown in figure 5d. Interferometric sensors are extremely sensitive to changes in strain and can function over long distances.

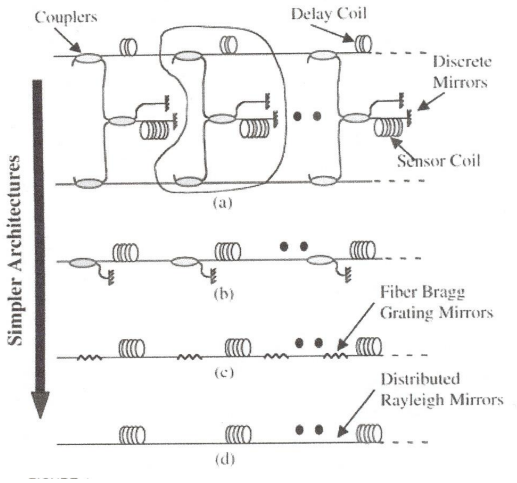


Figure 5 Interferometric Sensing Schemes [8]

All the approaches discussed have the potential to provide excellent static strain measurements, Bragg grating approaches can provide good dynamic strain monitoring while interferometric technologies have the greatest sensitivity and dynamic range to monitor dynamic strain (vibration signatures).

Bragg gratings, Raman scattering and Brillouin scattering are also used widely for distributed temperature measurements [9]. Bragg gratings have a temperature accuracy of 1$^{o}$C. The accuracy for Raman scattering is 0.5 $^{o}$C while Brillouin scattering also has an accuracy of 0.5$^{o}$C.

## Structural Monitoring for Bridge Safety

Bridge monitoring has typically looked for changes in static strain that may be caused by cracking or corrosion of structural members. Multiple strain sensors are mounted on the bridge and a baseline strain is determined. Deviation of strain over time is an indication that the structural health of the bridge is deteriorating and provides a signal for the need for preventive maintenance. However, it is unlikely that static strain measurements will provide an alarm to indicate that the bridge is on the verge of catastrophic failure such as the bridge failure in Minneapolis. Cracks at critical joints in the bridge may not cause significant deformation until the onset of catastrophic failure. It is hypothesized that a combination of static stain and dynamic strain measurements would improve the likelihood of preventive detection before the onset of the failure process. Monitoring the main structural members may not detect a crack in the interconnect of adjoining bridge sections but vibration tracking across joints could detect either vibration damping or amplification both of which could identify serious flaws as is shown conceptually in figure 6. Therefore, the addition of strategically placed distributive interferometric sensors or other fiber optic sensing approaches that can detect vibration in bridge monitoring schemes should be strongly beneficial.

There are several factors that will impact the full monitoring of bridge structural integrity.

1. The ability to look at both static and dynamic strain which can be accomplished with Bragg grating, inteferometric or Brillouin scattering (static only) technology based sensors
2. Distributed sensing in which a network of sensors can function from one electro-optic interrogator
3. The ability to integrate with wireless systems
4. The ability to transmit real time data to a central station and identify alarm conditions
5. Ease of installation
6. Robust behavior with minimal maintenance
7. Cost effective solutions

Bragg grating, and inteferometric technology based sensors are capable of static and dynamic detection. However, each technology has performance and cost benefits that will be key factors in sensing system design.

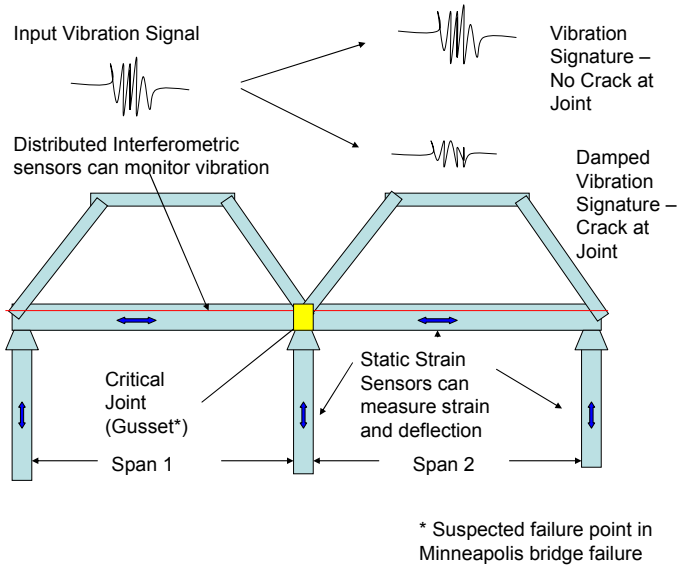


Figure 6 Monitoring Static and Dynamic Strain (Vibration Signature) Along Two Adjacent Bridge Spans [3]

## Road Tunnel Fire Detection

Due to the increase in vehicle traffic and a number of recent life-loss fires and potential terrorism threats, road tunnel fire safety measures will require much more advanced technical solutions. Fire detection systems are an essential element of fire protection systems of road tunnels (Figure 7). Fire detectors should provide early warnings of a fire incident at its initial stage and hence facilitate early activation of

emergency systems. Their role is crucial in preventing smoke spread in the tunnel, to controlling/extinguishing fires, and to aid in directing evacuation and firefighting operations [10-13].

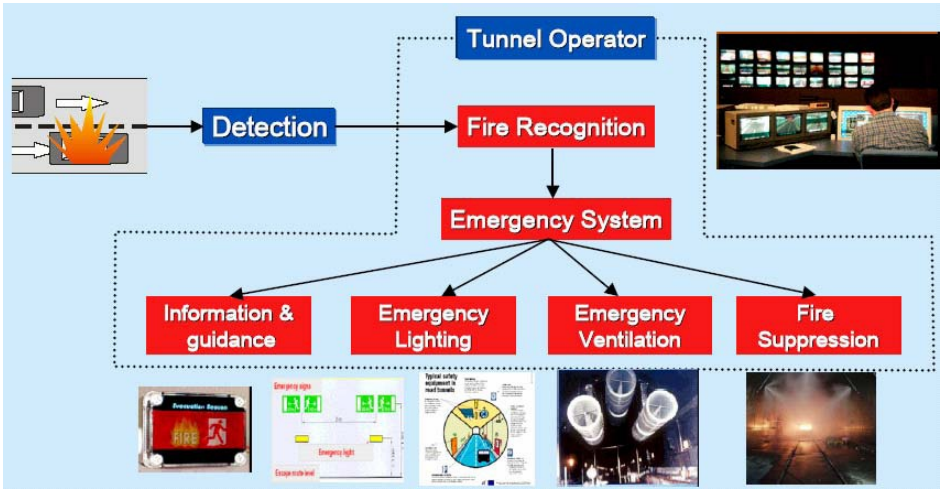


Figure 7 Road Tunnel Fire Protection System [14]

There have been a number of different technologies considered for this application that monitor heat, radiation image, smoke or gas. Most of the approaches use electrical or electro-optic configurations. In general, these devices are point sensors which are not efficient for large area surveillance.

Distributed temperature sensors (DTS) use the Raman scattering concept defined in figures 3and 4 previously. DTS is used for a wide variety of applications across diverse industries such as process control, asset assurance (integrity and/or safety) and condition assessment. The DTS approach has been used very broadly in smart oil wells and power cable monitoring. As a direct result of its features and benefits as well as commercial availability, it is especially well suited for fire detection.

The features and benefits are

- Identifies and locates the position of small temperature hot spots with no prior knowledge of performance characteristics
- Identifies and tracks fast developing and damaging abnormal temperature excursions
- Provides advanced warnings of potentially unsafe conditions
- DTS provides early fire detection and dynamic fire characteristic information (movement direction and speed) for ancillary control & safe evacuation.

A typical tunnel layout using Raman scattering (DTS) technology is shown in figure 8.

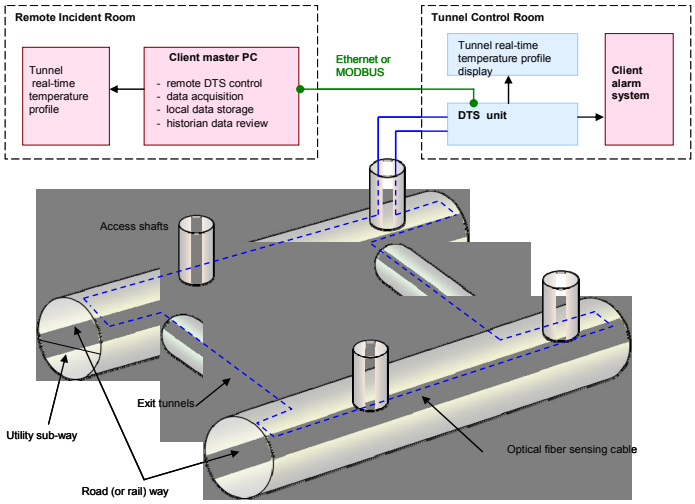


Figure 8 Typical tunnel layout [14]

## Summary

There are four fiber optic sensor technologies that can be used for distributed sensing configurations. Bragg gratings can be used for strain, temperature and moderate frequency vibration. They have been used in a variety of smart structure applications. Raman scattering is used for temperature monitoring and is the

dominant distributed fiber optic technology for temperature measurement. Brillouin scattering measures both strain and temperature. It has the potential for high sensitivity, but is not suitable for vibration measurement. It is in an early stage of commercialization. Interferometric sensors have been widely used for vibration measurement and have the highest sensitivity and dynamic range.

Bridge monitoring is best accomplished with a combination of static strain and vibration tracking to provide a real time picture of bridge health. Tunnel monitoring can benefit from strain measurement to look at structural health. However, the main concern is fire where temperature is the key parameter to provide an alarm.

Each bridge and tunnel application will require an analysis of need versus distributed sensing technology potential to determine the best cost benefit solution. In many cases an integration of multiple technologies will be required.

## References


1. Anonymous, Infrastructure, Urban Land Institute Report I18, May 2007.
2. R. Barsum, News Release, RIO, Inc. January 12, 2009
3. D. Krohn, Photonic Sensor Applications in Transportation Security, Optics East 2007, September, 2007.
4. D Krohn, Fiber Optic Sensors, ISA, 2000
5. D. Krohn, Overview of Fiber Optic Sensors KMI's 26TH Annual Newport Conference, October, 2003
6. M. Nikles, " Fibre Optic Distributed Scattering Sensing System", EWOFS 07, July, 2007
7. O. Sezerman, Fiber Optics Distributed Strain and Temperature Sensor (DSTS), www.ozoptics.com, September, 2008.
8. C. Kirkendall, R. Bartolo, A. Tveten, A Dandridge, High Resolution Distribute Fiber optic Sensing, NRL Review, 2004
9. P. Ficocelli, Fiber optic Thermal Monitoring Systems for SAGD, PTAC Technology Information Session, March, 2008
10. B. Brousse, "Comparison of fire safety problems for the various transport modes in tunnels," First International Symposium on safe & Reliable Tunnels, Prague 2004.
11. PIARC, "Fire and smoke control in road tunnels," World Road Association, 1999.
12. NFPA 502, "Standard for Road Tunnels, Bridges, and other Limited Access Highways," National Fire Protection Association, 2004
13. U.S. Department of Transportation, Federal Highway Administration, "Prevention and Control of Highway Tunnel Fires," FHWA-RD-83-032, 1984.
14. Paul Nicholls, Other DTS Applications – An Introduction, Annual DTS Summit, Oct , 2008

# Optimizing the optical components choice for performances improvement of multimode fiber gyroscope

H. Medjadba*[a], S. Lecler[b], L. M. Simohamed[a], A. Chakari[b], N. Javahiraly[b]
[a]Laboratory of Electronics and Optoelectronics Systems, BP 17, 16111 Bordj El-Bahri, Algeria
[b]Photonics System Laboratory, ENSPS/UDS, BP 10413, 67412 Illkirch, Strasbourg, France

## ABSTRACT

In this work, we report a theoretical study for optimizing the optical components choice to design a new low cost and high performances multimode fiber optic gyroscope (MFOG). This study shows that high performances can be obtained by using all optical components with the SI 50/125 multimode optical fiber associated with low coherence light source, such as a LED, and a photodetector with large active area. For further improvement of MFOG performances, we present a detailed analysis of the photo-detection circuits design considerations.

**Keywords:** Sagnac effect, multimode fiber, gyroscope, interference, mode coupling, rotation sensor.

## 1. INTRODUCTION

Accurate angular rotation measurement is of great importance in many fields such as land and space navigation. One of the most successful commercial rotation sensors, the Fiber Optic Gyroscope (FOG), is widely used in military and civilian applications [1]. Compared to the existing technologies, this success is due to its own characteristics which are high accuracy, compactness, reliability, solid-state technology, resistance to electromagnetic field, easiness of fabrication and ability to be embedded into other structures [2]. Interests in the FOG are growing rapidly in many companies around the world. Development, production, and system engineers are now getting involved, in addition to the scientific and technological communities that have conducted the research.

Optical gyroscopes with Multimode Fiber (MMF) offer a new means for reducing cost manufacturing of existing FOGs [3]. Such devices can be used in short time stabilization and should find useful application in automotives and robotics navigation [4]. The large numerical aperture of the multimode components allows high power coupled in the MFOG optical circuit and gives also a relaxed alignment tolerance to the optical components connection.

The multimode interference operation allows the MFGOs to have a stable output. Indeed, the random phase errors are averaged over a large number of modes [5]. In addition, non reciprocal effects such as backscattering, Kerr effect and environmental errors are expected to be lower because of the averaging over the modes. However, the presence of mode coupling due to imperfection of the fiber and modal dispersion induces non-rotationally errors which must be avoided.

The first MFOGs, using bulk optical components, were simple laboratory demonstrators [6-7]. The components of such devices must be aligned with each other, giving a critical arrangement incompatible with mechanical vibrations and inducing non-rotationally phase errors. Several theoretical and practical works have been achieved to improve performances of MFOGs [8-12].

Actual MFOGs are highly sensitive to launching conditions and environmental perturbations and still suffer from the effect of mode coupling, [13]. We notice that in prior MFOGs experiments, the choice of optical components were not vindicated especially the choice of multimode fiber.

The aim of this study is the development of a new high performance MFOG. To this end, an optimum choice of the MFOG optical components parameters such as the multimode fiber sensing loop, the light source, the couplers, the photodetector and the detection scheme are reported. The optimum choice analysis is mainly based on the modeling results obtained in our previous work in which the influence of components parameters on the MFOG performances are detailed [14]. This choice should offer better sensitivity to the proposed MFOG.

*Hocine.Medjadba@ulp.u-strasbg.fr; phone +33 (0)3 902 44 603; fax +33 (0)3 90 24 46 19; lsp.u-strasbg.fr

Photonics in the Transportation Industry: Auto to Aerospace II, edited by Alex A. Kazemi, Bernard C. Kress
Proc. of SPIE Vol. 7314, 731408 · © 2009 SPIE · CCC code: 0277-786X/09/$18 · doi: 10.1117/12.821003

## 2. MATHEMATICAL EQUATIONS

The basic open loop FOG is illustrated in figure 1. The light source is used to couple beam light in the input/output fiber coupler 1 that is used to ensure reciprocity [15]. Another coupler is used to split the light beam in two counterpropagating light beams in the fiber coil. After passing through the fiber coil, the two light beams recombine and are detected by means of a photodetector. The principle of operation of the FOG is based on the measurement of Sagnac phase shift between the two counterpropagating waves induced by a rotation [16]. This phase shift is given by the following expression:

$$\phi_s = \frac{4\pi RL}{\lambda c}\Omega \tag{1}$$

where $\phi_s$ is the Sagnac phase shift, $R$ is the fiber coil radius, $L$ is the total fiber length, Ω is the input rotation rate, $\lambda$ and c are the light wavelength and velocity in free space, respectively.

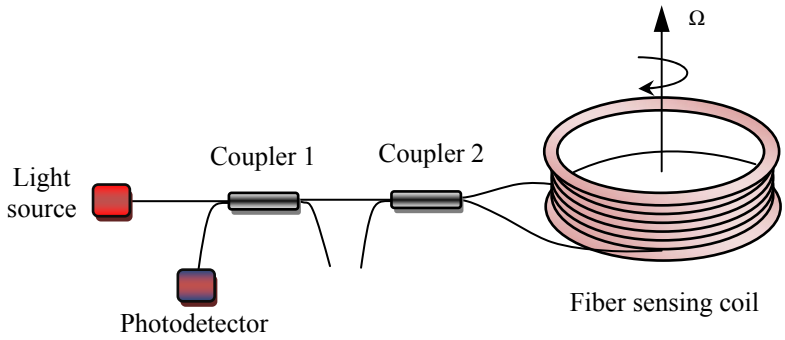


Fig. 1. Schematic illustration of the m main components of a multimode fiber optic gyroscope

In the case of FOGs with multimode optical fiber, the two counter-propagating waves are composed of several modes which have different propagation velocities. The Sagnac phase shift is the same for all modes because it is independent of their effective indices. Because of the use of low coherent source, there are no interferences between different modes, only counter-propagating modes of the same order does interfere, the MFOG operates as several independent single mode FOGs. In this case, any random phase error is averaged to zero and only the induced rotation phase is measured. However, in the real case, imperfections in the fiber manufacturing and external perturbations cause light to be coupled from a mode to others modes. So, the total MFOG output light intensity is the result of interference between fractions of light generated from different modes (direct and coupled modes). As reported in [14], the output light intensity of the first fringe when using low coherent light source and large active area photodetector can be approximated by:

$$I \approx \sum_{m=1}^{M}\sum_{n=1}^{M} I_{mn}^{+} + \sum_{m=1}^{M}\sum_{n=1}^{M} I_{mn}^{-} + 2\sum_{m=1}^{M}\sum_{n=1}^{M}\sqrt{I_{mn}^{+} I_{mn}^{-}}\cos\left(\phi_s + \phi_{mn}^{+} - \phi_{mn}^{-}\right) \tag{2}$$

where $I_{mn}^{+}$ and $I_{mn}^{-}$ describe the fraction of light which is coupled from the n*th* mode in the m*th* mode in both directions and $\phi_{mn}^{+}$ and $\phi_{mn}^{-}$ are the accumulated phase shift between these modes. $M$ is the total mode groups' number of the multimode fiber. This number is related to the fiber parameters by:

$$M = \sqrt{\frac{2\alpha}{\alpha+2}}\frac{\pi a \mathrm{NA}}{\lambda} \tag{3}$$

where α is the index profile parameter, $a$ is the radius of the fiber core and NA is the numerical aperture. We can see from the expression of the MFOG output in equation (2) that any changing in mode coupling yields fluctuations of the output intensity which is similar to the variation induced by rotation.

The intensity in the equation 2 can be written as follows:

$$I = I_{dc}\left[1 + C(M)\cos\left(\phi_s + \phi_e(M)\right)\right] \tag{4}$$

where $I_{dc}$ is a DC optical light components resulting from incoherent light interference, $C(M)$ is the fringe contrast which is given by:

$$C(M) = \frac{2\sum_{m=1}^{M}\sum_{n=1}^{M}\sqrt{I_{mn}^{+}I_{mn}^{-}}\cos\left(\phi_{mn}^{+} - \phi_{mn}^{-}\right)}{\sum_{m=1}^{M}\sum_{n=1}^{M}I_{mn}^{+} + \sum_{m=1}^{M}\sum_{n=1}^{M}I_{mn}^{-}} \tag{5}$$

and $\phi_e$ is an additional total phase error due to the presence of mode coupling in the fiber loop of the MFOG which can be expressed as follow:

$$\phi_e(M) = \arctan\left(\frac{I_{dc} - \sum_{m=1}^{M}\sum_{n=1}^{M}I_{mn}^{+} - \sum_{m=1}^{M}\sum_{n=1}^{M}I_{mn}^{-} + 2\sum_{m=1}^{M}\sum_{n=1}^{M}\sqrt{I_{mn}^{+}I_{mn}^{-}}\sin\left(\phi_{mn}^{+} - \phi_{mn}^{-}\right)}{I_{dc} - \sum_{m=1}^{M}\sum_{n=1}^{M}I_{mn}^{+} - \sum_{m=1}^{M}\sum_{n=1}^{M}I_{mn}^{-} + 2\sum_{m=1}^{M}\sum_{n=1}^{M}\sqrt{I_{mn}^{+}I_{mn}^{-}}\cos\left(\phi_{mn}^{+} - \phi_{mn}^{-}\right)}\right) \tag{6}$$

This phase error, similar to the rotation induced phase shift, is sensitive to external perturbations such as thermal variations and mechanical vibrations. As shown in figure 2, the total phase error is averaged to zero when the total mode groups number increase. This gives advantage for the MFOG to have a stable bias at rest. This stability becomes independent of the external perturbations.

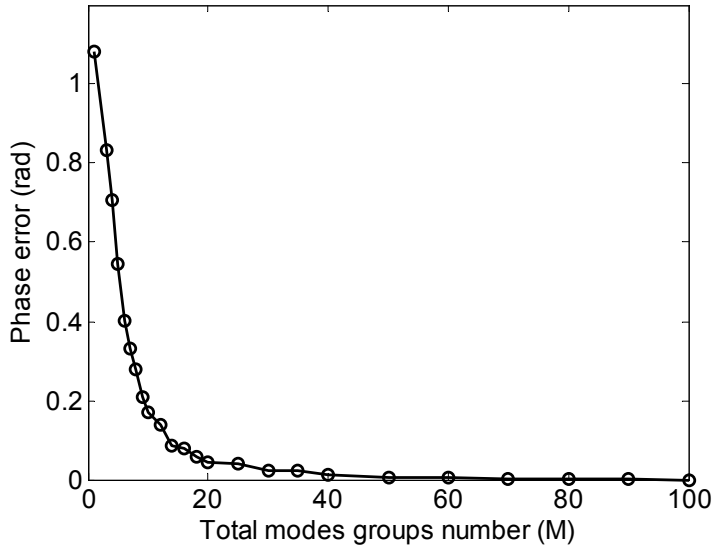


Fig. 2. Residual phase error as a function of the total mode groups number *M*.

Unfortunately, the increase in total mode groups number *M* has an opposite effect on the MFOG sensitivity. Indeed, the optical DC component becomes very significant compared to the interference component which cause reduction in the fringe contrast as illustrated in figure 3. The presence of high DC component at the photodetector generates a high level photonic shot noise. Therefore the sensitivity of the MFOG will be limited by this noise. Also, a low contrast can be caused by the efficiency of the photomixing at the photodetector and this may constitute a limitation for detection of low rotation rate.

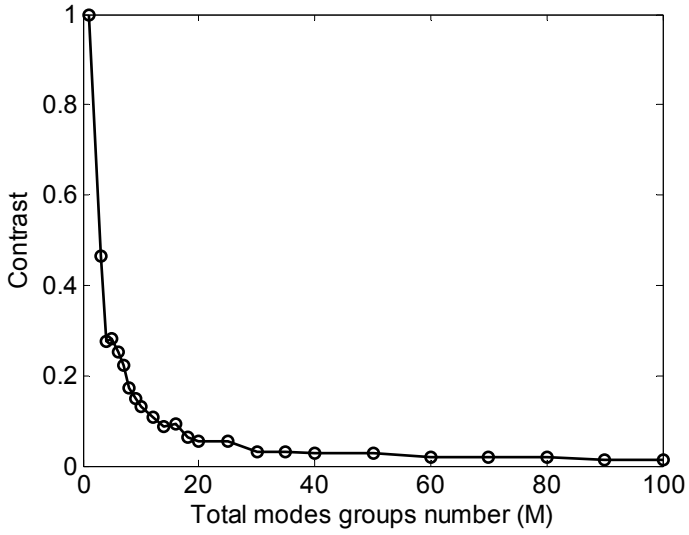


Fig. 3. Fringe contrast as a function of the total mode groups number *M*.

## 3. MFOG COMPONENTS CHOICE OPTIMIZING

### 3.1 Multimode fiber coil

The fiber coil is the sensing element in FOGs. So the choice of the multimode optical fiber to build the gyroscope is very important. Mainly, as we have previously seen, this choice is conditioned by the total number of mode groups (M) of the multimode fiber. The results of modeling show that the fringe contrast decreases when the total number of mode groups increases, which constitute a limitation to the sensitivity of the device.

However, the increase in the number of modes improves the bias stability by reducing the influence of the residual phase error, because this phase error is averaged over the modes. Therefore, it is necessary to find a compromise between sensitivity and bias stability by an appropriate choice of the total number of mode groups *M*. Consequently, selecting the optimum multimode fiber by choosing the parameters of the multimode fiber allows reaching the required compromise. To determine the optimal number of mode groups, we have used the following optimization cost function (figure 4):

$$f(\phi_e, C) = \frac{\phi_e(M)}{\max[\phi_e(M)]} + \frac{1/C(M)}{\max[1/C(M)]} \tag{7}$$

The optimal mode groups' number is the modes number which minimizes the cost function $f(\phi_e, C)$. This number can be expressed as follow:

$$M_{optimal} = \arg_M \min[f(\phi_e, C)] \tag{8}$$

The value of *M* which minimizes the cost function as illustrated in figure 4 is *10* modes. So, the optimum number of modes which makes it possible to reach the compromise between high sensitivity/stability is *M*=10. In practice, we have several multimode fiber types. We report in Table 1 a comparison between three standard multimode fibers, commonly used in optical communication, which are step index 50/125, 65,5/125 and 100/140. From this table, we can see that the standard SI 50/125 fiber (*M*=27) is the closest to the optimum choice. In addition, a low coherent light source with a coherence length of several nanometers is sufficient to eliminate the intermodal interference. Indeed, incoherent light does not have a significant influence because the FOG operates on the first fringe. For example a source with $\Delta\lambda$=20 nm gives approximately 25 fringes, which is largely acceptable (central fringe not affected by the contrast function).

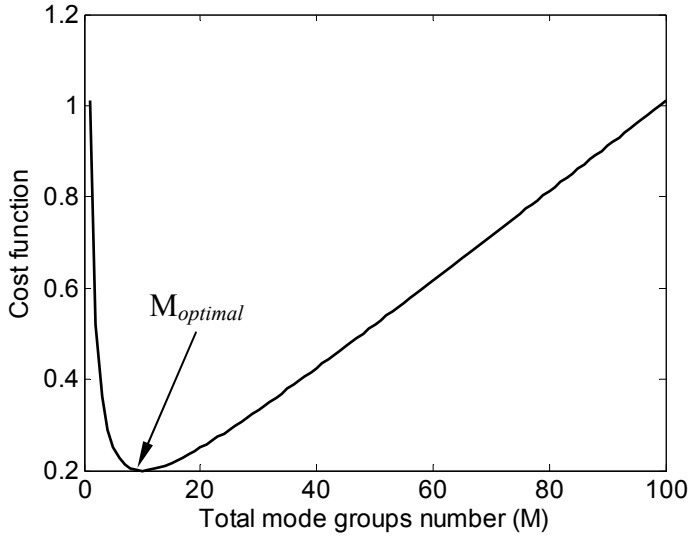


Fig. 4. Graph of the cost function used to find the optimum mode groups number.

Table. 1. Comparison of calculated total mode groups number of several step index multimode fiber optic types.

| **Fiber type** | **SI 50/125** | **SI 62,5/125** | **SI 100/140** |
|---|---|---|---|
| Core diameter (µm) | 50 | 62,5 | 100 |
| Cladding diameter (µm) | 125 | 125 | 140 |
| Fiber length (m) | 1000 | 1000 | 1000 |
| Operating wavelength | 850 | 850 | 850 |
| Relatif index Δ | 1% | 2% | 1,5% |
| Attenuation (dB/km) | 2,4 | 2,9 | 6 |
| Core index | 1,481 | 1,496 | 1,497 |
| Numerical aperture ON | 0.21 | 0,3 | 0,26 |
| Total mode groups number | 27 | 49 | 68 |

The choice of the step index fiber is more adapted for an optimal operation of the MFOG. Indeed, in this fiber type the modes propagate with different velocities. When using incoherent light source, they become uncorrelated after traveling into the fiber loop. Therefore, this eliminates their interference resulting in a phase error reduction. However, in graded index fiber the different modes travel into the fiber loop in the same time which makes the elimination of the interference between modes very difficult even with an incoherent light. Thus, the use of multimode graded fiber for MFOG is not recommended and the effect of interference of coupled mode remains.

In order to couple the maximum power in the fiber, it is useful to use a multimode fibre with a large numerical aperture which allows improving power level at the MFOG output and thus overcoming errors due to the photonic noise of the photodetector. More error reduction of transient effects can be achieved by an adequate coil winding like a quadrupolar winding technique [17] illustrated in figure 5. In this technique the winding starts from the middle of the fiber in the form of layers. Each set of layers is composed of two layers and each set is winded in opposite direction to the previous one.

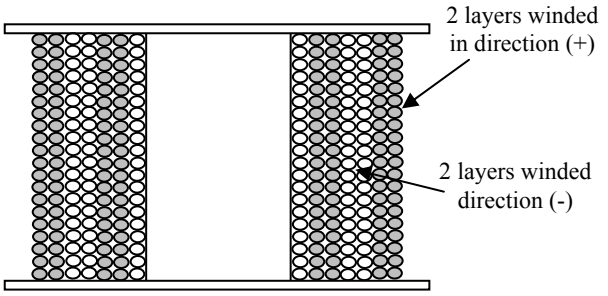


Fig. 5. Illustration of quadrupolar winding technique.

### 3.2 The coupler

The choice of the coupler is based on the following criteria:

- Ensure that the modal distributions at the coupler outputs are symmetrical;
- Respect the phase reciprocity;
- Fiber coupler type (X or Y).

We notice that the problem of the phase reciprocity is solved by using a configuration with two couplers. In addition, the use of 3 dB Y couplers compared to X coupler allows improving the light power at MFOG output by a factor of 3 and therefore the device sensitivity will be improved.

In FOGs, the light source is connected directly to the input port of the first coupler. For that reason, it is interesting to choose a coupler with a large numerical aperture. Such coupler ensures high power coupling between the source and the MFOG fiber coil. Thus, the low cost fused multimode fiber coupler largely used in optical communication is more useful for the MFOG.

Compared to the first coupler, the second one must be symmetrical, i. e. it affects equally the modal distribution between the various outputs ports. The micro-optic fiber couplers based on the use of a beam-splitter plate are more adapted to satisfy this condition.

### 3.3 The Light source

Primarily, several parameters have to be taken into account for the choice of a light source for a MFOG which are the emission wavelength λ, the spectral bandwidth Δλ and the light power of the source. The Sagnac phase shift is inversely proportional to the wavelength λ which means that the MOFG will be very sensitive in low wavelength. Therefore, a low wavelength appears as a result of an obvious choice. Moreover, the commonly used optical windows in optical fiber communications are 1550 *nm*, 1310 *nm* and 850 *nm*. Knowing that near IR wavelength supports maximum scale factor, and therefore maximum resolution, the wavelength λ =850 nm appears as the optimal choice.

In the modeling part, we have seen that intermodal interferences are the origin of errors and can be eliminated by using low coherent light source. Consequently, the MFOG performances can be improved. Also, due to back-reflection and backscattering error sources, the appropriate MFOG light source shall have limited coherence. The coherence length of the source $L_s$ necessary for the elimination of the intermodal interference must be less than the coherence length in the multimode fiber $L_f$ ($L_s<L_f$). This last is the smallest path difference between modes of the fiber which is given by:

$$L_f = L\Delta\left(\frac{\alpha-2}{\alpha+2}\right)\frac{1}{M^{\frac{2\alpha}{\alpha+2}}}\left[2^{\frac{2\alpha}{\alpha+2}}-1\right] \tag{9}$$

where $\Delta = \mathrm{NA}^2 / 2n_1^2$ is the relative refraction index and $n_1$ is fiber core refractive index.

In the case of step index fiber (α=∞) the coherence length in the fiber becomes:

$$L_f = \frac{3L\Delta}{M^2} \tag{10}$$

By using the expression for the coherence length of the source $L_s = \lambda^2/\Delta\lambda$ we can calculate the minimum required bandwidth $\Delta\lambda_{min}$ necessary to eliminate the intermodal interference as follow:

$$\Delta\lambda_{\min} = \frac{2n_1^2\lambda^2}{3L\mathrm{NA}^2}M^2 \tag{11}$$

We notice that the minimal bandwidth $\Delta\lambda_{min}$ of the light source is closely related to the optical and geometrical parameters of the fiber and is a function of the total mode groups number *M*. The table 2 shows some calculated values of required bandwidth for different type of fiber which are relatively equal.

As a result, light emitting diodes (LEDs) are more useful for MFOG instead of the laser diodes. The LEDs have generally a 10 nm to 100 nm bandwidth which can largely meet the condition $\Delta\lambda > \Delta\lambda_{min}$. In addition, such sources are available in the market at relatively low costs. Compared to the prior art, the use of pigtailed LED allows to avoid the problems related to coupling of light and alignment of the fiber and consequently can enhance the performances of the MFOG. In addition, the use of fused fiber splicer for connection between fibers can maximize also the coupling light in the input fiber.

Table. 2. Minimum required bandwidth calculated for different step index multimode fibers.

| **Fiber type** | **SI 50/125** | **SI 62,5/125** | **SI 100/140** |
|---|---|---|---|
| $\Delta\lambda_{\min}$ (nm) | 0,017 | 0,028 | 0,073 |

### 3.4 The Photodetector

The photodetector has an important role for the design of high sensitive MFOGs, especially for the detection of low rotation rates. The photodetection of the optical rotation induced signal is limited by the photonic noise generated by the photodetector. The amount of noise depends on the returned optical power to the photodetector. The related phase noise at the quantum limit [18] can be written as follow:

$$\phi_n = \sqrt{\frac{2hcB}{\eta\lambda P_{dc}}}\frac{1}{C(M)} \tag{12}$$

where η and *B* are the efficiency and bandwidth of the photodetector respectively, *h* is the Planck's constant and $P_{dc}$ is the incident continuous power on the photodetector. The rotation equivalent noise in this case can be expressed as follows:

$$\frac{\mathrm{NE}\Omega}{\sqrt{B}} = \frac{1}{4\pi RL}\sqrt{\frac{2h\lambda c^3}{\eta P_{dc}}}\frac{1}{C(M)} \tag{13}$$

As we shown above, the MFOG has a low contrast which means that the continuous optical component is much higher than the interference optical component. Indeed, the presence of this high level continuous component at the photodetector generates more shot noise and therefore degrades the signal to noise ratio. To limit this degradation, the quantum efficiency η should be as close to 1 as possible.

The silicon PIN photodiodes are more adapted for this purpose because of their high quantum efficiency (η≈0,8). In addition, the use of pigtailed PIN photodiode offers some advantages such as low loss, high photomixing, ensure that the modes are orthogonal and avoids the problems related to the fibers alignments.

Varieties of electric circuits are used in photodiodes. For high performances MFOG, attention shall be given to the photodiode circuit design. In fact, a photodiode can be operated in photovoltaic or in photoconductive (biased) mode. In the photovoltaic mode no bias voltage is applied. In this case, the only noise source is the thermal noise. Normally, photodetectors operating in this mode have extremely low noise [19]. On the other hand, photodetector operating in a biased mode the noise will be larger since the bias voltage generates a leakage current (dark current which result in shot noise).

The use of differential transimpedance amplifier configuration for photodiode in MFOG is advantageous and it can improve sensitivity. The benefit of this configuration is the common-mode rejection of coupled noise. By feeding the output of the current to voltage conversion into a differential amplifier stage, noise will show up as a common mode signal on both inputs and have a canceling effect at the circuit output.

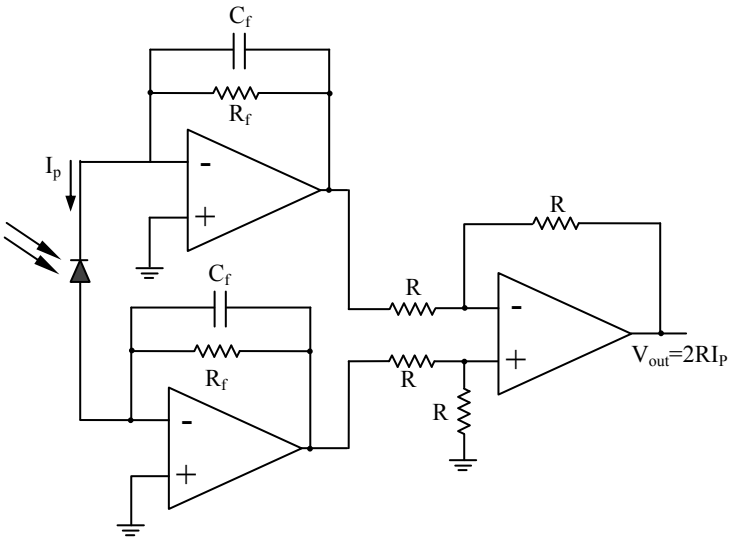


Fig. 6. Typical differential transimpedance circuit

## 4. CONCLUSION

This study constitutes a theoretical approach for the design of an optimized MFOG through an adequate choice of its components. The obtained results show that performances can be improved by using the SI 50/12 standard multimode fiber, a symmetrical coupler, a LED light source emitting at 850 nm and a silicon PIN photodiode with pigtail. To avoid connection loss, these optical components must be manufactured with the same fiber. In addition, this optimized choice of the components offers a low cost option for MFOG manufacturing in the future with relatively high performances. Such a rotation sensor should find useful applications in land navigation, robotics and for oil drillings, where their temperature insensitivity is particularly advantageous.

## REFERENCES


[1] Lawrence, A., [Modern inertial technology: Navigation, guidance and control], Springer Verlag, 169-205 (2008).

[2] Lopez-Higuera, J. M., and Yu, S. Y., [Handbook of optical fibre technology], Wiley, Inc, New York, 620-627 (2002).

[3] Fredricks, J. R., Johnson, D., R., "Low cost multimode fiber optic rotation sensor," Proc. of the SPIE on Fiber Optic and Laser Sensors V, 985, 106-116 (1987).

[4] Nawgboso, C., [Automotive sensory systems], Cluwer academic publisher, 141-156 (1993).

[5] Pavlath, G., and Shaw, H. G., "Multimode fiber gyroscopes," Proc. Of 1st conference on Fiber-Optic Rotation Sensors and Related Technologies, Springer Verlag, 32 (1982).
[6] Bessonova, S. V., et al., "Fiber optic ring interferometer with a multimode waveguide," Sov. J. Quantum Electronics, 13(10), 1403-1405 (1983).
[7] Alekseev, E. I., et al., "Ring interferometer with a multimode waveguide," Sov. J. Quantum Electronics, 14(11), 1436-1442 (1984).
[8] Bazarov, A. E., and Semenov, A., T., "Nonreciprocal effects in a ring interferometer with a multimode fiber waveguide," Sov. J. Quantum Electronics, 14(4), 522-257 (1984)
[9] Fredricks, J. R., and Johnson, D., R., "Performance enhancement of low cost multimode fiber optic rotation sensor," Proc. of the SPIE on Fiber Optic and Laser Sensors VI, 985, 218-226 (1988).
[10] Johnson, D. R., et al., "Multimode fiber optic rotation sensor with low cost digital signal processing," Proc. of the SPIE on Fiber Optic and Laser Sensors VIII, 1367, 140-154 (1990).
[11] Galkin, S. L., and Nikolaev, V. A., "Design characteristics of a multimode fiber gyroscopes," Priborostroenie, 33, 50-54 (1990).
[12] Bykov, M. M., Gorshkov, B., G., Zaslonko, I., K., "Investigation of a correlation fiber-optic ring interferometer based on multimode optical fiber," Springer, New York, 34(5), 607–610 (1991).
[13] Bouamra, M., and Meyrueis, P., "Multimode fiber optic gyrometer," Proc. Of the 15th Anniversary Conference on fiber optic gyros, 1585, 309-321 (1991).
[14] Medjadba, H., Lecler, S., Simohamed, L. M., Chakari, A., "Modeling a multimode Sagnac interferometer: application for an embarked fiber optic gyroscope," Proc. of the SPIE on optical fiber sensor, 7003, 700310 (2008).
[15] Bergh, R. A., Lefevre, H. C., Shaw, H. J.,"An overview of fiber-optic gyroscopes," J. Light. Tech. 2(2), 91-107 (1984).
[16] Vali, V., and Shortill, R. W., "Fiber ring interferometer," Appl. Opt. 15(5), 1099-1100 (1976).
[17] Ronald, H. S., "Experimental results on fiber gyro coil winding cost reduction," Proc. Of SPIE on Fiber Optic Gyros: 15th Anniversary Conference, 1585, 426-430 (1992).
[18] Wanser, K., H., "Fundamental phase noise limit in optical fiber due to temperature fluctuation," Electronic Letters, 28(1), 53-54 (1992).
[19] Graeme, J., [Photodiode Amplifiers,] McGraw Hill, New York, (1996).

# Multi-task single lens for automotive vision applications

Patrice Roulet, Pierre Konen and Simon Thibault
ImmerVision
2020 University St., Montreal, Canada H3A 2A5

**ABSTRACT**

The increasing trend to use vision sensors in transportation is driven both by legislation and consumer demands for higher safety and better driving experiences. Awareness of what surrounds an automotive vehicle can directly affect the safe driving and maneuvering of that vehicle. Consequently, panoramic 360° field-of-view (FoW) imaging is becoming an industry prerequisite. However, to obtain a complete view of the area around a vehicle, several sensor systems are necessary. This paper explains how panomorph optics can satisfy the needs of various vision applications with only one sensor or panomorph lens configuration.

A panomorph lens is a hemispheric wide-angle anamorphic lens with enhanced resolution in a predefined zone of interest. Because panomorph lenses feature an optimal pixel-per-degree relationship, the resulting vision systems provide ideal area coverage, which in turn reduces and maximizes the processing. Here we present how panomorph technology is one of the most promising ways to integrate many automotive vision applications (processing/viewing) onto one single camera module. For example: a single panomorph sensor on the front of a vehicle could provide all the information necessary for assistance in crash avoidance, lane tracking, early warning alerts, parking aids, road sign and pedestrian detection, as well as various video monitoring views for difficult areas such as blind spots.

Keywords: wide-angle lens, panoramic, panomorph, immersive, hemispheric, anamorphic, 360° vision systems, vision sensors, automotive vehicles, field of view, transportation, driver assistance systems, lane tracking, blind spot, pedestrian detection, road sign detection, parking assistance

## 1 INTRODUCTION

The increasing trend to use vision sensors in transportation is driven both by legislation and consumer demands for higher safety and better driving experiences. Awareness of what surrounds an automotive vehicle can directly affect the safe driving and maneuvering of that vehicle. Indeed, video and vision processing have become the fastest growing technologies deployed in automotive manufacturing. Increased integration of electronic components and the declining prices of electronics in general are the primary enablers of this trend. Lane keeping, driver monitoring, night vision and parking assistance are just a few of the applications "driving" the need for improved vehicle imaging systems. Many of the new applications using video imagers are for advanced safety systems, used to assist the driver in vehicle management or to autonomously control occupant safety systems.

With such a wide variety of system objectives and requirements, it is important that we examine how an enhanced vision system, equipped with an enhanced resolution wide-angle lens, can solve current vehicle vision application challenges while allowing integration with less sensor requirements.

There are two major objectives of this paper:

- The first is to present various needs related to computer vision-based applications (analytics) and viewing applications.
- The second is to present the novel *panomorph technology concept* patented by ImmerVision, explain how it compares to fisheye vision sensor systems, and show how it can be used to integrate many applications with only one vision sensor (case study).

Photonics in the Transportation Industry: Auto to Aerospace II, edited by Alex A. Kazemi, Bernard C. Kress
Proc. of SPIE Vol. 7314, 731409 · © 2009 SPIE · CCC code: 0277-786X/09/$18 · doi: 10.1117/12.821296

## 2 VARIOUS AUTOMOTIVE APPLICATIONS: VARIOUS NEEDS

In recent years, considerable efforts have been made to develop driver support systems which enhance safety by reducing accidents[1]. As an example:

- Lane detection vision systems can determine the lateral position of a vehicle and warn the driver in the event of an imminent lane departure. They can also help prevent collisions with other vehicles or fixed objects, or from literally driving off the road.
- Front-view detection is useful in preventing accidents by detecting objects such as vehicles, pedestrians and cyclists, and by piloting the cruise control using road-sign detection and forward vehicle tracking.
- Monitoring the vehicle's blind spots is useful before the driver changes lanes.

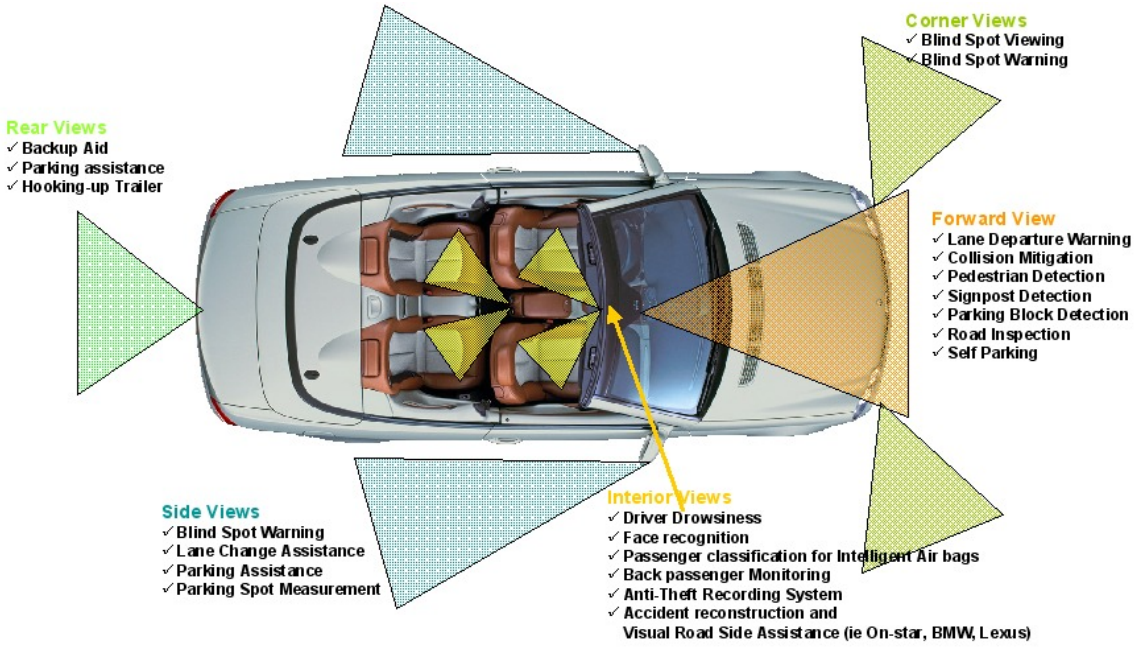


Table 1 and Figure 1 show a non-exhaustive list of information/applications that can be provided or required in respect to view zones.

Table 1: Developing the market for advanced sensor ability and safety

| View area | Information provided / Applications |
|---|---|
| Rear view | Back-up aids<br>Parking aids<br>Blind spots<br>Lane change assistance<br>Hooking up trailer<br>Lane departure warning |
| Forward view | Adaptive cruise control<br>Lane departure warning<br>Collision warning (cars and pedestrians)<br>Blind spots<br>Parking aids<br>Road sign detection (speed limits, etc.)<br>Pedestrian detection |

| | |
|---|---|
| | Self parking<br>Road inspection |
| Interior view | Passenger classification for airbag system<br>Driver drowsiness<br>Rear view (back seat, children)<br>Face recognition<br>Visual roadside assistance<br>Anti-theft/recording system |
| Side view | Parking aids<br>Blind spots<br>Lane change assistance<br>Collision warning (cars and pedestrians) |

Each application has different needs in terms of sensor position, orientation, resolution and coverage. Usually, to complete each functionality listed below, many sensors are required. In this paper, the authors explain how to realize the same applications with fewer cameras and less sensors, using panomorph technology.

## 2.1 Computer vision-based applications

### 2.1.1 Lane departure and lane curvature recognition

The lane departure warning system (LDWS) is designed to warn a driver when the vehicle begins to move out of its lane (unless the appropriate turn signal is activated) on freeways and arterial roads. The LDWS needs lane curvature information and the vehicle's position on the road as input. This starts with lane detection via a camera lens. The objective is to detect and track the line separating the lanes on the road to evaluate the trajectory of the vehicle and the road curvature.

Depending on the approach, the algorithm can use a front or rear camera. Regarding the field-of-view of these cameras, Takahashi[2] explains that a wide-angle lens has two main advantages over a narrow-angle lens: One, it is easier to detect lane marks because the camera can see the lane mark just under the vehicle; and two, there are many recognition clues due to the fact that the camera can search widely in a lateral direction.

Regarding the image resolution requirement, Takahashi[2] further notes that this type of application needs enough resolution to detect the gap between two lines -- for example the lines down the middle of a highway. He then demonstrates that the projective view of a wide-angle camera can accelerate image processing on a vehicle-embedded system (by using less processing power). After vehicle trajectory and road curvature detection information is collected, it can be sent to the driver, to the adaptive cruise control system (ACCS), or to the vehicle stability control system, which maintains lane position by applying gentle brake pressure.

### 2.1.2 Collision warning using vehicle detection

Collision warning applications regroup different functionalities such as "stop and go" ACCS -- forward collision warnings and intersection collision warnings using vehicle-detection algorithms. The goal is to detect an imminent collision and to warn the driver, the ACCS or the auto brake system. This type of algorithm uses pictures from a camera to detect, classify and localize a potential obstacle.

For an intersection collision warning (a situation during which obstacles can come from any direction around the vehicle), a wide-angle sensor is required. After the detection step, the picture of the potential obstacle is then extracted from the wide-angle picture. According to Zhang[3], the obstacle classification requires a 40*40 pixel image of an obstacle from which the detection system can provide a minimum of 10*10 pixel images. Zhang then reformats the images as a 40*40 picture. One can deduce that the required resolution for the classification algorithm is 40*40 pixels, even if the

classification algorithm works with a 10*10 image. After classification, the system can evaluate the position and speed of the potential obstacle and use other radar/lidar sensor information to obtain distance information (sensor fusion). This information can then be sent to the ACCS or for viewing on an on-board driver information display.

### 2.1.3 Road sign detection and recognition

In the future, being able to recognize traffic signs will be increasingly important for vehicle safety systems. Such systems could assist drivers with signs they failed to notice *en route*. Specifically, speed-limit sign recognition could inform drivers about the current speed limit, and alert the driver if the vehicle is being driven faster than the posted speed limit.
In futuristic scenarios, autonomous vehicles would *have* to be controlled by automatic road-sign recognition. As there is a preponderance of traffic signs for speed limits, directions, warnings, upcoming traffic lights, etc., this will become an essential feature. Road-sign detection and recognition systems can inform the driver or the ACCS about current speed limit restrictions, dangers or potential interdictions. In addition, the localization of road signs changes, depending on type of sign, regional driving laws, and whether the signs are permanent or temporary. For example: a road sign can be mounted on poles situated on street corners, hung from horizontal poles or be on wires strung over the roadway, before, at or after the actual intersection. The many variations around the road sign's possible location require a large field-of-view (FoV) camera sensor for effective detection.
After detection, the target road sign image is extracted from the wide-angle picture. The resolution in pixels of the sign depends on the distance from the sensor (camera). Alefs[4] explains that a road-sign detection and recognition system needs at least a 12 pixels-wide road sign for detection. Indeed, the system is able to detect 85% of objects which are12 pixels wide or more, and 95% of objects 24 pixels wide or more at a low false alarm rate. After successful detection, the information can then be sent to the ACCS or for viewing on an on-board driver information display.

The computer vision applications listed above offer active assistance to the driver. All of them are interconnected to ensure that the best decision is made possible. As described, they have several different requirements in terms of sensor field-of-view, resolution and image rectification, and projection. In this paper, the authors will explain how one single wide-angle sensor can be used to meet each application's needs.

## 2.2 Driver viewing applications: A new way to avoid blind zones

A vehicle's blind zones are the areas surrounding the vehicle where the driver can not see what, if anything, resides in that defined space (the blind zone). The size of the blind zone depends on the vehicle design (driver position, windows and mirror positions).

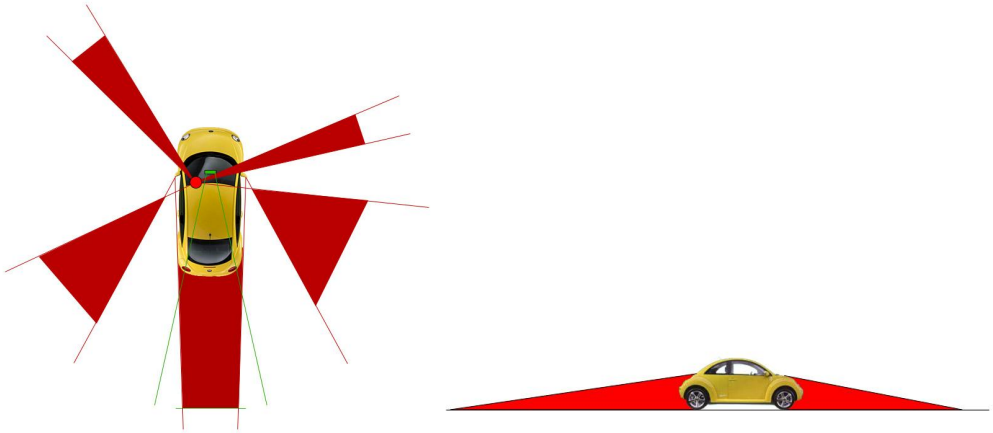

Figure 2: Blind zones for a standard left-hand side driver's car

For many years now, flat mirrors have helped drivers reduce blind zones. In the 80s, custom shape mirrors and wide angle Fresnel lenses further improved blind zone coverage. More recently, cameras and on-board displays appeared, providing another point of view for the driver. The most famous application to date is the rearview camera, which assists drivers with challenging parking. The on-board display shows the video produced by the rear camera, and effectively helps the driver overcome the rear blind zone.

Blind zone reduction is necessary for reducing injuries, especially in the case of vulnerable objects/items/elements (pedestrians, bicycles). Hughes[5] explains that some legislation has been proposed by several governments (Europe, Japan and USA) that requires the diminution of blind zones using a mirror or camera device. To drastically reduce the blind zones without increasing the number of sensors and mirrors, wide-angle lenses must be considered as a serious option.

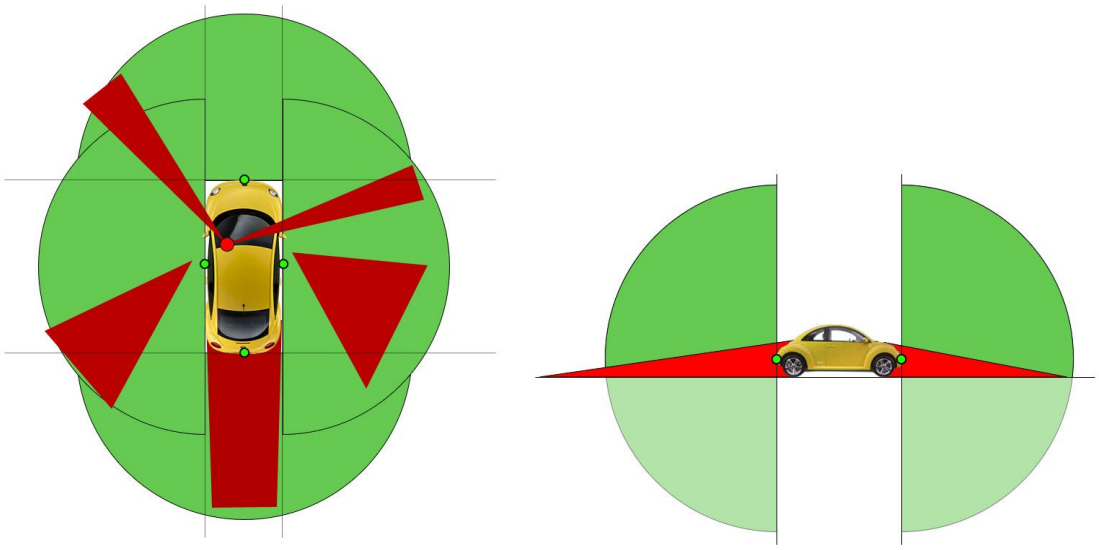

Figure 3: Blind zone avoidance using four (4) wide-angle lenses

Several manufacturers, including Honda, Mitsubishi and Fujitsu, provide on-board systems which use multi-camera systems (four or five cameras) located all around the vehicle (see reference on companies' web sites). These systems provide different types of viewing, depending on the driver's needs, and successfully eliminate most of the blind zones.

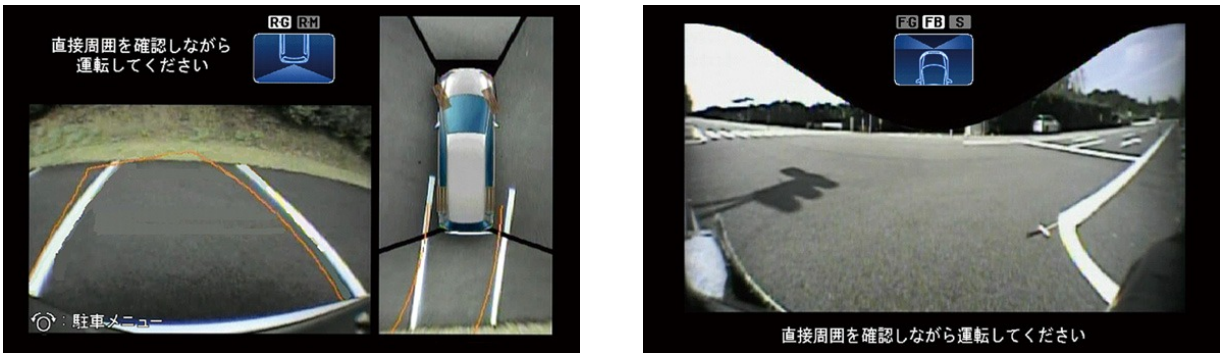


Figure 4: Honda's multi-camera viewing system

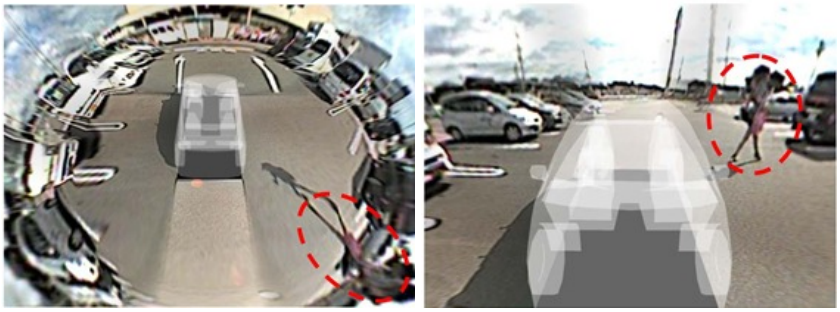

Figure 5: Fujitsu's multi-camera viewing system

In the next section, the authors will explain how the panomorph lens may provide the ideal solution to the modern driver's viewing requirements. We will also explain how to use the panomorph lens' key features to avoid blind zones, and we will demonstrate how just one panomorph sensor can provide a variety of different views.

## 3 THE CONCEPT OF PANOMORPH TECHNOLOGY

Many lenses with a camera sensor (CMOS or CCD) are naturally suited to provide surround-monitoring of vehicles. However, due to the camera's large field-of-view (FoV), any virtual view generated electronically and pointed in a specific direction suffers from low resolution[1]. Consequently, to get a high-resolution surround image, a high-resolution sensor is required, which leads back to the issue of cost.
Panomorph lenses, on the other hand, can control distortion. This alone is considered a major enhancement in panoramic vision[6]. By using a distortion-control approach and anamorphic image mapping, both patented by ImmerVision, panomorph lenses provide a unique full hemispheric field coverage. In contrast to other types of panoramic imagers that suffer from blind zones (catadioptric cameras), low-image numerical aperture and high distortion -- the panomorph lens uses distortion as a design parameter, to provide a higher-resolution coverage where needed.

Panomorph lenses also feature an anamorphic image mapping of the full hemispheric field, resulting in an ellipse-image footprint rather than the circle or annular footprint that other types of panoramic imagers produce. This feature provides an *immediate* 30% gain in pixels on the sensor (the ellipse footprint matches the ratio of a CCD or CMOS imager). This combination of distortion control and anamorphic design provides an important gain in resolution pixel/degree in the zones of interest, and an advantage over all other types of panoramic imagers. Finally, the main benefit of panomorph optics is its custom-design approach, meaning that the panoramic lens and the image projection software can be customized to meet real and very specific needs in visible or infra-red applications[7].

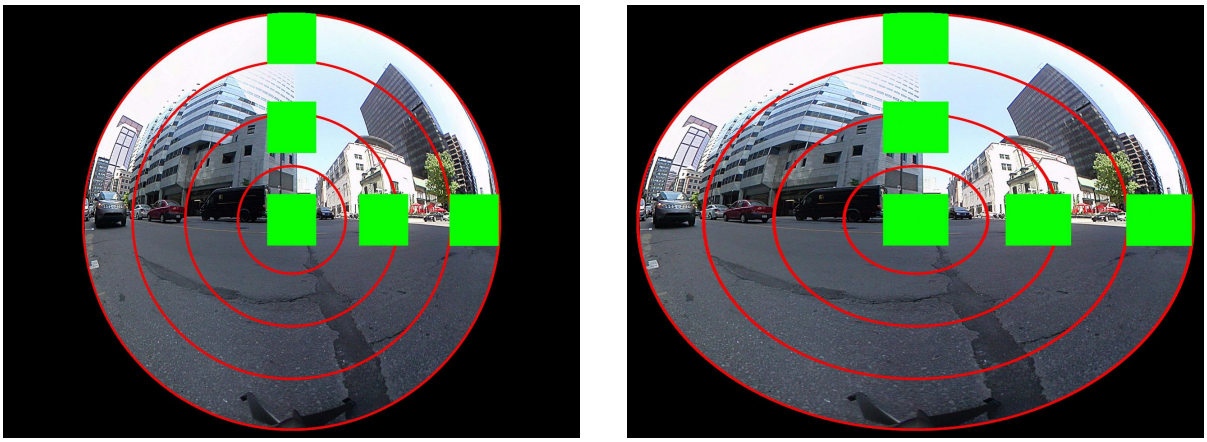

Figure 6a and 6b: Images taken with a fisheye lens (6a, left) and with a panomorph lens (6b, right).
Green boxes represent equivalent areas.

Figure 6 shows the front-view image from a car in a parking lot, produced by a fisheye lens (6a) with equidistance projection (perfect linear [f-theta] mapping) and the same image produced by a panomorph lens (6b). The green boxes show the relative dimension of an object in the field. The elliptical footprint on the right produces an anamorphic correction, and the panomorph lens provides increased resolution along the long axis of the sensor.

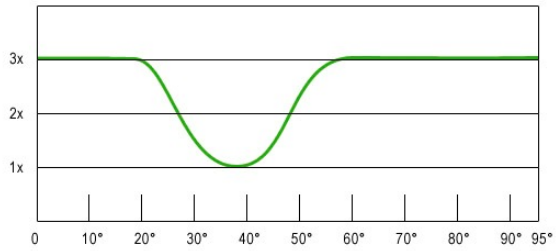


Figure 7: Associated pixels/degrees distortion curves

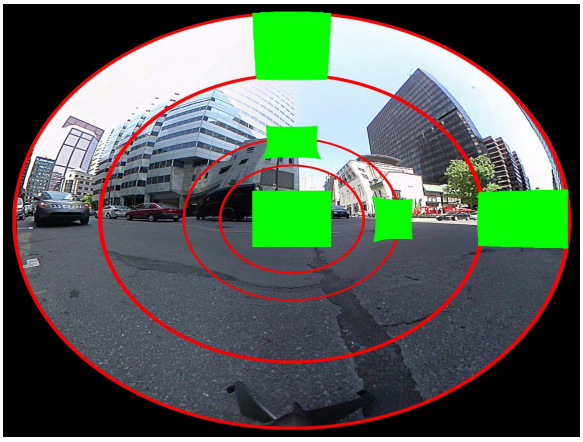

Figure 8: Increased resolution with a panomorph lens

Figure 7 shows the same image taken by a panomorph lens with increased resolution in the center and along the border. Figure 8 shows the resolution ratio of the lens (pixels ratio/degrees). The resolution along the border is three times higher than in the center. Where the resolution is higher, the camera is able to see for a longer distance. The viewing algorithms embed the proper resolution curve/algorithms to correct the distortion (please refer to section 4.4). This custom image mapping is the resolution distribution required for a typical application. As another reference, we refer readers to a published case study[8] for a panoramic imaging security scenario.

## 4 A CASE STUDY: FOUR APPLICATIONS – ONE LENS DESIGN

Consider the simplified situation of a camera flush-mounted on the front of a vehicle. The goal of this section is to determine the appropriate parameters of the panomorph lens and the projection (un-warping) algorithms which correspond to the application requirements.

Lens and algorithm parameters to be determined:

- Field-of-view (FoV) of the application
- Lens distortion, anamorphosis ratio and resolution
- Lens mathematical model and calibration
- Software projection type, treatment and performance

Applications requirements:

- Lane departure and lane curvature recognition:
  - Large FoV: Larger than 180° to increase the robustness of line tracking
  - Projection algorithms to rectify the image and provide a straight line for recognition
- Collision warning using vehicle detection:
  - Large FoV to detect oncoming vehicles from all sides of a road intersection
  - 2-meter vehicle width must cover 10 to 40 pixels wide

- Road sign detection and recognition:
  - Large FoV to detect road signs at different locations
  - 0.5-meter sign width must cover 12 to 24 pixels wide
- Blind zone avoidance:
  - Large FoV: Larger than 180° to avoid blind zones
  - Projection algorithms to rectify the image and provide a user-friendly view to the driver

### 4.1 Field-of-view (FoV) of the application

Each application listed above needs a large field-of-view (FoV), so a wide-angle lens is required. Depending on the tolerances in the lens position, a FoV of up to 190° is required to guarantee a full hemispheric FoV. There are different types of wide-angle lenses, as the author has explained in a previous paper[9]. Mirror imager and PAL are not studied due to inappropriate fit-form-function factors (i.e. the blind zone in the middle of the FoV). In this case study, the authors will consider only fisheye and panomorph lenses, and will demonstrate the benefits of the panomorph lens utilization.

### 4.2 Lens distortion, anamorphosis and resolution

Fisheye lenses have a radial distortion across the hemispherical field-of-view (FoV). The radial distortion of the fisheye lens depends on the design itself, and introduces some variation in the resolution (pixels/degrees) over the entire FoV. This variation can be quantified as a departure from the ideal theoretical fisheye lens, which has a theoretical linear (f-theta) mapping. According to Kumler and Bauer[11], different types of fisheye lenses have different performances regarding the departure of perfect linear (f-theta) mapping, which can go up to 16%, especially along the border (20 last degrees). The panomorph lens uses distortion as a design parameter, in order to provide high-resolution coverage in a specific zone of interest. For this academic exercise, we will consider the "theoretically perfect" fisheye lens with 190° FoV and 0% departure (linear resolution), and a panomorph lens with 190° FoV and an adapted resolution (distortion).

Fisheye lenses produce a circular footprint on the sensor. Fisheye lenses don't have any anamorphosis. Panomorph lenses produce an elliptical footprint on the sensor. The anamorphic design of the panomorph lens provides a customizable coverage of the sensor. Depending on the mechanical and assembly tolerances, the panomorph lens is designed to ensure that the footprint fits into the sensor, using small border merges. For this academic exercise, we will choose a 4/3 sensor and the border merges will be negligible.
A panomorph lens can be used with any sensor format (VGA, XGA, SXGA etc.) as long as the lens performance matches the Nyquist frequency of the sensor. For this academic exercise, we chose a 1.2 mega pixel sensor (1280 x 960 pixels) called a target sensor.

A collision warning application needs to have at least 10 pixels to define a two-meter wide object (vehicle). As defined by Thibault[12], a fisheye lens is 5.04 pixels/degree on the targeted sensor (1280*960) over the entire FoV.

(1) $$\alpha = \frac{Size_p}{\mathrm{Re}s_{P/\circ}}$$

Where $Size_p$ is the object size on the sensor in pixels, and $\mathrm{Re}s_{P/\circ}$ is the resolution of the system lens-sensor in pixels/degree: A 10-pixel object represents a $\alpha$=1.98° FoV and a 40-pixel object represents a $\alpha$=7.9 FoV.

(2) $$d = \frac{Size_m}{Tan(\alpha)}$$

Where $Size_m$ is the object size in meters: A 10-pixel object is d=57.8 meters from the car. This means that a two-meter wide object will illuminate 10 pixels or more when the objects are within 57.8 meters.

With a panomorph lens, we can customize the distortion mapping to provide better resolution where required. Based on Figure 9 (used only for indicative purposes), we define three zones of interest in the horizontal plane. The first area of interest in which we would like to increase resolution is the forward view. The second and third areas are to the right of the left-corner views (see Figure 7 for suggested distortion curve).

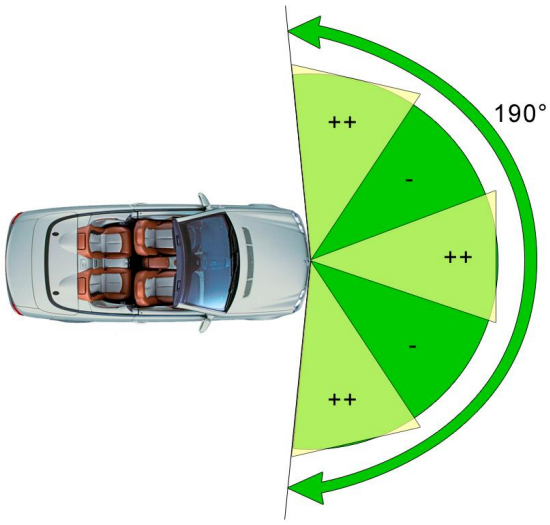


Figure 9: Augmented-resolution areas of interest for a panomorph front view lens.

**For a collision warning application**, there is a need to see farther on both sides when crossing an intersection. One needs also to see farther right in the middle, to detect a vehicle in the same lane. Figure 9 shows the resulting areas of interest over the entire FoV. As defined by Thibault[12], the resolution of this type of lens is 8.42 pixels/degree on the targeted sensor within the zone of interest. Using formulas (1) and (2), a 10-pixel object would be 97 meters from the car, a 70% increase compared to a theoretical fisheye lens within the same area of interest.

The safe distance between two vehicles is based on the driver's reaction time; some governments have determined that this reaction time is at least the distance travelled during two seconds. We can deduce the following formula:

$$ds_{meter} = 0.56 \times V_{km/h}$$

Table 2: Safe distance between two vehicles at conventional speed limits

| Speed | 50 km/h | 70 km/h | 90 km/h | 110 km/h | 130 km/h |
|---|---|---|---|---|---|
| Safe distance | 28 m | 39 m | 50 m | 62 m | 73 m |

Considering this, the panomorph lens is a serous option, because it can provide enough resolution for a collision warning application during different traffic conditions (city driving to highway driving).

**Road sign detection and recognition** applications need to have at least 12 pixels to define road signs of widths from one (1) meter up to 1.5 meters[13].

With a fisheye lens, using formulas (1) and (2):

- For a one-meter wide road sign, a 12-pixel object is 24 meters from the car and a 24-pixel object is 12 meters from the car.
- For a 1.5-meter wide road sign, a 12-pixel object is 36 meters from the car and a 24-pixel object is 18 meters from the car.

With a panomorph lens, using formulas (1) and (2):

- For a one-meter wide road sign, a 12-pixel object is 40 meters from the car and a 24-pixel object is 21 meters from the car.
- For a 1.5-meter wide road sign, a 12-pixel object is 60 meters from the car and a 24-pixel object is 30 meters from the car.

Again, because of the specific panomorph resolution pattern suggested in this case study, panomorph optics will increase the distance in its areas of interest (++ areas on Figure 9) by a factor of 70% compared to a theoretical fisheye lens.

**For a lane departure warning system**, the painted lines are right in the zone of interest of the suggested panomorph lens as in Figure 9. This distortion pattern improves the resolution of the road line in front of the car to provide the best image quality for detection. Also, a specific viewing function will be suggested in order to simplify processing (see section 4.4).

**For side views (blind spot monitoring),** a higher resolution image will significantly enhance the viewing of far-away objects and vehicles on the periphery of the optical area.

### 4.3 Lens mathematical model and calibration

The panomorph geometrical model (PGM)[9] and lens calibration is required when the targeted application needs a projection algorithm to compute a special view. This will be explored in more detail in the next section.

Lens calibration might be required when:

- localization or measurement of targets on the panomorph image have to be determined;
- different sensors need to be stitched/integrated into one logical image;
- other types of sensors (radar, ultrasounds, etc) must be fused into a panomorph video feed;
- 3D reconstruction and/or camera localization (X,Y,Z spatial coordinates) is needed when using multi-camera imaging;
- 3D reconstruction and object measurement is needed when using only one camera combined with car displacement data.

Ramalingam[10] explains in his thesis how to calibrate and reconstruct a 3D scene using a unified camera calibration model. This model encloses different camera types as pinhole cameras and omni-directional cameras, up to non-parametric mapping cameras. The panomorph lens calibration model can be customized to the unified model, relying on its pixel projection mapping. For example, the lens suggested in this case study cumulates polynomial radial distortions with an anamorphic ratio. This theory is described further by the authors in a previous paper[9].

All algorithms using a camera calibration function easily with the panomorph lens calibration model -- such as image stitching or fusion, motion estimation, camera position estimation or 3D reconstruction. Figure 13 is an example where this type of calibration is required. Indeed, to stitch four panomorph camera images and provide a fused view, we need to know the position of each panomorph camera in the real world. As a camera can move from its initial position, a dynamic calibration is required, using intrinsic and extrinsic camera parameters. When a panomorph lens design provides the theoretical intrinsic parameters, a self-calibration algorithm fine-tunes the intrinsic parameters and computes the extrinsic parameters using interest-point matching. Again, for this type of application the panomorph lens can improve the results by increasing the resolution along the border, where interest-point geometry is known (for example: a car's geometry).

### 4.4 Software projection types, manipulations and performances

For collision warning and road sign detection and recognition, the size of the object is not big enough to be influenced by the distortion of the lens. A projection algorithm is not necessary. For lane departure and lane curvature recognition, however, the projection algorithm is important in reducing the CPU load. Indeed, using a PGM model of the lens, we can

create a projection table (LUT) that transforms the panomorph picture into a picture dedicated to lane departure and lane curvature recognition algorithms.

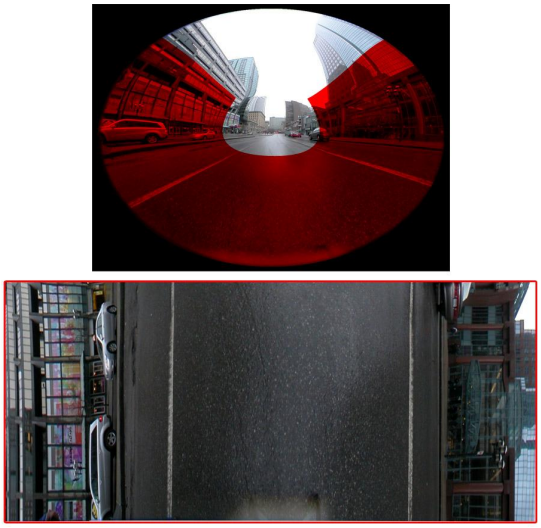

Figure 10: Lane departure custom projection rendering

The goal of this projection is to provide a straight line to simplify the line recognition algorithm and reduce the car-embedded computation. The pixels used to create the projected view are highlighted on the panomorph view.

For blind zone coverage there are many types of viewing possible with a panomorph lens (for example, to avoid a blind zone at a garage entrance created by vehicles parked on the street side).

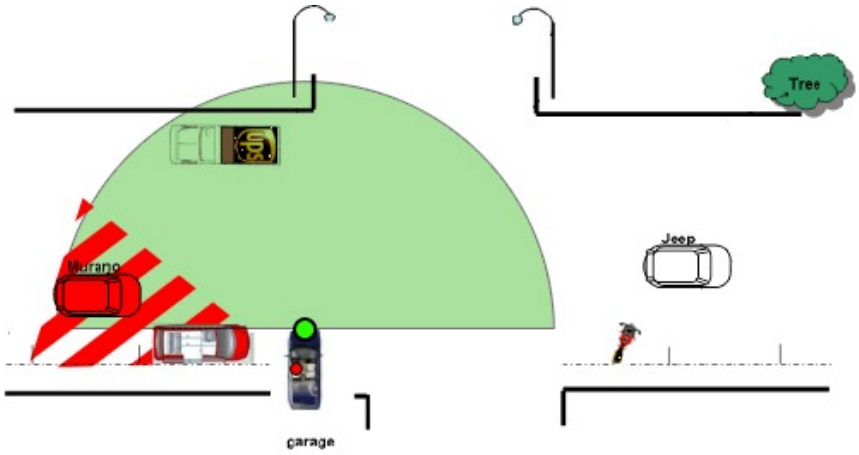


Figure 11: Panomorph coverage of a blind zone created by a parked vehicle

Using the PGM, different software projection types can be created, depending on OEM requirements. The two following figures show ways to display a view of the intersection to the driver while avoiding the blind zone created by a parked vehicle. This type of projection is simply a pixel displacement that has been computed during the calibration phase on a production chain. This can be hard coded in a lookup table in the camera module. No special CPU horse power is required.

Figures 12 and 13 show ways to avoid a blind zone. The driver can see everything in the blind zone using his/her on-board display. The panomorph lens design suggested in this paper increases the resolution of objects along the border and right in the middle. Where the resolution is higher, the camera is able to see for a longer distance. The panomorph distortion is optimized for this type of application. The driver is able to see far down each side of the street.

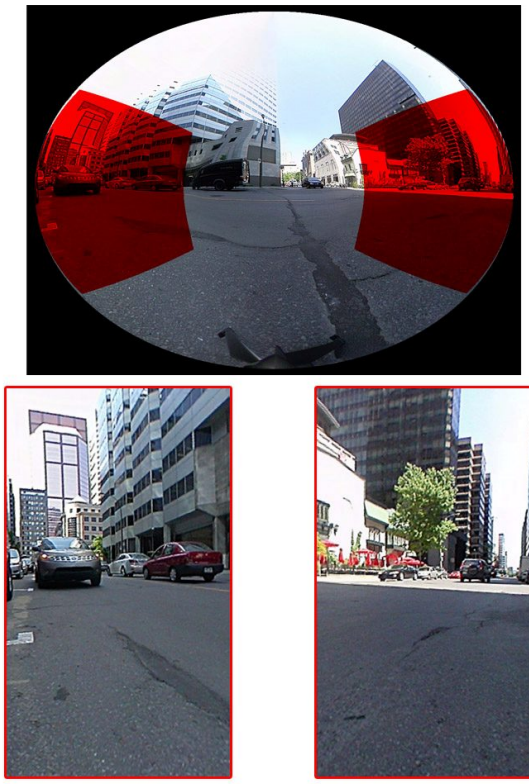

Figure 12: Two views rendering either side of the intersection

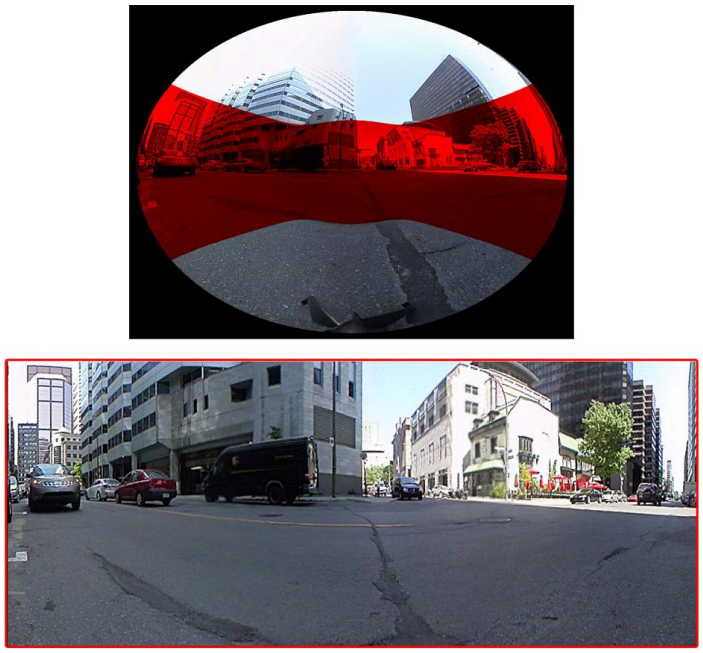

Figure 13: 190° strip integrating full intersection

In Figures 12 and 13, the topmost image is the panomorph picture with certain areas highlighted. The lower ones show the projections as processed from the pixels in these areas.

There are no limitations in terms of projection ability, although the scope for real applications requires imagination and, ultimately, driver understanding. For example, one could mount four (4) panomorph lenses all around the vehicle to provide a complete view for parking assistance (Figure 13) with the added benefits of panomorph technology's augmented resolution.

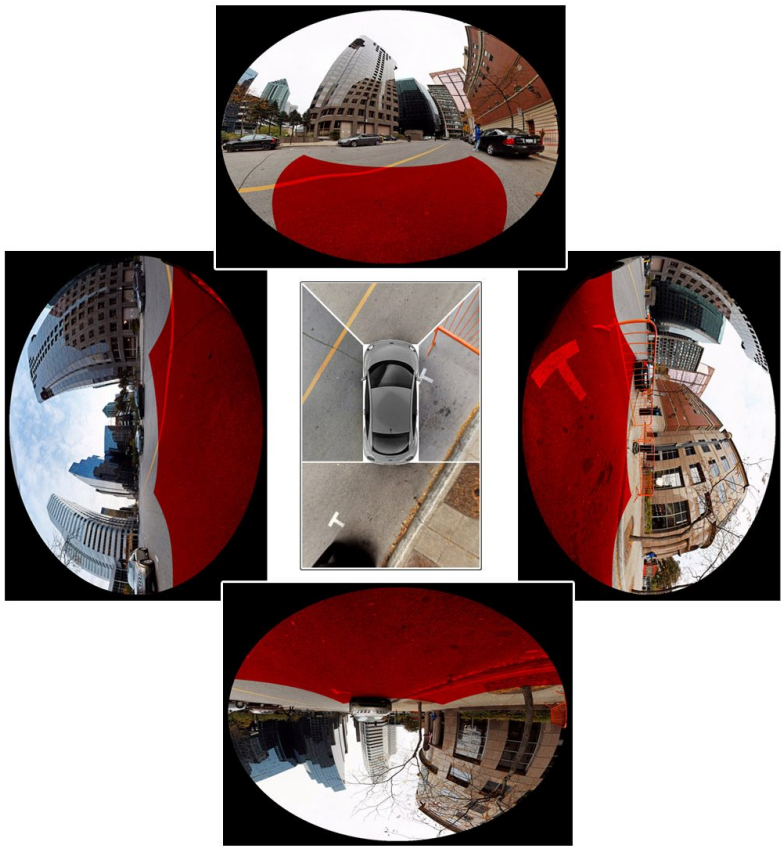

Figure 13: View of area surrounding vehicle using four (4) panomorph lenses.

## 5. CONCLUSION AND OPPORTUNITIES

This paper presents a variety of viewing needs related to specific automotive applications, now and into the future. Computer vision-based applications (analytics) will require various resolution factors (pixel per degree) in various areas of a vehicle's field-of-view (FoV), depending on the position of the objects to be analyzed, as well as distance and size. Viewing application requirements, on the other hand, will focus on the clarity and quality of the images to be displayed to the driver. We also saw that the objects to be detected, analyzed and viewed can literally be everywhere around the vehicle. We demonstrated that a novel panomorph technology (optics and software) performs significantly better than other traditional panoramic vision systems in fulfilling various needs relating to automotive applications. In conclusion, the novel pixel-optimization characteristic of panomorph optics allows the integration of many applications with the use of fewer vision sensors.

Finally, we demonstrated in the case study that, because of the specific panomorph resolution pattern suggested in this case, panomorph optics can increase the distance by a factor of 70% compared to a fisheye lens. It can also reduce computation time, while at the same time achieving high recognition performance. All of these benefits will bring a total cost reduction to the automotive industry for the various systems that require vision sensing.

## 6 . REFERENCES


1. T. Gandhi, M.M. Trivedi. Vehicle Surround Capture: Survey of Techniques and a Novel Omni-Video-Based Approach for Dynamic Panoramic Surround Maps, IEEE Transaction on Intelligent Transportation system. Vol 7, No 4, December 2006, pp. 293-308.

2. A. Takahashi, Y. Ninomiya, M. Ohta, M. Nishida, and M. Takayama. “Rear view lane detection by wide angle camera” in Proc. IEEE Intell. Vehicle Symp., Vol. 1, pp. 148-153, Jun. 2002.

3. Yan Zhang, Arnab S. Dhua, Stephen J. Kiselewich and William A. Bauson. “Challenges of Embedded Computer Vision in Automotive Safety Systems”. Embedded Computer Vision, Advances in Pattern Recognition. ISBN 978-1-84800-303-3. Springer-Verlag London Limited, 2009, p. 257

4. B. Alefs, G. Eschemann, H. Ramoser, C. Beleznai: Vortrag. "Road Sign Detection from Edge Orientation Histograms". IEEE Intelligent Vehicle Symposium 2007, Istanbul; 13.06.2007 - 15.06.2007; in: "Proceedings of the 2007 Intelligent Vehicle Symposium", IEEE, Catalog Number 07TH8947 (2007), ISBN: 1-4244-1068-1; S. 993 - 998.

5. Hughes, C; Glavin, M; Jones, E; Denny, P. "Wide-angle camera technology for automotive applications: a review". IET Intelligent Transportation Systems 3(1), Page(s): 19-31.

6. Thibault S. Distortion Control Offers Optical System Design a New Degree of Freedom. Photonics Spectra, May 2005, pp. 80-82.

7. Thibault S. “IR panomorph lens imager and applications”. Infrared Technology and Applications XXXIV. Edited by Andresen, Bjørn F.; Fulop, Gabor F.; Norton, Paul R. Proceedings of the SPIE, Volume 6940, pp. 69401A-69401A-11 (2008).

8. Simon Thibault. Enhanced Surveillance System Based on Panomorph Panoramic Lenses. Proc. SPIE vol. 6540, paper 65400E, 2007.

9. Thibault, Simon; Konen, Pierre; Roulet, Patrice; Villegas, Mathieu: “Novel hemispheric image formation: concepts and applications”. Infrared Technology and Applications XXXIV. Edited by Andresen, Bjørn F.; Fulop, Gabor F.; Norton, Paul R. Proceedings of the SPIE, Volume 6940, pp. 69401A-69401A-11 (2008).

10. S. Ramalingam. “Generic Imaging Models: Calibration and 3D Reconstruction Algorithms”, Ph. D. Thesis, *Institut National Polytechnique de Grenoble*, Nov. 2006, http://perception.inrialpes.fr/Publications/2006/Ram06.

11. Kumler, James (Jay); Bauer, Martin L. "Fish-eye lens designs and their relative performance". Proc. SPIE Vol. 4093, p. 360-369, Current Developments in Lens Design and Optical Systems Engineering, Robert E. Fischer; R. Barry Johnson; Warren J. Smith; William H. Swantner; Eds.

12. Thibault, Simon, "360 degree vision system: opportunities in transportation". Photonics in the Transportation Industry: Auto to Aerospace. Edited by Kazemi, Alex A.; Baldwin, Christopher S. Proceedings of the SPIE, Volume 6758, pp. 67580H (2007).

13. French Ministry of Equipment, « *Instruction Interministérielle sur la signalisation routière* » Article 5-3. P9 Edited by *Journaux Officiels*.

# Fiber Optic Cryogenic Liquid Level Detection System for Space Applications

Alex A. Kazemi*, Chengning Yang**, Shiping Chen**
* The Boeing Co., Missile Defense System, Integrated Defense Systems, Anaheim, CA 92806

**ABSTRACT**

Liquid hydrogen and oxygen are widely used as fuels in space vehicles. Because both are highly dangerous materials prone to explosion, detection of the liquid level in fuel tank becomes a critical element for the safety and efficiency in space operations. Two liquid level sensing techniques are presented in this paper. The first technique is based on optical fiber long period gratings. In this technique, the full length of a specially fabricated fiber is the body of the probe becomes the length of the sensing fiber that is submerged in the liquid can be detected by the interrogation system. The second system uses optical fibers to guide light to and from an array of point probes. These probes are specially fabricated, miniature optical components which reflects a substantial amount of light back into the lead fiber when the probe is gas but almost no light when it is in liquid. A detailed theoretical study by computer simulation was carried out on these two techniques in order to determine which technique was more suitable for experimental investigation. The study revealed that although the first technique may provide more potential benefits in terms of weight and easy installation; a number of technical challenges make it not suitable for a short term solution. The second, probe array based technique, on the other hand, is more mature technically. The rest of the research program was therefore focused on the experimental investigation of the probe array detection technique and the test results are presented in this paper.

**Key Words:** Fiber Optic Liquid Level Sensors, Liquid Leak Monitoring, Cryogenic Environment, Space Applications

• Corresponding author e-mail address: alex.kazemi@yahoo.com
** Formerly with University of Maryland, Smart Materials and Structures Research Center, Department of Mechanical Engineering.

Photonics in the Transportation Industry: Auto to Aerospace II, edited by Alex A. Kazemi, Bernard C. Kress
Proc. of SPIE Vol. 7314, 73140A · © 2009 SPIE · CCC code: 0277-786X/09/$18 · doi: 10.1117/12.821374

## 1. INTRODUCTION

Since 1960s, a number of liquid-vapor (L-V) interface sensing devices have been studied which use differences in resistance, capacitance, acoustic impedance and viscous damping. Among them, capacitance based sensor system has been successfully commercialized for aerospace application. However high cost, slow response, heavy weight and potential liquid fuel in tanks.

In comparison, an optical fiber based liquid level detection system potentially has some distinct advantages [1-2].

1. An optical fiber based systems are electronically passive and inherently spark free. When being applied in the explosive environments such as liquid hydrogen or oxygen, the feature enhances the safety, reduces maintenance load and increases operation efficiency.
2. Optical fibers are four times lighter per unit volume and six times stronger than copper wires while each electronic point sensor requires two copper wires to read, a miniature fiber optic probe can be accessed via a single fiber.
3. An optical fiber sensor system neither produces nor is prone to electromagnetic interference (EMI), no shielding or insulation is therefore necessary.
4. Since the existing sensor system is electronics based, it has inherent risk of spark. To reduce this danger, the entire system has to be well insulated and constantly checked to ensure safety, which not only makes the system more complex and heavy, but also significantly increases the maintenance cost and reduces operation efficiency.
5. The optical fiber based probe is much smaller than capacitance based ones, its response can potentially be much faster and more consistent among different probes.
6. Due to the fast advancing telecommunication industry, the cost of optical system components has become very competitive.
7. The combination of the above factors makes the optical fiber based sensor system substantially lighter and cheaper than their electric counterpart. Such weight and cost reduction is crucial to aerospace application.

Previously optical fiber based sensor for liquid level detection in cryogenic environment have been reported. A rectangle prism was used as optical sensor. The amount of light transmitted from the source to the detector depends on whether the liquid is present. The light is launched from an optical fiber and collimated via a gradient-index (GRIN) lens, and refocused through another GRIN lens form the prism into second fiber transmitting to the detector [3].

In our system the optical sensor we produced is based on the similar principle. However, the optical probe only consists of a prism and one fiber with a GRIN lens, instead of using two fibers. It miniaturizes the sensor and may reduce the response time. And also the probes were integrated in a read-out scheme based on an Optical Time Domain Reflectometer (ODTR), which provide possibility for distributed sensing.

The long term objective is to develop state-of-the-art fiber optic cryogenic liquid level detection system to be used for commercial and military launch vehicles, Constellation, Space Station, Ares and industrial hydrogen facilities. Figure 1 show illustrates Delta IV heavy, Ares and Space Station.

**Figure 1. Long term objective is to develop fiber optic liquid level sensor for launch vehicle, Ares and Space Station.**

## 2. THE OPERATION PRINCIPLE AND SYSTEM DESIGN

In this section, two detection systems and operating principles of the two detection technologies are described.

### 2.1 Optical Fiber Long Period Gratings (LPG)

As shown in Figure 2a, an optical fiber LPG is a section of optical fiber which has periodical changes of refractive index inside its core region. The pitch of the index pattern, Λ, is in the order of several hundred micrometers and the total length of the grating, L, is normally in the range of several centimeters. Such a grating is normally fabricated by periodically illuminate strong ultraviolet (UV) light from an UV laser onto the fiber core to generate the pattern of permanent refractive index change. As illustrated in Figure 2b, the effect of a LPG to the light traveling in the fiber core is that it diffracts the light energy that falls within a wavelength band centered at a wavelength, $\lambda_p$, from the fiber core to the cladding. This characteristic LPG wavelength can be expressed as

$$\lambda_p = (n_{cl} - n_{co})\,\Lambda \qquad 1)$$

where $n_{co}$ and $n_{cl}$ is the effective refractive index of the fiber core and cladding, respectively. The spectral width of this diffraction band, measured as full width at half maximum (FWHM), can be expressed as

$$FWHM = 0.8\lambda_p\Lambda\,/L \qquad 2)$$

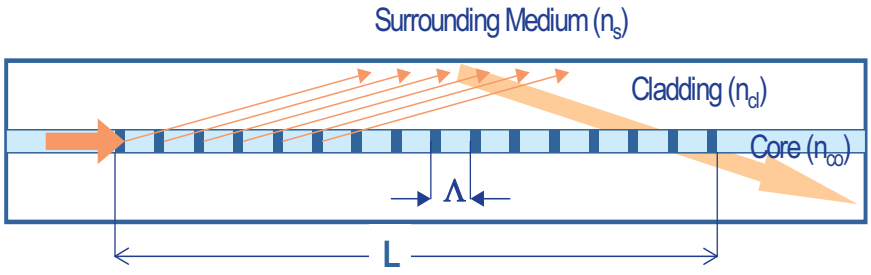


**Figure 2a. Optical fiber long period grating.**

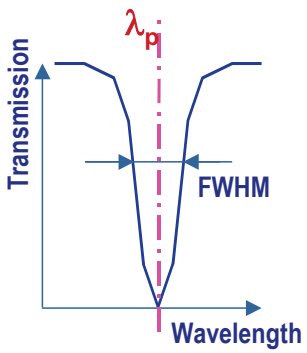


**Figure 2b. The diffraction band of a LPG**

These two parameters are the key to the performance of a LPG based liquid level sensor as we will describe later.

### 2.2 Optical Time Domain Reflectometer (OTDR)

The OTDR is a standard device widely used in telecommunication industry to detection the loss and faulty points along an optical fiber link. As shown in Figure 3, it acts like a one-dimensional radar by sending a very short light plus (<1ns) down the optical fiber under test and then records the strength of the reflected light along the delay time after the probing pulse. This delay time is actually the time of fly of the light and is therefore directly proportional to the distance long the fiber. For a perfect fiber link, the strength of reflected light (in dB) reduces linearly alone the fiber due to inherent fiber loss. The slope of the curve in power

versus distance chart is proportional to loss. Normally, an optical fiber has an inherent loss of less than 1 dB per kilometer. However, if the light encounters a high loss section, the slope will increase, which can be detected by the OTDR form the increased slope in the curve. Partial reflective points can be detected.

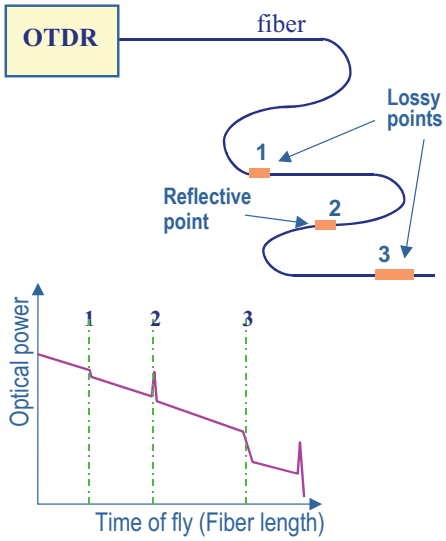


**Figure 3. OTDR and its output curve.**

### 2.3 Total Internal Reflection (TIR)

The reflective index, n, of an optical medium indicates its density to light travel. As shown in Figure 4, when light travel from one dense medium ($n_1$) to less dense medium ($n_2$ and $n_1 > n_2$), it will change its direction of travel. When the incident angle, $\alpha$, at the interface is smaller than critical angle, $\alpha_C = \sin^{-1}(n_2/n_1)$ the light will still enter the less dense medium. However, when $\alpha > \alpha_C$, the light energy will be completely reflected back to the denser medium. This phenomenon is called total internal reflection (TIR). Furthermore, when a light ray crosses the boundary of two isotropic media of different reflective index, $n_1$ and $n_2$, if $n_1 > n_2$, there is a critical angle $i_c$, which is determined by:

$$\text{Sin } i_c = n_2/n_1$$

When incident angle $i_1$, the boundary acts as an ideal mirror, all the rays will be reflected to medium 1, or TIR is created.

### 2.4 LPG Based Liquid Level Detection System

As illustrated in Figure 5, the LPG based liquid sensor consists of a bare LPB and a short section of it is coated with a mode stripping overlayer. The light traveling down the fiber is a narrow (from a laser). When the LPB is in gas, the wavelength of the source is spectrally positioned away from the diffraction band of the LPG and, therefore, has a very low transmission loss. The effective refractive index of the fiber cladding, $n_{cl}$, is dependent upon the refractive indices of both the cladding and the material surrounding it. According to Equation 1, the position of the LPG diffraction band can shifted by the change of surround material. When the LPG is in liquid, which has a higher refractive index than its gas from, the LPG diffraction band is shifted to the spectral position of the light source. The light in the fiber is then diffracted to the cladding by the LPG

and absorbed by the mode stripping coating. The transmission loss becomes very high. The increase of transmission loss can therefore serve as the indicator of the presence of liquid. The total length of such a LPG sensor is 10 cm.

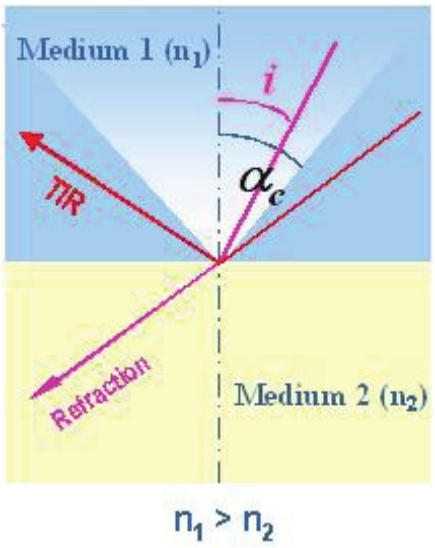


**Figure 4. Critical angle for total internal reflection**

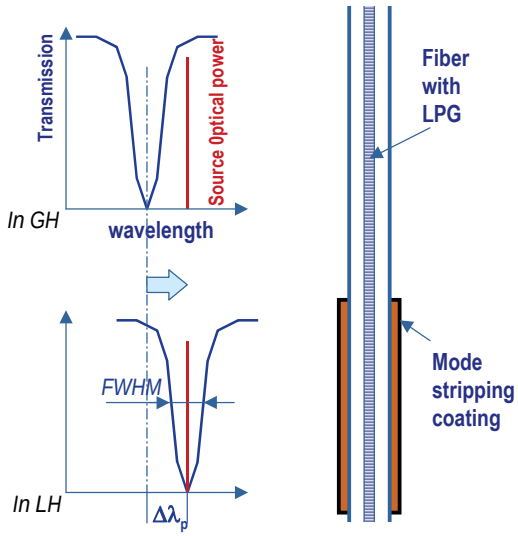


**Figure 5. Operating principles of LPG liquid sensors**

As shown in Figure 6, a large number of above described liquid sensors can be fabricated along a single length of optical fiber and interrogated using a precision OTDR. The sharp bent in the output curve of the OTDR indicted the point of increased transmission loss, which coincides the gas-liquid interface as described in the above section.

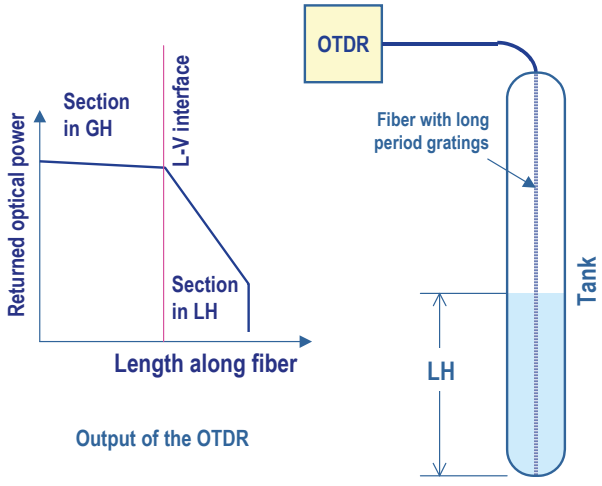


**Figure 6. Interrogation of LPG based liquid sensor**

## 2. 5 TIR Based Liquid Level Detection System

Two optical level sensor designs illustrated in Figure 7 were built. Both of the schemes use a right angle prism as a sensor. One is the prism's shorter face down while the other is hypotenuse face down. Light from the optical fiber is collimated by the GRIN lens (collimator) and propagates parallel to the optical axis. Because of the geometry of the right angle prism, it hits the face of the prism at a precise 45° incident angle. The light will be reflected back from the prism and refocused to the same fiber. From Table 1 it can been seen that, if the sensor is in vapor environment, 45° is larger than i, all the light will be reflected into the fiber. If it is in liquid environment, the critical angle is smaller than the 45° incidence angle and most of light energy will be refracted into liquid. By monitoring the intensity of the reflected light, whether the probe is in vapor or liquid can be detected.

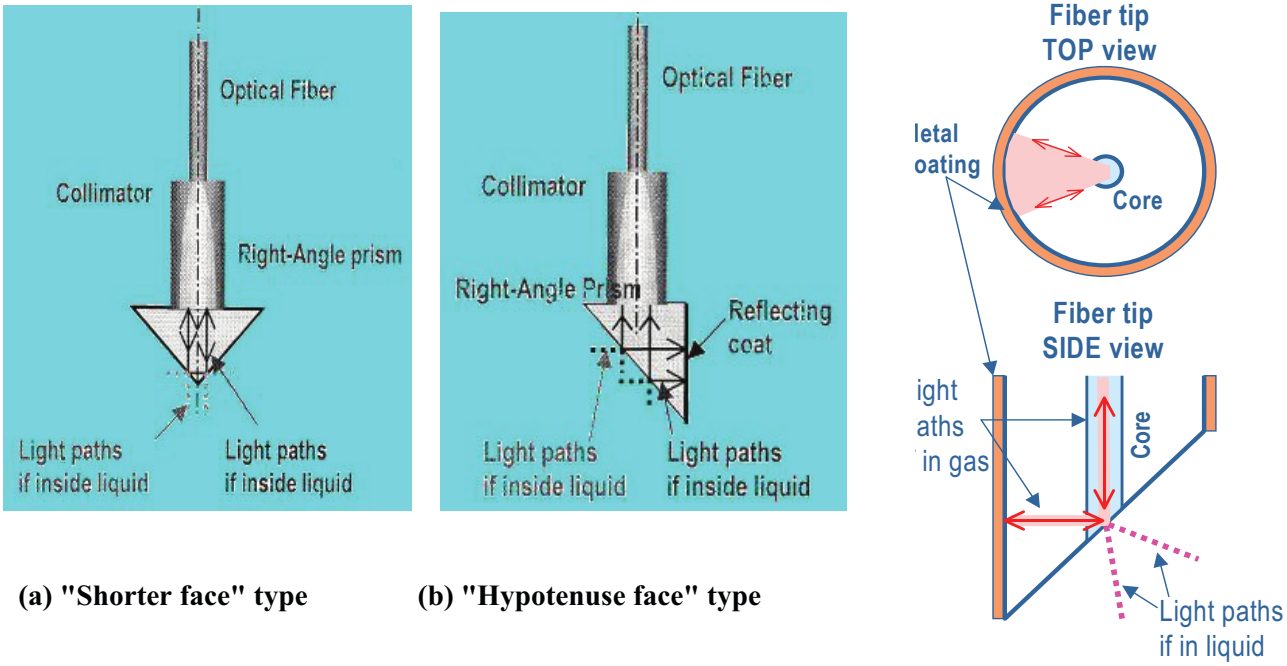


**(a) "Shorter face" type** **(b) "Hypotenuse face" type**

**(c) Point sensor "hypotenuse face" type**

**Figure 7 Operating principles of TIR point liquid sensor**

The difference between the two types of sensors is the location of the sensing point. In the "shorter-face" type, the light reflects from the surface of the prism's shorter face around the tip of the prism; in the "hypotenuse-face" type, the light reflects in the middle of the hypotenuse surface of the prism. This results in a different sensor performance in various liquid environments, which will be discussed later.

To detect the liquid surface level an array of probes is installed at the different positions inside the fuel tank to monitor the liquid level shown in Figure 8. Optical Time Domain Reflectometer (OTDR) is used for signal processing. OTDR is the primary tool for installing and maintaining fiber optic links. It allows a link to be measured from one end. OTDR launches a very short duration of light pulse from a laser diode source into a fiber. A measurement is made of its backscatter as a function of time. The time values can be easily converted to distance by multiplying the velocity of light in the fiber. Thus, the OTDR displays the relative power of the returned signal versus distance. Light reflected from probes located at different distances from the OTDR device can be separated in the output curve by peaks along the horizontal axis at and related to

different sensor locations. The height of these peaks corresponds to the intensity of the reflection. This configuration avoids moving the optical sensor up and down to find the level of the liquid surface.

## 3. EXPERIMENTAL RESULTS

Figure 9 shows a fabricated "shorter face" type sensor. An optical fiber. An optical fiber network linking an array of probes was assembled in the lab as shown in Figure 10. Two "shorter face" type probes were integrated with optical fiber couplers. The length of the fiber was controlled so that the corresponding peak of the probes could be separated on the OTDR. The OTDR was used in a model for communication cable maintenance, whose spatial resolution is 10 meters. Thus, additional length of fibers connected to the network is needed to ensure more than 10 meters (actually 20 meters length is used) length difference between the lead fibers to the two probes. The test was performed only using liquid nitrogen, as it is easy to handle. There is no difficulty to extend its use to liquid hydrogen.

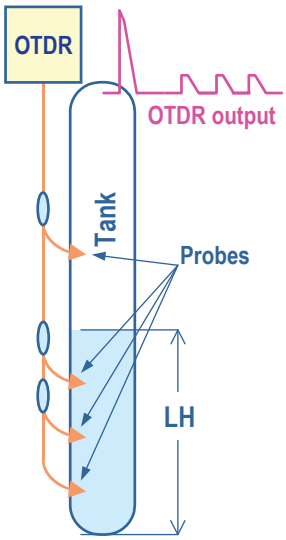


**Figure 8. OTDR interrogation of multiple liquid probes**

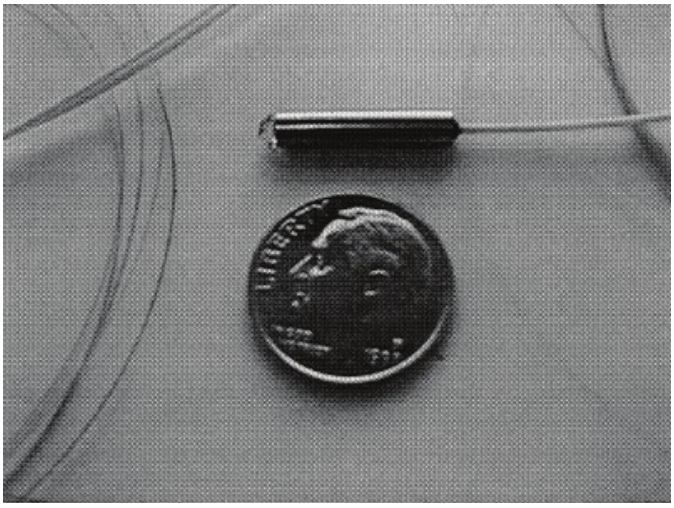

**Figure 9. The fabricated "shorter face" type sensor**

Figure 11 shows the curve of the OTDR output when all of the probes were in gas nitrogen (Figure 5a), and when probe 1 was in gas nitrogen and probe 2 in liquid nitrogen (Figure 11b). For the former case the most left peak of three reflection peaks appeared on the screen corresponds to the reflection from the first fiber connector that links the network to the OTDR. The rest two peaks were produced by the two probes. The second peak to the left is produced by probe 1 because its lead fiber is shorter than that of probe 2. When probe 2 was in liquid nitrogen and probe 1 in nitrogen gas, the curve in Figure 11b shows that the peak associated with probe 2 disappeared completely while the peak from probe 1 still remains. The vertical straight line in the curve is only the cursor. The result demonstrate the feasibility of using single OTDR device to interrogate an array of point probes.

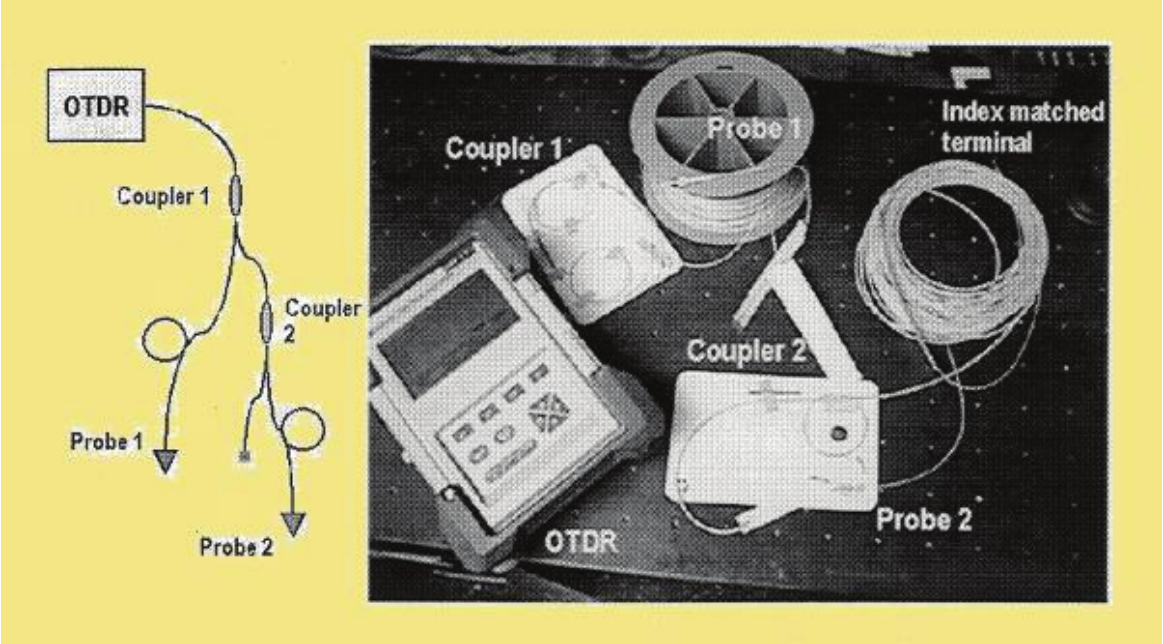


Figure 10. Demonstration of probe array interrogated by a single OTDR

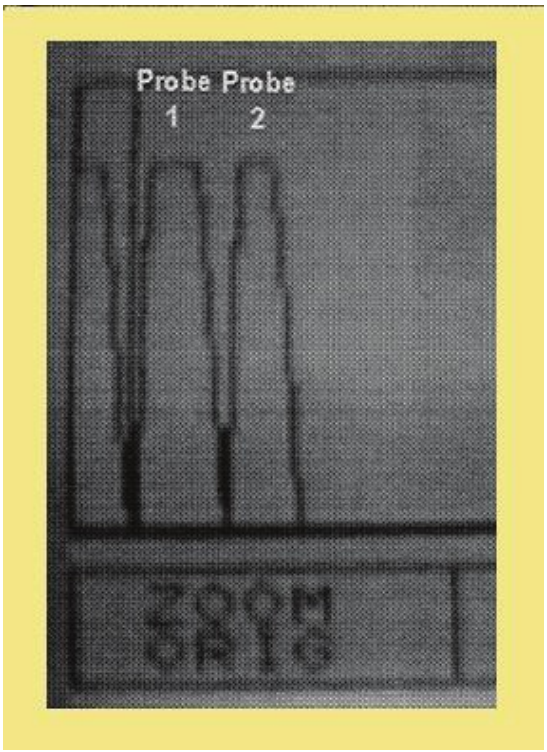


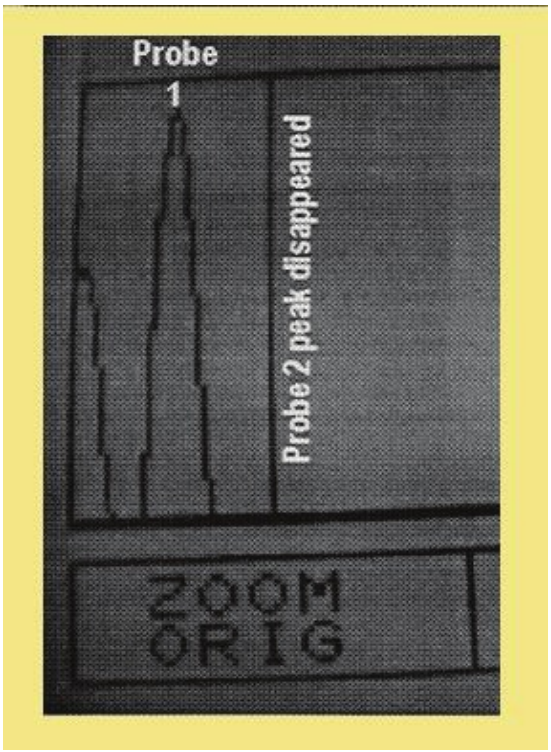


**(a)** **(b)**

**Figure 11. Output curves on the OTDR when both probes in air (Figure 11a), and probe 1 in air and probe 2 in liquid Nitrogen (Figure 11b).**

In order to measure the response time of the device a test apparatus shown in Figure 12 was setup. The liquid-level sensor probe is mounted on the tip of a stick, which was cycled rapidly up and down driven by shaker. The vibration frequency was controlled by a single generator. The sensor probe travels between liquid and vapor environment. The reflected light is detected by the detector and then recorded by a digital oscilloscope. A Linear Variable Differential Transducer (LVDT) is used to transform the displacement to voltage signal to the trace the position of the probe. Due to high cost of liquid Hydrogen experiment, in this preliminary stage we tested the sensor in liquid Nitrogen instead to study sensor performance in cryogenic environment.

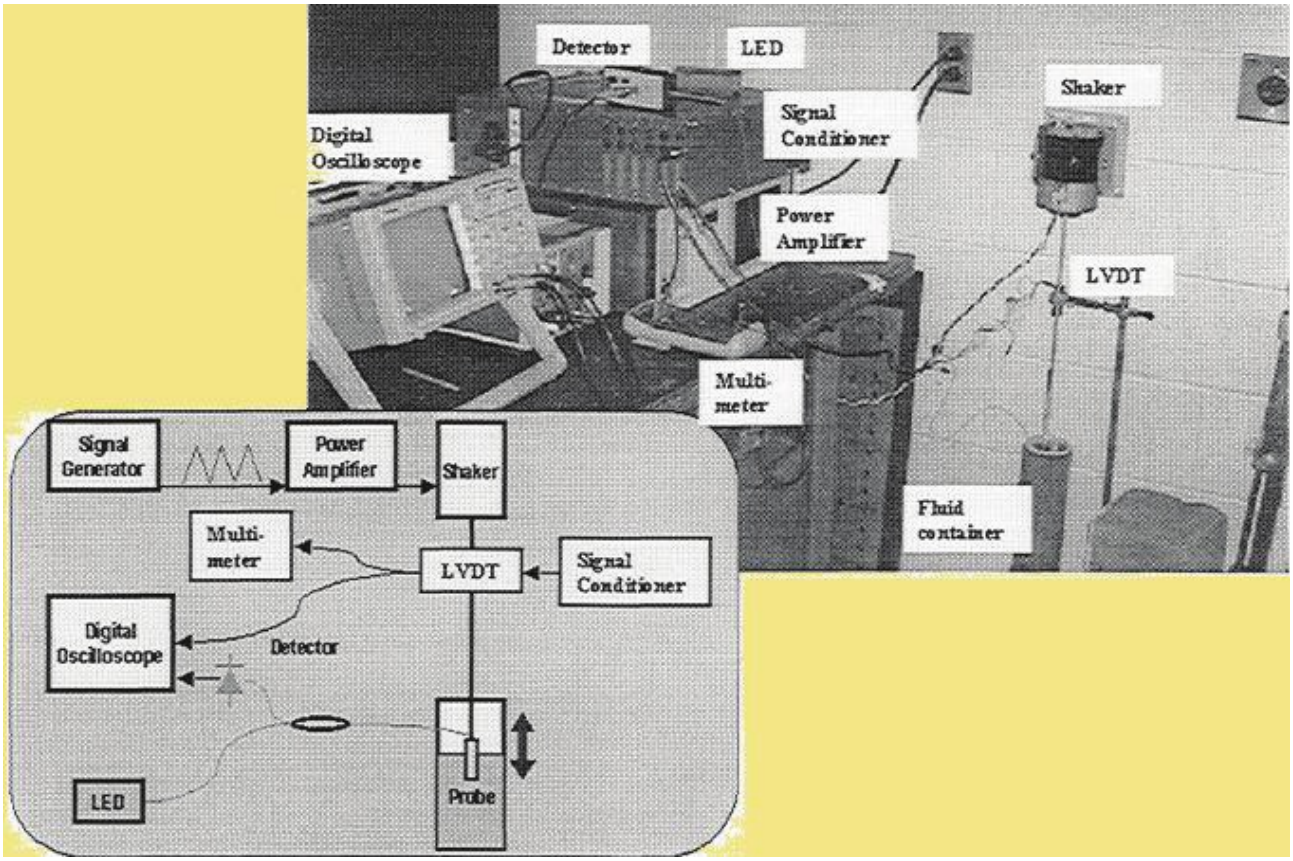


**Figure 12. Experimental setup for the measurement of probe response time.**

The response time of the probe as the time lag between the time of liquid to vapor transition measured from the LVDT and the time that the corresponding signal change detected by the optical sensor reaches 63% (1/e) of the full scale. It in fact, includes two different response time, namely the liquid to vapor (L-V) and the vapor to liquid (V-L) response time. Two types of sensors were tested in both water and liquid nitrogen. Due to the interaction of the liquid and the probe surface in liquid nitrogen and water environment, two types of probes were installed with orientation up and down to track the sensor response. Table 2 gives the summary of the result.

Figure 13 shows the results of 0.5 Hz cycle testing in water of the "shorter face" type sensor with tip up. The response time can be determined from the enlarged portion in Figure 13b and c. The response time was: V-L,

60 ms. However, the response time becomes -10 ms for V-L and 180 ms for L-V. Figure 14 is the signal output in liquid nitrogen test with prism tip facing down. The V-L response time is 30 ms and LV is 670 ms.

**Table 2. Response time of the sensor in different cases (unit: ms)**

| | | Water | | Liquid Nitrogen | |
|---|---|---|---|---|---|
| | | V-L | L-V | V-L | L-V |
| "Shorter face" Type Sensor | Orientation Up | 40 | 60 | | |
| | Orientation Down | -10 | 180 | 30 | 650 |
| "Hypotenuse face" Type Sensor | Orientation Down | | | -30 | 130 |

The question is why the V-L response time is negative. In an ideal case, it is impossible. After the further analysis, we found that the error came from the method we defined the time of liquid to vapor transition measured from the LVDT when the sensor passing through the interface.

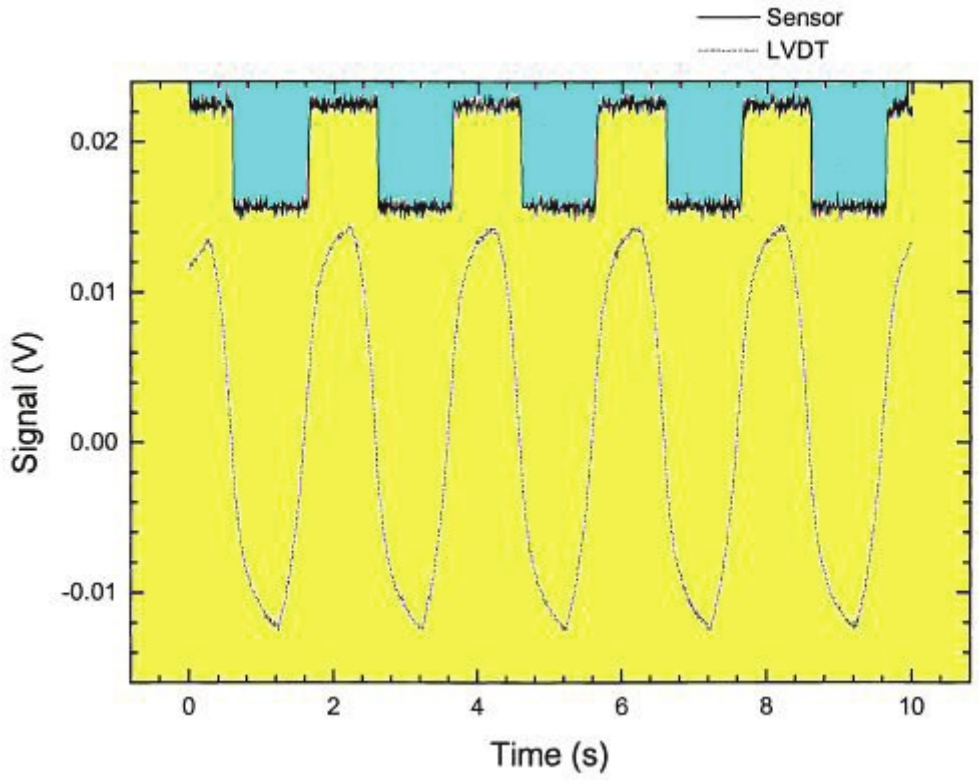


**Figure 13 (a). Signal output in water test using shorter face type sensor with tip facing down.**

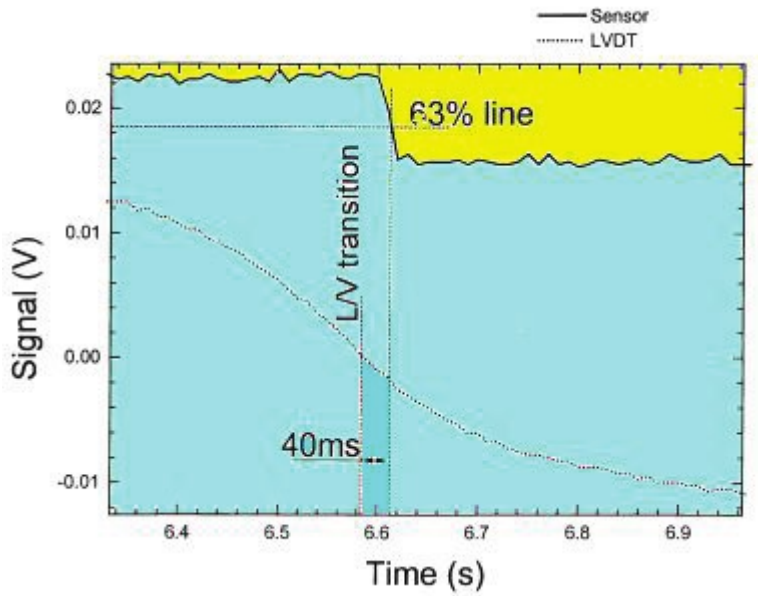


**Figure 13 (b). Signal output in water test using shorter face type sensor with tip facing down.**

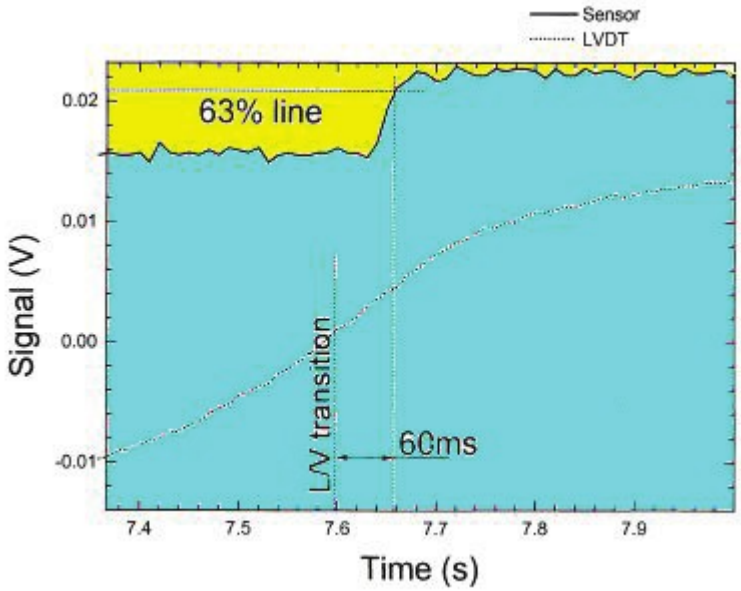


**Figure 13 (c). Signal output in water test using shorter face type sensor with tip facing down.**

When the first time placed the probe into the liquid to read the LVDT output, the probe was dry. Because of water surface tension, the water surface would bend down when the probe tip started to penetrated the water. With the prism kept entering into the water, at a certain moment, the surface tension could not resist the surface expansion. The bending water surface would suddenly bounce back. We took this moment as the time when the sensor was on the interface. Actually, after the experiment began, the probe became wet. In this surface would bounce back earlier, which meant the sensor signal changed before the moment we defined the sensor passing through the V-L interface. However, in current stage, we can just use eyes to catch the "interfacing" moment without apparent reference. It is only a question of the selection of reference point. Considering this, the "-10 ms " response can be treated as responding almost simultaneously.

On the other hand, when "hypotenuse face: sensor enters liquid nitrogen from gas nitrogen, the probe tip touches the liquid nitrogen first, the boiling bubbles make liquid nitrogen splash on the middle part of the hypotenuse surface, where is the sensing point of the "hypotenuse face" probe, then the sensor starts to give the "liquid" signal. However, we defined the time that the sensing point is on the interface as the time the sensor would start to change signal, that explains why the V-L response time of "hypotenuse face" sensor was negative.

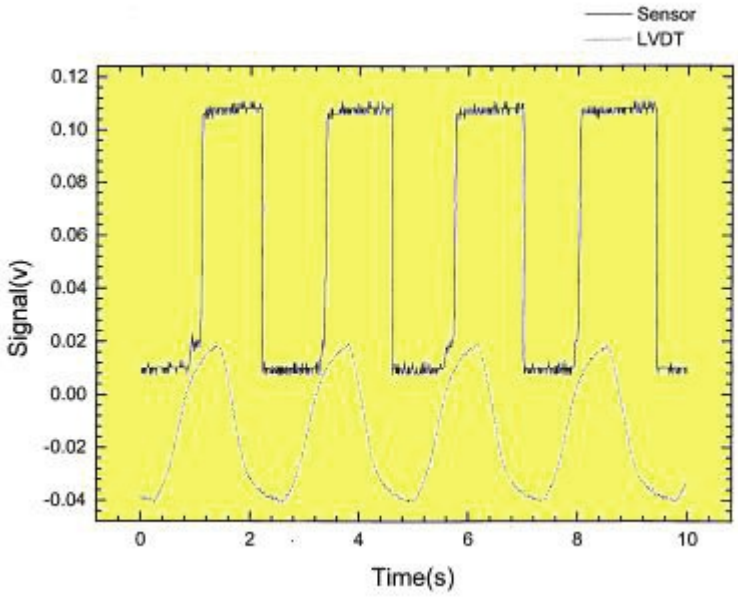


**Figure 14 (a). Signal output in liquid nitrogen test using shorter face type with tip facing down.**

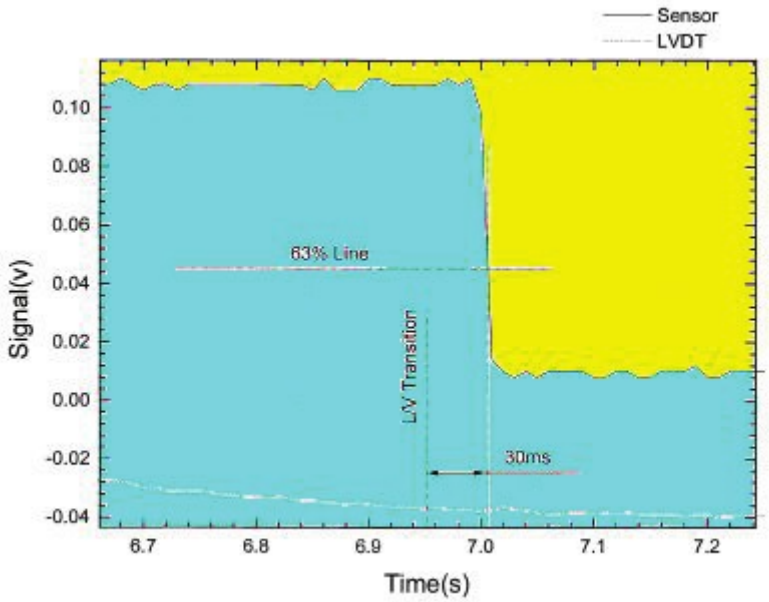


**Figure 14 (b). Signal output in liquid nitrogen test using shorter face type sensor with tip facing down.**

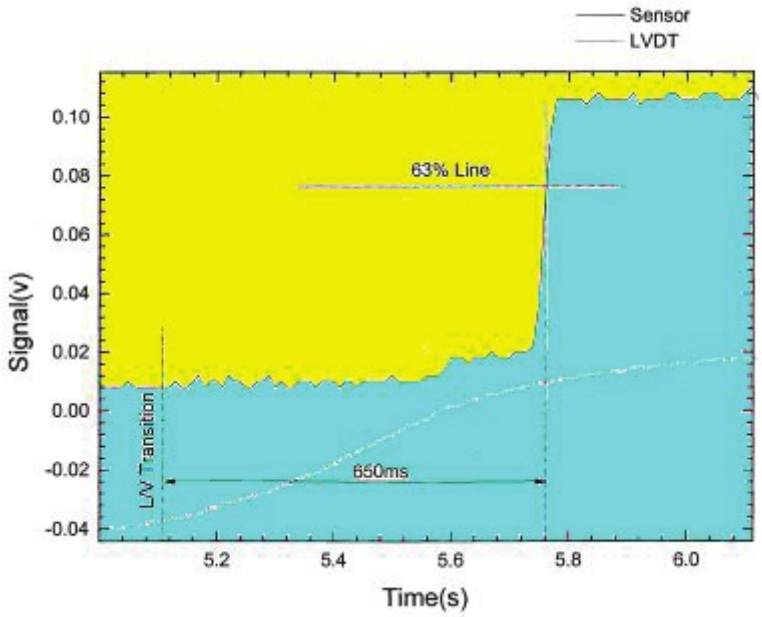


**Figure 14 (c). Signal output in liquid nitrogen test using shorter face type with tip facing down.**

## 4. CONCLUSION

Preliminary experimental work have been carried out to investigate an optical fiber liquid level detection system based on the total internal reflection principle. Prototype point sensing probes with two different designs have been tested. They performance characteristics, especially the response time were measured and compared. Factors affecting the response time of a liquid probe have been investigated. A vapor/liquid signal ratio of -13Db in hydrogen and a sensor response time of 8Oms have been achieved. Finally a sensor system comprising multiple multiplexed probes have been successfully demonstrated.

In theory, the response of the optical sensor to the presence of liquid on the probe surface is of no delay. The response time mostly depends on the property of liquid, the interaction between the liquid and sensor surface, and the sensor surface. A solution to the problem is to coat a hydrophobic film on the sensor surface to avoid the residual liquid on the sensor surface.

In conclusion, the experiment results in this paper show the feasibility of using optical fiber sensors for the liquid surface level detection under cryogenic environment.

## 5. REFERENCES

[1]. S. Chen, C. Yang, C. Uremovic, J. Sirkis, A. Kazemi, "Liquid Level Detection in Cryogenic Environment", SPIE, Vol. 3670, pp. 237-246, 1999.

[2]. C. Yang. S. Chen and A. A. Kazemi, “Fiber optical liquid level sensor under cryogenic environment”, SPIE, Vol.4024, pp. 206-216, 2001.

[2]. J. D. Siegwarth, R. O. Voth and S. M. Snyder, “Liquid-vapor surface sensors for liquid Nitrogen and Hydrogen Cryogencis, Vol. 32, pp. 236-242, 1992.

# Distributed network of integrated 3D sensors for transportation security applications

**Vic Hejmadi and Fred Garcia**
Universal Semiconductor Inc.
1925 Zanker Road
San Jose, CA 95112 (USA)

**ABSTRACT**

The US Port Security Agency has strongly emphasized the needs for tighter control at transportation hubs. Distributed arrays of miniature CMOS cameras are providing some solutions today. However, due to the high bandwidth required and the low valued content of such cameras (simple video feed), large computing power and analysis algorithms as well as control software are needed, which makes such an architecture cumbersome, heavy, slow and expensive.
We present a novel technique by integrating cheap and mass replicable stealth 3D sensing micro-devices in a distributed network. These micro-sensors are based on conventional structures illumination via successive fringe patterns on the object to be sensed. The communication bandwidth between each sensor remains very small, but is of very high valued content. Key technologies to integrate such a sensor are digital optics and structured laser illumination.

**Keywords**: 3d sensors, camera network monitoring, diffractive optics, micro-optics.

Photonics in the Transportation Industry: Auto to Aerospace II, edited by Alex A. Kazemi, Bernard C. Kress
Proc. of SPIE Vol. 7314, 73140B · © 2009 SPIE · CCC code: 0277-786X/09/$18 · doi: 10.1117/12.821381

## 1. INTRODUCTION

Today, surveillance camera networks are widely used to provide security in critical areas such as ports, airports, malls, etc…
However, in many cases, these cameras remain simple CCTV cameras, although they can be now integrated in very small packages [1]. Such camera networks are perfect candidates when the task on hand is to simply record video footage of several areas, without having to take decisions or action in real time (IP cameras). They are used for passive surveillance and video footage storage. For real time processing the number of required human viewers would get quickly prohibitive.
Fig. 1 shows a typical camera network using conventional camera and video monitor technologies.

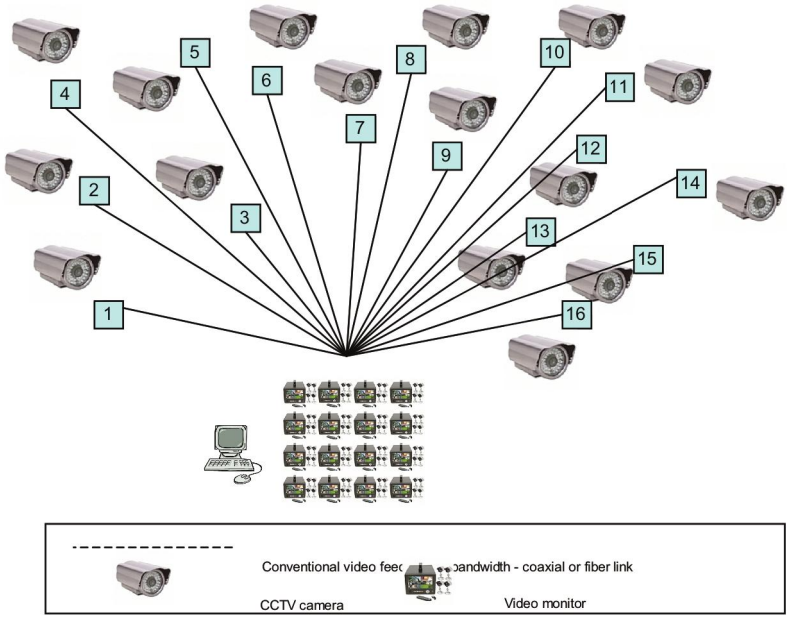


*Fig.1. Conventional CCTV camera networks*

Our aim is to build a wireless camera network which task is to acquire 3D shapes and compare them to an on board shapes library. Once the shape is recognized, only then data is sent to the hub, in very small quantity, like "shape type x recognized at node y at time z", which can be done wirelessly without taking on a large bandwidth. Fig. 2 shows such a smart camera sensor network deployment.

3D sensors based on structured illumination already exist today in industry, and are applied to numerous tasks such as conveyor belt object scanning, human body proportion scanning (for clothing), dental scanning, etc… However, such systems use conventional technologies such as digital projectors and video cameras which make them bulky, large and expensive. Our task is to miniaturize these sensors, as depicted in Fig.3, in a package less than 1/3 or an inch, in which all the optical elements are pre-aligned onto a single diffractive glass window.

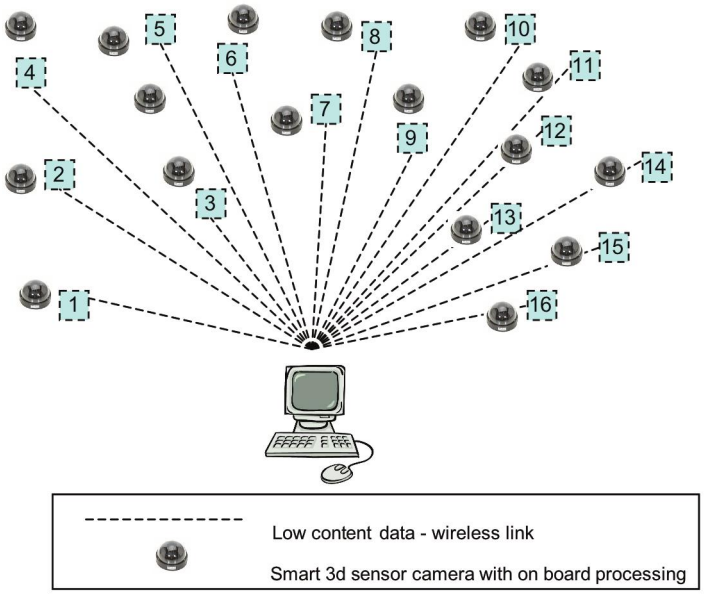


*Fig. 2: Deployment of smart 3D camera sensor network.*

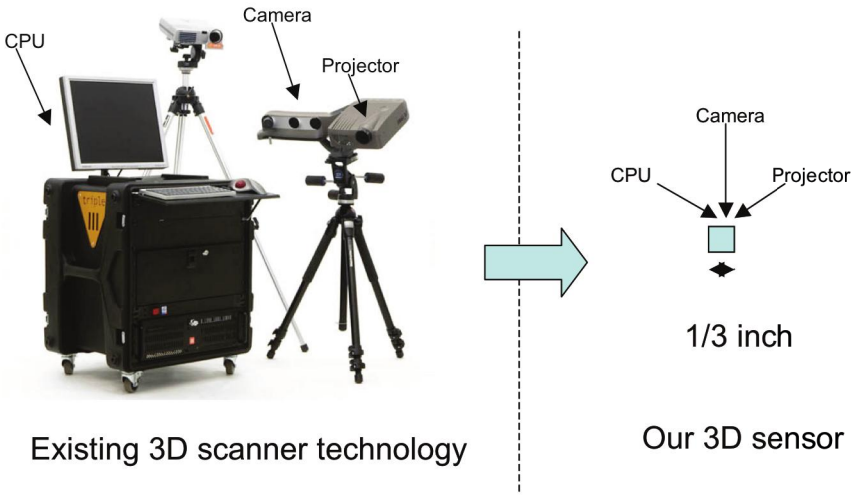


*Fig.3: The task on hand*

## 2. CONVENTIONAL 3D SENSORS USING STRUCTURED ILLUMINATION

A wide variety of 3d sensors based on structured illumination are available today in industry. Such systems come in various configurations, and use a projector and a camera. Fig.4 shows the projection and acquisition geometry used in most of these systems.

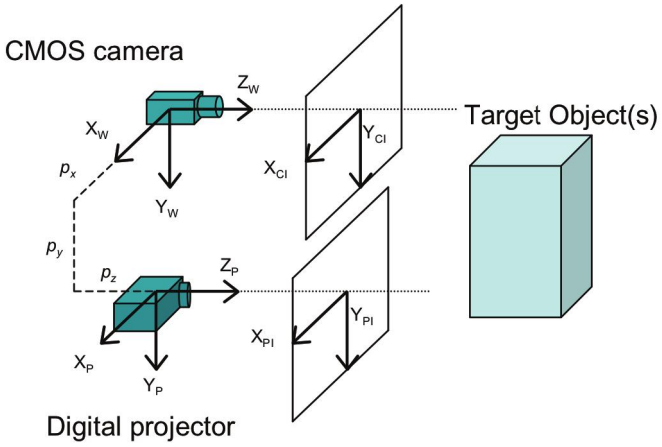


- Camera projection center at (0,0,0)
- Projector at ($p_x$, $p_y$, $p_z$)
- Parallel optical axes
- Pinhole projection model for camera and projector

*Fig.4: Principle of 3D sensing by the use of structured illumination*

Fig. 5 shows some of the existing systems available today, in both active and passive implementations

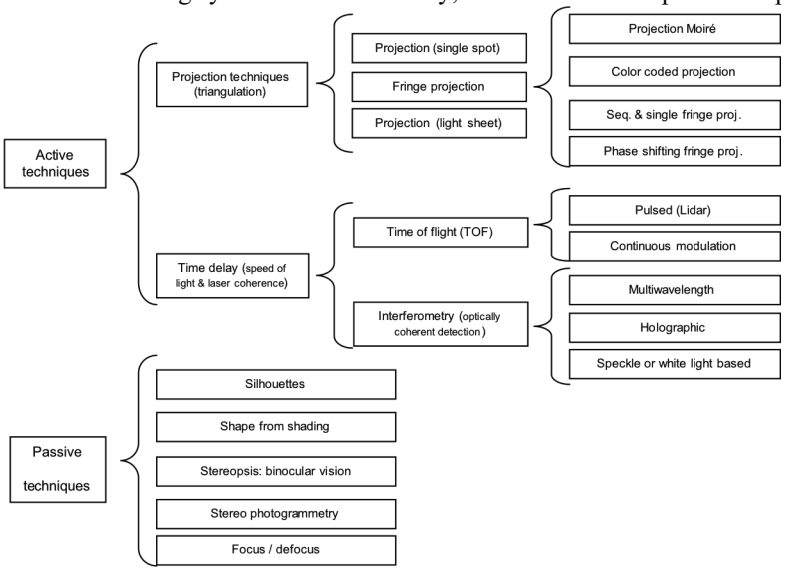


*Fig.5: Structured illumination 3D sensor systems available today*

These systems are cumbersome and expensive, since they require a traditional projector and a camera system. Besides they have to focus the fringe pattern on the object via an objective, thus requiring continuous auto-focus ability for both the projection system as well as for the acquisition system.

## 3. FAR FIELD STRUCTURED LIGHT PROJECTORS

In order to simplify the projection system, far field projectors have been developed. These systems are based on laser projection and either scan the field (laser scanners) or project a far field pattern on top the

scene (diffractive projectors). Fig. 5 shows some of these projectors. The diffractive projectors are still being developed in industry, whereas the laser scanner as already a mature technology.

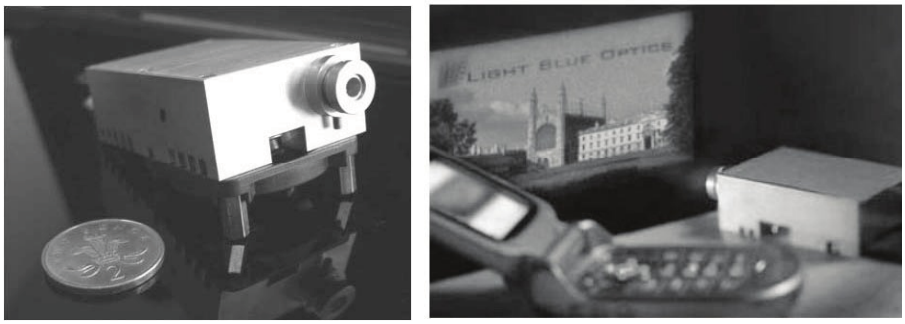


*Fig.6: Far field projection of fringe patterns via laser scanners or diffractive projectors*

Diffractive projectors have numerous advantages over traditional projectors, but have also numerous disadvantages. They are listed below:

Advantages of diffractive fringe projectors.

- Far field projection of fringes (no need to objective lens)
- Laser projection (can be visible or IR)

Disadvantages of diffractive fringe projectors.

- Complex to develop an integrated (projects Fourier transform of pattern)
- Requires a microdisplay controller and complex driving electronics
- Low projection angles require additional angle enlarger objective
- Speckle pattern appearing on fringes
- Low resolution due to limited number of pixels and pixel sizes in microdisplay
- Conjugate and higher orders appearing in the field of view
- Larger zero order appearing in middle of field

These far field projection systems do not require auto-focus capabilities and can therefore be used on any subject, close and far at the same time. The capture via a conventional objective lens however needs to have an autofocus capability in order to acquire the scene at the desired depth.

## 4. REQUIREMENTS FOR INTEGRATED 3D SENSOR NETWORKS

The basic requirements for a passive 3D sensor network based on structures illumination are as follows:

- Cheap and mass replicable optics
- Compact, miniaturized and easy packaging technology
- Low bandwidth required between sensor and hub
- Low power consumption (no complex microdisplay drivers, high efficiency projector, no moving parts)
- Far field projection (always in focus)
- Frame acquisition performed by fixed camera objective (no focusing)
- Stealth mode allowing night operation (IR laser projection)

Our novel system provides solutions to all previous requirements.

## 5. ARCHITECTURE OF THE INTEGRATED 3D SENSORS

### 5.1.) Projection side:

Our 3D sensors are based on a static diffraction projection system linked to a static extended depth of view CMOS sensor. Both systems are integrated in the same package. All optics are fabricated on a single substrate (diffractive projectors as well as CMOS camera lens).

Our projector system uses etched diffraction gratings linked to array of lasers (visible or IR). The diffractive elements are calculated by iterative optimizat9opn algorithms [2] based on scalar theory of diffraction [3].
Our camera system uses an extended depth of focus objective lens optimized for the projection wavelength.

The CMOS sensor as well as the lasers are integrated onto a PCB board underneath a quartz window. This quartz window bears both the various diffractive elements which project the fringes

Fig. 7 shows the internal structure of our 3D sensor.

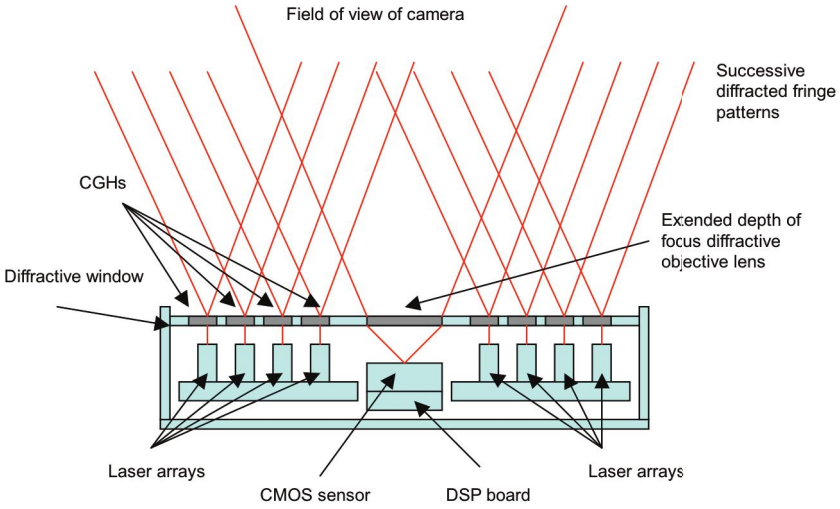


*Fig. 7: Internal structure of our 3D camera sensor*

Unlike in diffractive projectors, we can here produce very accurate fringe projections since we are not limited by neither the number of pixels on the microdisplay nor their size (our sensor can project directly the fringes over the desired angular cone without needing an angle enlarger).

### 5.2) Camera side:

Fig.8 shows more compact and cheap CMOS cameras packages as proposed by Tessera inc, by using wafer scale objective lenses fabrication [1].

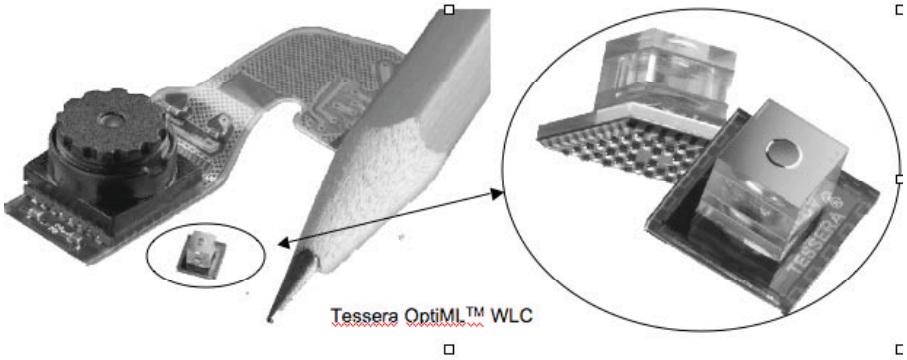


*Fig.8: Miniature CMOS cameras from Tessera.*

We propose to use the same type of fabrication technology for our objective lenses, however our lenses will be diffractive (i.e. planar) and will be optimized only for a single wavelength (the wavelength of the lasers used to project the fringe patterns). The lens and the various diffractive elements projecting the successive fringe sets are fabricated on a single window, thus simplifying considerably the integration of the various components in our 3D camera sensor, and therefore enabling the mass production.

Most CMOS sensors are produced with an on-board DSP chip underneath the sensor which compensates for the various aberrations of the imaging lens. In our case, we use this DSP to burn the fringe interpretation software as well as the lens aberration compensation.
The extended depth of focus diffractive objective lens is implemented as a special Fresnel diffractive lens with circular focal length modulations over 360 degrees. Fig. 9 shows both the design layout and a close up photograph of the modulated lens.

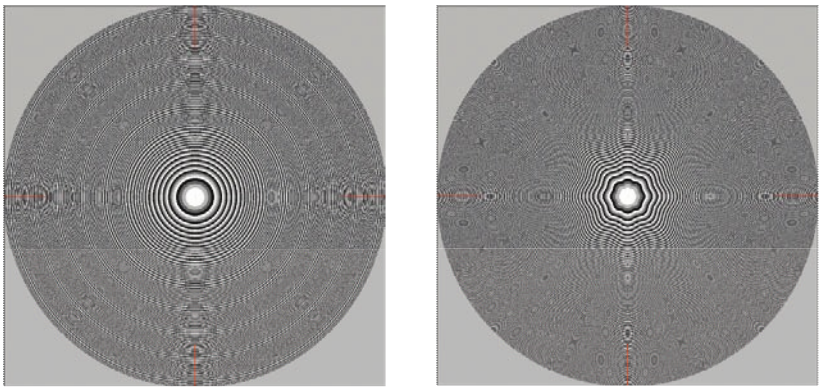


*Fig.9 Extended depth of focus diffractive objective lens.*

The extended depth of focus can be implemented in two different ways, as depicted in Fig.9:

- by radial modulation of the focal length
- by circular modulation of the focal length

The extended depth of focus lens is optimized for a single wavelength (the illumination wavelength). An additional visible/IR filter is added on the outside surface of the window in order to let only the desired IR illumination out and the desired illumination in. This remove any other shape from
Note that such a lens cannot be fabricated as a refractive lens, since the equivalent defractive surface profile would be too complicated to shape.

## 6. FABRICATION OF THE FIRST GENERATION SENSOR WINDOW

Fig. 10 shows a microphotograph of the first generation sensor window comprising the computer generated holograms as well as the extended depth of focus diffractive CMOS objective lens.

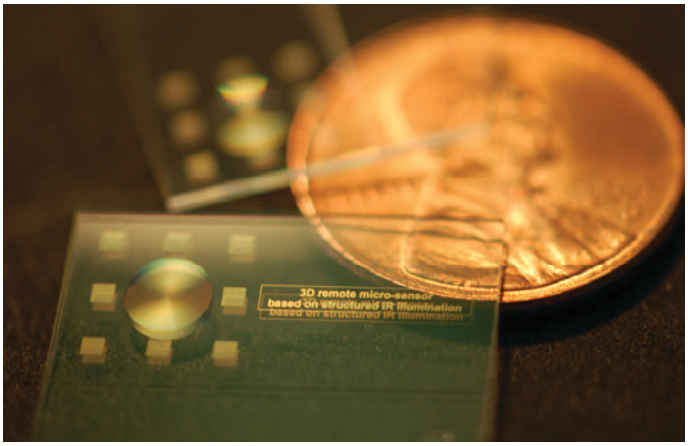


*Fig. 10. Microphotograph of the first generation diffractive sensor window*

## 6. OPERATION PRINCIPLE OF OUR SENSOR

The operational flow chart of our sensor is as follows:

- A sequence of fringes is projected by lighting the lasers one after the other. The sequence here consists of sets of phase shifted sinusoidal fringes followed by sets of binary Gray code fringes.
- The CMOS sensor acquisition is synchronized with the various lasers.
- After processing the successive deformed fringe patterns, the algorithm on the DSP provides an estimate of the 3D object
- The resulting 3D shape is compared to a series of shapes stored on board of a look up table (LUT).
- If one of the shapes on the LUT is recognized, the sensors sends a simple message to the hub such as: shape # n in LUT detected by sensor # m at time T). Such an info can be easily transferred over IP or even Bluetooth and does not hold up any data bandwidth as a video feed would do.
- Such a 3D shape can therefore be followed by various sensors in the sensor network area and swift action can be decided by the hub receiving this information.

Fig. 11 shows an example of fringe projection over a human body shape with a red diode laser array and acquired by a CMOS camera.

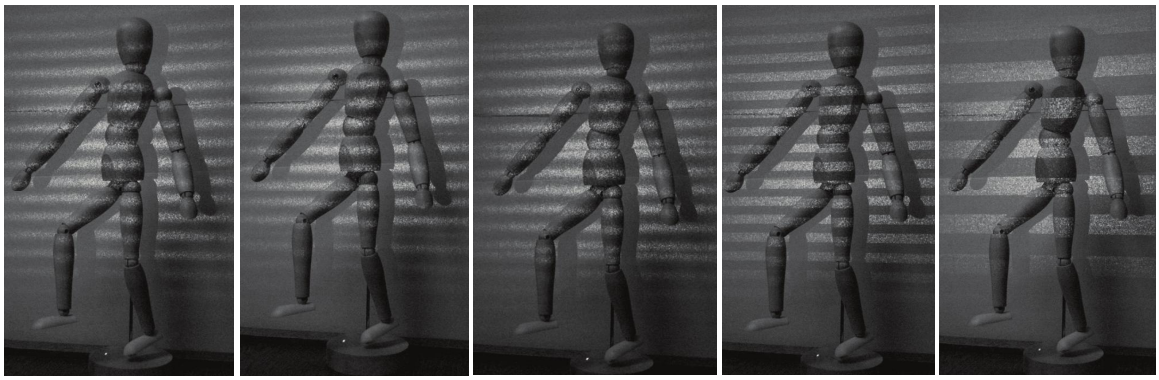


*Fig. 11 shows the operation with visible laser on a test shape (human body shape).*

The CGHs used to project the sets of fringes in Fig.11 are located on the sensor window (see Fig.12).

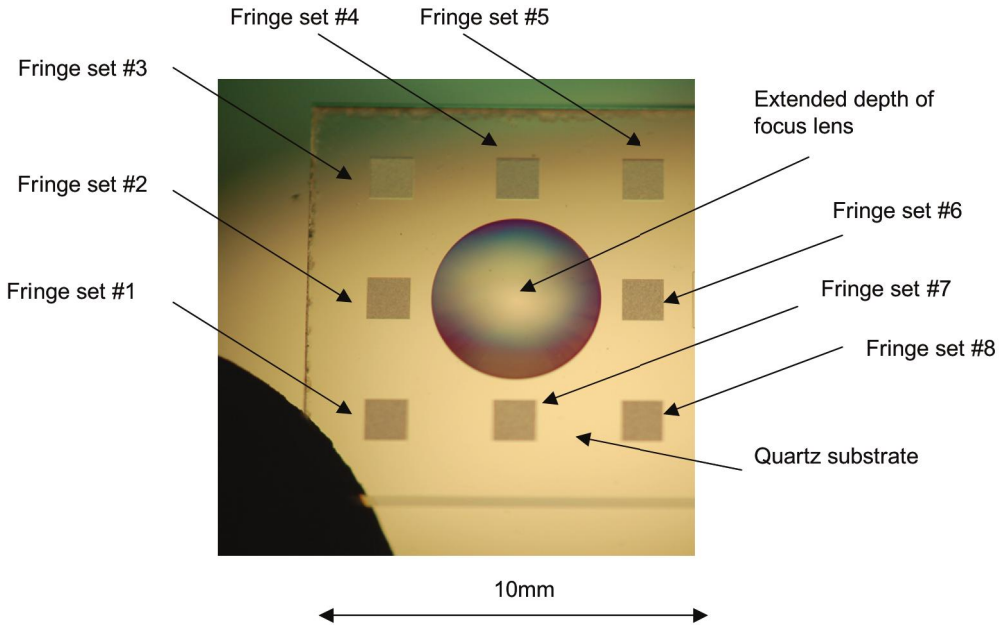


*Fig.12: CGHs used to project the sets of fringes in Fig.11.*

## 6. SPECKLE REDUCTION STRATEGY

In order to reduce the speckle pattern on the fringes, we use various laser/CGH couples to project a single set of fringes. The CGHs are optimized to produce a same fringe pattern, however bearing a different phase map, therefore creating a different speckle pattern on the fringes. By integrating the various speckle patterns on the camera the fringe pattern can be smoothed out. For example, by using 4 different lasers/CGHs couples, one can produce four sets of orthogonal speckle states on a same fringe pattern and thus reduce dramatically the speckle pattern on the resulting image acquired by eth CMOS sensor over the four projections.

Fig. 13 shows the speckle dance on a single fringe by using three different initial phases in the CGH design process.

As arrays of IR laser are becoming cheap, thanks to the 10Gb Ethernet optical lines utilizing up to 4x12 arrays of 850nm VCSEL lasers, one can integrate such a scheme without developing any custom laser system.

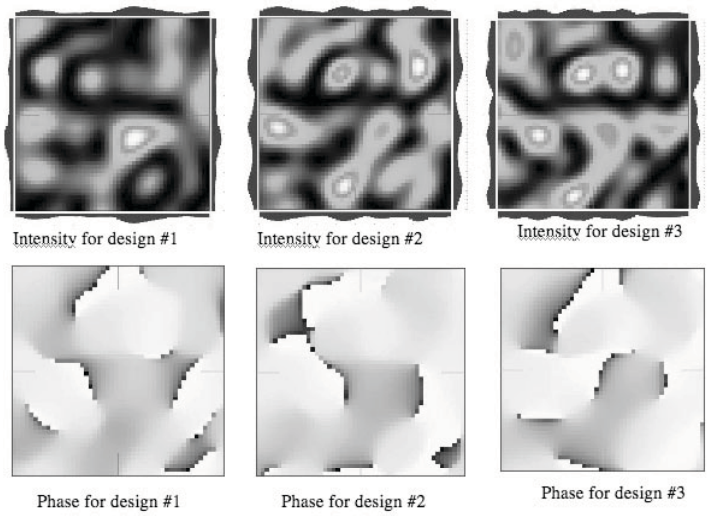


*Fig. 13: Speckle dance from different CGHs projecting the same fringe pattern.*

## CONCLUSION

We have demonstrated the architecture and operation of an integrated 3D sensor based on diffractive optics. The sensor is static without any moving parts. All the optics are implemented as diffractive optics for a specific and unique wavelength and fabricated on a single quartz window placed over an array of lasers and a CMOS sensor.
We have proposed to apply this sensor to a network in order to detect and follow specific 3D shapes in a confined environment such as an airport, a port or a mall.

## REFERENCES

[1] http://www.tessera.com/technologies/imagingandoptics/Pages/waferleveloptics.aspx
[2] Bernard Kress and Patrick Meyrueis. "*Applied Digital Optics: from micro-optics to nanophotonics*" Publisher John Wiley and Sons (April 2009).
[3] Joseph Goodman, *Introduction to Fourier Optics*, Mc Graw Hill College Division (1968)

# Fiber Optic Oxygen sensor using Fluorescence Quenching for aircraft inerting fuel tank applications

Allen Panahi*
Accro USA LLC, Pasadena, CA91117

## ABSTRACT

On July 18, 2008, the FAA mandated that new aircraft are to include inerting technology to significantly reduce the potential for flammable vapor spaces in center wing fuel tanks. All passenger aircraft constructed since 1991 must also be retrofitted with this technology. This ruling is the result of 18 aircraft that have experienced fuel tank flammable vapor ignition incidents since 1960. Included in these are the TWA 800 and Avianca Flight 203 incidents that resulted in 337 total fatalities. Comprised of heavier hydrocarbon components, jet fuel is much less volatile, with Jet A having a flash point of approximately 100°F and JP-4 having a flash point of approximately 0°F. In contrast, straight-run gasoline has a flash point of approximately -40°F. The flash point is the minimum temperature where a liquid fuel can generate enough vapor to form a flammable mixture with air. If the temperature is below the flash point there isn't enough fuel evaporating to form a flammable fuel-air mixture. Since jet fuel and gasoline have similar flammable concentration limits, gasoline must produce much more vapor at a given temperature to have such a low flash point; hence gasoline is much more volatile than jet fuel. In this paper we explore Fluorescence Technology as applied to the design and development of O2 sensors that can be used for this application and discuss the various test and measurement techniques used to estimate the O2 gas concentration. We compare the various intensity based approaches and contrast them with the frequency domain techniques that measure phase to extract fluorescent lifetimes. The various inerting fuel tank requirements are explained and finally a novel compact measurement system using that uses the frequency heterodyning cross correlation technique that can be used for various applications is described in detail while the benefits are explored together with some test data collected.

**Key Words:** Fiber optic Oxygen, Fluorescence Quenching, inerting, aircraft fuel tanks

## 1. INTRODUCTION TO INERTING FUEL TANKS FOR COMMERCIAL AIRCRAFTS:

Like gasoline, jet fuel is generally safe under normal operating conditions. What is concerning the aviation industry is abnormal circumstances, for instance where the fuel is heated by reject heat from the plane air conditioning system, increasing the vapor generated such that the flammable range is reached. With the new mandate, the FAA is stating that this hazard is substantial enough to require additional measures (inerting technology) to reduce the risk of fuel system explosions. The FAA has decided that it is time to reduce the hazards of these abnormal conditions by requiring gas inerting equipment for aircraft.

## 2. FLUORESCENCE LIFETIME MEASUREMENTS IN TIME AND FREQUENCY DOMAINS

Fluorescence lifetimes in the nanosecond range have typically been measured by either of two methods, Time Correlated Single Photon Counting (TCSPC) or phase modulation. Phase modulation methods have enjoyed widespread success in the past for the relative simplicity of the instrumental setup. TCSPC, on the other hand, has been seen as the more complex method, relying on expensive detectors and complex electronics. Furthermore, the TCSPC method was generally implemented with either flash lamp sources (100 KHz pulse rates) which were very slow in data collection or with complex fast-pulsed lasers which were restricted to several distinct wavelength regions. In effect, TCSPC was a complex method confined (when using lasers) to large well-equipped laser laboratories and relied on a large degree of expertise. Recently, however, the emergence of new LED and laser diode technologies along with miniaturized electronics has enabled Time Correlated Single Photon Counting (TCSPC) methods to gain more widespread use. Such miniaturization of the electronics for TCSPC onto a single PC board with software control has at a stroke made the method much more accessible.

* Corresponding author e-mail address: allen.panahi@verizon.net

Photonics in the Transportation Industry: Auto to Aerospace II, edited by Alex A. Kazemi, Bernard C. Kress
Proc. of SPIE Vol. 7314, 73140D · © 2009 SPIE · CCC code: 0277-786X/09/$18 · doi: 10.1117/12.821732

Semiconductor LEDs and lasers as fluorescence excitation sources have improved dramatically in the past decade and will revolutionize fluorescence lifetime measurement systems. LED devices can now offer excitation wavelengths of between 380 nm and 600 nm with pulse rates in excess of 1 MHz and pulse widths of ~1 ns, which is ideal for mainstream biological fluorescence lifetime studies. A further development has been the emergence of commercial violet GaN laser diodes in the past two years. These lasers are compact, capable of pulse widths less than 100 ps, and are easily incorporated into fluorescence lifetime systems. The use of fluorescence lifetimes as a sensor method has attracted widespread interest in the past decade. Analytes such as halides, oxygen, and carbon dioxide, have been monitored using fluorescence lifetimes. Fluorescence lifetime based techniques have several advantages over more traditional fluorescence intensity methods which are susceptible to changes in excitation light intensity, to photobleaching, variation in light scattering and absorption of the sample.

### 2.1 Fluorescence Quenching Technology for O2 Sensor

The partial pressure of oxygen is inversely proportional to the intensity of the fluorescence exhibited and is described by the Stern-Volmer equation:

$$I0 / I = 1 + k\,(PO2)$$

where I0 is the fluorescence intensity of a standard at zero pressure of oxygen; I is the fluorescence intensity of a standard with a pressure within the high end of the working range and k is the Stern-Volmer constant, which is dependant on the chemical composition of the sensor. This equation functions well for lower values of partial pressure, but for samples over 20 kPa, the second order polynomial algorithm is required, which is as follows:

$$I0 / I = 1 + k1\,(PO2) + k2\,(PO2)$$

## 3. BASIC SETUP FOR FLUORESCENCE LIFETIME MEASUREMENT TECHNIQUES

The fluorescence measurement is a simple experiment, but intrinsic and basic information can be directly measured and analyzed [1]. Among the specific techniques it offers are fluorescence lifetime and fluorescence resonance energy transfer [2,3]. Fluorescent samples have a characteristic time behavior between excitation and emission, which is determined by the time dependent quantum mechanical overlap between states [4]. For many fluorophores, this behavior can be simply represented by a single exponential decay function with a characteristic fluorescence lifetime [5]. Historically, there are two complementary techniques of lifetime measurement: time-domain and frequency domain. In frequency-domain, the fluorescent sample is excited by a modulated source of light. The fluorescence emitted by the fluorophore has a similar waveform, but is modulated and phase-shifted from the excitation source spectrum. The fluorescence lifetime can be calculated from the observed modulation depth and phase shift. Traditional fluorescence-lifetime measurement in frequency-domain has been done by a cross- correlation phase-modulation technique. In the cross-correlation technique, the fluorescence emission is detected by a photomultiplier tube modulated at the same base radio frequency as the modulation source plus a low cross-correlation frequency. The FM mixing technique is adapted to analyze lifetime information. Recently, for frequency-domain methods there has been proposed and constructed a FD spectrometer with a blue light-emitting diode (LED) as an excitation source and a photodiode as a photodetector. There has been constructed a direct LED driving circuit for radiofrequency modulation as an excitation source and a high bandwidth oscilloscope to record both excitation and emission spectra. P. Harms et al. have proposed and constructed a frequency-domain lifetime spectrometer using a RF lock-in amplifier. The RF lock-in directly provided the ac signal used to modulate the intensity of the blue LED excitation source and the emission was measured by a photomultiplier tube connected to the RF lock-in. In this paper, we have designed and constructed a simple frequency-domain (FD) fluorescence-lifetime measurement system using a Blue-violet laser diode, a photomultiplier tube, and an oscilloscope system. Both excitation and emission intensity have been recorded by oscilloscope and analyzed by using the custom-made FFT algorithm in the Matlab program.

Therefore, the fluorescence lifetime can be easily calculated from the result of a frequency-modulated experiment. In order to determine the fluorescence lifetime, we designed and constructed a simple but accurate spectrometer using a violet laser diode.

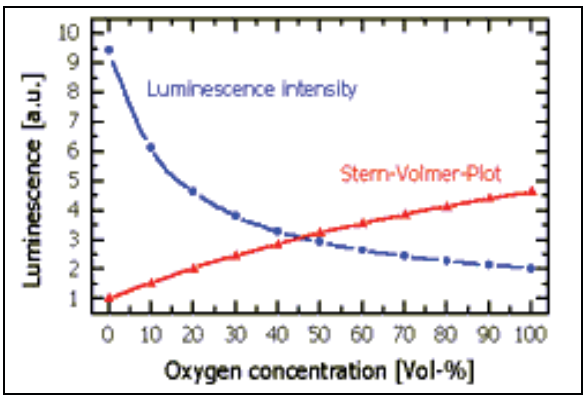


(a)

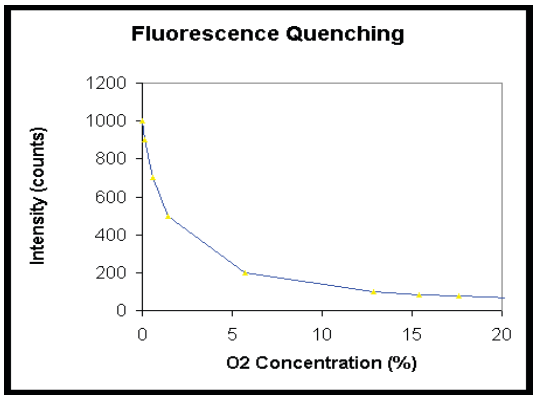


(b)

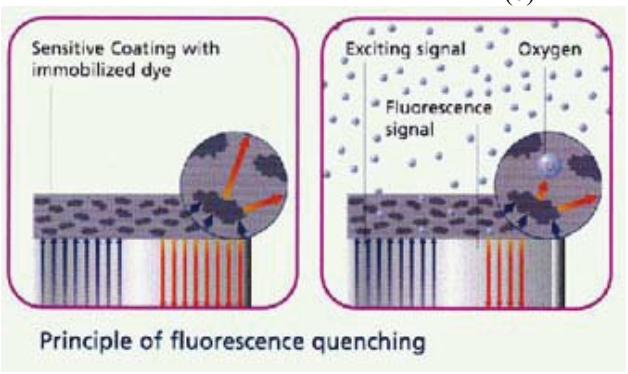


(c)

**Figure 1. Sensors use Fluorescence quenching technology to measure O2 gas concentrations that respond to O2 partial pressure: this follows the Stern-Volmer relationship as shown in the above figures a, and b. Figure c is a pictorial of the fluorescence quenching in action. Rhuthenium based Sol-gel sensors are exposed to Blue light from LED or Lasers @ 470 nm and the reflected Fluorescence optical signal is measured with a orange filter centered at 600nm.**

### 3.1 Time Domain Fluorescence lifetime measurements

We present an alternative approach to real-time lifetime determination, which is based on the fact that for a single exponential decay, the fluorescence lifetime is equal to the average time lag between an excitation laser pulse and the subsequent detection of a fluorescence photon. For each photon, a time-to-amplitude converter ~TAC! generates a pulse of an amplitude proportional to the time lag between fluorescence photon and excitation pulse. The resulting sequence of pulses, with exponentially distributed amplitudes and inter-pulse times, is then subjected to a count rate independent fluorescence intensity at different time delays after the pulse. As a result, an averaging procedure start. It utilizes a pulsed light source (an LED, a laser diode or a nitrogen/dye laser) and measures Fluorescence Lifetime Measurements

• There exist two methods to measure fluorescent lifetime:
  – Time domain: using pulse fluorimetry
• pulse length is << τF
• measure time dependent intensity decay
• fit lifetime curve to data
  –In the frequency domain measure: phase shift / modulation ratio
• Excite sample with intensity modulated light at high frequency
• Calculate decay based on either
  – Phase shift (delay)

Demodulation (change in amplitude)

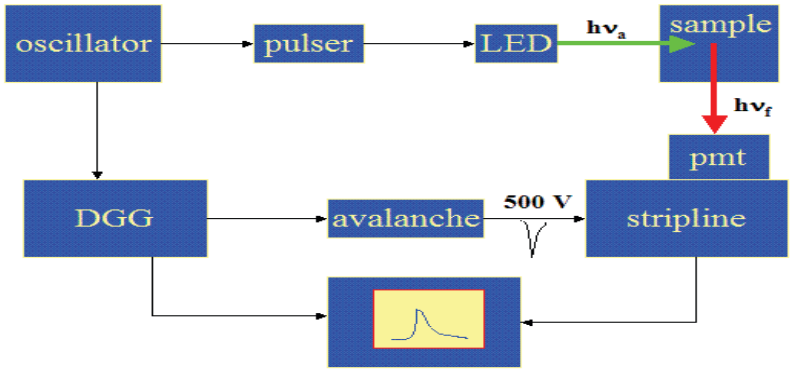


**Figure 2. Simple setup for lifetime measurements in the time domain.**

## Meaning of Lifetime Decay

- $dn(t) / dt = -(\Gamma + k_{nr})\, n(t)$ , where $n(t)$ is the number of excited molecules
- $n(t) = n_0 \exp(-t/\tau)$
- Experimentally observe – intensity, $I(t)$ , which is proportional $n(t)$
- $I(t) = I_0 \exp(-t/\tau)$
- Time at which intensity reaches 1/e
- Plot log $I(t)$ versus $t$
- Average period of time fluorophore in excited state – complicated with multiexponential decay

## Phase Modulation Lifetimes

- Modulation of emission is measured relative to modulation of the excitation m = (B/A)/(b/a)
- Phase angle ($\phi$) – measured from the zero-crossing times of the modulated components
- $\tau_\phi = \omega^{-1} \tan \phi$ ; $\tau_m = \omega^{-1}[1/m^2-1]^{1/2}$

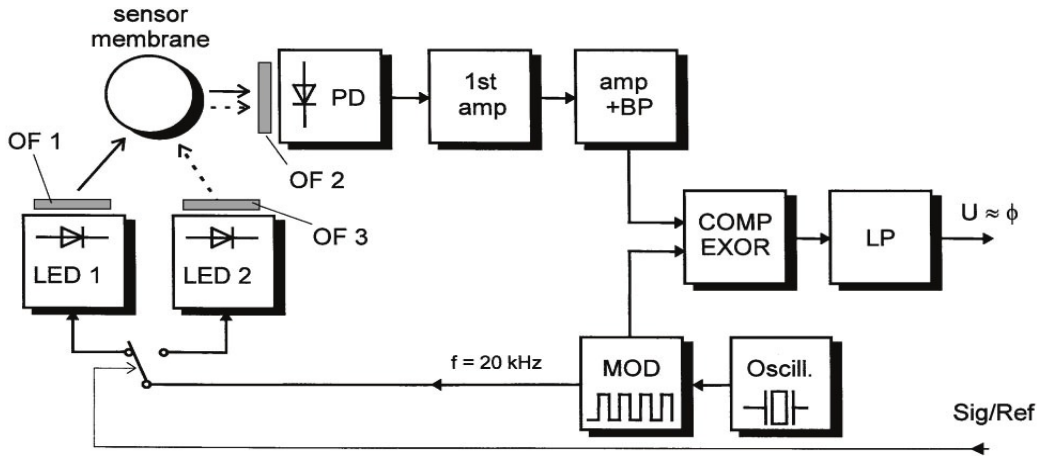


**Figure 3. Simple O2 measurement system using frequency measurements instead of the Intensity**

The two LEDs used have different filters in front of them. A Blue and a RED. The Blue is for the Excitation and the RED is for the Reference. . The Fluorescence signal is optically detected using an Shortwavelenth APD ( Avalanche photodiode) or PIN detector and its phase shift is measured relative to the reference response.

The Phase difference is a measure of the O2 Gas concentration.

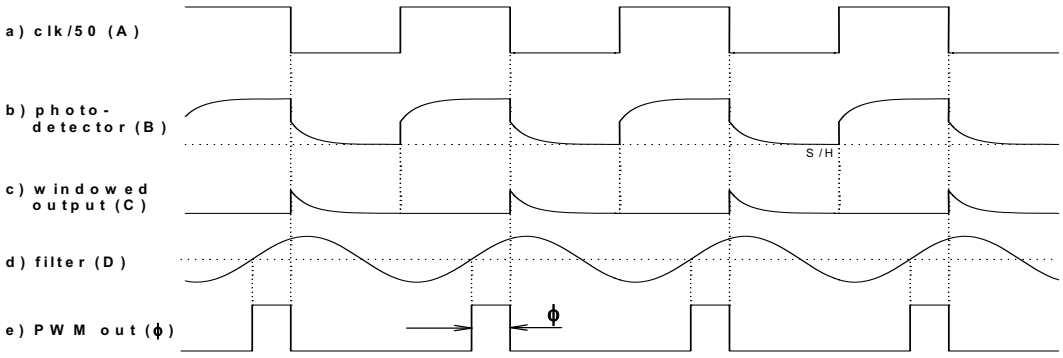


**Figure 3.1. Shows the various signal outputs showing the excitation square wave(a) the resulting Photodetector result (b), The windowed out (c) and the Bandpass filtered output(d) and the final PWM out put Phase difference (e)**

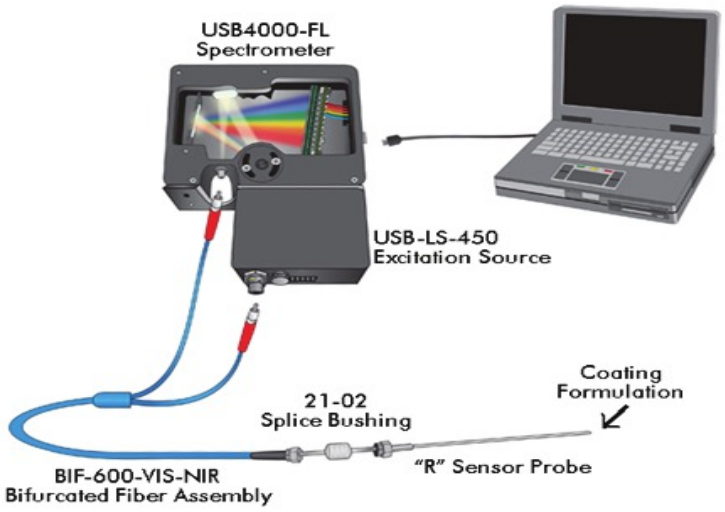


**Figure 4. The intensity of the fluorescence signal is measured using a UV-VIS Spectrometer**

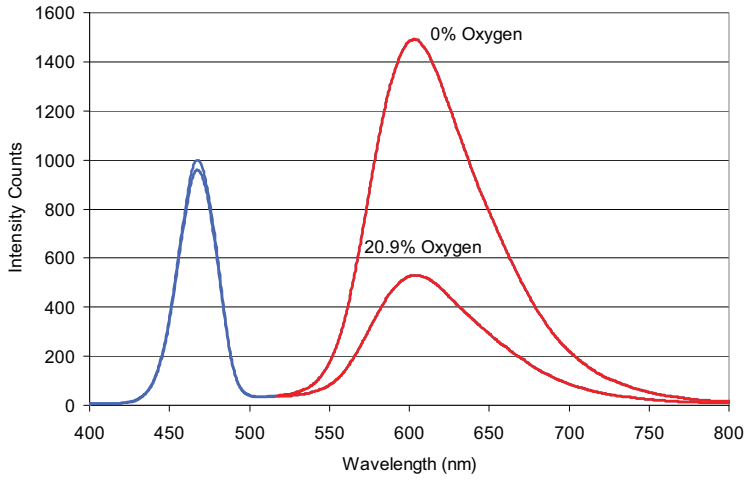


**Figure 5. Intensity counts of the excitation and resulting emission measured with a Spectrophotometer.**

Blue curve is the LED excitation at 470 nm. Red curves are the Fluorescence response of the O2 sensor when exposed to the Blue Light. The 20.9 % O2 reading is lower because of O2 being quenched. The no O2 or zero reading is higher. It produces more fluorescent signal

## 4. FIBER OPTIC SENSOR DEVELOPMENT

The fiber optic sensor is based on fluorescence quenching of the O2 gas when excited with Blue light source that can use an LED or Blue laser source ( 470 nm). The reflected fluorescence signal is emitted at 600nm or Orange in the visible spectrum. Below we describe in detail the basic properties and materials used for the O2 sensor and cover the Sol-gel process of the materials used in the sensor.

### 4.1 Oxygen sensor

Optical sensors for oxygen are attractive in that they are fast, do not consume oxygen and are not easily poisoned. The most common method adopted is based on the quenching of fluorescence from an appropriate chemical species. The variation in fluorescence signal, I, or fluorescence decay time, r, with oxygen concentration
[02], is described by the Stern-Volmer equations:

$$I/0 = 1 + Ksv[O2] \quad (1)$$
$$Iro = 1 + Ksv[O2] \quad (2)$$
$$Ksv = k'c0 \quad (3)$$

where I0 and r0 are respectively the fluorescence signal and excited-state lifetime in the absence of oxygen, Ksv is the Stern-Volmer quenching constant and k is the bimolecular quenching constant. The ruthenium complex, Ru(II)tris( 4,7-diphenyl-l,10-phenanthroline) = Ru(Ph2phen) 32+, was chosen for this work as it exhibits high oxygen sensitivity due to its long unquenched lifetime ro (~ 6 IJs). Furthermore, in common with other ruthenium polypyridyl complexes, it absorbs strongly at blue green wavelengths and has a relatively large Stokes shift. As is clear from Eqs. (1) and (2), oxygen concentration may be measured by monitoring fluorescence intensity or decay time. Both approaches have been adopted by us, with the latter approach overcoming many of the problems (such as reagent photodegradation, aging of source or detector) associated with intensity-based sensors. The performance of a phase fluorimetric oxygen sensor based on decay-time measurements is described elsewhere in this volume. Only intensity-based results will be presented here.

The sensor substrate generally used by us was a 10 cm length of 600 lam core polymer-clad silica (PCS) optical fibre, which was declad along most of its length by mechanical means followed by an etching process. The fibre was then dip coated with a thin (~ 300 nm) layer of sol-gel-derived silica containing the Ru(Ph2phen) 23+ complex, resulting in the structure shown in Fig. l(a). Prior to testing, the fibres were cured at 73 °C for about 24 h to produce a tough, inert coating that is intrinsically bound to the silica fibre core. Sol-gel films of about 50 mm length provided good signal-to-noise ratios under high-intensity blue LED excitation. The experimental configuration used to characterize the oxygen sensitivity and to demonstrate the viability of a low-cost portable system is shown in Fig. l (b). The light source is a high-intensity blue LED (Ledtronics, USA) the spectral output of which peaks at 450 nm and which delivers more than 1 mW of c.w. optical power. Furthermore, the LED emission spectrum has considerable overlap with the absorption spectrum of the ruthenium complex. The output light is first passed through a short-wave pass filter (2~u~_o~-= 505 nm) and then launched into the optical fibre. The fibre is mounted in a gas cell through which precise mixtures of nitrogen and oxygen may be passed via mass-flow controllers.

Optical, chemical, and biochemical sensors are the subject of extensive research and development with a view to their application in industrial, environmental and biomedical monitoring [1]. The degree of interest derives from a number of attractive features offered by this technology. These include the choice of a multiplicity of optical techniques already well established for routine chemical and biochemical analysis, the availability of materials and components from the rapidly expanding optoelectronic technology and the geometric flexibility, which enables configurations ranging from miniature disposable optical waveguides to remote fiber-optic probes to be achieved. The use of the sol gel process to produce sensor materials for optical chemical sensors and biosensors is attracting considerable research interest [2]. This is due to a number of advantages, principal among which are the ease of fabrication and the design flexibility of

the process. In most applications the sol-gel-derived material is used to provide a micro-porous support matrix in which analyte-sensitive species are entrapped and into which smaller analyte molecules may diffuse and interact. Such materials have been used in a range of sensor configurations. These include monoliths and deposited films, end-coated and side-coated optical fibres and planar waveguides, and some novel configurations such as packed capillary tubes. In this paper an overview is presented of the state-of-the-art of optical sensors that employ sol-gel-derived coatings. In particular, the benefits of employing an evanescent-wave configuration are highlighted. Examples of chemical and biological sensors are presented, reflecting those research groups most active in this area worldwide. Finally, the technical issues that need to be addressed in order to advance this technology to the commercial stage are discussed.

## 4.2 Sol-gel process

The sol-gel process is a relatively straightforward method of producing high-quality glasses and ceramics. In the context of optical sensors the process is generally employed in the production of silica or titania glass, or mixtures of these two. Sol-gel derived silica or titania glasses are prepared from hydrolysis and condensation polymerization of the appropriate metal (silicon or titanium) alkoxide solution, followed by a temperature program which controls the densification process. The process parameters can be selected to produce a micro-porous glass, which can act as a support matrix for analyte-sensitive reagents that are added to the precursor solution [2-5]. The reagent molecules are encapsulated in the nanometer-scale cage-like structure that grows around them, but smaller analyte molecules can still permeate the interconnected pores.

The generic precursor solution for sol gel derived silica may be represented by Si(OR)4 + H20 + ROH + acid/base catalyst where R is an alkyl group. The most frequently used alkoxides in this case are tetraethyl orthosilicate (TEOS) and tetramethyl orthosilicate (TMOS). The hydrolysis that initiates the process may be acid or base catalysed and the hydrolysis rate is very dependent on pH. Consequently, this pH value, together with other process parameters such as the temperature programme and the water/alkoxide ratio, has a significant influence on the micro-structural properties of the final material. Although the microporous material may be post-doped with the appropriate sensor molecules this will not provide entrapment, which can only be achieved by adding the dopant to the precursor solution. A range of specific recipes has been used by different research teams in accordance with their particular requirements [3,13,15]. An alternative and more rapid approach to achieving sol gel-derived thin films is the use of the commercially available Liquicoat solutions (Liquicoat Si ZLI-2132 and Liquicoat Ti ZLI-1857, available from Merck). These are metal alkoxide colloidal solutions containing 7% silica and 9% titania, respectively. Sensor dyes can be added directly to these solutions before a simple coating and rapid curing (e.g., 100°C for 10 min) procedure is carried out [16]. The importance of these materials lies mainly in the ease with which they can be mixed to achieve coatings of any required refractive-index value between the extremes for silica (~1.46) and titania (~2.3). Therefore, the fluorescence lifetime can be easily calculated from the result of a frequency-modulated experiment. In order to determine the fluorescence lifetime, we designed and constructed a simple but accurate spectrometer using a violet laser diode.

In the figure below we show the following results obtained:

(A) Changes in predicted, fluorescence and polarographic oxygen partial pressures against time
(B) Correlation plot of fluorescence and polarographic measurement techniques (R2 =0.99)

The modulation-depth for each LED for the frequency range up to 500 MHz is given in Table I. The modulation is defined as:

$$m = \frac{AC/2}{\langle DC \rangle},$$

where $AC/2$ is half the value of the average alternate component of the signal—that is half the value peak-to-valley of the signal at the cross-correlation frequency—and $\langle DC \rangle$ is the average value of the direct component. For both LEDs, good modulation was achieved up to 400 MHz (the 3dB point being at about 100 MHz). The modulation behavior was measured using Chronos™; that it is the result of the frequency response of the radio frequency amplifier used to amplify the signal at frequency (f + Δf) sent to the light detectors of the instrument; and it is a function of the frequency

response of the light detectors electronic circuitry. To achieve satisfactory lifetime measurements, a modulation of 20% is sufficient.

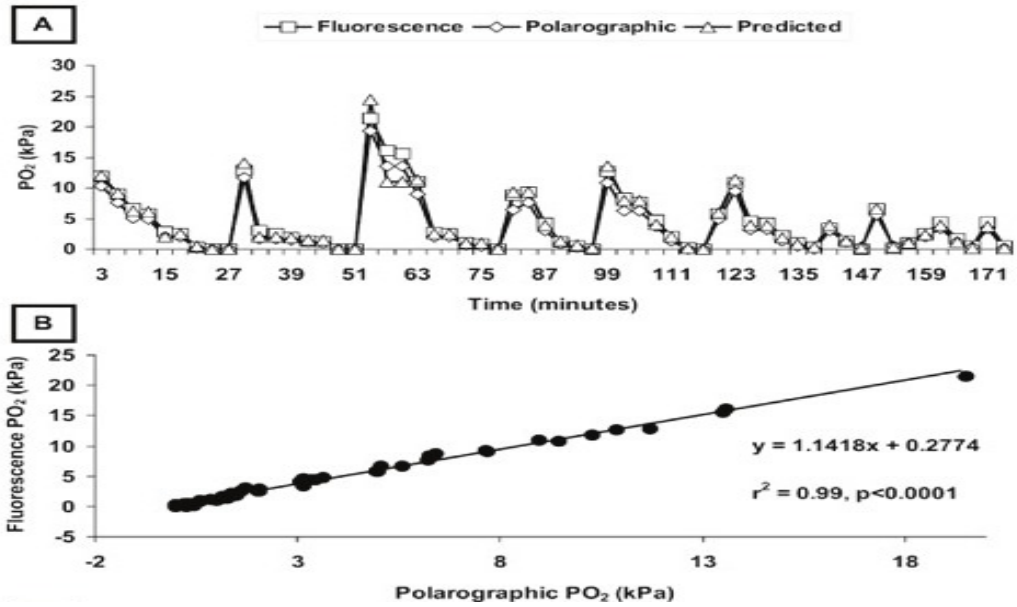


**Figure 6. Partial pressure of various concentration of O2 is measured with the Spectrophotometer from Ocean Optics. The results of the sensor are in excellent agreement with the O2 gas concentrations .The confidence R factor is 0.99**

## 5. INERTING FUEL TANK AND THE O2 SENSOR REQUIREMENTS

Main features and requirements of the O2 sensor for the aircraft inerting fuel tank are listed below:

- Intrinsic safety, and immunity to EMI
- Meet the stringent temp, pressure and O2 concentration of fuel tank
- Easy to calibrate and reliable drift free operation /low maintenance
- Chemical resistance to fuel liquid and vapor
- Lightweight and small size and low power
- Fast response – in the seconds
- Moderate resolution and accuracy: 0.001- 0.005 atm O2
- Sensor data should be compatible to aircraft control systems
- Cost effective solution

The Fuel tank environment is very specific to the altitude and pressure, and the temperature that the O2 sensor will be exposed to during many hours of flight.

Aircraft Fuel Tank Environment are as follow:

- Temperature - 50 ºC to + 50º C (operational range)
- Total Pressure 2 PSIA to 2 ATM
- Composition Fuel Vapor/Fuel Liquid / Air
- O2 levels 0.04 – 0.16
- (explosive range) 0 – 0.4 ATM

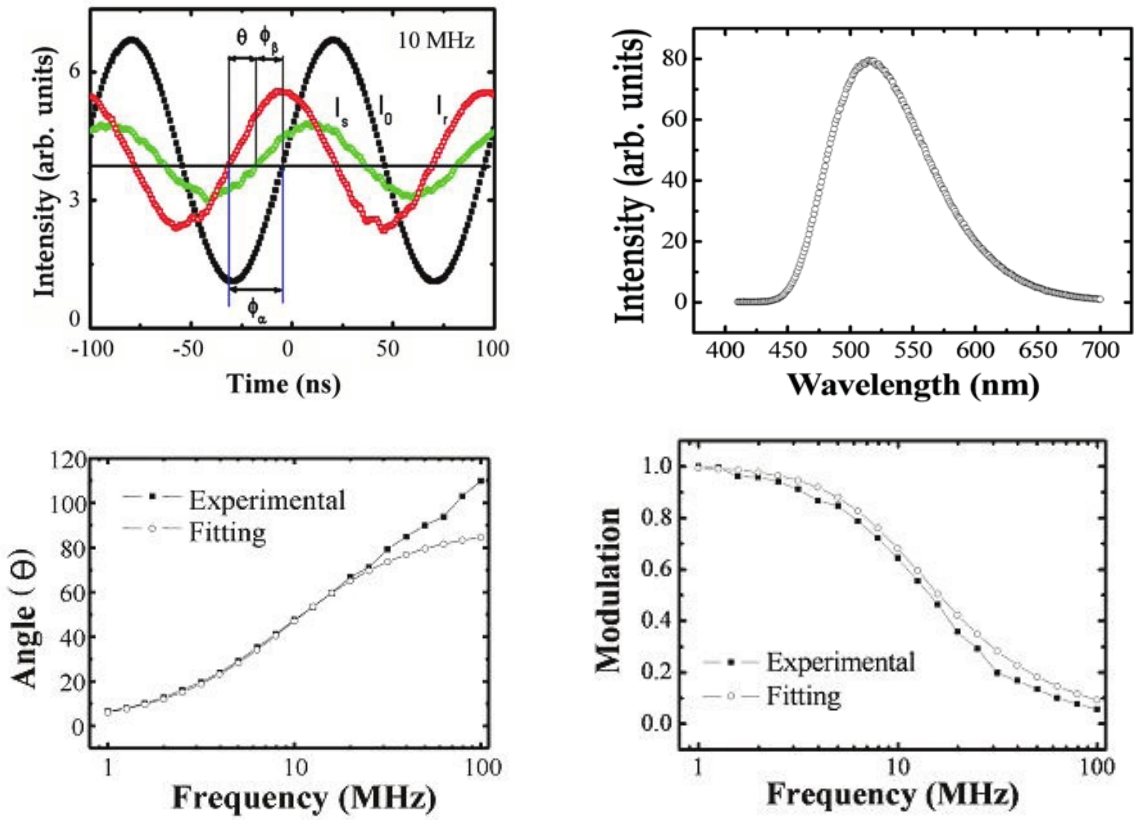


**Figure 7. Intensity measurements of the excitation and resulting emissions in the time domain showing the phase difference. Also shown is the Phase difference as a function of the sweep frequency. The bottom plot is the resulting Amplitude modulation depth as a function of frequency with exponential time constant fitting curves.**

## 6. NOVEL FLUORESCENCE LIFETIME MEASUREMENT SYSTEM USING CROSS CORRELATION TECHNIQUES

In the last few decades, fluorescence methods have become extremely important in many areas of science and technology including analytical chemistry, biophysics, cell biology, clinical chemistry and biotechnology, to name but a few. Determinations of the excited state lifetimes of fluorescent molecules are often critical for quantitative evaluation of the processes or reactions of interest. Fluorescence lifetime measurements have traditionally been realized using either the impulse response method (in which excitation is by a very brief pulse of light after which the direct decay of the fluorescence is observed) or the frequency domain method (in which the intensity of the excitation light is modulated sinusoidally and the phase shift of the fluorescence, relative to the excitation, is determined). These methods have been reviewed numerous times (see, for example, [1-4]). The frequency domain approach has also been utilized with high-repetition rate pulsed sources [5]. Recently, McGuinness et al. described the use of a new class of LEDs that emit near 280-nm as the excitation source for time-domain fluorescence lifetime measurements on proteins. In this report we evaluate the use of this class of LED as an excitation source for frequency domain time-resolved measurements.

The earliest fluorescence lifetime measurements using frequency domain RF Heterodyning technique was established by Dr: Lakowicz and later by his student Dr: Holub and Dr: Gratton. This technique has been well established and is recognized as the most mature of the frequency domain techniques. The main drawbacks is that these measurement set ups are big, bulky, expensive and not very suitable for miniaturization in view that their main source of detectors is the PMT, all their signal sources for the RF , biasing , and modulation come from bench top test instruments . Although

PMTs are very popular in the world of Fluorescent spectroscopy they are built on older vacuum technology with their inherent shortcomings in spite of their many advantages for their time. We at ROI, have built the Airborne Fluorescence imaging system around the popular Hamamatsu R928 multiplier tube. The biggest drawback is the high voltage supplies needed to operate them and the big ,bulky, and power hungry RF amplifiers needed to modulate the second dynode (Gain modulation) . We are in the process of converting detectors from PMTs to low voltage Si APDs.

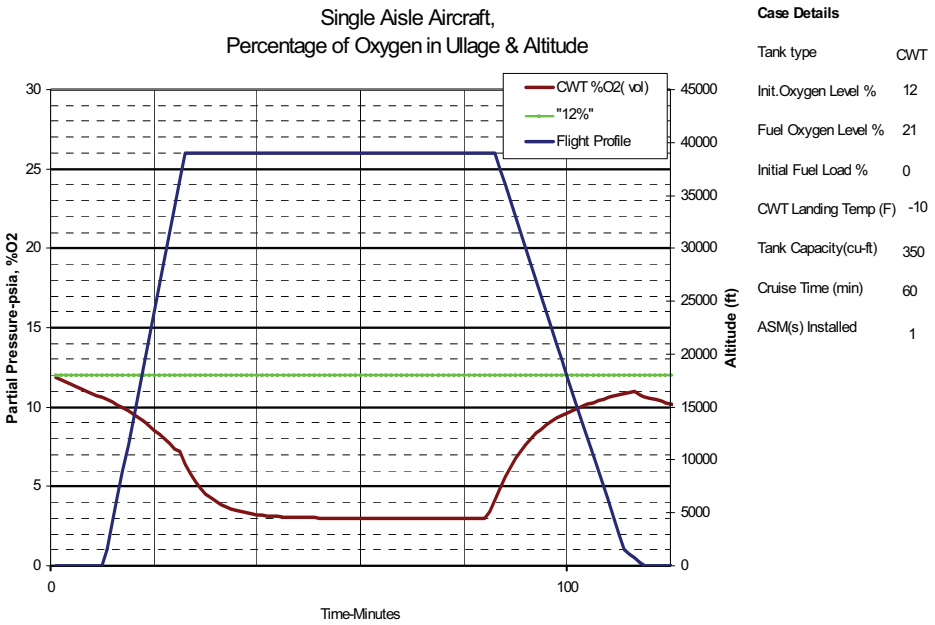


**Figure 8. Smith Industry data for an hour flight using single Aisle aircraft showing the O2 partial pressure versus altitude, and the sensor reading**

We propose a novel Cross correlation technique based on frequency domain response that use a compact, light-weight portable UV fluorescence Spectrometer, battery operated low power ( target < 3.5 W) , fluorescence identification and measurement system that provides fast and reliable tagging and identification system due to its robust design, High Laser output power, good receiver sensitivity, operating with resulting in good S/N due to cooled APD operation and Dual powerful 250 MHz DDS ( direct digital Synthesizer) Ics The proven fast and accurate frequency domain cross correlation lifetime measurement system that can accurately scan the frequency domain and resolve multi-exponential lifetime time constants in minutes. In the fast scan zero crossing mode the single dominant lifetime can be estimated in under 30 secs after exposure to the UV light source or Blue LED/Laser. The reliable, power efficient design will be airborne qualified for O2 monitoring of gas concentrations in the 0 to 25% range with accuracy better than 0.5 % by volume in air over extended temperature range from -50 to + 60 degC. The combined in situ and remote capability of this dual mode portable spectrometer. Based on ACCRO's leading expertise in integrating state-of-the-art transceiver and miniaturized optical packaging ,low power CMOS circuit technology with automated telecommunications and high grade reliable small instrumentation grade optical components with innovative packaging, and CMOS electronics, it is poised to produce a next-generation, high performance, UV-VIS fluorescence Spectrometer.

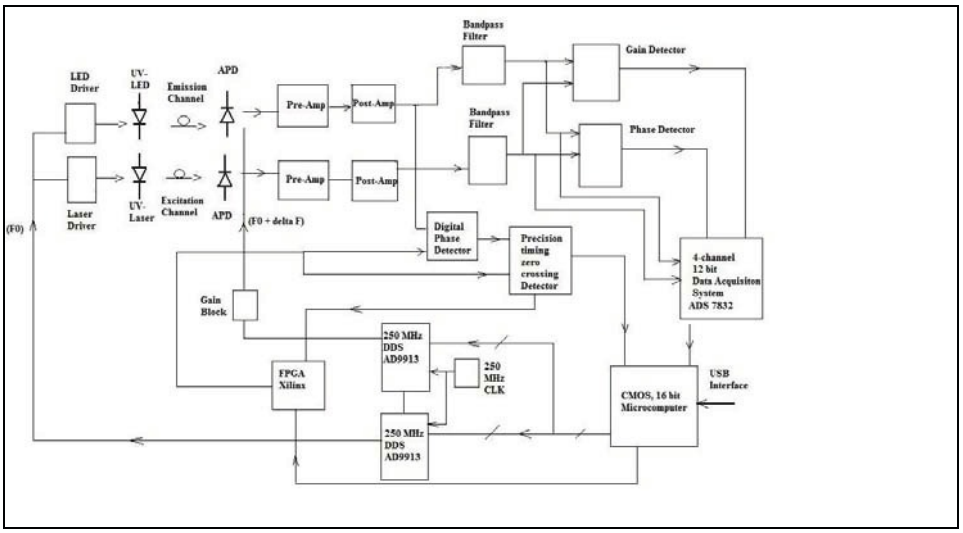


**Figure 9. High level Block Diagram of the Proposed Frequency Domain Measurement System of UV-VIS Fluorescence Lifetime for various sensors including O2**

Compared to commercial bench-top and Laboratory instrumentation and experimental setups, the proposed system has many advantages and commercial attractions. These include:

1) Portable, reliable, efficient and compact Semiconductor UV-VIS-LED and UV-VIS-Laser for the Light source operating in a constant power mode or near constant mode for temperature and Wavelength stability.
2) Use of Dual Thermo-electrically cooled APDs for high Gain, optimum S/N, and Gain modulated for Lifetime measurements. APDs Gains in excess of 200 can be achieved with low voltage APDs that can be gain modulated with up to 250 MHz with good modulation depths.
3) All CMOS electronics design including high speed 10 MIPS 16 bit processor, lowest power 250 MHz DDS IC from Analog Devices AD9913, and Laser/LED driver from IC Haus.
4) Combination of fast time resolved fluorescence lifetime estimation with steady state Spectral Analysis results in the most accurate and conclusive technique to identify mineral fluorescence based on wavelength spectral signature of minerals and their fluorescent specific lifetimes.
5) Advanced fluorescent lifetime extraction application software using Least squares fit for Multi-component Lifetime identification

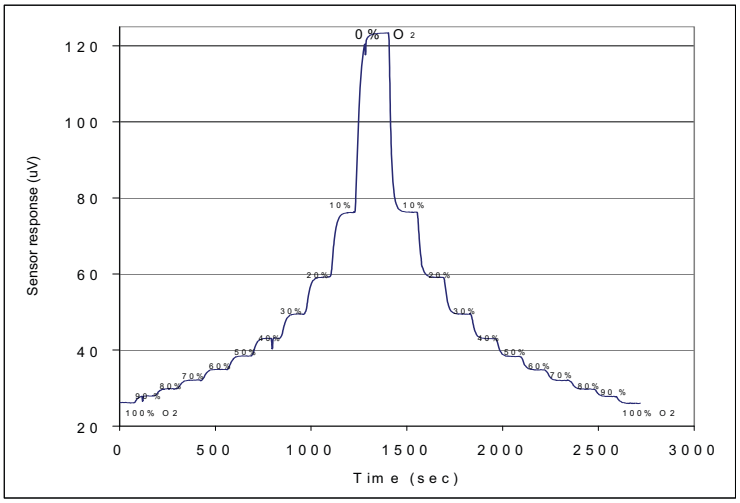


**Figure10. O2 sensor reading as a function of time when exposed to 0 to 100% O2 in N2 gas. For this application we are interested in the 0 to 25% O2 range**

## 7. CONCLUSIONS

In this paper we have explored the stringent requirements of the O2 sensor and proposed a novel frequency domain lifetime measurement system to accurately estimate the O2 gas concentration as a function of temperature and pressure for the future planned inerting fuel tanks to be used in commercial aircrafts. The various time domain , intensity based fluorescent lifetime measurements techniques have been compared with the frequency domain approaches that use resulting phase difference and amplitude modulation depth to estimate the lifetimes and concluded that it is a faster and more reliable approach. It is also shown that very simple electronics coupled to off the shelf low cost lasers/LED and PIN or APD photo detectors can be used to obtain fast and accurate temperature and O2 gas concentrations. We propose a novel lifetime measurement system that is low cost , portable, and low power that utilizes COTS components that compare very favorably to commercially available measurement systems that are bulky and expensive, and not particularly suitable for airborne applications.

We also point to the challenges of the O2 sensor development for the Fuel tank applications that has to operate reliably in the harsh jet fuel vapor and liquid phase at high atmospheric pressures. This area is still under scientific research to develop special coating material to slow the photo bleaching process to extend the lifetime of the SOL-Gel based Rhutenium sensors.

## 8. ACKNOWLEDGEMENTS

The author would like to acknowledge the help and useful discussions of the O2 sensor and various aspects of the measurement systems used in arriving and interpreting the various results during the course of the research and development phases. In particular, I would like to sincerely thank the contributions of Dr: Edgar Mendoza of Redondo Optics Inc and Dr: Mahmoud Shahriari of Ocean Optics. I am also greatly indebted to Dr: Alex A. Kazemi of Boeing for his vision and insight into the various aspects of this research and development which will greatly benefit the future safety of commercial airlines.

## 9. REFERENCES

1) Lakowicz, J. R. 1983. Principles of Fluorescence Spectroscopy. Plenum Press, New York, NY.

2) Lakowicz, J. R., I. Gryczynski, Z. Gryczynski, and M. L. Johnson. 2000. Background suppression in frequency-domain fluorometry. Analytical Biochemistry.

3) Liebsch, G., I. Klimant, B. Frank, G. Holst, and O. S. Wolfbeis. 2000. Luminescence lifetime imaging of oxygen, pH, and carbon dioxide distribution using optical sensors. Applied Spectroscopy.

4) Mills, A. and M. Thomas. 1997. Fluorescence-based thin plastic film ion-pair sensors for oxygen. Analyst. 122(1):63-68.

5) Rowe, H. M., S. P. Chan, J. N. Demas, and B. A. DeGraff. 2002. Elimination of fluorescence and scattering backgrounds in luminescence lifetime measurements using gated-phase fluorometry. Analytical Chemistry.

# Optical Engine Initiation: Multiple Compartment Applications

**Jeffrey H. Hunt**
**The Boeing Company**
**Boeing Research and Technology**
**El Segundo, CA 90009**

## Abstract

Modern day propulsion systems are used in aerospace applications for different purposes. The aerospace industry typically requires propulsion systems to operate in a rocket mode in order to drive large boost vehicles. The defense industry generally requires propulsion systems to operate in an air-breathing mode in order to drive missiles. A mixed system could use an air-breathing first stage and a rocket-mode upper stage for space access. Thus, propulsion systems can be used for high mass payloads and where the payload is dominated by the fuel/oxidizer mass being used by the propulsion system. The pulse detonation wave engine (PDWE) uses an alternative type of detonation cycle to achieve the same propulsion results. The primary component of the PDWE is the combustion chamber (or detonation tube). The PDWE represents an attractive propulsion source since its engine cycle is thermodynamically closest to that of a constant volume reaction. This characteristic leads to the inference that a maximum of the potential energy of the PDWE is put into thrust and not into flow work. Consequently, the volume must be increased. The technical community has increasingly adopted the alternative choice of increasing total volume by designing the engine to include a set of banks of smaller combustion chambers. This technique increases the complexity of the ignition subsystem because the inter-chamber timing must be considered.

Current approaches to igniting the PDWE have involved separate shock or blast wave initiators and chemical additives designed to enhance detonatibility. An optical ignition subsystem generates a series of optical pulses, where the optical pulses ignite the fuel/oxidizer mixture such that the chambers detonate in a desired order. The detonation system also has an optical transport subsystem for transporting the optical pulses from the optical ignition subsystem to the chambers. The use of optical ignition and transport provides a non-toxic, small, lightweight, precisely controlled detonation system.

**Key Words:** Optical, Engine Initiation, Multiple Compartment

- Corresponding author e-mail address: jeffrey.h.hunt@boeing.com

Photonics in the Transportation Industry: Auto to Aerospace II, edited by Alex A. Kazemi, Bernard C. Kress
Proc. of SPIE Vol. 7314, 73140E · © 2009 SPIE · CCC code: 0277-786X/09/$18 · doi: 10.1117/12.821741

# 1.0 INTRODUCTION

The role of rocket propulsion is more important than ever before. The growing constellations of orbiting communications hardware that have enabled the information superhighway are in place because of the rocket engines that powered them there. As these continue, propulsion systems will require increasing efficiency. The so-called pulse detonation wave engine (PDWE) is very attractive because its exothermic chemical reaction is designed to operate in a zero change of entropy design. Obviously, the specific impulse will be proportional to the volume. The implication is that larger volumes become necessary, complicating the construction. This can be alleviated by going to multiple chambers.

However, the initiation of this architecture becomes very tricky, because the chambers must ignite at the same time. Failure to do so will frequently lead to catastrophic mechanical imbalances during the start-up transients. Stated more deliberately, if the engines to not start simultaneously, the engine can rip itself apart.

Optical ignition has the potential to address this issue. Unlike conventional ignition systems, the delay and jitter times are in the nanosecond regime. We discuss here a review of engine ignition and discuss how optical ignition can be a viable means to start the exothermic reaction associated with propulsion systems.

Regardless of the type of engine ignition used, the same chemical pre-reaction must take place where fuel is in the presence fan oxidizing agent, be it hydrogen with molecular oxygen or JP-10 and peroxide. Each of these molecular species is stable, even in the presence of one another. So the idea is to make the chemicals unstable.

To ignite a propellant combination that is, to drive the chemical reaction the oxidizing agent must be changed into radical constituents. For molecular oxygen, this means separating the oxygen molecule into individual atoms. Molecular oxygen cannot attack the fuel and drive the reaction, but atomic oxygen can. Once an oxidizing agent has been created, only a small amount of additional energy per atom is needed to drive the reaction; that is, to make the reaction self-initiating.

Over the nearly six decades that rocket propulsion has been a practical reality, the ignition methods to do that have progressed from the primitive to the highly sophisticated. But from the hurried placement oaf burning wick arrangement below the nozzle to permanent spark igniters built into the propellant main injector, the intent has always been to start the combustion process.

Over the years, several kinds of igniters have come into use, basically through empirical methods. And always, the goal has been to break up sufficient density of the oxidizing agent so that it can attack the fuel, begin the combustion process and reach a self-sustaining condition. Since the chemical reaction is exothermic, once the burn is started, it continues without help. But if there is one similarity among current ignition techniques, it is that while most parameters are understood well enough for effective use, molecular chemical behavior has not been well addressed and each method has its shortfalls.

Spark plug ignition is the simplest and most widely used approach for liquid engines, with a spark plug built directly into the injector. Essentially a high-voltage, inductive-discharge device, the plug produces a 1O-kV arc across the propellants at a 10-Hz repetition rate. Microscopically, the plug first generates a large electric field across the spark gap. Localized ionization within the oxidizer-fuel combination occurs, allowing current to flow between the electrodes. As more ionization occurs, the resistance of the space between the electrodes drops to a point where a conductive path is created between the electrodes and the spark can form.

There is considerable ionization which occurs within this arc and there is also a certain amount of gas breakdown. When sufficient density of oxidizer constituents have been created, they can inter- act with the fuel and allow the combustion process to proceed.

Sparkers have been used for some time, so their operating characteristics are fairly well understood and they can be used to re-Eight an engine if necessary, a very important plus. But there are problems. Typically, sparkers are large and heavy and there is a considerable time lag between introduction of the spark and the ignition of the propellant mixture. Further, the oxidizer/fuel mixture ratio used when the engine is completely turned-on is not lightable with the spark. Usually, the engine has to be started in a fuel-rich condition, leading to transient pops in the ignition.

A second igniter option, pyrotechnic ignition uses a solid propellant squib of a few seconds burning duration. The solid propellant is electrically ignited and produces a hot flame within the chamber. This technique is very simple, but can be used only once (since the squib completely burns), negating the option to relight an engine.

With a third method, hypergolic or auxiliary fluid ignition, a chemical is injected with the propellants, reacting with either the fuel or oxidizer or generating a combination which is self-initiating. But, depending on the fluid used, there can be considerable time delays in ignition. There is also the additional complexity of requiring separate storage tanks and plumbing to handle the highly toxic hypergolic fluid.

## 2.0 OPTICAL IGNITION

Laser or optical ignition is a vastly different approach with much promise. Since the chemical reaction of the propellants in a rocket engine is exothermic, ignition occurs when the right amount of fuel and oxidizers is present in chemical combinations necessary to make the reaction self-initiating. This means taking a fuel/oxidizer combination and, by introducing the right amount of light energy at the correct intensity, creating the right number and density of chemical constituents to bring the reaction into a self-initiating condition.

The use of optical radiation or lasers has been used to induce chemical reactions or study their progression for some time. However, practical applications have yet to be realized. A mole of molecules contains $6x10^{23}$ molecules, while a laser pulse with a joule of energy (a large amount for a laser to produce) contains $10^{18}$ photons. Consequently, there is a 5 order of magnitude mismatch in terms of using lasers to actually drive chemical reactions.

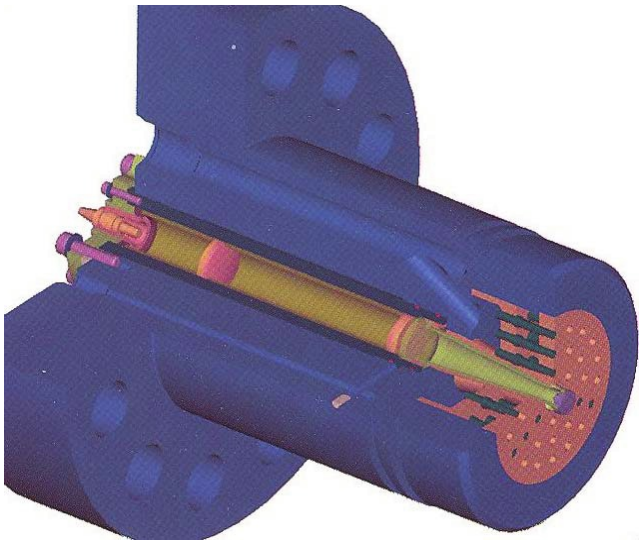

**Figure 1: Laser injection system. Laser energy enters from the left and is focused to an optic which distributes it across the fuel/oxidizer injection plate.**

However, if a chemical reaction is exothermic (it generates heat), it can be self-sustaining and the laser can be used to get it over the activation energy potential The basic precept here is to use the laser to generate enough chemical pre-reaction species to make the chemical reaction begin (and sustain itself) without any subsequent chemical assistance.

The laser is used to heat and eventually light a series of solid igniters, which, in turn, ignite the engine, somewhat like kindling for the main engine. The laser, however, never gets close to the actual propellant. In 1985, Princeton researchers used exciter lasers for the ignition of$H_2/0_2$ or $H_2$/air mixtures by photolysis of $O_2$ into O atoms. A year later, an exciter laser was operated to photolysis $O_3$ into O and $O_2$ in the presence of $CH_4$ and $H_2/0_2$. The results of each of these experiments showed that the concept works well, with the laser energy producing chemical radicals in large densities.

However, these experiments were performed in the linear absorption spectral regime of the oxidizer. This means that lasers had to be used which could produce very short laser pulses at UV wavelengths. With those requirements, the only option would be an excimer laser, which is very large, very cumbersome, and requires large amounts of electrical power and cooling.

More encouraging, however, was the work of Miziolek and Foreh in 1987. The scientists successfully demonstrated ignition in premixed $H_2/0_2$ and $H_2/N_2O$ flows with lasers operating at 225.6 nm wavelengths. This work was admittedly done with a large laboratory laser system. But the fact that the ignition process could be performed at this wavelength brought the use of optical ignition much closer to engine implementation.

The optical process starts with an optical source, a laser. The laser light must be brought from the source to the region where it is needed, requiring a number of optical elements. The laser light interacts with the propellants to couple the optical energy into the mixture. And finally, the molecular-optical interaction creates products capable of driving the reaction.

A major advantage of optical ignition is its ability to locate the laser remotely from the engine propellant and to couple the light energy into the reaction chamber, ideally through the use fan optical fiber. There, the frequency of incoming laser light is made to coincide with a material resonance so that the material absorbs the light and transfers its energy into internal energy.

But there can be problems. Just as mechanical systems have nonlinear responses when they are driven hard, so, too, do optical systems. In an optical context, driven hard means that the incoming light has a high peak power, on the order oaf $MW/cm^2$. At those levels, the medium can absorb two photons of light as if it were one. Of course, since the absorption is nonlinear, the interaction will be much weaker than the linear case. Nevertheless, with a high enough intensity, reasonable amounts of power can be absorbed by the medium in question.

A straightforward calculation shows that for intensities on the order oaf few $MW/cm^2$ (not difficult to produce), absorption coefficients on the order oaf few percent per centimeter are possible. Also, unlike the linear case, which is independent of the intensity, the absorption coefficient can be made higher by using higher intensity.

In fact, the coefficient is proportional to the intensity of the incoming laser beam which will prove useful when designing the optical coupling into the propellant materials.

In our tests, the effort was configured to use a laser system for the ignition oaf multiple coaxial element injector. Also at that time, there was interest in igniting and operating gas generators at low-mixture ratios because of the heat loads normal- ly created by the turbomachinery. But that meant operating below the flammability limit, implying that ignition by standard techniques would, at best, work poorly and possibly not at all.

Specifically, standard ignition under these conditions would result in un-ignited injector zones, causing ignition delays and combustion pops from sudden ignition propellant mixtures accumulated inside the chamber. By contrast, one of the potential advantages of using a laser for direct ignition of high velocity propellants is that individual-element ignition assures even flame distribution, thus eliminating combustion pops.

The main objective here was to duplicate the laser ignition process and then extend it to the ignition faulty-element coaxial elements at low chamber mixture ratios specifically, high-velocity $H_2/0_2$ propellants at simulated gas generator conditions. These tests were to be conducted at a variety of mixture ratios, even outside the flammability limit.

During a conventional spark ignition, propellant velocities are kept high to allow for ignition downstream or below the ion post tip where the propellant is delivered to the combustion chamber. At high mixture ratios (>1.0), the first element in the series ignites, detonating the propellants in the chamber and halting the propellant flow. Random turbulence occurring in the combustor is sometimes sufficient to force the single ignited element to cross-flow onto the element next to it, lighting it.

This detonation process never occurred during the optical ignition process. It was found, rather, that multiple-element ignition is not dependent on chamber mixture ratio,

concurring with the ignition theory that UV laser ignition is a function of laser intensity and positioning rather than mixture ratio.

In conventional spark ignition, all the propellants in the chamber are ignited, so the flame holding zone is optical ignition by default. Since the laser has the ability to place the energy exactly where it is needed, the alignment is established to position the laser spot in the flame holding zone. As long as the laser was placed at the point of flame holding, the ignition process was unaffected by the mixture ratio. In fact, at very low mixture ratios ($< 0.4$) the ignition delay time was minimal. This is in sharp contrast to spark ignition where mixture ratios of this level would result in long ignition delay or no ignition at all.

Multi-element ignition of the injector was achieved consistently. Ignition of the coaxial elements was achieved at chamber mixture ratios of 0.4 and as low as 0.1. This testing established laser ignition as a viable solution to flame propagation and multi-element ignition of low mixture ratio.

After the successful series of tests at the field labs, there were still a few steps to go before reaching a really useful ignition device. The experiments had demonstrated a resonant enhancement in the activity of the oxidizer, but measurements showed that the enhancement was not necessary for optical ignition implementation. Simulations that showed once the oxygen molecules were dissociated into atoms, very optical additional energy was needed to make the reaction self- initiating. Put in a more generic context, the data showed that it was possible to take an extremely reactive chemical mixture and make it still more reactive. Connecting this specific resonance with an existing laser, however, was another matter.

We undertook a series of laboratory experiments to understand the nature of the optical breakdown when the laser is focused to a very high intensity. In these experiments, we focused laser light to a small spot (10 micron diameter) and allowed the oxygen molecules to be broken apart, which then prompted the question regarding the exact nature of the breakdown. Specifically, we wanted to know what was in the excited state after the laser pulse generated the breakdown. It was found that most of the breakdown product was ionized molecular oxygen. This would be of only academic interest, were it not for the fact that we were driving a chemical reaction.

These experiments, although not ignition tests in themselves, were important for two reasons: First, they demonstrated that the laser pulse could generate substantial amounts of atomic oxygen. The nature of energy considerations in the breakdown was such that the oxygen atoms generated had enough internal energy to drive the $O_2/H_2$ mixture into a self-initiating condition. In other words, when the oxygen molecules fell apart, they were already in a condition where they could initiate the propellant reaction, even in the presence of molecular hydrogen. Second, the ultraviolet wavelength was chosen not because it was in resonance with any of the propellant absorptions, but because it was easily produced by existing solid state lasers.

Obviously, it was important to design and implement hardware that was as close as possible to a real design. This meant that we had to create a design that could receive the laser energy and couple it into the reaction volume. The light would have to be directed to the flame

holding zones within the particular injector design chosen and the optical elements would have to operate in the less-than-optimum environment present in a propulsion chamber.

Once the optical elements had been specified, it was decided to go with three concentric annular injectors. Tests had shown that it was important to get the optical energy to the flame holding zones in an area where the oxidizer/fuel combinations were at optimum mixture. In order to create a smooth ignition, we wanted to light three symmetrical points on the injector face, requiring that the laser energy be divided equally and that each f1ame holding zone receive the same intensity. In order to split the energy into three equal amounts and turn the corner to the injector face, a special optic was designed a three-sided pyramid, with each side at 45 degrees to the pyramid base. After passing the pyramid, the beam is aligned to pass over three injector holes, lined up at 12, 4 and 8 o'clock. Since we wanted to have the posts light simultaneously, we designed the focus to occur at the second post.

The optical ignition tests were successful. In each case, laser intensities on the order of a few $MW/cm^2$ were sufficient to initiate propulsion. Optical ignition now has real potential for use on the linear aerospike and other propulsion areas.

## 3.0 CONCLUSION

As currently envisioned, future propulsion systems will carry multiple compartment engines with many thrusters. Because of the uncertainty in the ignition delay with a sparker and the fact that the compartments must be started simultaneously that method is unacceptable. In fact, the only usable existing ignition source is a combustion wave detonator, but it too brings problems in amounts of plumbing, with the associated weight and complexity.

Optical ignition, however, alleviates these problems. Among virtues already described, only a single laser would be needed to provide the ignition source to each of the compartments. An optical fiber could be routed through the system without the constraints associated with the combustion wave propagation. And since optical ignition, by nature, provides very short ignition delay times, the compartments would start simultaneously.

Other applications might be in the realm of hypersonic craft where propellants speed through the combustion chamber at incredible velocities. The big plus here is that light, no matter how fast the propellants are moving, will always move much faster. Consequently, the laser will always see the propellants in a mechanically static flow situation.

Optical ignition could also be an excellent choice in the broad area of non- toxic propellants. Single-stage vehicles are being investigated to perform various missions and the deployment of many payload types. Popup upper stages conceptually could expand the optical ignition of advanced spacecraft, allowing for wider ranges of payload deployment. Performing the spacecraft delivery mission requires the use of an upper stage which has high ignition, is operationally safe, and can be effectively packaged (along with the spacecraft) within smaller payload bay volumes. Optical ignition could be used here to good effect.

## 4.0 RERERENCES


1. A.W. Miziolek and B. E. Forch, Combustion Science and Technology **52**, p. 151, 1987.
2. D.R. Cohn, M.P.Hacker, B. Lax, W.J. Halverson, Appl. Phys, Letts, **46**, p.668, 1988.
3. A.W. Miziolek and B. E. Forch, Opt. Lett **11**, p. 129, 1987.
4. J. E. Goldsmith, J. Chem. Phys. **78**, p, 1610, 1983.
5. M. C. Grey, Rep, Prog, Phys, **38**, p. 621, 1975.
6. M. Lavid and J.G. Stevens, Combustion and Flame **60**, p.195, 1985.
7. J. R. McDonald, A.P. Baranovski, V.M. Donnely, Chem. Phys. **33**, p.161, 1978.

# The exploitation of thin film coatings for fibre sensors for the application of chemical sensing

T. Allsop, R. Neal, K. Kalli ,E. Davies, S. Rehman, R. R.J. Maier, J. Barton, D.J. Webb, J.D. Jones I. Bennion

T.Allsop
t.d.p.allsop@aston.ac.uk, Photonics Research Group, Aston University, Aston Triangle, Birmingham, B4 7ET, UK.
R. Neal
R.Neal@plymouth.ac.uk, Dept of Communications and Electrical Engineering, Facility of Technology, University of Plymouth, Plymouth, PL4 8AA, U.K.
K. Kalli
kkalli@cytanet.com.cy, Cyprus University of Technology, Department of Electrical Engineering and Information Technology, 31 Archbishop Kyprianos, Lemessos 3036, Cyprus
E. M. Davies,
daviesem@aston.ac.uk, Photonics Research Group, Aston University, Aston Triangle, Birmingham, B4 7ET, UK.
S. Rehman
s.s.rehman@usa.net, STR Fiber Technologies, United Kingdom.
R. R. J. Maier,
R.R.J.Maier@hw.ac.uk, Heriot Watt University, School of EPS, Edinburgh EH14 4AS, UK
J. Barton
j.s.barton@hw.ac.uk, Heriot Watt University, School of EPS, Edinburgh EH14 4AS, UK
J.D. Jones
j.jones@hw.ac.uk, Heriot Watt University, School of EPS, Edinburgh EH14 4AS, UK
D.J. Webb
d.j.webb@aston.ac.uk , Photonics Research Group, Aston University, Aston Triangle, Birmingham, B4 7ET, UK.
I. Bennion
i.bennion@aston.ac.uk , Photonics Research Group, Aston University, Aston Triangle, Birmingham, B4 7ET, UK.

## ABSTRACT

We report on the use of thin film coatings, both single and multi-layered, deposited on the flat side of a lapped, D-shaped fibre to enhance the sensitivity of two kinds of surface plasmon resonance based optical fibre sensors. The first kind involves the use of a tilted Bragg grating inscribed within the fibre core, prior to fibre coating, while the second relies on a surface relief grating photoinscribed after the fibre has been coated. Some of the devices operate in air with high coupling efficiency in excess of 40dB and an estimated index sensitivity of $\Delta\lambda/\Delta n$ = 90nm from 1 to 1.15 index range showing potential for gas sensing. Other sensors produced index sensitivities ($\Delta\lambda/\Delta n$) ranging from 6790nm to 12500nm in the aqueous index regime. The materials used for these fibre optical devices are germanium, silica, silver, gold and palladium.

Keywords: Index Sensing, Coatings, gratings, surface plasmon resonances

Photonics in the Transportation Industry: Auto to Aerospace II, edited by Alex A. Kazemi, Bernard C. Kress
Proc. of SPIE Vol. 7314, 73140F · © 2009 SPIE · CCC code: 0277-786X/09/$18 · doi: 10.1117/12.821112

## 1. INTRODUCTION

There has been a strong interest in recent years in using gratings in fibres to produce chemical sensors, including long period gratings (LPGs) [1, 2, 3], fibre Bragg gratings (FBGs) and tilted fibre Bragg gratings (TFBGs). At present the majority of these sensors are used to detect the heavier organic/inorganic compounds, such as detection of organic aromatic compounds in paraffin [3]. Whilst the index of sensitivity of most grating based devices is highest for solutions that have an index of approximately 1.44, which is good for various organic hydrocarbon compounds, there is a need to increase sensitivity of these devices to aqueous solutions for biochemical applications, where index values typically range from 1.333 to 1.380 (aqueous index regime); for example, the effective index of a cell is about 1.36 to 1.38 [4,5]. Such sensors would also be appropriate for the detection of the lighter hydrocarbon compounds used for Aviation fuel [6] and if their response could be enhanced at even lower refractive indices, for gas detection. Another type of sensor based upon surface plasmon resonance (SPR) is showing the potential to yield high index sensitivities. Surface plasmon resonance is an important optical phenomenon that involves a resonant transfer of the incident light energy to a surface-plasmon (SP) mode in the form of collective electron oscillations in a metal [7]. The plasmons exist at a metal–dielectric interface and obey the following dispersion relation for two homogeneous semi-infinite media [8]:

$$\beta = k\sqrt{\left(\frac{\varepsilon_m \cdot n_s^{\,2}}{\varepsilon_m + n_s^{\,2}}\right)} \qquad (1)$$

where k is the free space wave number, $\varepsilon_m$ is the dielectric constant of the metal ($\varepsilon_m = \varepsilon_{mr} + i\,\varepsilon_{mi}$) and $n_s$ is the refractive index of the dielectric.

The need for high sensitivity at low indices is being addressed with the use of tilted Bragg gratings to assist in the generation of surface plasmon resonances in a fibre configuration [9, 10]. There is very little published with regards to multi-layered thin film SPR fibre devices, and the majority of these papers, such as [11] and [12], address the SP's optical properties and not their sensing potential.

In this paper, we report on two novel SPR fibre devices whose spectral sensitivities can be modified by using various coatings, in either single or multiple layers. A general observation of these devices is that they have polarisation dependence; the spectral location of maximum coupling to the SPR is highly dependent upon the polarisation state of the illuminating light and can be tuned from 1100nm to 1700nm.

Firstly, we describe a fibre device utilising a TFBG to enhance the coupling of the illuminating light to a SP generated on a coated, lapped single mode fibre [9,10]. It was observed that the spectral location of maximum coupling to the SPR was highly dependent upon the polarisation state of the illuminating light and could be tuned from 1100nm to 1700nm, thus producing various SP probe depths, dependent upon the polarisation. It was found that for a device that is still to be fully optimised, the maximum spectral index sensitivity ($d\lambda/dn$) was 3365 nm for the index range 1.335 to 1.370 with coupling strength in excess of 25dBs.

Secondly, we describe a fibre device based upon a surface relief grating-type structure inscribed with UV light into a multi-layered thin film deposited on the flat side of a lapped, D-shaped fibre. The single layered devices were fabricated from germanium, while the multilayered ones comprised layers of germanium, silica, silver and gold. Some of the devices operated in air with high coupling efficiency in excess of 40dB and an estimated index sensitivity of $\Delta\lambda/\Delta n$ = 90nm from 1 to 1.15 index range while others provided an index sensitivity of $\Delta\lambda/\Delta n$ = 12500nm for refractive indices from 1.33 to 1.39.

## 2. FABRICATION AND CHARACTERISATION

The fabrication of the first type of SPR fibre device begins with the inscription of a grating in a UV photosensitive single mode fibre (hydrogenated standard telecommunications fibre) using a uniform phase mask (mask period = 1.0157μm) mounted on a goniometer, tilted to a specific angle. Labels are added to indicate the orientation of the tilted grating. Next, the fibre is lapped down to 10μm from the core-cladding interface; it has been estimated that the error associated with this lapping is approximately ±1 μm. The labels on the fibre are used to indicate which region of cladding is to be removed so that the grating vector, the fibre axis and the normal to the lapped surface all lie in a plane. Thirdly, the flat of the lapped fibre is then coated with either gold or silver layer with a thickness of 38nm and 35nm respectively, using a sputter machine and mask.

The second type of SPR device is fabricated by firstly mechanically lapping a standard SMF fibre down to 10μm from the core-cladding interface. Secondly, using RF sputtering, a series of coatings are deposited upon the flat of

the lapped fibre. These coatings consisted of various numbers of layers and materials used such as germanium, silicon dioxide, silver and gold as described below. Thirdly, the coated fibre was exposed to a UV light interference pattern produced by a uniform phase mask with period 1.018μm through laser beam scanning and multi-exposure. This produced a surface relief structure which has dominant spatial periods of ~0.5μm and ~1μm. A series of fibre devices were investigated that consisted of various coatings with the two coupling mechanism that produce the surface plasmon resonances, see table 1.

**Table 1** Materials and their thickness used in the fabrication of SPR fibre devices

| Sensor Type | Materials used in the construction | 1st layer | 2nd layer | 3rd layer | |
|---|---|---|---|---|---|
| | | Germanium nm | Silica nm | Silver nm | Gold nm |
| UV grating inscribed in the fibre core | Device Ag Tilted | - | - | 35 | - |
| | Device Au Tilted | - | - | - | 38 |
| | Device Au Tilted | 48 | 48 | - | 32 |
| UV post processed coating | Device Ge overlay | 48 | - | - | - |
| | Device $SiO_2$ overlay | 48 | 48 | - | - |
| | Device Ag overlay | 48 | 48 | 32 | - |
| | Device Au overlay | 48 | 48 | - | 32 |

The rationale for using these materials is in two parts. The first concerns the optical constants of the materials and the requirement that their dispersion relationships must allow coupling to surface plasmons at a metal–dielectric or semiconductor-dielectric interface; both Ge and Ag exhibit this behaviour. Secondly, Ge and $SiO_2$ layers are used due to the fact that it is known from studies of grating formation [12] that when exposed to UV light, Ge/GeO produces photo-bleaching and compaction of the material, thus producing a surface corrugation on the multi-layered structure.

Prior to UV processing the polarisation dependence had been investigated and a small variation in the overall transmitted optical power with polarisation was found. After UV exposure the devices were further characterised by observing the spectrum of the transmitted light as the azimuth of the polarisation state was changed. These devices now showed a significant variation with polarisation, which is discussed in reference 10. To do this characterisation, light from a broadband light source was passed through a polariser and a polarisation controller before illumination of the sample, with the transmission spectra being monitored using an optical spectrum analyser (accuracy of 0.005nm). The change in polarisation of the illuminating light was monitored with a polarimeter (Tektronix, PAT 9000B) via a polarisation maintaining coupler, see figure 1.

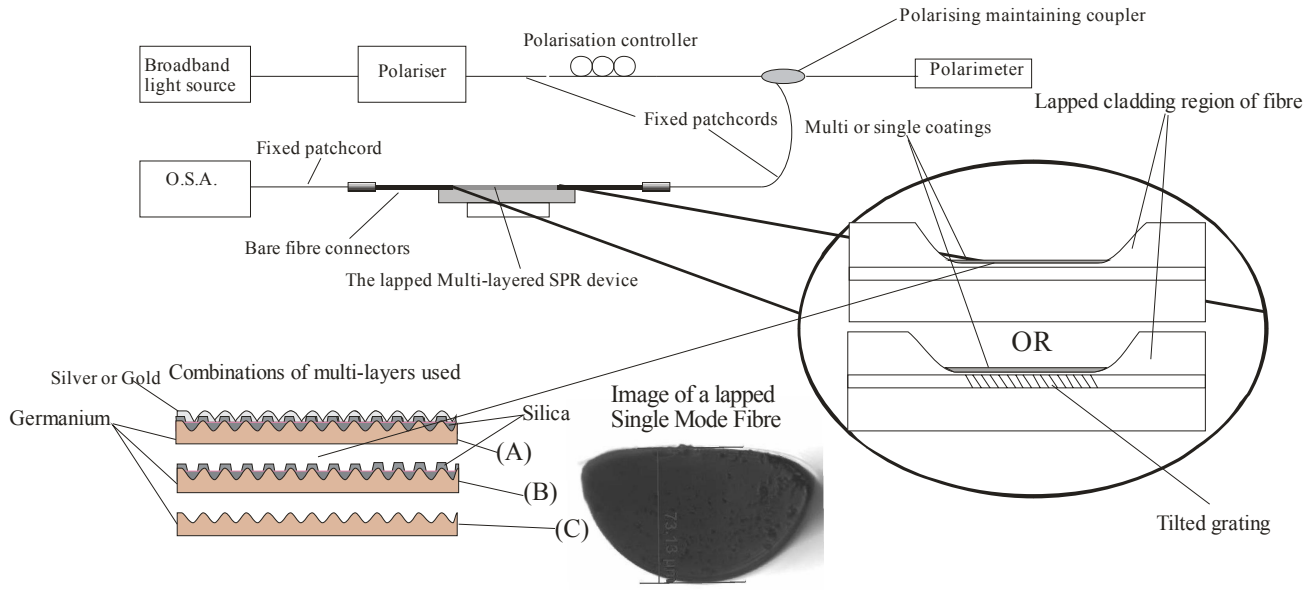


**Figure 1.** Scheme used for the characterisation of the lapped and multi or single-layer coated fibre devices; typical examples of combinations of layers used in the samples (A) Ge-$SiO_2$-(Ag or Au), (B) Ge-$SiO_2$, (C) Ge; a typical cross-section of the devices.

All the fibre devices showed polarisation dependence but the spectral responses differed between the two types of devices. Firstly, the tilted Bragg grating devices could be tuned and produced large extinction ratios over a very wide wavelength range; this occurred for either single or multi-layered coatings, see figure 2.

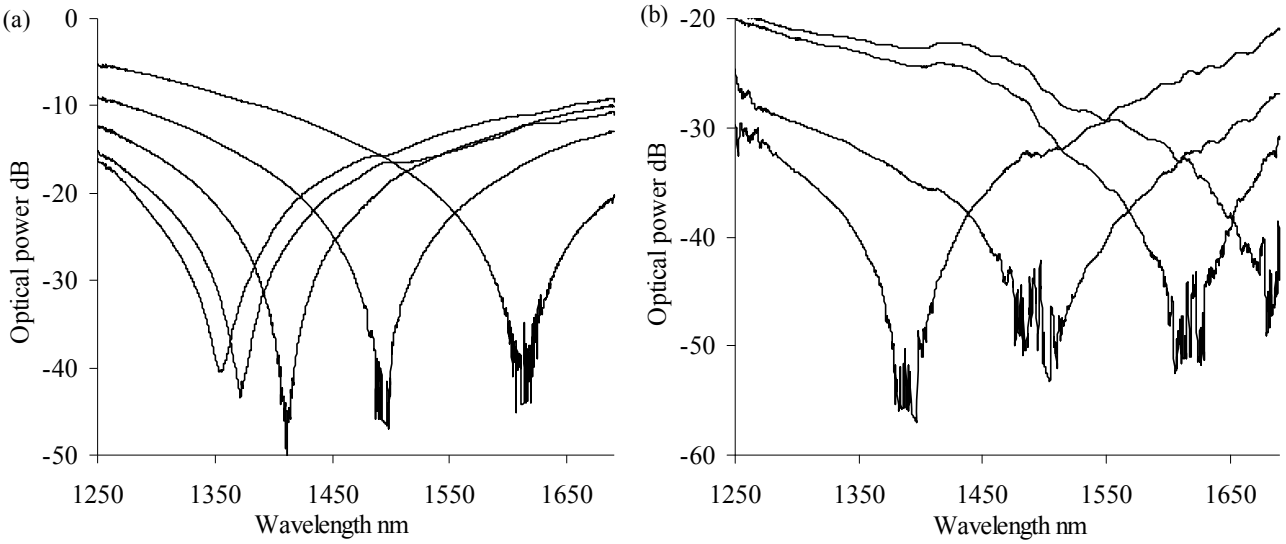


**Figure 2** Evidence of surface plasmon resonances obtained at different wavelengths by varying the polarisation of the illuminating light on one device, (a) Au-TFBG, (b) Au-$SiO_2$-Ge-TFBG. Both devices had a 7 degree tilt angle and were submerged in a medium with a refractive index of 1.36.

Varying the polarisation for the surface relief type SPR fibre devices produced two resonances over the observed wavelength range, see figure 3.

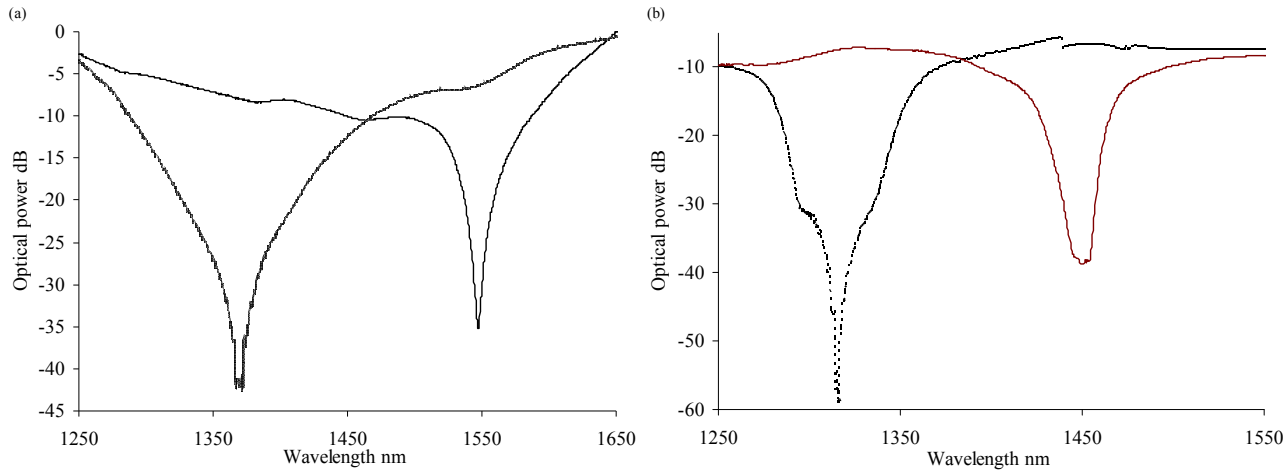


**Figure 3** Transmission spectra of the Ge-$SiO_2$-Ag (a) and Ge-$SiO_2$ (b) coated fibre devices surrounded by air for two polarisation states of the illuminating light

It was also observed that polarisation sensitivity varied from device to device investigated, figure 4 and figure 5 show typical examples of the sensitivities of these devices

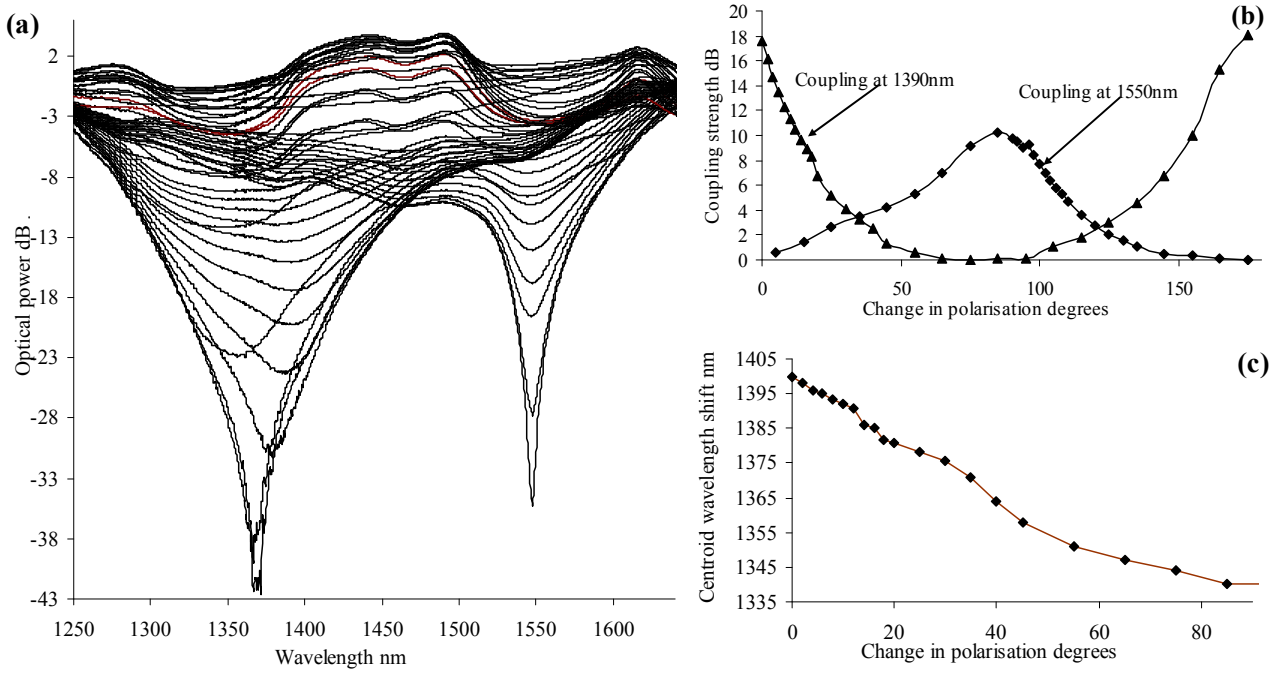


**Figure 4** (a) Transmission spectra of the Ge-$SiO_2$-Ag coated surface relief fibre device as a function of changing polarisation from maximum coupling in air. (b) The coupling efficiency of the resonances at 1390nm and 1550nm and (c) the wavelength shift of the coupling feature at 1390nm as the azimuth of polarisation of the illuminating light is changed from the position providing maximum coupling.

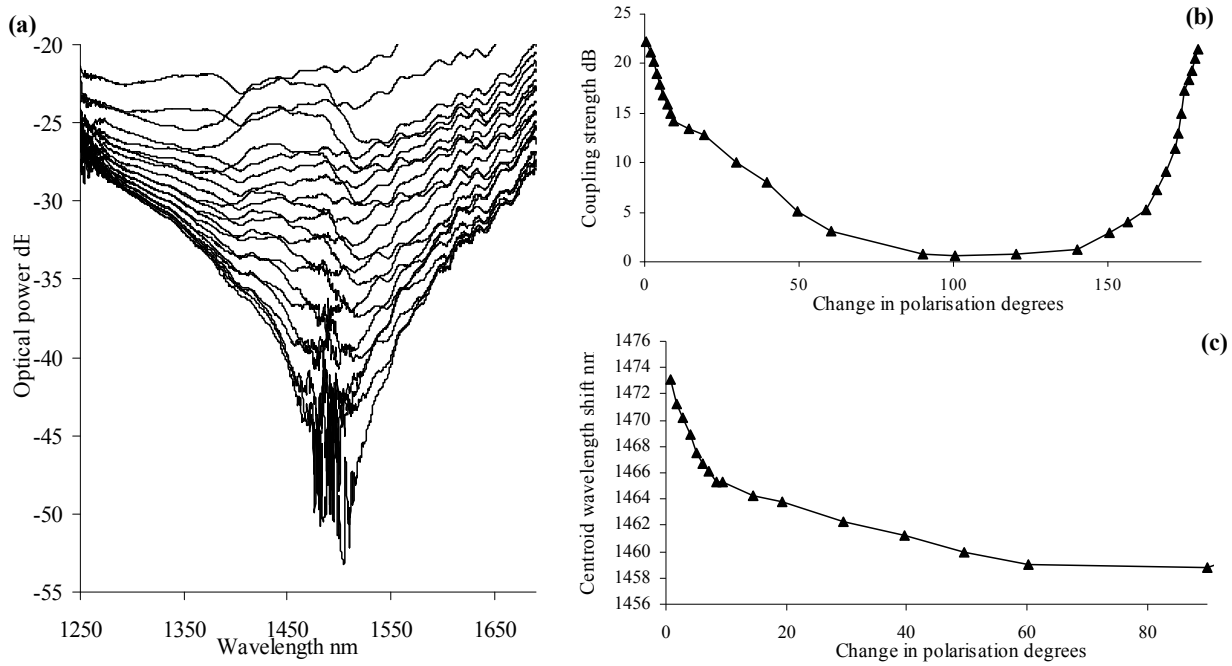


**Figure 5** (a) Transmission spectra of the Ge-$SiO_2$-Au coated tilted Bragg fibre device as a function of changing polarisation from maximum coupling with a surrounding medium of 1.36. (b) The coupling efficiency of the resonance at 1480nm and (c) the wavelength shift of the coupling feature at 1480nm as the azimuth of polarisation of the illuminating light is changed from the position providing maximum coupling

We are mostly interested in the potential of these SPR devices for chemical and biochemical sensing applications using wavelength and intensity interrogation. Whilst it may seem that the polarisation sensitivity of theses SPR devices may be problematic, this can potentially be overcome by using polarisation maintaining fibre [13], or can be seen as another spectral property to be exploited. A detection scheme that does exploit this behaviour is angular interrogation [14]. Inspecting the transmission spectra in figures 2 and 5, there is no significant observed spectral feature associated with Bragg reflection from the gratings themselves. This is expected due to the fact their transmission profiles are very weak and that the interrogating light source is broadband and swamps the response.

## 3. REFRACTIVE INDEX SENSITIVITY

For refractive index sensitivity measurements the devices were placed in a V-groove and immersed in certified refractive index (CRI) liquids (supplied by Cargille laboratories Inc.) which have a quoted accuracy of ±0.0002. The devices and V-groove were carefully cleaned, washed in ethanol, then in deionised water and finally dried before immersion into the next CRI liquid. The V-groove was made in an aluminium plate, machined flat to minimise bending of the fibre. The plate was placed on an optical table, which acted as a heat sink to maintain a constant temperature. The V-groove was used in conjunction with the apparatus shown in figure 1. Figures 6 to 9 show some typical spectral index sensitivities measured for the devices.

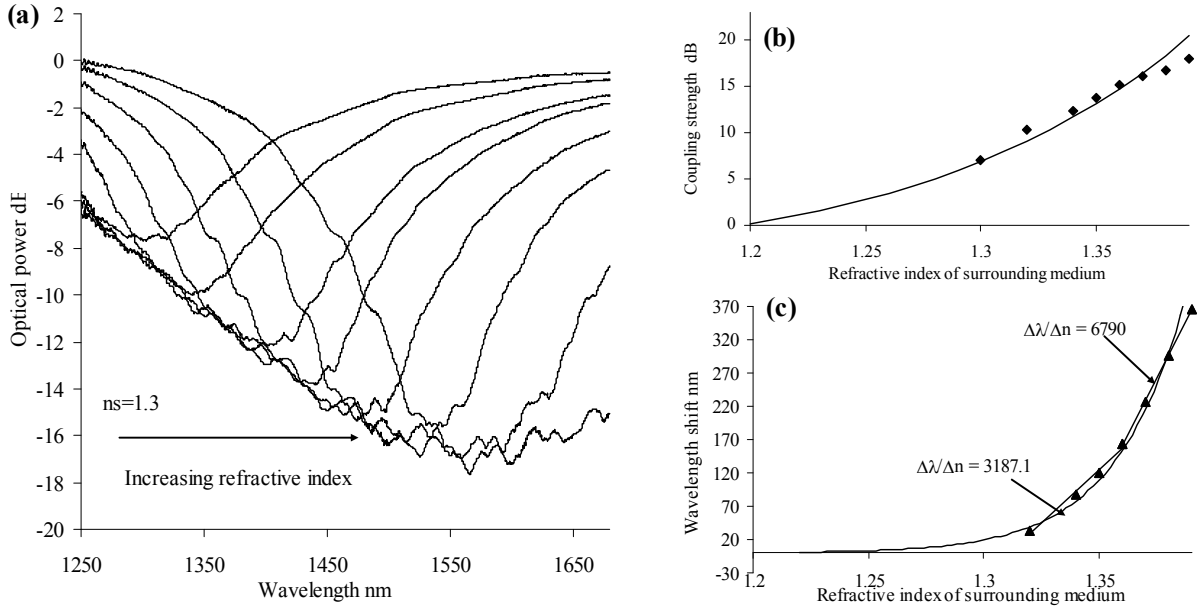


**Figure 6**. (a) Transmission spectra of the Ge coated surface relief device as a function of refractive index (polarisation of the illuminating light chosen to maximise coupling at index 1.3). (b) Coupling strength and (c) Wavelength shift of the resonance as a function of refractive index.

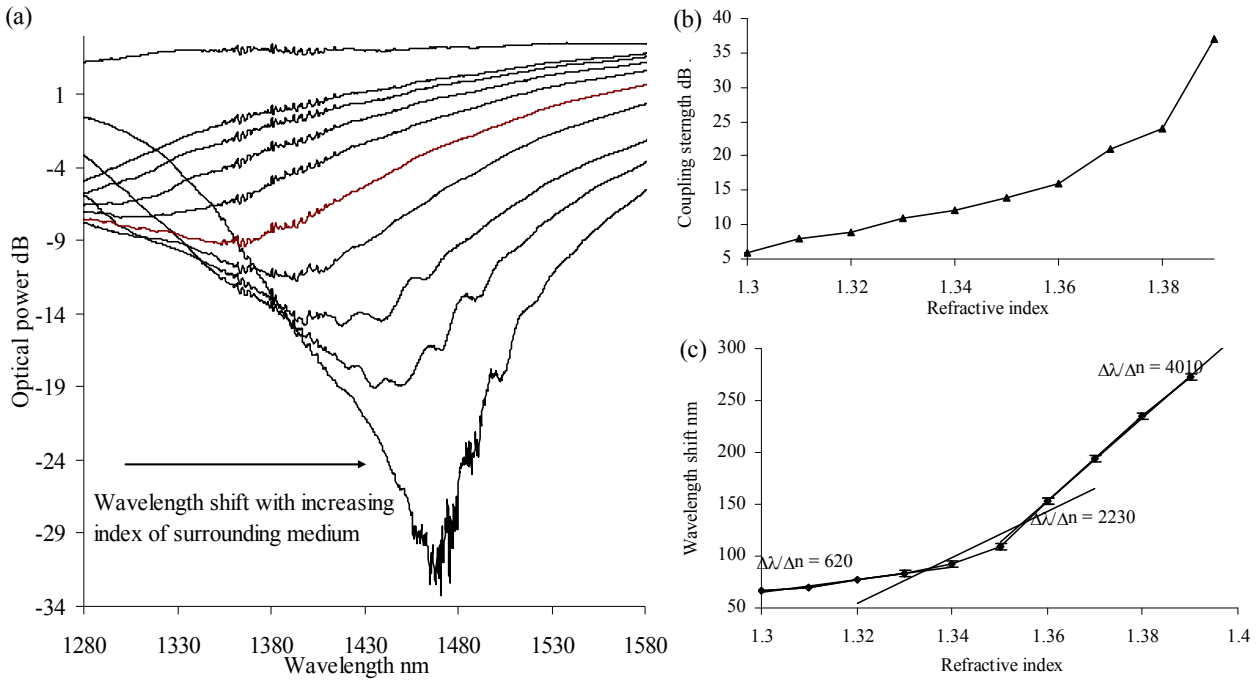


**Figure 7** (a) Transmission spectra of the Ge-$SiO_2$-Au coated surface relief device as a function of refractive index (polarisation of the illuminating light chosen to maximise coupling at index 1.36). (b) Coupling strength and (c) Wavelength shift of the resonance as a function of refractive index.

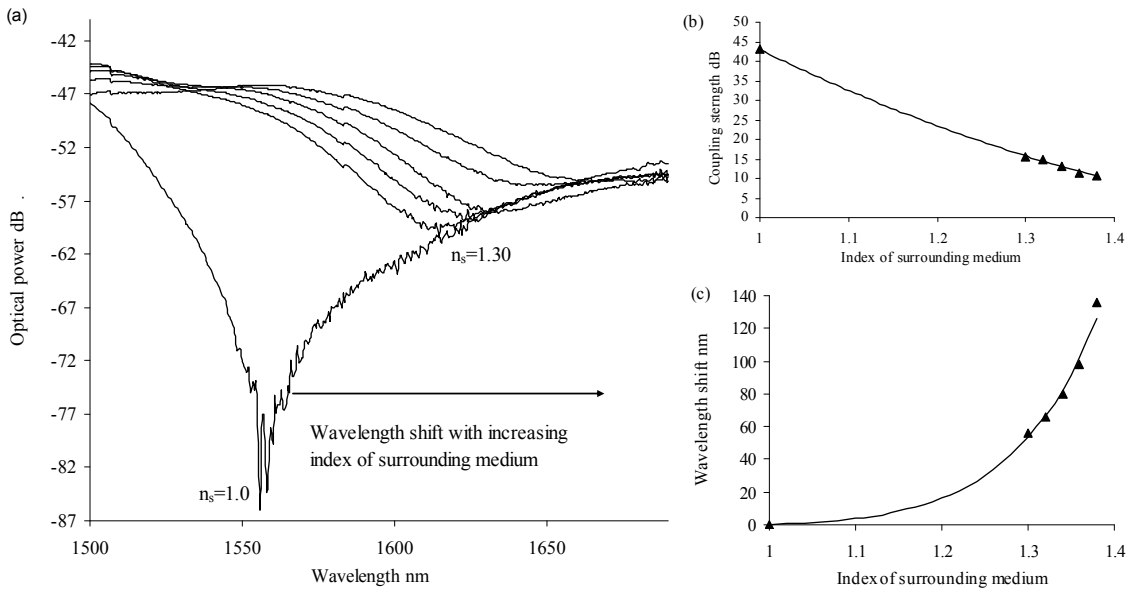


**Figure 8** (a) Transmission spectra of the Ge-$SiO_2$-Ag coated surface relief device as a function of refractive index (polarisation of the illuminating light chosen to maximise coupling at index 1.36). (b) Coupling strength and (c) Wavelength shift of the resonance as a function of refractive index.

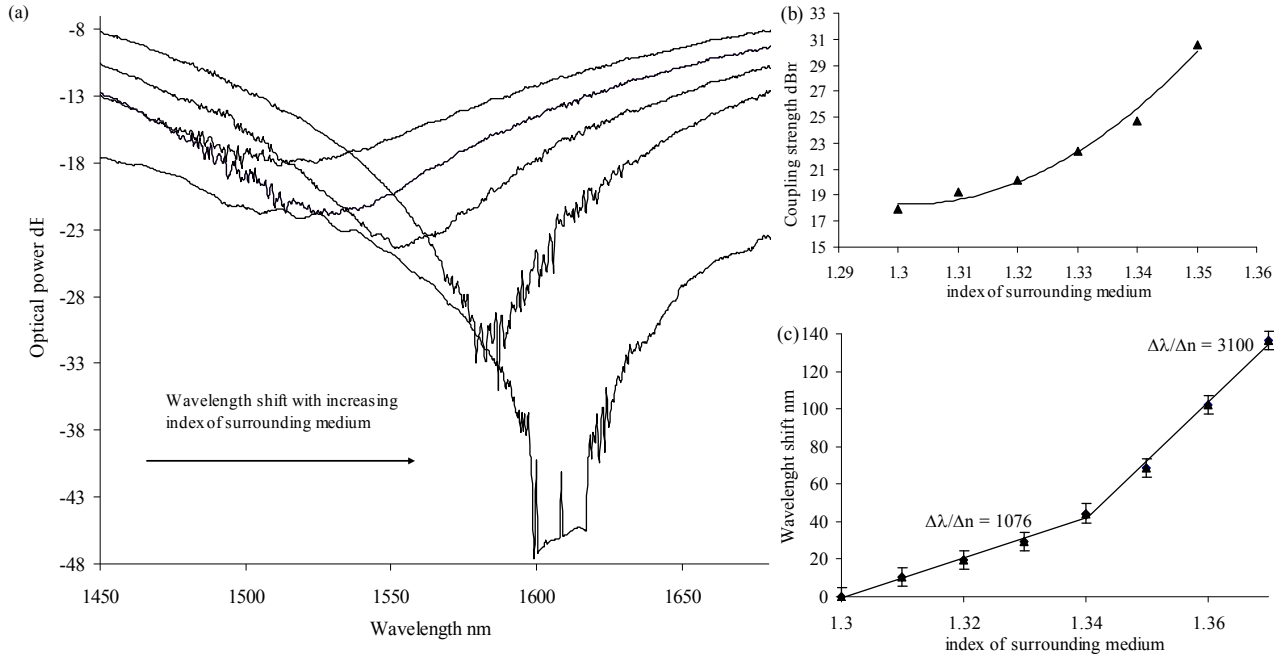


**Figure 9** (a) Transmission spectra of the Ag coated tilted Bragg device (7 degrees) as a function of refractive index (polarisation of the illuminating light chosen to maximise coupling at index 1.36). (b) Coupling strength and (c) Wavelength shift of the resonance as a function of refractive index.

The highest wavelength spectral sensitivity to index was obtained with the Ge coating, which provided $\Delta\lambda/\Delta n$ ranging from 3200 nm to 12500nm, see figure 6. Some the devices exhibited strong coupling in air such as the Ge-$SiO_2$-Ag surface relief device which shows a decrease in coupling strength with increase in index, varying from 40dB in air to 7dB with a surrounding index of 1.39 and having a spectral sensitivity ranging from 710nm to 1200nm in the aqueous regime. The Ge-$SiO_2$-Au surface relief device gave index sensitivities ranging from 2000nm to 4500nm with increasing

coupling strength from no coupling to 37dB. Considering the low index regime ranging from 1 to 1.15, the gold overlay fibre showed no coupling but the Ge-$SiO_2$-Ag and Ge-$SiO_2$ gave promising results with wavelength shifts of 90nm and 40nm along with 30dB and 17dB changes in optical coupling from index 1 (air) to 1.3, respectively. The differently configured SPR devices yielded different responses for various index regimes results with some out-performing others for a given index range. This behaviour is expected due to the different dispersion relationships for each of the materials used in the coatings along with how the surface plasmons are supported by the different physical structures of the coatings.

To obtain an estimate of the spectral sensitivity of these SPR devices for low refractive indices from 1 to 1.1 we use the approach given in REF 15, which is to calculate the propagating modes of a D-shaped fibre with coating using a conformal mapping technique and then implement Fresnel's equations for a four layered system. The optical constants used in Fresnel's equations were estimated by an effective medium approximation, the Maxwell-Garnett theory [16], which yields an effective dielectric function as a function of the fractional volume of the metal/semi-conductor within an effective layer. In this work the effective change of the surrounding index is determined within a sensing volume, which is the area of the coating multiplied by the spatial extension of the evanescent field associated with the surface plasmon perpendicular to the coating's surface; a more detailed description is given in REF 6 and REF 11.

The experimental and theoretical results for wavelength and optical power spectral sensitivities are combined and shown in figures 10 and 11. These results are compared to a long period grating with a period of 240μm and a length of 5cm inscribed into standard single mode telecoms fibre. To attach any worth to these fibre sensors, their performance has to be compared to other sensor types in terms of wavelength shift (spectral sensitivity) and coupling strength variation (intensity sensitivity) as a function of index change. These results suggest the devices have potential in the low index regime and should demonstrate dramatic improvement in sensitivity/performance over LPG fibre devices in the aqueous index regime.

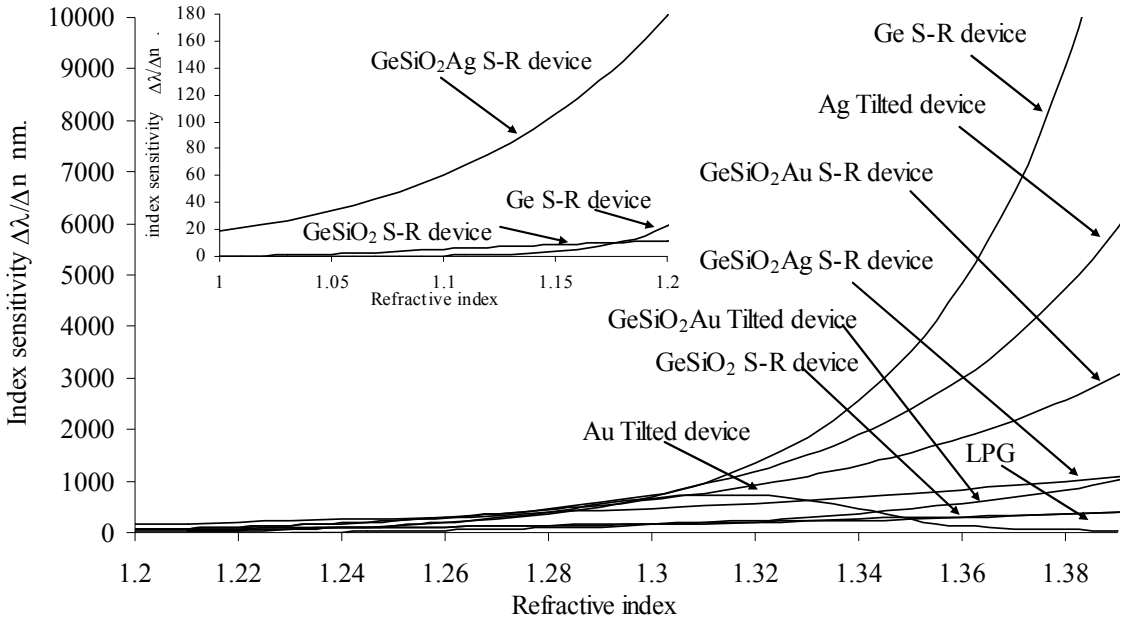


**Figure 10** Simulated and experimental wavelength spectral sensitivity comparison of some of the coated fibre devices (Tilted devices; SPR fibre devices that have a tilted Bragg grating written into the core of the fibre, S-R devices; SPR fibre devices with a surface-relief corrugation of the fibre coatings) as a function of refractive index along with a long period grating (period = 240μm, length 5cm).

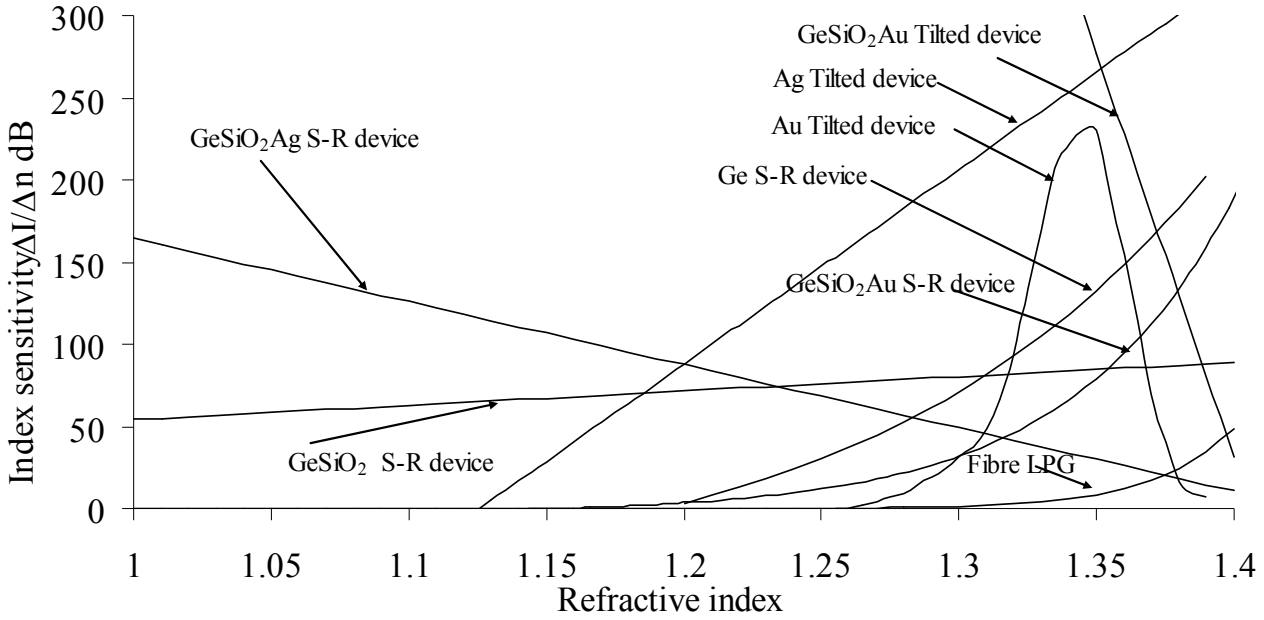


**Figure 11** Simulated and experimental optical power sensitivity comparison of some of the coated fibre devices (Tilted devices; SPR fibre devices that have a tilted Bragg grating written into the core of the fibre, S-R devices; SPR fibre devices with a surface-relief corrugation of the fibre coatings) as a function of refractive index along with a long period grating (period = 240μm, length 5cm).

## 4. CONCLUSION

We have investigated two types of surface plasmon resonance fibre devices with coupling mechanisms based upon either tilted fibre Bragg gratings or a surface relief structuring of the coating itself produced by ultra-violet exposure through a conventional fibre phase mask. The coatings used were both single and multi-layered thin films deposited on the flat side of a lapped D-shaped fibre. The various devices yielded different index sensitivities, with the single Ge coated device possessing the highest sensitivity in the aqueous regime while evidence suggests that the Ge-$SiO_2$-Ag coated device should be the most sensitive at low indices, both devices outperforming LPGs in these regimes. Some of the SPR devices have high coupling efficiency in excess of 40dB in air and the Ge-$SiO_2$-Ag coated device possessed an estimated index spectral sensitivity of $\Delta\lambda/\Delta n$ = 90nm and a coupling strength sensitivity of $\Delta I/\Delta n$ = 165dB in the index range from 1 to 1.15. A device with a single layer of Ge demonstrated an index spectral sensitivity of $\Delta\lambda/\Delta n$ = 12500 nm over the index range of 1.36 to 1.39 with higher sensitivities obtained at higher indices.

### References

[1] S. Vasilev et al, "Long-period refractive index fibre gratings: properties, applications and fabrication techniques", Proc. SPIE 4083, pp.212-223, 2000.
[2] R.P. Espindola, R. Windeler, A. Abramov, B. Eggleton, T. Strasser, D. DiGiovanni, "External refractive index insensitive air-clad long period fibre grating", Electron. Lett., vol.35, no.4, 327-328 1999.
[3] T. Allsop et al, " Detection of Organic Aromatic compounds in Paraffin by a long period fiber grating optical sensor with optimised sensitivity", Opt. Commun. ,vol 191, pp181,2001.
4 A. Dunn and R. Richards-Kortum, "Three-dimensional computation of light scattering from cells," IEEE J. Sel. Top. Quantum Electron. 2, pp. 898–905, 1996.
[5] Joseph M. Schmitt and Gitesh Kumar, "Optical scattering properties of soft tissue: a discrete particle model", Appl. Optics, Vol. 37, No. 13, pp.2788-2798, 1998

[6] Sean D. Puckett and Gilbert E. Pacey, “Detection of water in jet fuel using layer-by-layer thin film coated long period grating sensor”, Talanta, Vol. 78, Issue 1, pp.300-304, 2009
[7] S. Patskovsky et al, “Properties and sensing characteristics of surface plasmon resonance in infrared light”, J. Opt. Soc. Am. A, Vol.20, No. 8, pp.1644-1650, 2003.
[8] ‘‘Surface Plasmons on smooth and Rough Surfaces and on Gratings’’, H. Raether,, eds. (Academic, New York, 1997),
[9] T. Allsop et al, “Surface Plasmon Resonance Generation Utilising Gratings for Biochemical Sensing”, OFS-18 Cancun Mexico, Biological and Medical Sensors, paper WA4, Oct 2006.
[10] T. Allsop et al, “Characterization of infrared surface plasmon resonances generated from fiber optical sensor utilizing tilted Bragg gratings”, JOSA B, Vol. 25, No. 4, 2008
[11] A K. Sharma et al, “Influence of dopants on the performance of a fiber optic surface plasmon resonance sensor” Optic Comms Vol. 274, pp.320–326, 200
[12] M. Csete, et al, “Atomic force microscopical and surface plasmon resonance spectroscopical investigation of sub-micrometer metal gratings generated by UV laser-based two-beam interference in Au–Ag bimetallic layers”, Applied Surface Science, Vol. 253, pp.7662–7671, 2007.
[13] M. Piliarik et al, “Surface plasmon resonance sensor based on a single-mode polarisation-maintaining optical fiber”, Sensors and Actuators B, Vol. 90, pp.236-242, 2004
[14] E.M. Yeatman, “Resolution and sensitivity in surface plasmon microscopy and sensing”, Biosensors and Bioelect., Vol. 11, No. 6, pp.635-649, 1996.
[15] T. Allsop et al, “The exploitation of multilayer coatings for infra-red surface plasmon resonance fibre sensors”, Appl. Optics., Vol.48, pp. 276–286, 2009
[16] D. E. Aspnes, J. B. Theeten, F. Hottier, “ Investigation of effective-medium models of microscopic surface roughness by spectroscopic ellipsometry,” Phys. Rev. B 20, No. 8, pp.3292 – 3302, 1979.

# Micro/nanomanufactured THz electromagnetic metamaterials as a base for applications in transportation

H.O. Moser[*a,b], H.S. Chen[c,d], L.K. Jian[a], M. Bahou[a], S.M.P. Kalaiselvi[a], S. Virasawmy[a], S.M. Maniam[a], X.X. Cheng[d], S.P. Heussler[a], Shahrain bin Mahmood[a], B.-I. Wu[c]
[a]Singapore Synchrotron Light Source, National University of Singapore, 5 Research Link, Singapore 117603
[b]Department of Physics, National University of Singapore, 2 Science Drive 3, Singapore 117542
[c]Research Laboratory of Electronics, Massachusetts Institute of Technology, Cambridge, Massachusetts 02139, USA
[d]The Electromagnetics Academy at Zhejiang University, Zhejiang University, Hangzhou 310058, China

## ABSTRACT

Micro/nanomanufactured electromagnetic metamaterials in the THz spectral range may help extending the use of metamaterials in transportation. S-string based THz metamaterials as manufactured by SSLS, in particular, the meta-foil, provide a promising platform for applications. Special emphasis may be given to antennas being conformal or quickly steerable or tunable for inter-traffic communication. Achievements by SSLS in co-operation with MIT and Zhejiang University are discussed and potential applications outlined.

**Keywords:** Electromagnetic metamaterials, meta-foil, micro/nanomanufacturing, THz frequency range, antennas, transformation technology, transportation

## 1. INTRODUCTION

Electromagnetic metamaterials ($EM^3$) have been considered for a broad variety of applications in automotive transportation ranging from radar to night vision in the THz and optical frequency spectral range. Examples include antennas for collision-warning systems and high-performance absorbing and shielding materials [1, 2]. $EM^3$ are expected to provide new applications and functionalities, drastic improvements of performance, simple architectures, reductions of cost, size, and weight, and more, in future automotive electronics and, potentially, photonics applications. Such applications include beam steering antenna systems for radars, mobile communication antennas, novel magnetic materials for electric motors, and high-performance absorbing and shielding materials for electromagnetic compatibility [1, 2]. By analogy, aerospace may also benefit from such new elements and functionalities for the development of advanced systems.

Up to date, potential applications were mostly aiming at the GHz spectral range with antenna concepts and developments frequently based on transmission line technology [1, 2]. However, during the past years, the development of $EM^3$ has spread to the THz range up to the visible [3-12], thus opening up new opportunities for applications with regard to the information rate that can be transmitted, the size and weight of components such as antennas, resonators, filters, reflectors, and absorbers. Ultimately, THz optical systems may be shrunk to the nanoscale as proposed by Engheta and co-workers [13].

Since 2002, SSLS has been working on micro/nanomanufactured $EM^3$ in the THz range [3-8] based on the LIGA process including deep X-ray lithography [14]. This is a fresh technology that will enable new applications in transportation because of the new parameter range accessible. Using either rod-split-ring [3] or S-string designs [6] for the resonator structures, SSLS has developed high-aspect-ratio and free-standing $EM^3$ for frequencies extending from 1 THz upwards to 216 THz. Free-standing $EM^3$ do no longer need plastic matrices to embed metallic particles nor substrates upon which

*moser@nus.edu.sg; phone 65 6516 7930; fax 65 6773 6734; http://ssls.nus.edu.sg

Photonics in the Transportation Industry: Auto to Aerospace II, edited by Alex A. Kazemi, Bernard C. Kress
Proc. of SPIE Vol. 7314, 73140G · © 2009 SPIE · CCC code: 0277-786X/09/$18 · doi: 10.1117/12.820970

the metallic structures are deposited. Instead, they are either held in free suspension by window-frames or, most lately, they come as self-supported all-metal grids that are locally rigid and globally flexible like foils for which reason we dub them “meta-foils”. Window-frame-held chips already cover a comparably large active area of 56 mm$^2$. As the refractive index of such materials may vary from positive to negative, quite special spectral and spatial properties of filters, absorbers, reflectors, and antennas may be achieved.

Such materials represent an extension of the “tool kit” for future applications in transportation. In the following, we first give a short overview of Singapore Synchrotron Light Source (SSLS) as it provides the technology basis, describe then the status of THz EM$^3$ production and characterization at SSLS, and finally present a short outline of ideas for transportation applications.

## 2. TECHNOLOGY BASIS

SSLS is a user research facility with a user base of more than 500 [15]. It also works on commercial contracts like a “foundry” and an “analytical lab”. It features six operational beamlines and experimental facilities, and one new beamline is under construction. Research carried out by users and SSLS extends over many of the current hot topics as indicated in Table 1. A schematic layout including the experimental methods installed at the beamlines is given in Fig. 1

Table 1: Research fields active at SSLS

| | | | |
|---|---|---|---|
| Accelerator physics/technology | Environmental | Materials research | Quantum technology |
| Art authentication | Ferroelectrics | Micro/nanomanufacturing | Semiconductor |
| Bioengineering | Forensics | Molecular electronics | Spintronics |
| Catalysis | Fuel cells | Nanoscience/technology | Thin films |
| Data storage | Graphene | Oxides | Water technology |
| Dilute magnetic semiconductors | Hydrogen storage | Pharmacology | Zeolites |
| Electromagnetic metamaterials | Imaging | Polymer electronics | Zoology |
| Engineering | Life sciences | Physics | |

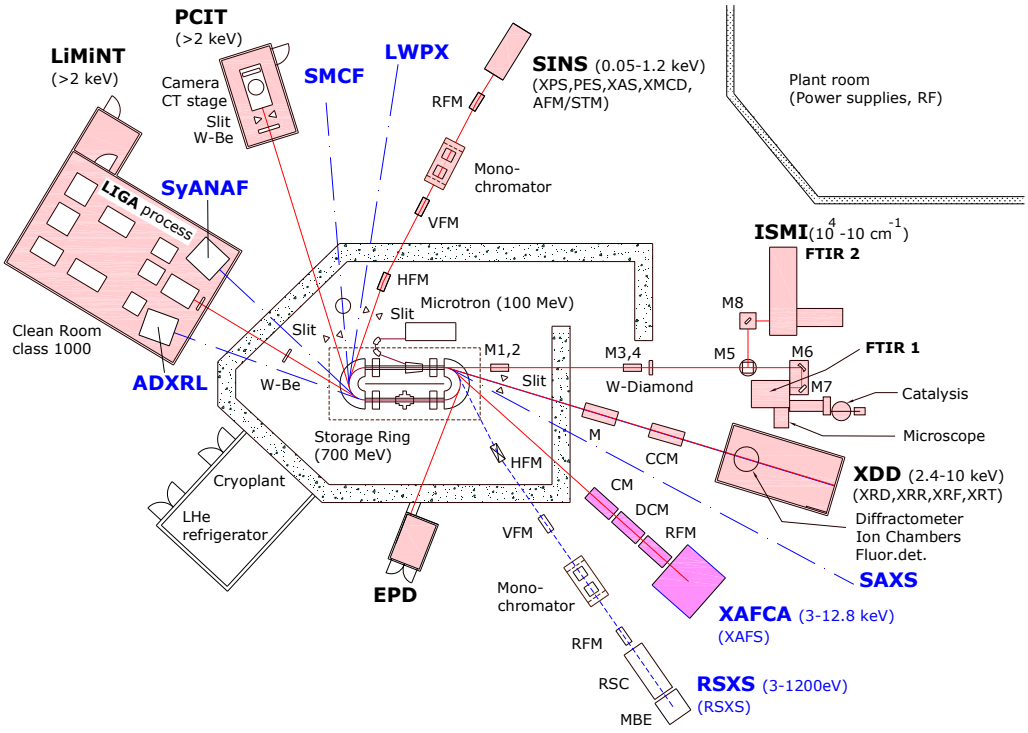


Fig. 1: Schematic layout of SSLS.

where acronyms stand for: LiMiNT – Lithography for Micro and Nanotechnology: micro/nanomanufacturing facility; PCIT – phase contrast imaging and tomography; SINS – surface, interface, and nanostructure science; ISMI – infrared spectro/microscopy; XDD – X-ray development and demonstration; EPD – electron and photon beam diagnostics (all operational); XAFCA – X-ray absorption fine structure spectroscopy for catalysis (under construction); RSXS – resonant soft X-ray scattering (pending approval); remaining ADXRL, SyANAF, SMCF, LWPC, SAXS being proposals in various stages.

The development of THz metamaterials is one focal area of SSLS' research. It involves micro/nanomanufacturing at LiMiNT and the spectral characterization by Fourier transform interferometry at ISMI. LiMiNT is a one-stop shop for micro/nanomanufacturing by means of the LIGA process network. Fig. 2 schematically details the process technology installed mostly in a cleanroom class 1000, and shows a photograph of the latter. For primary pattern generation, either laser writing at the DWL 66 (Heidelberg) or e-beam writing at the scanning electron microscope (FEI Sirion with Nabity Nanopattern Generator) is used. X-ray deep lithography is performed at the DXRL scanner. For electroplating and hot embossing, an MOT wet bench and a Jenoptik Mikrotechnik HEX 01 press are available. Auxiliary equipment for magnetron sputter deposition, plasma cleaning, spin coating, resist development in a fume hood, optical metrology, polishing, and dicing is completing the processes.

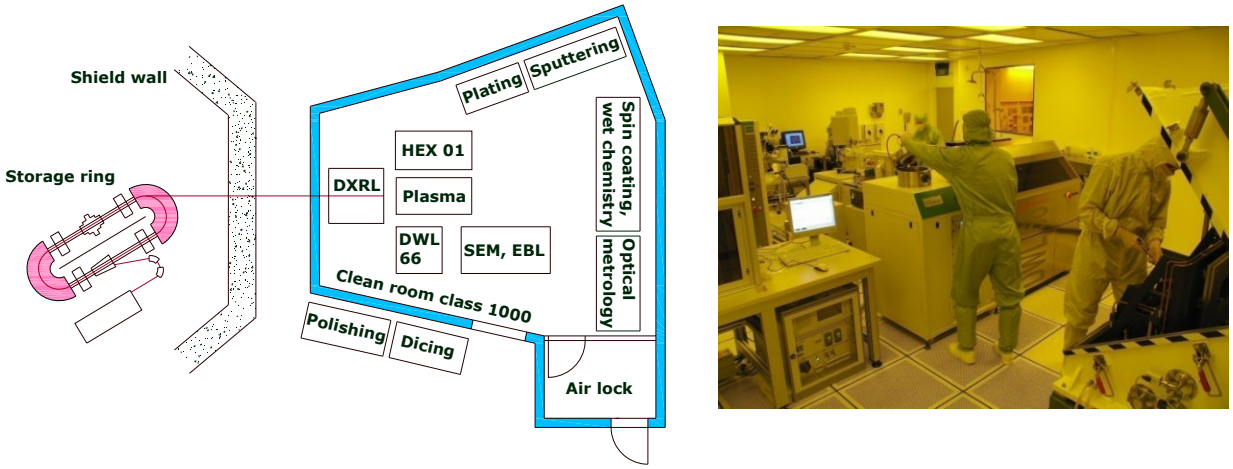


Fig. 2: LiMiNT facility for micro/nanomanufacturing based on the LIGA process (left); View of the cleanroom with DXRL scanner (foreground right), hot embossing press (foreground left), direct write laser system (centre right), and others (right).

ISMI is a state-of-the-art facility for infrared spectro/microscopy including the use of synchrotron radiation (Fig. 3) [16].

Fig. 3: ISMI facility with the IFS 66v/S under the dust hood, the Hyperion 2000 microscope being uncovered, and the HR 125 to the right.

It features a Bruker IFS 66 v/S Fourier transform interferometer with an infrared microscope Hyperion 2000 attached as well as a Bruker HR 125. Both FTIRs are operating under vacuum. The medium-resolution IFS 66 v/S is mainly used for the spectral characterization of the EM3.

## 3. MANUFACTURING OF THZ METAMATERIALS AT SSLS

Since 2002, SSLS is pursuing the development of rod-split-ring resonators and their tall high-aspect-ratio modification, the split-cylinders [3-5,8], as well as S-string metamaterials [6,7] introducing the first THz rod-split-ring EM$^3$ in 2003 and free-standing S-string bi-layer chips in 2008. Their left-handed resonance pass-bands are located in the range from 1 to 216 THz. For an individual metamaterial, the precise control of the geometrical parameters via lithography and micro/nanomanufacturing is used to determine the resonance frequency. Figs. 4 and 5 show a series of rod-split-ring and split-cylinder examples as well as free-standing S-string bi-layer chips, respectively. In the latter, two window-frames each holding a free-standing array of S-strings are assembled under careful alignment such that the two S-string array layers are separated by a gap of typical width between 0.6 to 6.1 μm [6].

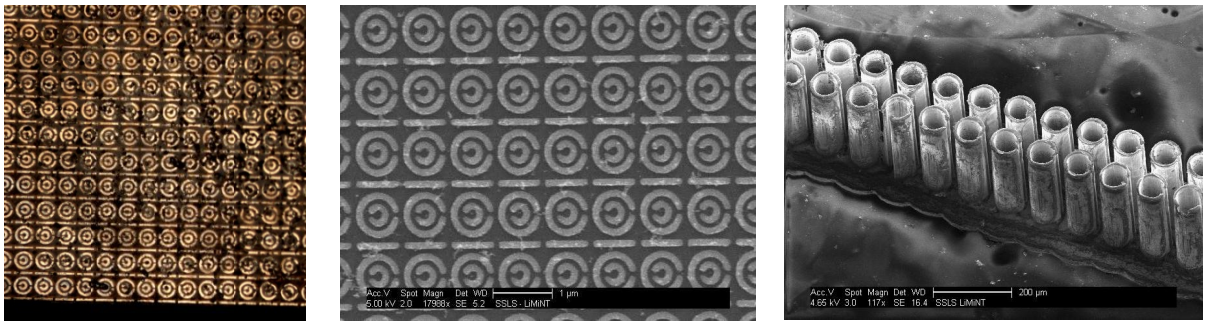


Fig. 4: First rod-split-ring EM$^3$ at 2.4 THz. 73 μm outer diameter (left); at 186 THz. 710 nm outer diameter (centre); double row of Ni split cylinders 300 μm tall. Scale bar 200 μm (right).

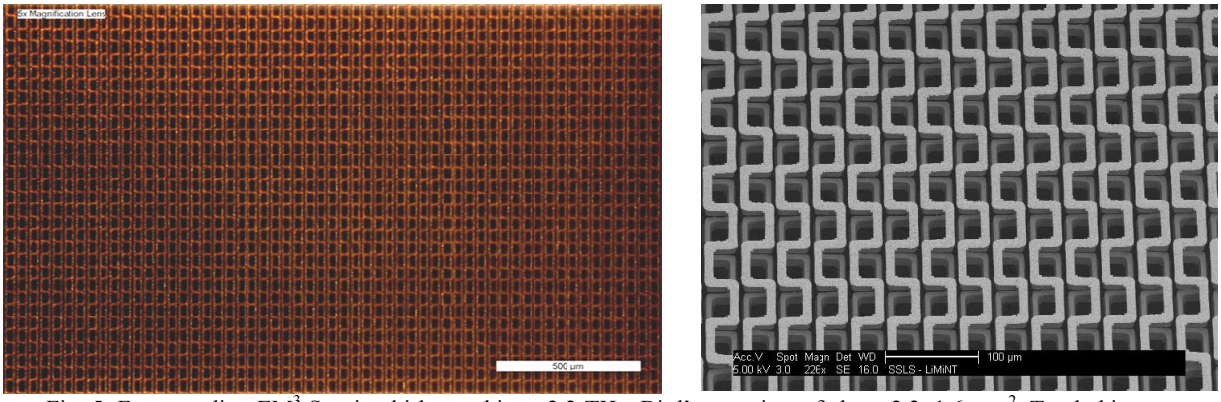


Fig. 5: Free-standing EM$^3$ S-string bi-layer chip at 2.2 THz. Bird's eye view of about 2.2×1.6 mm$^2$. Total chip area 56 mm$^2$ (left); SEM close-up (right).

The latest development aims at free-standing all-metal grids of upright S-strings interconnected by transverse metal rods, the meta-foil. Fig. 6 depicts a drawing in which parallel S-strings and transverse rods occurring at every second period can be seen. Such a space grid is locally rigid and globally flexible. It can be handled like a foil and fulfills the common notion of a material. Fig. 7 shows a meta-foil made of gold. The left-handed resonance pass-band is at 3.2 THz. With the meta-foil, we have a powerful and flexible technology that may be used for various components from which THz optical systems may be built. Filters, reflectors, absorbers, and quarter-wave plates [17] may be achieved by designing the geometry such as to set the refractive index n and the wave impedance Z to the required values. Fig. 8 shows an example of the variation of n versus frequency for various values of the parameter "a" that stands for the length of an S. This result implies that with a precise control of the geometric parameters in the micro/nanomanufacturing processes, meta-foils with different refractive indices may be realized.

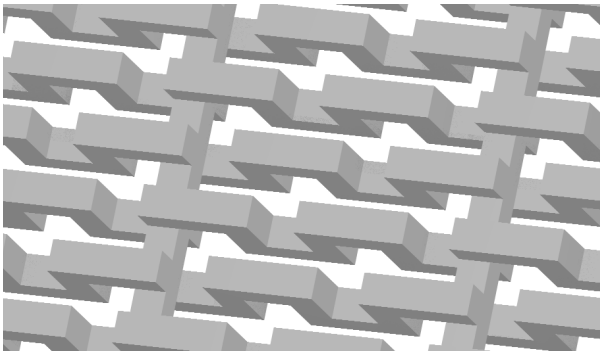

Fig. 6: Drawing of a free-standing all-metal space-grid formed by S-strings and interconnecting rods.

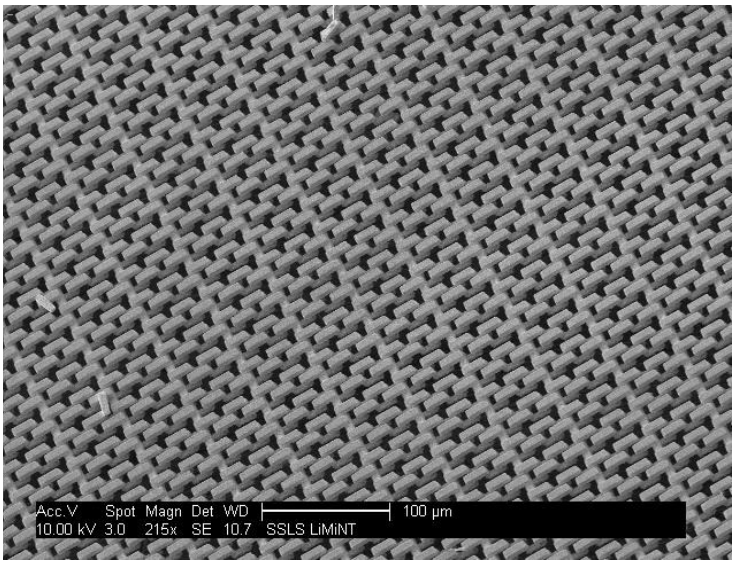


Fig. 7: Meta-foil consisting of free-standing all-metal space-grid formed of upright S-strings and interconnecting rods. Scale bar 100 µm.

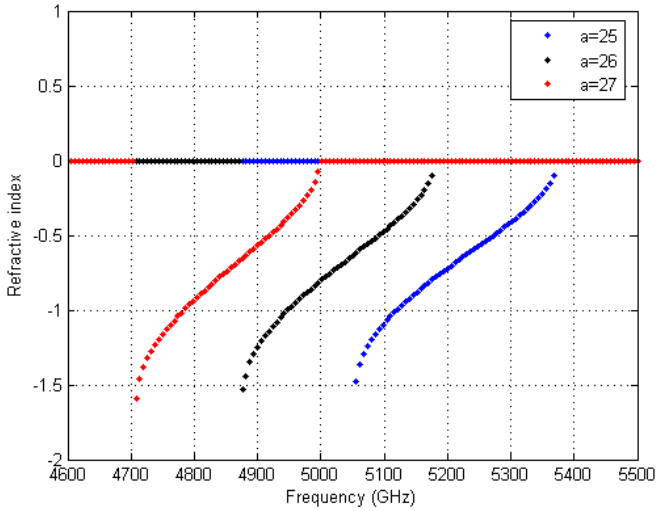


Fig. 8: Variation of refractive index of a meta-foil versus frequency for various values of the length of an S.

## 4. APPLICATION IDEAS

Transportation involves (tele)communication between traffic participants as a very essential element. Information about position, velocity, and acceleration of the individual participants and its update at a sufficiently fast rate are vital. The optimization of speed, travel duration, and, relatedly, energy consumption, the travel safety such as avoidance of collisions, undue excursions of orbits in space and on the road, all require a detailed knowledge of the respective orbits of all traffic participants. This holds for earthbound automotive transport as well as for air traffic and space flight.

The interest in developing automotive radar sensors for adaptive cruise control and pre-crash safety systems has greatly increased [1]. Considering traffic on roads, the importance of avoiding collisions with any object, not only other traffic participants, but also civil engineering structures like bridge pillars, beam barriers, and trees cannot be overstated. In addition to the negative aspect of avoidance of accidents and damages, there is also a very positive one which is centered on the optimization of traffic in terms of energy consumption, travel time and comfort. It strongly depends on speed and throughput of telecommunication systems, in other words, on bandwidth, quality, and minimal cross-talk of transmission systems. Assuming existence of such systems, a smart swarm management may become possible to save energy which would enable a strong distance and velocity dependant coupling among participants. In trains, such coupling is achieved mechanically. If it is to be realized electromagnetically, then fast diagnostics coupled with fast energy storing and releasing systems and a coupling from participant n to participant n+m by broadcasting the status information among all participants of a swarm will be needed.

Such visions require advanced communication systems which THz $EM^3$ could contribute to. Antennas are key components of such communication systems. If they are made from or including metamaterials, they may have advantages in terms of ease of steering, directivity, good tunability, conformability, size and weight. Metamaterial-based antennas can have a good steering capability because both the permittivity and permeability (or the refractive index) of the metamaterial can be tuned from negative to positive values, and therefore, it is much easier to design different phase distributions to get (or steer) different radiation pattern of the antenna. The tunability of the metamaterial can be achieved with microwave varactors in the microwave frequency band. Fig. 9 (left) shows one type of the metamaterial sample which is based on the single side paired S-ring resonators [18]. In each S-ring unit, Philips BB-143 type varactors are mounted in the center to control the electromagnetic properties of the cell. Only one external voltage bias is required to control all the cells simultaneously in the experiment. Fig. 9 (right) shows the far field radiation pattern of the prism-like sample as a function of the voltage bias at 3 GHz. We could see that the beam can be steered by controlling the voltages. Fast steering of antennas at a rate that cannot be attained by mechanical means may be of a premium. At a car speed of 108 km/h corresponding to 30 m/s, the determination of car position, velocity, and acceleration should be made in less than 3.3 ms such that translations do not become larger than, say, 0.1 m to avoid collisions or derouting. This might be difficult to achieve with mechanical systems.

By incorporating semiconductors in critical regions of metallic split-ring resonators, tunable metamaterials operating at THz frequencies can also be realized. Chen et al. demonstrated that external optical control results in tuning of the metamaterial resonance frequency by 20% [19]. Moreover, since metamaterials can work in a pass-band mode when both their permittivity and permeability are negative, and in a stop-band mode when either permittivity or permeability is negative, we can control the metamaterial, by properly changing the capacitive value of the varactor, to work in a stop-band mode so that the wave cannot radiate out. In this case, the antenna is turned off and working in a stealth mode. Therefore, a metamaterial-based antenna can be controlled to work in transmission mode or in stealth mode.

For a moving object, aerodynamic or hydrodynamic considerations often result in strict requirements on the shape of the antenna. Conformal antennas are therefore very important because they can be integrated with aerodynamic structures and reduce drag. With the introduction of metamaterials, it is much easier to design antennas that can be conformal to any shape but still keep the designed radiation pattern. For example, designing an antenna array with high directivity but conformal to a curved surface (or a very rough surface) is not easy to achieve based on conventional antenna design technology. Luo et al. have shown a new concept of conformal antenna utilizing transformation technology and inhomogeneous metamaterials, based on which a spherical coating with some proper current source distributed in the inner surface has the same radiation pattern as a three-unit array antenna [20]. Fig. 10 shows the radiated field distribution of the spherical conformal antenna and that of a three-unit array antenna, respectively. From the results we can see that the conformal antenna has an identical far-field distribution as the array antenna.

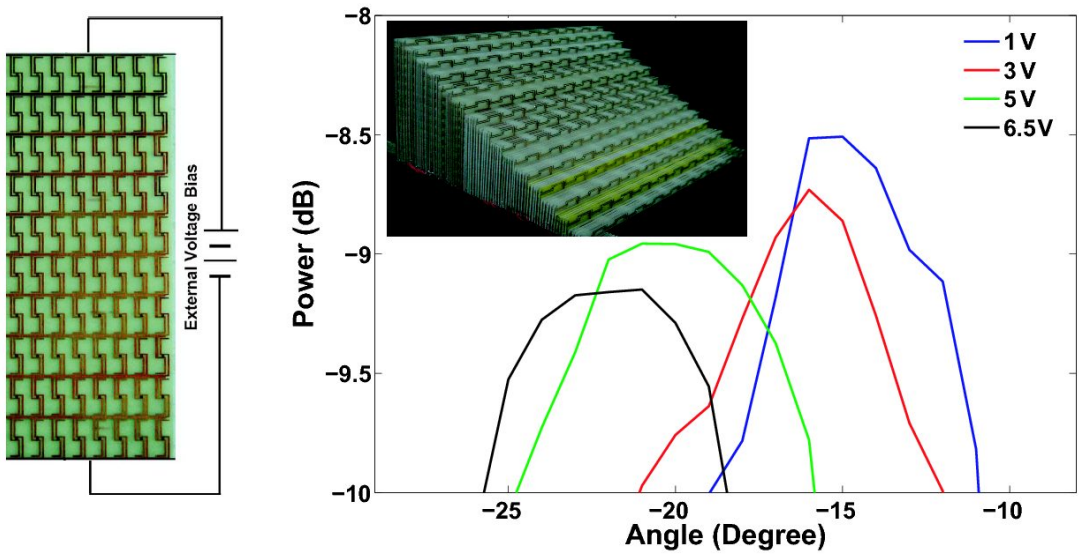


Fig. 9: The controllable LHM pattern printed on FR4 substrate (left); Beam steering results (right), the inset shows the prism-like metamaterial sample [18].

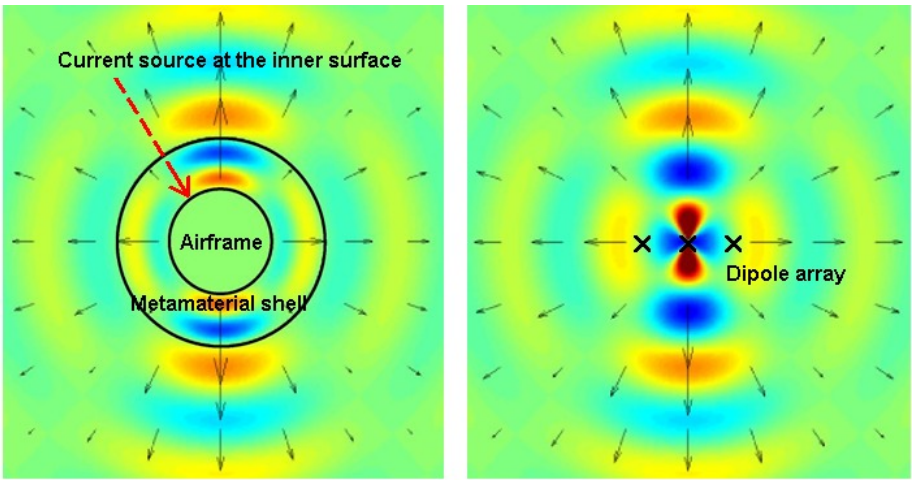


Fig. 10: Radiation field of a metamaterial-based antenna conformal to a spherical airframe (left); Radiation field of a three-dipole array antenna (right) [20].

With the combination of the metamaterials and the transformation technology, Kong et al. have shown how focusing parabolic antennas may be replaced by low profile planar ones [21]. In the original parabolic antenna design, the feeding source is located at the focal point. The electromagnetic wave excited by the feeding source can form a highly directive beam after the reflection from the parabolic conducting surface, as shown in Fig. 11 (left). In a low profile planar antenna design, a thin metamaterial slab with inhomogenous and anisotropic parameters is used in front of the source. When the wave is radiated from the source into the metamaterial slab, it will be guided, reflected, and radiated out with a similar pattern as that of the parabolic antenna. The field distribution of the low profile planar focusing antenna is shown in Fig. 11 (right) where we can see that the far field distribution is almost the same as that of Fig. 11 (left).

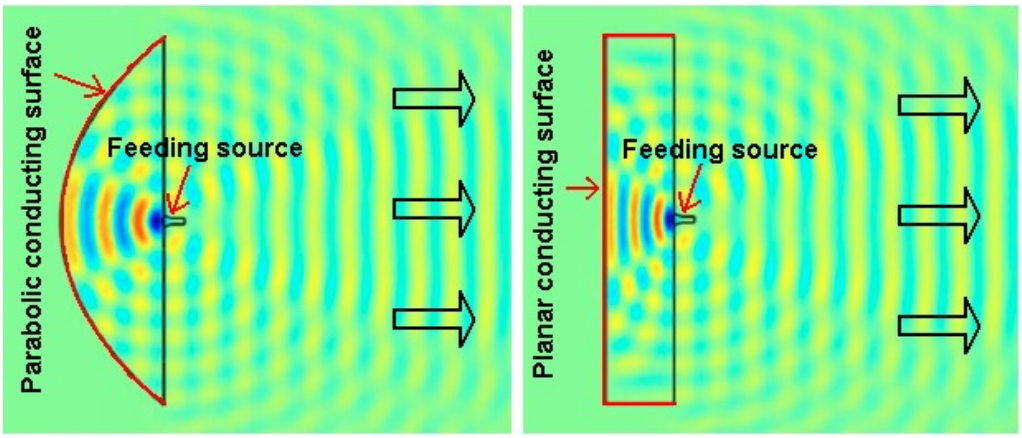


Fig. 11: Electric field distributions of a parabolic antenna (left) and a planar antenna (right) [21].

In addition, the use of metamaterials to direct the emission of an embedded source into a small solid angle was analysed by Enoch et al. [22]. As another example of directivity, Zhang et al. studied a spatially variant metamaterial to show how the emitted rays can be arbitrarily directed depending on the position of the source dipole in the metamaterial [23]. These metamaterial-based antenna designs are very helpful for space and transportation applications.

The payoff of the metamaterial-based design technology is potentially very significant. It may redefine the way steering antenna structures are built. Expensive and heavy electronic modules may be replaced by simple lightweight metamaterial substrates equipped with some active elements so that significant gains in space, weight, and cost can be obtained. These properties indicate the superiority of the metamaterial-based antenna in future applications.

Meta-foils as described above are natural candidates for systems architectures following the MIT/CETA work [21, 23]. They can also be directly used for concepts as described by Enoch et al. [22]. Related components such as sub-wavelength cavity resonators as introduced and discussed by Engheta and coworkers [24, 25] require sandwiching a metamaterial in between metal slabs, thus, meta-foil slabs would be ideally suited for such kind of geometry as well.

## 5. CONCLUSION

Micro/nanomanufactured THz electromagnetic metamaterials, in particular, meta-foils are a powerful and promising technology platform for interesting applications in transportation with a special emphasis on antennas that may be conformal, quickly steerable, and tunable.

## ACKNOWLEDGEMENTS

Work partly performed at SSLS under DARPA HR0011-06-1-0030, NUS Core Support C-380-003-003-001, A*STAR/MOE RP 3979908M and A*STAR 12 105 0038 grants. HSC would also like to acknowledge the Chinese National Science Foundation under contract 60801005 and the ZJNSF under grant R1080320.

## REFERENCES

[1] K. Sato, T. Nomura, S. Matsuzawa, and H. Iizuka, Progress In Electromagnetics Research Symposium, pp. 1122-1125, Hangzhou, China, March 24-28, 2008

[2] K. Sato, R&D Review of Toyota CRDL, vol. **41**, no. 4, pp. 1

[3] H.O. Moser, B.D.F. Casse, O. Wilhelmi, B.T. Saw, Phys. Rev. Lett. **94**, 063901(2005)

[4] B. D. F. Casse, H. O. Moser, L. K. Jian, M. Bahou, O. Wilhelmi, B. T. Saw and P. D. Gu, J. Phys:Conf Series **34**(2006)885-890

[5] B.D.F. Casse, H.O. Moser, J. W.Lee, M. Bahou, S. Inglis, L.K. Jian, Appl. Phys. Lett. **90**, 254106(2007)

[6] H.O. Moser, J.A. Kong, L.K. Jian, H.S. Chen, G. Liu, M. Bahou, S.M.P. Kalaiselvi, S.M. Maniam, X.X. Cheng, B.I. Wu, P.D. Gu, A. Chen, S.P. Heussler, Shahrain bin Mahmood, L. Wen, Opt. Express **16**, 13773-13780(2008)
[7] H.O. Moser, M. Bahou, A. Chen, S.P. Heussler, L.K. Jian, S.M.P. Kalaiselvi, G. Liu, S.M. Maniam, Shahrain bin Mahmood, P.D. Gu, L. Wen, J.A. Kong, H.S. Chen, X.X. Cheng, B.I. Wu, B.D.F. Casse, C. Rockstuhl, F. Lederer, Proc. of SPIE Vol. **7029**, 70290E, (2008)
[8] B.D.F. Casse, H.O. Moser, M. Bahou, J.W. Lee, S. Inglis, L.K. Jian, Adv. Syn. Rad. **1**, 1-12(2008).
[9] S. Linden, C. Enkrich, M. Wegener, J. Zhou, T. Koschny, C. M. Soukoulis, Science **306**, 1351-1353 (2004).
[10] T.J. Yen, W. J. Padilla, N. Fang, D. C. Vier, D. R. Smith, J. B. Pendry, D. N. Basov, X. Zhang, Science **303**, 1494-1496 (2004).
[11] G. Dolling, C. Enkrich, M. Wegener, J. Zhou, C.M. Soukoulis, S. Linden, Opt. Lett. **30**, 3198-3200 (2005).
[12] W.J. Padilla, D.R. Smith, D.N. Basov, J. Opt. Soc. Am. B **23**, 404-414 (2006).
[13] N. Engheta, A. Salandrino, A. Alu, Phys. Rev. Lett. **95**, 095504(2005)
[14] E.W. Becker, W. Ehrfeld, P. Hagmann, A. Maner, D. Muenchmeyer, Microelectron. Eng. **4**(1986)35
[15] H.O. Moser, M. Bahou, B.D.F. Casse, Ao Chen, E.P. Chew, M. Cholewa, C.Z. Diao, P.D. Gu, S. Inglis, L.K. Jian, Z.W. Li, Hua Miao, Shahrain bin Mahmood, Li Wen, J.H.W. Wong, Ping Yang, X.J. Yu, Wei Chen, X.Y. Gao, Tao Liu, A.T.S. Wee, AIP CP**902**, 3-6(2007)
[16] M. Bahou, L. Wen, X. Ding, B. Didier F. Casse, S. P. Heussler, P. Gu, C. Diao, H. O. Moser, W.-S. Sim, J. Gu, Y.-L. Mathis, AIP CP**879**, 603-606 (2007).
[17] A. C. Strikwerda, K.B. Fan, Hu Tao, D. V. Pilon, X. Zhang, R. D. Averitt, Opt. Express **17**, 136(2009)
[18] D. Wang, L. Ran, H. S. Chen, M. Mu, J. A. Kong, and B.-I. Wu, Appl. Phys. Lett. **91**, 164101 (2007)
[19] H. T. Chen, J. F. O'Hara, A. K. Azad, A. J. Taylor, R. D. Averitt, D. B. Shrekenhamer, W. J. Padilla, Nature Photonics **2**, 295 (2008)
[20] Y. Luo, J. Zhang, L. Ran, H. S. Chen, J. A. Kong, IEEE Antennas and Wireless Propagation Letters **7**, 508 (2008).
[21] F.M. Kong, B.I. Wu, J.A. Kong, J.T. Huangfu, S. Xi, H.S. Chen, Appl. Phys. Lett. **91**, 253509(2007)
[22] S. Enoch, G. Tayeb, P. Sabouroux, N. Guerin, P. Vincent, Phys. Rev. Lett. **89**, 213902(2002)
[23] J.J. Zhang, Y. Luo, H.S. Chen, B.I. Wu, Opt. Express **16**, 10962-10967(2008)
[24] N. Engheta, IEEE Antennas and Wireless Propagation Letters **1**, 10(2002)
[25] Th. Hand, S. A. Cummer, N. Engheta, IEEE Transactions on Antennas and Propagation **55**, 1781(2007)

# Multimaterial photosensitive fiber constructs enable large-area optical sensing and imaging

Ayman F. Abouraddy[1] and Yoel Fink[2,3]

[1]*CREOL, The College of Optics and Photonics, Orlando, FL 32816, USA*
[2]*Research Laboratory of Electronics,* [3]*Department of Materials Science and Engineering, Massachusetts Institute of Technology, Cambridge, MA 02139, USA.*

## Abstract

The process of optical imaging and the use of a glass lens have been hitherto inseparable since it is the lens that is responsible for mapping incoming rays to form an image. While performing this critical role, the lens, by virtue of its geometry and materials composition, presents constraints on the size, weight, angular field of view, and environmental stability of an optical imaging system as a whole. Here, a new approach to optical imaging is presented. Tough polymeric light-sensing fibers are suspended on a frame to form large-scale, low-density, two- and three-dimensional photonic meshgrids. While a single grid can indeed locate a point of illumination, it is the stacking of a multiplicity of such grids, afforded by their essential transparency, which allows for the detection of the direction of illumination with a wide angular field of view. A surface-spanning-arrangement of such fibers is used to extract an arbitrary optical intensity distribution in a plane using a tomographic algorithm. Lensless imaging is achieved by a volumetric fiber assembly that extracts both the phase and intensity distributions of an incoming electromagnetic field, enabling one to readily determine the object from which the field originally emanated.

The use of lenses for optical imaging has dominated optics since antiquity with no fundamental changes since, except for improvements in design and fabrication. The performance and size of any optical imaging system is usually determined by the quality and size of the lens(es) included in that system. The search for alternative approaches to optical imaging that do not rely on lenses, so-called lensless imaging, has had a venerable history. The common factor amongst all previous attempts is the introduction of a new optical system, usually an interferometer, which transforms the optical field before recording the intensity using a conventional optical-detector array. A recent attempt demonstrated three-dimensional lensless imaging using a sophisticated interferometric arrangement and a novel computational algorithm [1]. In this paper we demonstrate a distinct, *non-interferometric* approach to lensless optical imaging that relies on a volumetric sampling of the electromagnetic field that is enabled by semitransparent 3D arrangements of photodetecting fibers.

Photonics in the Transportation Industry: Auto to Aerospace II, edited by Alex A. Kazemi, Bernard C. Kress
Proc. of SPIE Vol. 7314, 73140H · © 2009 SPIE · CCC code: 0277-786X/09/$18 · doi: 10.1117/12.821209

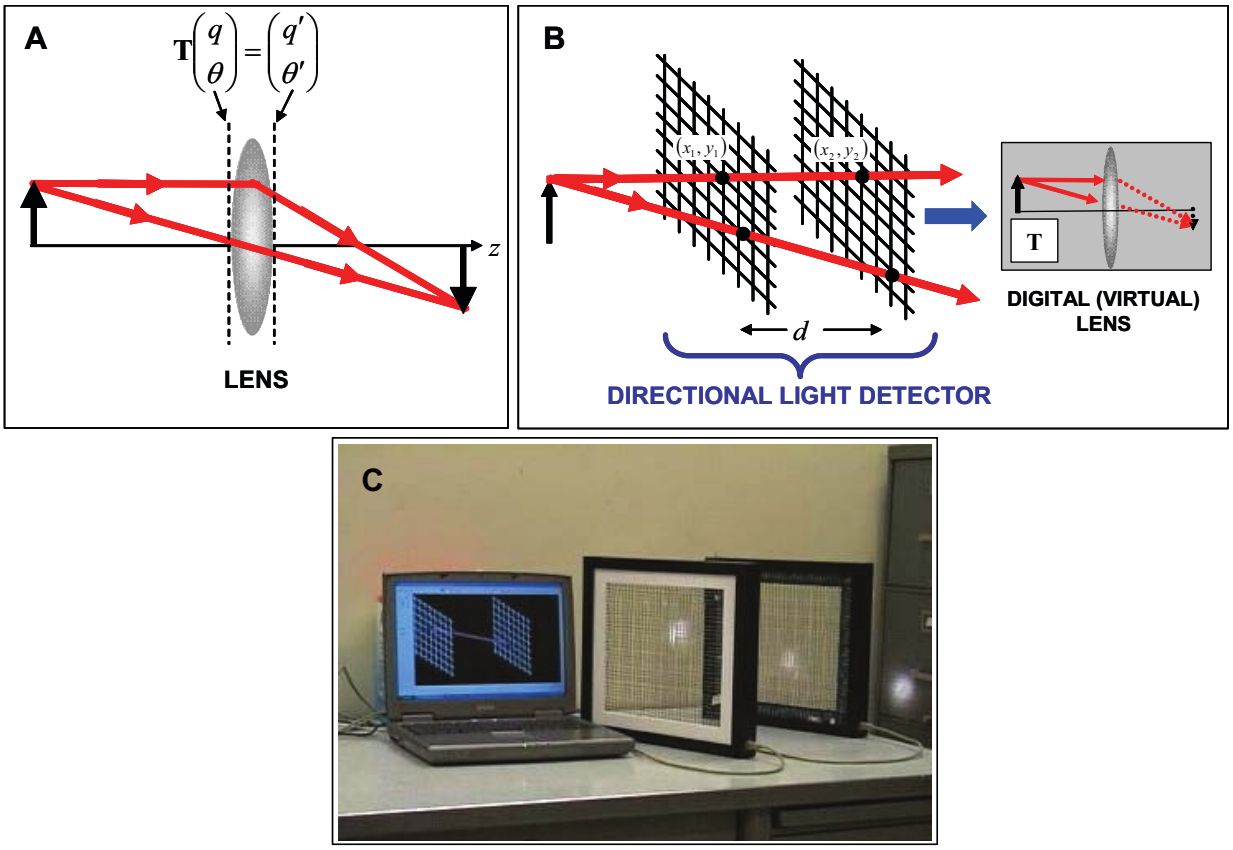


**Fig. 1.** (**A** to **C**) Directional optical detection and optical imaging in the limit of geometrical optics. (**A**) A lens implements a linear transformation **T** that results in forming an image of the object. Each ray of light is characterized by its location $q$ and direction $\theta$. (**B**) A directional light detector, composed of two planar, transparent optical-detector arrays, can determine the location and direction of a ray of light through detection of the intersections of the ray with the two planes. A computer maps the *physical* incoming beam to a *virtual* outgoing beam via the lens transfer operator **T**, digitally replicating the effect of a real lens placed in the beam path. The incoming beam, however, is left largely undisturbed. (**C**) Photograph of two fiber webs demonstrating directional light detection by displaying the path of a ray of white light in three dimensions.

In the limit of geometric optics, where diffraction and interference effects are negligible, light is described by rays. A complete description of a ray is given in terms of a direction of propagation vector and a point of intersection with a plane [2]. The function of an optical component, such as a lens (shown schematically in Fig. 1A), may be represented in this limit by a matrix which maps the incoming rays to outgoing ones. In other words, a lens is an analog computer that applies a specific transformation, determined by the shape and index-of -refraction of the lens, to the parameters representing each ray. One of the main goals of this paper is to demonstrate that complete identification of the parameters describing the rays enables one to replace this analog computer (lens) with a digital computer. This is of importance for the long-standing effort in microscopy devoted to improving the resolution of diffraction-limited imaging [3]. However, optical detectors normally register only the *location* of an incident ray, but not its *direction*. An optical detector capable of registering both, in other words a directional light detector, would then acquire all the parameters needed to implement the

effect of any optical device or process *computationally* by simply performing the corresponding transformation (not necessarily restricted to being linear) or series of transformations.

In the wave-optics formulation of optical imaging, light is represented with a complex field distribution. The intensity of the diffracted field transmitted or reflected by an object, and recorded by a 2D optical-detector array, has little resemblance to the object at distances much larger than the wavelength of light. A lens, in this case, provides a phase modulation to the incident diffracted field that leads to the formation of a sharp image when combined with the effect of free-space propagation for a specified distance after the lens [2]. While conventional optical detectors measure the amplitude (intensity) of the field, there is no direct access to the phase. However, if the amplitude *and* phase of the diffracted field are detected, one could simply 'back-propagate' the optical field computationally (by implementing the Hermitian conjugate of the propagation operator) until a sharp image is formed at the correct distance separating the object from the detection plane. In X-ray imaging, similar lensless approaches have recently been demonstrated [4, 5] motivated by the lack of large-numerical-aperture X-ray lenses. Optics, however, cannot benefit from this class of lensless approaches since an extremely large detector array would be required at optical wavelengths.

An optical detector obstructs the path of a ray since light detection is, in general, a destructive process. Nevertheless, an optical array made sufficiently sparse will offer little disturbance to the incident field. If one arranges for two such arrays to be placed in the beam path, the location *and* direction of a ray is easily determined. In Fig. 1B we show one possible implementation of a directional light detector in the geometric-optics limit that makes use of two transparent optical-detector arrays separated by a distance *d*. The first array registers the location of the input beam, which continues its path, only slightly perturbed, to the second web which records the new position of the beam. One may then easily compute the angle of the beam from knowledge of the two locations and the distance between the planes of the webs. The angular resolution of this arrangement is determined by the ratio of the spatial resolution of a web to *d*, and the angular bandwidth is limited by the ratio of the size of the array to *d*.

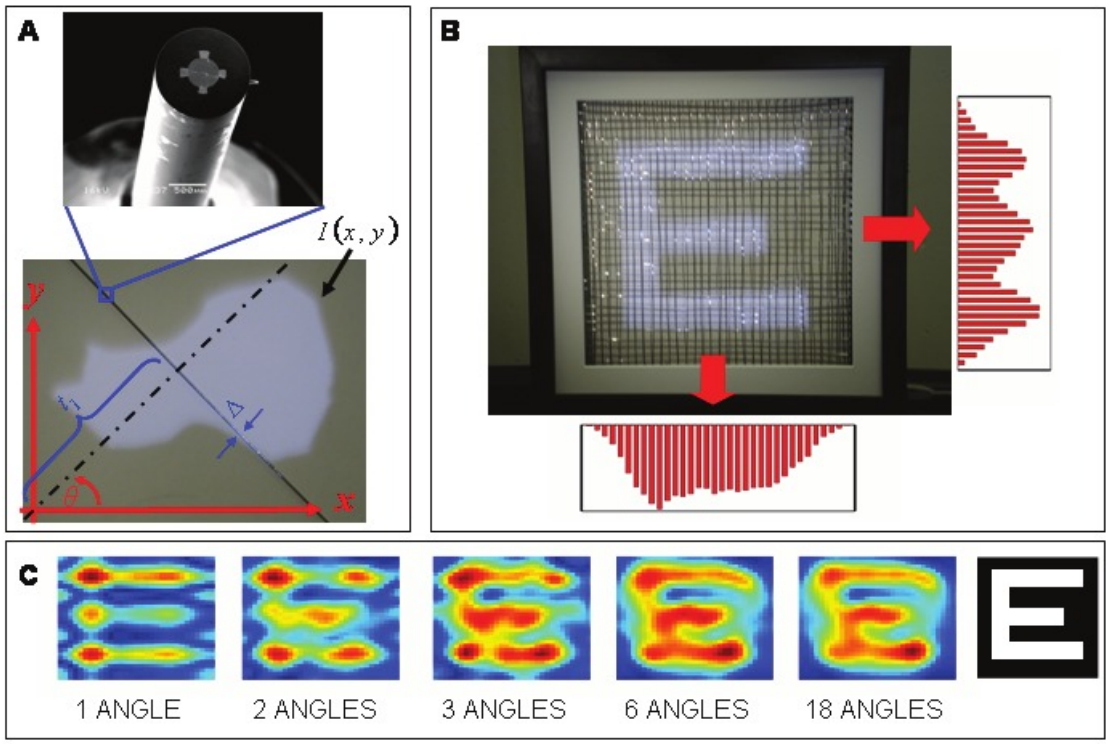


**Fig. 2.** (**A** to **C**) (**A**) An optically sensitive fiber (diameter $\Delta$) detects a line integral of the incident intensity distribution $I(x,y)$. The inset shows an SEM micrograph of the metal-semiconductor-metal fiber cross-section (1.25-mm outer diameter) showing four electrodes in contact with a photoconductive glass core. (**B**) An image of the letter 'E' is projected onto a 32×32 fiber web. The detected signal from the web rows and columns (constituting 2 orthogonal parallel projections) are also shown. The image of the letter 'E' itself is formed on a white sheet placed behind the essentially transparent web. (**C**) Reconstructing the image using the backprojection algorithm as a function of the number of angles the projections are taken at. These projections are obtained by rotating the object transparency (shown on the far right), 1 angle: 0º; 2 angles: 0º, 45º; 3 angles: 0º, 30º, 60º; 6 angles: 0º, 15º, 30º, 45º, 60º, 75º; and 18 angles: 0º to 85º in 5º steps.

Several obstacles, however, make the physical implementation of such a conceptually simple scheme prohibitive. One obstacle concerns the area of the optical-detector array. Typically, the array is constructed out of point, zero-dimensional (0D), detectors in the form of pixels integrated on a chip (such as CCD chips), which are limited to small areas, and a lens is required to collect the light and deliver a focused image to the chip. Alternatively, an arrangement of separate, individual point detectors can cover a larger area, but only a small portion of the field is intercepted by each detector. To obviate the above restrictions, we construct a transparent optical detector array that minimally impedes the propagation of the incident beam. The use of two such arrays, separated by some distance, allows one to easily determine the path that the light ray traversed. (Fig. 1C shows a photograph of such an arrangement.) Unlike other detectors, our arrays can be made arbitrarily large and hence have large angular bandwidth, corresponding to the numerical aperture having a value of 1. Our approach consists of constructing the array from one-dimensional (1D) light-sensitive elements in lieu of 0D elements. This is made possible by our recent success in fabricating a family of optoelectronic

fibers [6], constructed from insulators, semiconductors, and metals, which are particularly suitable for our purpose by virtue of combining optical and electrical functionalities. Specifically, the class of fibers that we make use of in this paper is that of fibers constructed of a photoconductive glass [7] core contacted to metal electrodes that run along the length of the fiber [8], and is then surrounded by a protective, transparent polymer cladding [9] (see the inset of Fig. 2A). When light impinges on the external surface of this fiber, an electrical signal is produced in the form of a change in current in an external circuit. This fiber structure offers several advantages that address the abovementioned difficulties of 2D arrays. First, the array consists of only O($N$) 1D elements that are sensitive to light along their whole length and collect a considerable amount of optical power, hence allowing the construction of sparse arrays. Second, these fibers can be of long length, resulting in large-area arrays. The fact that the electrodes run along the fiber in contact with the core alleviates the problem of electrical connections. Third, the fibers are mechanically tough, yet very flexible, which facilitates the construction of an optical array on a curved surface such as a sphere or a cylinder [10]. This also opens up the exciting prospect of incorporating such a fiber array in a fabric, thus producing optically functional clothing. Fourth, the fibers are essentially transparent, and an optical beam incident on an array of such fibers is only slightly perturbed. This advantage, when coupled with the flexibility of the fibers, allows the exploration of 3D arrays of arbitrary geometry which are capable of performing optical tasks beyond those of conventional 2D arrays, such as lensless imaging, for example. To distinguish our proposed optical-detector arrays constructed out of 1D optoelectronic fibers from conventional arrays, we call them 'fiber webs'.

Consider a 2D web constructed of straight fibers on a square grid (although arbitrary grid geometries may also be constructed). The location of an incident ray of light, or any separable intensity distribution $I(x,y)$ in the form $I(x,y)=I_1(x)I_2(y)$, may be determined in a straightforward manner from the signals detected by the rows and columns. However, it is not obvious how such an array can determine the distribution of an arbitrary intensity distribution. An important observation brings to the fore which body of theoretical work is of relevance to this problem. Note that each fiber detects the incident intensity distribution along its whole length. A fiber, of length $L$ and thickness $\Delta$ ($\Delta << L$) placed along the line $x\cos\theta + y\sin\theta = t_1$ in an optical field having a two-dimensional intensity distribution $I(x,y)$, as illustrated in Fig. 2A, generates a photocurrent that is proportional to the intercepted optical power, $P_\theta(t_1)$, given by

$$P_\theta(t_1) = \iint\limits_{\text{fiber area}} dxdy\, I(x,y) \approx \Delta \iint dxdy I(x,y)\delta(x\cos\theta + y\sin\theta - t_1)\,; \qquad (1)$$

where $t_1$ is the intercept of the fiber with the $t$ axis, which makes an angle $\theta$ with the $x$ axis. The intercepted power is thus a *line integral* of the intensity distribution along the fiber. Consequently, the measurements performed by a set of parallel photodetecting fibers form a *parallel projection* of the incident intensity distribution. The term 'parallel projection' is that used in the literature on computerized axial tomography

(CAT) [11] and refers to the measurements performed by a linear array of point detectors placed on one side of a 2D object of interest, when a linear array of point sources (*e. g.*, X-rays) is placed on the opposite side of the object. Each point detector measures the line integral of the *X-ray attenuation* of the object along the line connecting it to the opposing point source. In our case, each fiber records the line integral of *the intensity distribution of the optical field* along its length. An example of a parallel projection produced by a fiber web is shown in Fig. 2B, where a 32×32 fiber web (of dimensions 24×24 $cm^2$) intercepts an image of a letter E. The image is produced by a white-light lamp (Xe-Hg) illuminating a transparency with dimensions 14×14 $mm^2$ placed at a distance of 1.2 m from the web. No lens is needed to form an image of the object transparency in this case because of the large dimensions (relative to the wavelength of light) used, highlighting the unique advantage of an array having such a large area. The two orthogonal parallel projections obtained by the rows and columns of the web are displayed, demonstrating the uniformity of the responses of the different fibers to the incident intensity distribution.

Although the physical mechanisms of X-ray detection in a CAT arrangement and the detection of light using a fiber web are completely different, they are, surprisingly, mathematically isomorphic, allowing us to import the theoretical foundations of CAT for use in the problem at hand. In particular, we may employ the backprojection algorithm [11], commonly used in CAT, to reconstruct an estimate of the impinging optical intensity distribution. This algorithm enables one to reconstruct an arbitrary two-dimensional distribution from one-dimensional parallel projections taken along different directions. In the case of X-ray CAT scans, the array of point sources and point detectors are usually rotated simultaneously around the object. In the case of fiber webs there are several strategies to achieve this: (1) rotating the fiber web; (2) using adjacent or interleaved fiber webs, each rotated by an angle with respect to each other; or (3) rotating the object that is imaged. In Fig. 2C we show the reconstruction results of the image, obtained using the backprojection algorithm, while increasing the number of projections recorded while rotating the object transparency. Note that the image, consisting of 1024 pixels, is produced by using 64 fibers only.

Having the intensity distribution in hand, we are now in position to discuss the general case of optical imaging using electromagnetic diffraction theory. We demonstrate that two fiber webs can be used to reconstruct an object from diffraction intensity measurements employing the phase retrieval algorithm [12-14]. In its simplest form, this algorithm iteratively obtains the phase of a wavefront if the amplitude is known in two different planes. The idea proceeds as follows. We use two planar fiber webs, located at two distinct diffraction planes, and obtain the incident 2D intensity distributions from both (by means of the CAT algorithm outlined above); we then implement the phase retrieval algorithm to retrieve the phase of the wave front [15]; knowing the complex field at the first web, we can 'back-propagate' the wave front computationally until an estimate of the object is obtained.

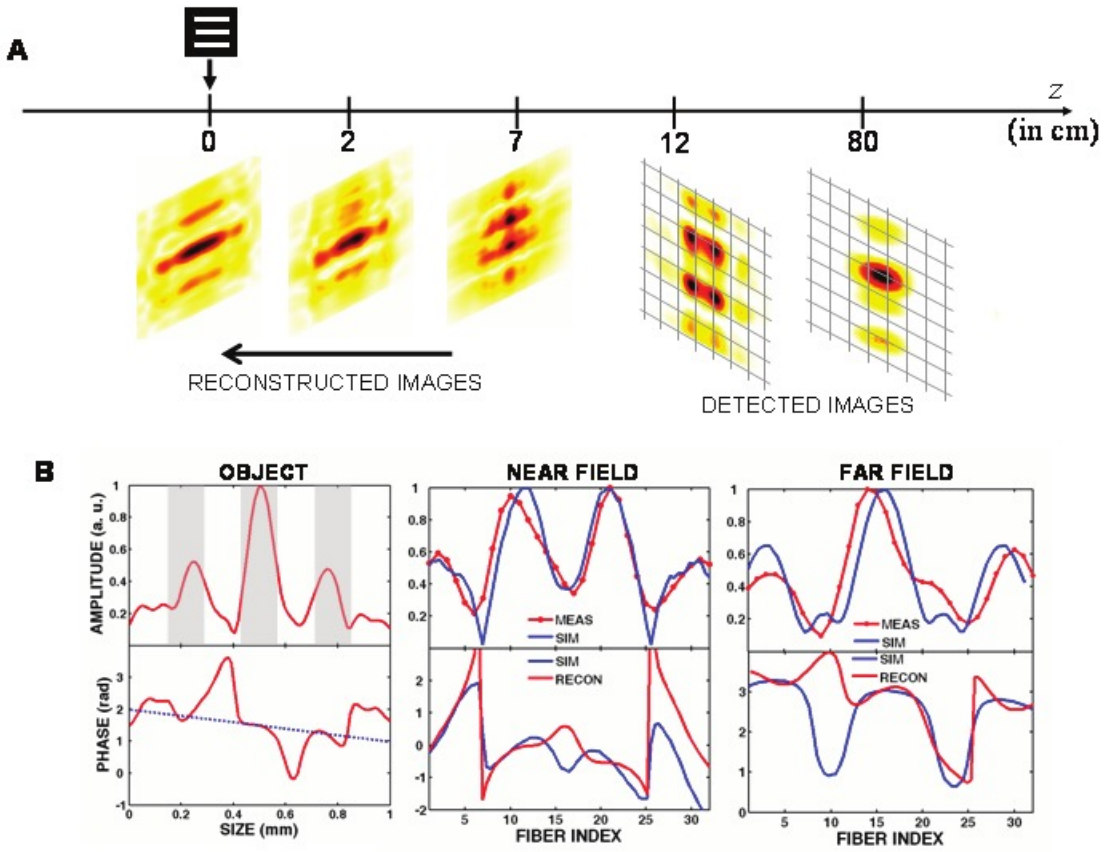


**Fig. 3.** (**A** to **B**) Lensless imaging using two fiber webs. (**A**) Two intensity images at two different locations (near field, 12 cm, and far field, 80 cm, shown on the right) are obtained using fiber webs. The phase retrieval algorithm is used to obtain back-propagated images in the direction receding from the webs towards the object (at 0 cm, shown on the left). The reconstructed images are blurred, but a clear image is obtained at the location of the object. (**B**) The amplitude and phase of the electromagnetic field at the near- and far-field locations and in the object plane.

We demonstrate the feasibility of this approach by producing the image of a pattern consisting of three slits (of width 158 μm, separated by 158 μm each) illuminated with light at 830 nm. The 2D intensity distribution data obtained by a fiber web at two different locations in the far-field of the object is depicted in Fig. 3A. We implemented the phase retrieval algorithm on the two obtained intensity distributions to reconstruct the phase of the wave front, and subsequently we estimated the field at distances receding from the first web. A set of these estimates is shown in Fig. 3A. All the estimates are blurred until we approach the location of the object where a clear image is formed. Calculated fields back-propagated beyond this distance are blurred once again. Images of objects with more detail will require webs with a larger number of fibers. Note that this system has an infinite depth of focus, i.e., an image is formed of the object regardless of the distance of the object from the webs, provided that the diffracted field, at the locations of the two webs, is intercepted. Furthermore, the image reproduces the object with its real physical dimensions and also determines its physical distance from the webs. In Fig. 3B we plot the amplitude and phase of the optical field at three locations: the planes of the two fiber

webs and the object plane. The measured amplitudes at the planes of the two webs are compared to the amplitudes calculated using the object by employing diffraction theory and the reconstructed phases are compared to calculated phases. Note that discrepancy occurs between the reconstructed and calculated phases only at those locations where the amplitude is small, and the phase become less meaningful. Note that the reconstructed phase at the object plane reveals a linear phase distribution across the object plane instead of the expected zero phase, which indicates that the plane of the slits was slightly tilted with respect to the incident beam wave front.

It is important to stress that the amplitude and phase represent a complete representation of the optical field. The human eye, for example, implements a specific transformation (that of an iris followed by a lens) with variable parameters, before detecting a 2D intensity distribution. Any such optical process may be carried out on a digital computer by manipulating the full information about the field. One could, for example, prepare a hologram using this information. One may also implement object-recognition algorithms that will benefit from the availability of the complex optical field instead of relying on a 2D intensity image. Moreover, although the specific demonstration reported here makes use of a coherent light source (optical bandwidth of approximately 6 nm), a white light source could also be used. This would require using a generalized phase retrieval algorithm that formally handles broadband light, which has been explored and demonstrated in Ref. [16] for an approximately 200-nm wide optical spectrum.

In principle, by virtue of obtaining a complete description of the electromagnetic field, this approach may be used to image 3D objects that are translucent enough so that excessive occlusion does not occur. Furthermore, one can arrange for the photoconductive glass core in the fibers to be responsive in different regions of the optical spectrum [17]. One can also arrange to reduce the detected optical bandwidth by surrounding the fibers with resonant photonic-bandgap structures [6, 18, 19]. Using fibers provided with optical sensitivity at different wavelengths allows one to produce color images. Although the fiber webs used in this paper detect light and form an optical image (and in that sense can be said to ‘see’), one can substitute the photoconductive glass in the core with other families of glasses that are sensitive to other physical quantities, such as temperature or chemical contaminants [20]. Webs constructed of these fibers, coupled with the use of the same principles outlined above, will yield ‘images’ in these parameter spaces, and can thus be said to see, sense heat, and smell.

In conclusion, we have demonstrated non-interferometric lensless optical imaging using a three-dimensional photonic-fiber meshgrid. Such a meshgrid determines the position and direction of rays of light or the amplitude and phase of an electromagnetic field. Using a combination of a tomographic algorithm and the phase retrieval algorithm, a computational image of an object is formed with its physical dimensions and at its true location. Finally, one of the scientific objections to H. G. Wells’ 1897 novel, “The Invisible Man,” [21] was that such a man would necessarily be blind. Although our fiber meshgrids are not strictly invisible, we have shown that objects that are almost transparent may, in a meaningful sense, ‘see’.

This work was supported in part by DARPA/Carrano and DARPA/Griggs, DARPA QUIST, the ARO, the ONR, the AFOSR HEL-MURI, the US DOE, the ISN, and the Materials Research Science and Engineering Center (MRSEC) program of the NSF with use of their Shared Experimental Facilities.

## REFERENCES

[1] D. L. Marks, R. A. Stack, D. J. Brady, D. C. Munson, Jr., and R. B. Brady, "Visible cone-beam tomography with a lensless interferometric camera," *Science* **284**, 2164-2166 (1999).

[2] B. E. A. Saleh and M. C. Teich, *Fundamentals of Photonics* (Wiley, New York, 2001).

[3] E. Abbe, "Beiträge zur Theorie des Mikroskops und der mikroscopischen Wahrnehmung," *Arch. Mikroskop. Anat.* **9**, 413-420 (1873).

[4] J. Miao, P. Charalambous, J. Kirz, and D. Sayre, "Extending the methodology of X-ray crystallography to allow imaging of micrometer-sized non-crystalline specimens," *Nature* **400**, 342-344 (1999).

[5] I. K. Robinson, I. A. Vartanyants, G. J. Williams, M. A. Pfeifer, and J. A. Pitney, "Reconstruction of the shapes of gold nanocrystals using coherent X-ray diffraction," *Phys. Rev. Lett*. **87**, 195505 (2001).

[6] M. Bayindir, F. Sorin, A. F. Abouraddy, J. Viens, S. D. Hart, J. D. Joannopoulos, and Y. Fink, "Metal-insulator-semiconductor optoelectronic fibres," *Nature* **431**, 826-829 (2004).

[7] The photoconductive glass used was the amorphous chalcogenide semiconductor $As_{40}Se_{50}Te_{10}Sn_5$.

[8] The kilometer-long fiber was obtained from a macroscopic cylindrical preform, 33-mm diamater and 25-cm length, which consists of a $As_{40}Se_{50}Te_{10}Sn_5$ core [4] contacted by four tin (Sn) metal conduits that are encapsulated in a protective polymer Polyethersulfone (PES) cladding.

[9] M. Bayindir, A. F. Abouraddy, F. Sorin, J. D. Joannopoulos, and Y. Fink , "Fiber photodetectors codrawn from conducting, semiconducting and insulating materials," *Opt. and Photon. News* **15**, 24 (2004).

[10] Compare to a case where an array of optical sources where placed on a grid on the outer surface of a cylinder in: H. O. Jacobs, A. R. Tao, A. Schwartz, D. H. Gracias, and G. M. Whitesides, "Fabrication of a cylindrical display by patterned assembly," *Science* **296**, 323-325 (2002).

[11] A. C. Kak and M. Slaney, *Principles of Computerized Tomographic Imaging* (IEEE Press, New York, 1988).

[12] R. W. Gerchberg and W. O. Saxton, "A practical algorithm for the determination of phase from image and diffraction plane pictures," *Optik* **35**, 237-246 (1972).

[13] W. O. Saxton, *Computer Techniques for Image Processing in Electron Microscopy* (Academic Press, New York, 1978).

[14] J. R. Fienup, "Phase retrieval algorithms: a comparison," *Appl. Opt.* **21**, 2758-2769 (1982).

[15] J. R. Fienup, "Phase-retrieval algorithms for a complicated optical system", *Appl. Opt.* **32**, 1737-1746 (1993).

[16] J. R. Fienup, “Phase retrieval for undersampled broadband images,” J. Opt. Soc. Am. A **16**, 1831-1837 (1999).

[17] For example, by changing the percentage of Te in the glass we used we can change the absorption edge from 0.8 μm (0 %) to 1.5 μm (20 %).

[18] S. D. Hart, G. R. Maskaly, B. Temelkuran, P. H. Prideaux, , J. D. Joannopoulos, and Y. Fink, , “External reflection from omnidirectional dielectric mirror fibers”, *Science* **296**, 511-513 (2002).

[19] G. Benoit, S. D. Hart, B. Temelkuran, J. D. Joannopoulos, and Y. Fink, “Static and dynamic properties of optical micro-cavities in photonic bandgap yarns,” *Adv. Materials* **15**, 2053-2056 (2003).

[20] These glasses belong to the same family of chalcogenide glasses that we used in the construction of the fibers discussed in this paper. The only difference is in the change of the chemical formula for the glass. For example, Te-rich glasses have a high thermo-electric coefficient.

[21] H. G. Wells, *The Invisible Man: A Grotesque Romance* (Modern Library, New York, 2002).

Invited Paper

# Low Cost Replicable Plastic HUD combiner element

**Bernard Kress, Victorien Raulot, Pierre St Hilaire (*), Patrick Meyrueis**
Photonic Systems Laboratory (LSP), Universite de Strasbourg, 67400 Illkirch, France
(*) All View Research LLC, All View Way, Belmont, CA 94065, USA

**ABSTRACT**

We present a novel technique to fabricate low cost mass replicable plastic HUDs for the transportation industry. HUD are implemented in numerous sectors today (in avionics, automobile, military, machinery,…). Typical implementations include an optical combiner which produces the desired virtual image while leaving the field mostly unaffected by the optics. Such combiners optics are usually implemented as cumbersome catadioptric devices in automobile, dichroic coated curved plates, or expensive volume holograms in commercial and military aviation.
We propose a novel way to design, model and fabricate combiner masters which can be replicated in mass by UV casting in plastic. We review the various design techniques required for such elements and the novel mastering technology.

**Keywords**: Head Up Display, Helmet Mounted Displays, Holography, Diffractive Optics, Plastic embossing.

Photonics in the Transportation Industry: Auto to Aerospace II, edited by Alex A. Kazemi, Bernard C. Kress
Proc. of SPIE Vol. 7314, 73140I · © 2009 SPIE · CCC code: 0277-786X/09/$18 · doi: 10.1117/12.821372

## 1. INTRODUCTION

The transportation industry is a heavy user of displays today. Avionics have usually introduced the technology which has been adapted afterwards to the automotive industry. This is the case for flat panel displays (CRTs, LCDs and more recently OLEDs) displays, which are now becoming standard features in cars for GPS and video display, and touch screen displays based on the same technology. This is also true for Head Up Displays (HUDs). HUDs have been introduced to avionics in the 1960s, and have been transferred to automotive in the early 1990s, first in police and other specialized vehicles, and today in higher class cars, such ash the Chevrolet Corvette; the Pontiac Grand Prix, in Mercedes, BMW and the Citroen C6. In most cases; the technology consists of an optical combiner and a display system incorporating imaging optics (see fig.1) [1].

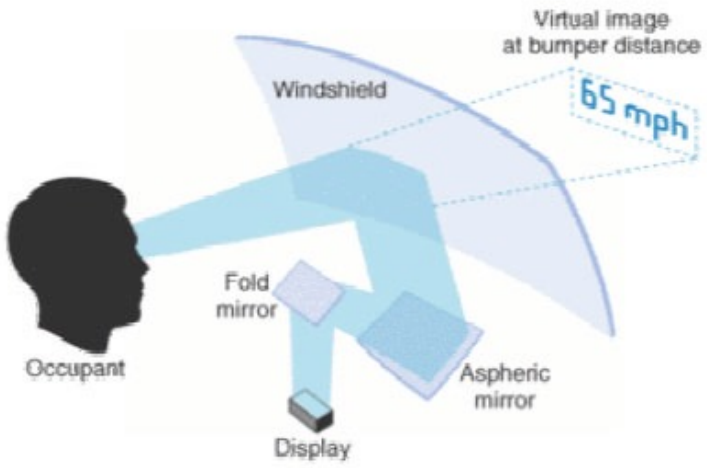


*Fig.1: Conventional HUD architecture in automotive today.*

The optical combiner is a key element in the HUD system. We review below the various combiners used today in the transportation industry.

## 2. HUD SYSTEMS AVAILABLE TODAY IN INDUSTRY

### - HUD systems using holographic combiners

Holographic combiners are volume Bragg gratings which are acting as transparent plates for the incoming field and reflection or transparent holograms for the display to be superimposed on the field. Such elements can introduce imaging characteristics which are very desirable since the number of imaging optics can be reduced dramatically (footprint, weight, volume). In the case of reflection holograms, the Bragg planes are nearly parallel to the substrate, whereas in transmission holograms, the Bragg planes are more or less normal to the substrate. Holographic combiners have been introduced very early, for military avionics applications. HUDs based on volume hologram combiners are very performant and relatively small, but have a short lifetime due to the deterioration of the organic polymer composing the holographic media (Dichromated Gelatin –DCG-, Silver Halides, Photopolymers, …), under UV, humidity and high temperature exposure. Furthermore, most holograms are not perfectly transparent to the field, and therefore create a darkened field area which can be dangerous for the driver during night operation.

**- HUD systems using curved dichroic combiners**

Dichroic combiners are made of several thin films which act as a mirror for a specific illumination angle and color (the HUD display), and as a transparent substrate for other angles (i.e. the field). When curving the dichroic substrate, one can introduce a diverging lens functionality which will produce in the driver's field of view a virtual image floating in front of the vehicle. Such combiners can be made of plastic [2] and can thus be replicated with relatively low costs by plastic molding followed by a thin film coating. However, such combiners need to have a non planar surface in order to implement optical imaging; which is in most cases not desirable, especially in automotive applications. Similarly to holographic combiners, dichroic combiners are not completely transparent, tend to have a color hue and thus darken the field.

**- HUD systems using catadioptric optics and windshield combiners**

Using the windshield as the natural combiner element seems to be the most straightforward way to implement an HUD in the automobile industry. However, this configuration poses several problems. First, the windshield has to be relatively reflective on its first surface to produce enough brightness in the image when viewed in sunlight. Second, parasitic reflections from the outer surface of the windshield (or from intermediate surfaces) should be reduced to avoid ghosts. Third, the curvature of the windshield (different from car to car) has to be compensated in the design of the large catadioptric reflective mirrors used to produce the virtual image (usually buried within the dashboard). Fourth, a large amount of space is used to produce the relay optics in the dashboard to produce the desired image. Nonetheless, this technique is now implemented in many high end cars on the market (Corvette, etc…).

**- Other HUD systems.**

Other combiner technologies have been proposed in order to alleviate the problems encountered with the previous three technologies. These include projecting an infrared image onto a doped windshield which would in turn produce a fluorescent image [3] to the driver. However, this image will be located in the windshield, not in front of it. Another technique consists of using a laser scanner a projecting a wire framed or pixelated image in full RGB colors in the far field, by using a flat combiner [4], or by using a dynamic holographic projector to project an image in the far field [5].

## 3. REQUIREMENTS FOR HUD IN AUTOMOBILE

In order to define a better way to design an optical combiner for HUD applications, let us review the various requirements [6] for HUD combiners:

a) - an HUD combiner for automotive has to integrate both the combining and imaging functionalities (no large optics hidden in the dashboard)
b) - an HUD combiner for automotive has to be cheap, and mass replicable.
c) - an HUD combiner for automotive has to be transparent to the field (neither darkening nor coloring the field)
d) - an HUD combiner for automotive has to be safe, therefore should be made of plastic instead of glass.
e) - an HUD combiner for automotive should be as small as possible, and integrate all the functionalities in the substrate (potentially also the display generation).

## 4. DIGITAL DIFFRACTIVE COMBINER SOLUTION

In order to address the various requirements described in the previous section, we propose to use a plastic diffractive combiner replicable in mass by UV embossing. Our first architecture works in transmission with an LED or laser pico-projector (see fig.2).

- Full color is achieved by time sequencing the three colors generated by three lasers (or LEDs) and a single microdisplay.

- Optical power is achieved by the introduction of an off-axis Diffractive Fresnel lens phase profile [7],[8] which is optimized for the off-axis illumination scheme described in fig.2.

- Diffraction of the three wavelengths is achieved by the use of Harmonic (or multi-order) diffractive structures, a technique that has been developed originally for hybrid optics [9] [11].

- High overall diffraction efficiency through effective analog surface relief elements is achieved by binary sub-wavelength grating carriers [8], which implement an effective refractive medium (EMT: Effective Medium Theory) [10], [12], [13]. Therefore, although the structures constituting the element are sub-wavelength, the resulting diffracted angles remain small (several degrees).

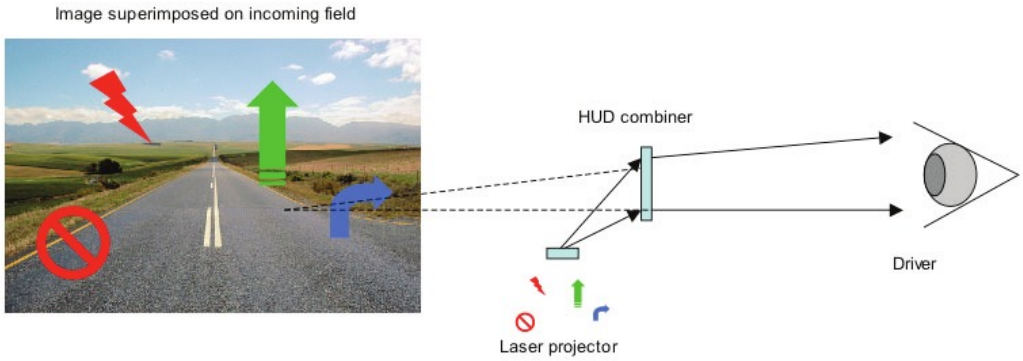


*Fig.2: Digital diffractive HUD combiner architecture*

## 5. DESIGN OF THE DIGITAL DIFFRACTIVE COMBINER ELEMENT

The basis of our HUD combiner architecture resides in the way it discriminate between the diffraction efficiency at one (or several) specific wavelengths for a fixed angle (the projected image onto the combiner), and the diffraction efficiency of the wide spectrum incoming field (which is relatively normal to the combiner). In an ideal case, the first should be maximal and the latter minimal. This can be achieved by slanting the sub-wavelength gratings into a direction that produces the highest efficiency for the laser illumination and the lowest efficiency for the incoming field.
We are thus triggering the effects of volume hologram Bragg gratings (spectral and angular bandwidths in the various Bragg regimes) with a thin diffractive element with tilted sub wavelength structures.
The whole gamut of optical design techniques are used for our digital element (see Fig.3), beginning with ray tracing in a conventional optical design program to compute the aspheric

phase profile, to fringe generation and broadband diffraction operation through scalar diffraction theory to rigorous electromagnetic methods through the effective medium theory (EMT).

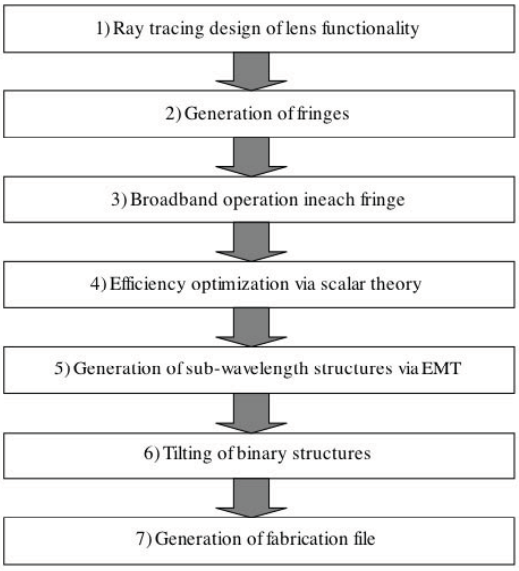


*Fig.3: Flow chart of the design process for our digital diffractive combiner.*

## 7. FABRICATION TECHNIQUES USED TO PRODUCE THE COMBINER MASTER

### a) Conventional mastering techniques

Conventional fabrication of microstructures that can yield high efficiency such as multilevel surface relief elements [14] [15] can be performed by optical lithography using several successive masking layers (see fig. 4).

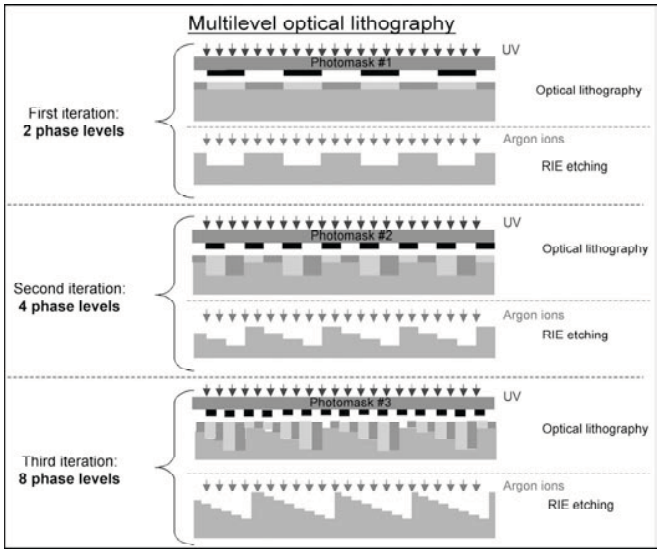


*Fig.4: Conventional fabrication technology*

**b) Optimized techniques for slanted gratings**

In order to produce more complex structures required to produce the diffraction efficiency selections from wavelength and angle, we propose to use a fringe writing technology linked to a fringe locking scheme as depicted in Fig. 5.

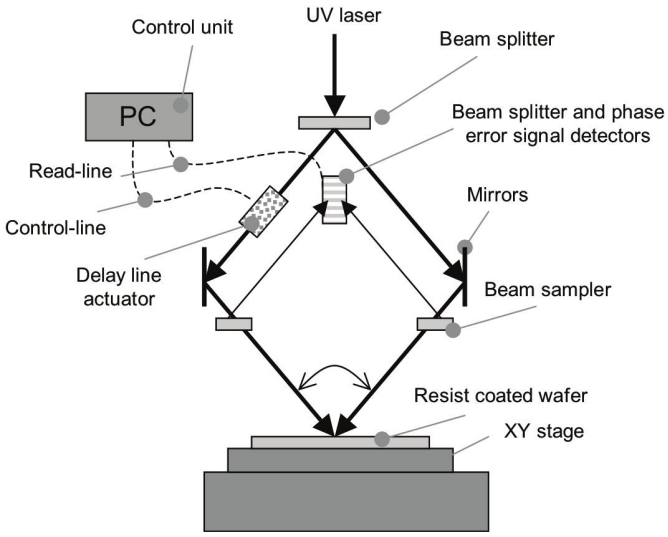


*Fig.5: Direct holographic write in thick resist with a fringe locker*

Such a fringe write can produce slanted gratings and other type of structures which cannot be produced by traditional lithography methods.

## 8. REPLICATION TECHNIQUES TO MASS PRODUCE THE COMBINER

The replication of our diffractive combiners will be performed in plastic sheets by UV embossing or roll embossing (see fig.6), or even with nano-imprint techniques [16].

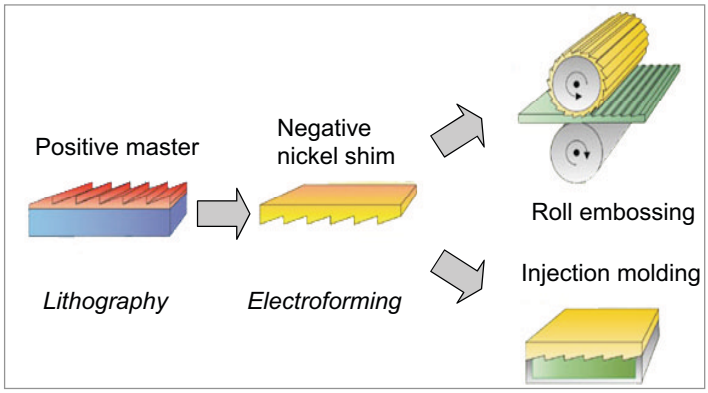


*Fig. 6 Mass replication of diffractive structures using embossing or injection molding*

## 9. FIRST EXPERIMENTAL RESULTS

We have fabricated the first generation of digital diffractive combiners in a quartz substrate. The combiner is shown in Fig.7 as well as the surface topology of test structures implementing the EMT effective index.

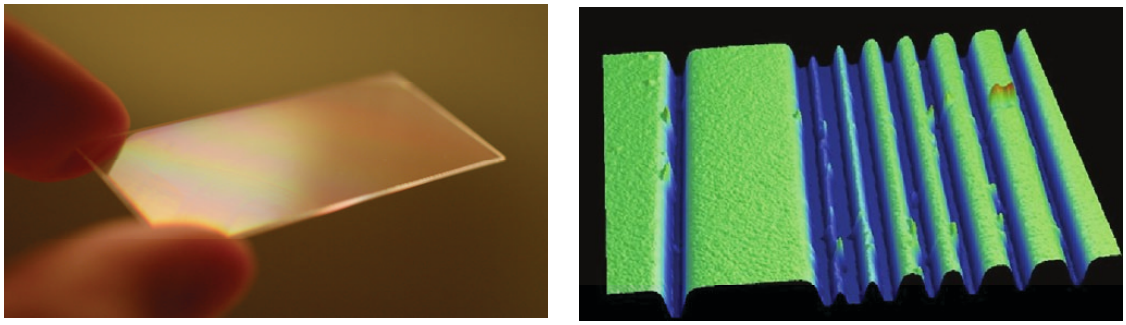

*Fig. 7: First generation digital diffractive combiner and surface topology of test structures implementing the EMT effective index.*

Fig. 8 shows the first optical experiments with this combiner on an LCD display in transmission. The original object (image on the microdisplay) is shown on the top part. The focus is set on the microdisplay color pixels. We show here the results through two off-axis diffractive combiner lenses, one with standard binary structures, and the other with subwavelength EMT structures. The digital combiner on the lower left side has been lithographically patterned as a conventional binary off-axis diffractive lens, thus yielding two conjugate orders, carrying both the virtual and real images generated by the microdisplay.

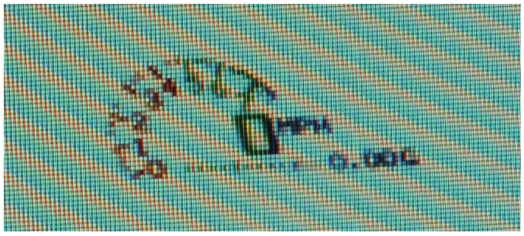

Original object on HUD microdisplay (focus is on the color microdisplay pixels)

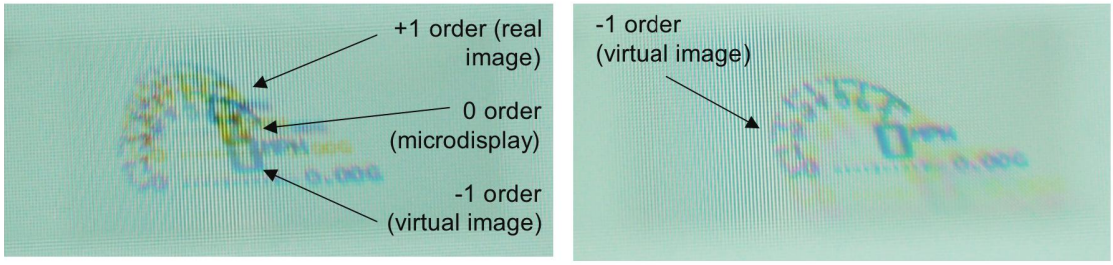


Binary lens without standard structures

Binary lens with sub-wavelength EMT structures

*Fig. 8. First optical tests on digital binary combiners*

The digital combiner on the lower right side has been fabricated with binary vertical sub-wavelength EMT structures, this yielding only one diffraction order, carrying the virtual image of

the microdisplay. The microdisplay used was here a simple color LCD screen, thus showing that such combiners (both in conventional and EMT modes) can produce decent images with sources that have neither temporal nor spatial coherence. However, for better efficiency and a sharper image, a laser pico-projector will be used.

## 10. CONCLUSION

We have proposed a novel way to design and fabricate a planar digital HUD combiner that can be replicated in mass by plastic embossing. The digital combiner mimics the traditional angular bandwidth of thick volume Bragg holograms with thin plastic sub-wavelength tilted binary structures. First prototypes have been using EMT theory and conventional lithography. Next prototypes will be fabricated as slanted structures by a fringe writer with phase locking capabilities.

## ACKNOWLEDGEMENTS

We wish to thank Prof Bruno Serio for the surface topology measurements on the generation 1 digital binary combiner.

## REFERENCES

[1] Yvonne Carts-Powel, Laser Focus World, March 2005.
[2] AC Delco / Huges /GM automotive HUD display for law enforcement vehicles
[3] http://www.superimaging.com
[4] http://www.microvision.com
[5] http://www.holoeye.com
[6] “Quantifying HUD pedestrian detection benefits for older drivers,” RJ Kiefer, Proceedings of the 16th International Technical Conference on the Enhanced Safety of Vehicles (1998), NHTSA Paper 98-S2-0-10
[7] K. Miyamoto, “The phase Fresnel lens”, JOSA 17 (1961), 17-21.
[8] S. Sinzinger et al: «Transition between diffractive and refractive micro-optical components», Applied Optics, Vol.34, No.26, 5970-5976, (1995).
[9] H-P. Herzig, “Micro-Optics: elements, systems and application”, Taylor and Francis, London (1997)
[10] R. Petit, “Electromagnetic theory of gratings”, Spriger Verlag, Berlin (1980)
[11] W.Li et al: «Hybrid diffractive refractive broadband design in visible wavelength region», SPIE Vol.2689, 101-110, (1996)
[12] M.E. Motamedi, et al, “Antireflection surfaces in Silicon Using binary Optic Technology,” Applied Optics, 1 August 1992, Vol, 31, No 22, pp 4371-4376. Farn 1992
[13] H. Haidner, et al, “Zero-order gratings used as an artificial distributed index medium”, *Optik* 89, 107-112 (1992).
[14] G.J. Swanson, «Binary optics technology: The theory and design of multi-level diffractive optical elements», MIT/Lincoln Lab Technical Report 854, (1989).
[15] Daeschner, et al, “One step lithography for mass production of multilevel diffractive optical elements using High Energy Beam Sensitive (HEBS) grey-level masks"” Proc. SPIE Vol. 2689, pp. 153-155, 1996
[16] B. Kress and P. Meyrueis “*Digital Diffractive Optics*” (published 09/2000) and “*Applied Digital Optics: from Micro-Optics to Nano-Photonics*” (published 02/2009), edited by John Wiley and Sons, Chichester, UK.
[17] Nano-Opto Corp. Sommerset, NJ. USA (*www.nanoopto.com/files_tech.html)*

# LOW COST, HIGH DATA RATE WHITE LED (WLED) TRANSCEIVER DEVELOPMENT

Eric Chan, Dennis Koshinz, William Krug and Harold Hager
Boeing Research and Technology, Seattle, Washington, USA 98124-2207

## ABSTRACT

Recently there has been strong interest in wireless white LED (WLED) communication link applications in airplanes and avionics platforms for size, weight, cost, and electromagnetic interference (EMI) reduction. Wireless WLED link has additional advantage of providing network security because the optical signal from WLED link is well confined within an airplane or avionics vehicle. In this paper we discuss and analyze commercial-off-he-shelf WLED design and color measurement results. An experimental implementation of a low cost WLED transceiver which shows error free free-space operation at 10Mb/s is successfully demonstrated. The feasibly of implementing free space optical link which meets both lighting and communication requirements using WLED array is analyzed by mathematical modeling using MATLAB simulation technique.

**Keywords:** White LED (WLED), transceiver, free space optical link, wireless WLED link, EMI, network security

## 1. INTRODUCTION

Recent publications [1] [2] have drawn considerable interest in using white LED (WLED) for wireless communication in airplanes and space vehicles. WLED is already widely accepted as the lighting for our future environment. Using WLED wireless communication in airplane has great potential for size, weight, power, cost and EMI reduction; this is because of the following reasons:

1) EMI immunity improvement-Using the lighting WLEDs for communication reduces the wirings needed to use in the airplane.
2) Power Saving-Communication using WLED which is already powered for lighting, it minimizes additional power needed for communication.
3) Low cost-WLED is a mature component technology in the lighting industry; WLEDs are low cost and highly reliable.
4) Network Security-As compare to RF signal, WLED optical signal is confined by walls and closed compartments, it cannot be tapped externally.
5) No licensing issues-WLED communication links do not require licensing like RF links which need government agency approval for the spectrum being used.

While there are extensive publications in analyzing wireless WLED communication networks and topologies, the technology readiness level (TRL) for transition to avionics applications is still in its early stage. Establishing an infrastructure that supplies the components to build the avionics networks economically is very crucial to achieve the goal of WLED communication links in airplanes and space vehicles. In this paper, we explore the feasibility of implementing transceiver with low cost commercial-off-the-shelf (COTS) WLED; the results are significant for understanding the technical issues for wireless WLED transceivers to be used in airplane's communication networks.

## 2. WHITE LED TECHNOLOGY

There are two types of COTS WLEDs; the first type is a device which combines the red, green and blue (RGB) LEDs to provide a broad white light spectrum. The second type is a blue InGaN LED coated with YAG phosphorous. The blue LED emission excites the phosphor to emit yellow light; the combined spectral output of the LED is a broadband white spectrum. This type of LED is called the phosphorous converted white LED (PC-WLED).

Photonics in the Transportation Industry: Auto to Aerospace II, edited by Alex A. Kazemi, Bernard C. Kress
Proc. of SPIE Vol. 7314, 73140J · © 2009 SPIE · CCC code: 0277-786X/09/$18 · doi: 10.1117/12.821115

## 2.1 Tri-color WLED

The tri-color LED combines the red (R), green (G) and blue (B) LED in one package to produce the white color spectrum. Blue and green LEDs are made of InGaN material, the red LED is made of either GaAsP or AlInGaP material. Figure 1 shows a tri-color WLED in a single 5 mm epoxy dome shape package with 4 electrical leads. With the LED chips are mounted in junction-side down configuration, it has one lead for the cathode of each LED and a lead for the common anode. The color spectrum of the each individual LEDs are show in Figure 2(a), the combined white spectrum of the tri-color WLED is shown in Figure 2(b). The spectrum of Figure 2(b) is the superposition of the color spectrum of the three individual colors of the RGB LEDs. Figure 3 shows the chromaticity diagrams of the RGB LEDs and the combine white LED output. The tri-stimulus value of the combined white LED output lies within the RGB color triangle as shown in Figure 3(d).

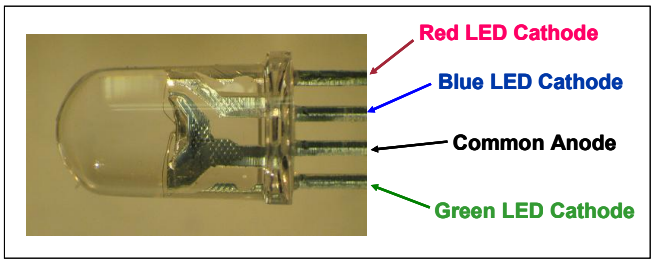


Fig. 1. Tri-color white LED package in a 5 mm epoxy dome shape header with 4 electrical leads.

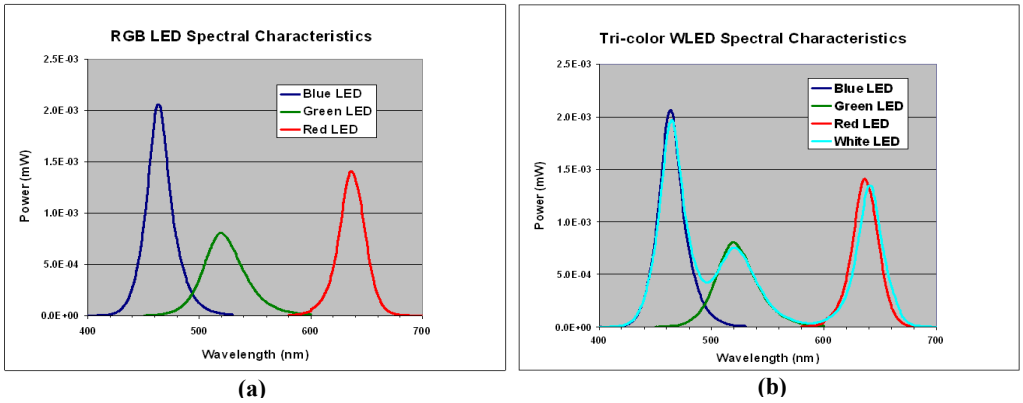


Fig. 2. (a) Spectrum of each LED in the tri-color LED package shown in Fig. 1. (b) Combined spectrum of the red, green and blue LED in the same package.

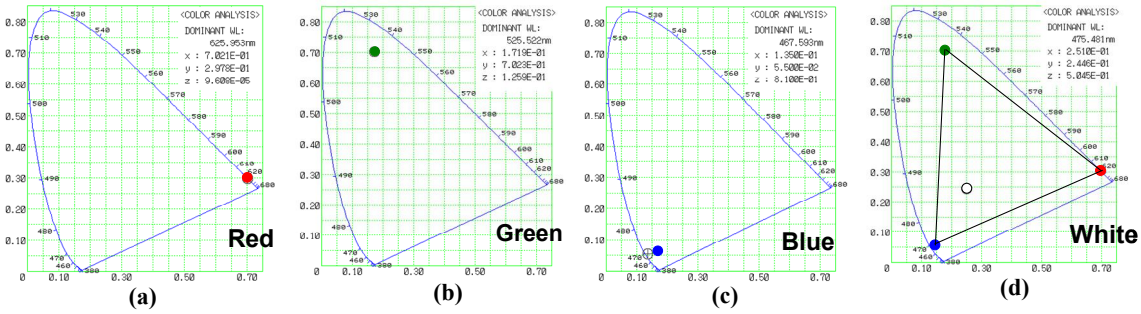


Fig. 3. Chromaticity diagram for (a) Red LED (b) Green LED (c) Blue LED and (d) Combined white LED.

## 2.2 PC-WLED

PC-WLED is made of InGaN blue LED with a uniform conformal coating of a YAG phosphor layer. Phosphor emits yellow light when excited by the blue LED light emitted from the InGaN LED. The combined light output produces the white color spectrum. Figure 4(a) shows the packaging of a PC-WLED in a 5 mm dome shape epoxy package with two electrical leads. Figure 4(b) shows the detail of the PC-LED chip packaging. The InGaN LED die is flip chip bonded on a submount which functions as a heat sink to the LED to dissipate the heat when the LED is turned on. The coated LED chip with the submount is attached at a cup-shape pedestal with side reflector to enhance the efficiency of the WLED output. The spectrum of a PC-WLED is shown in Figure 5; it has a blue peak at 453.5 nm and a yellow peak at 545 nm. The combined spectrum has a center wavelength (λc) at 520.6 nm and spectral width (Δλ) of 124.3 nm.

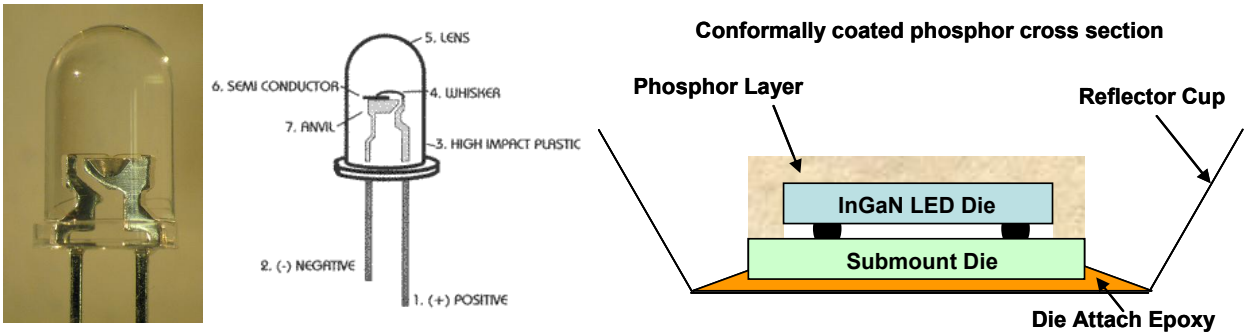


Fig. 4. (a) Photo and circuit of a PC-WLED in a 5 mm dome shape header and (b) Details of PC-WLED packaging schematic.

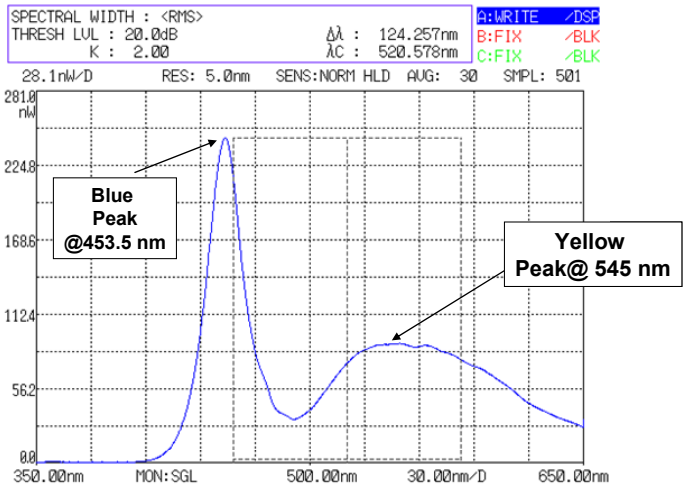


Fig. 5. Spectrum of the PC-WLED shown in Figure 4.

## 2.3 Color comparison of tri-color WLED to PC-WLED

The chromaticity diagrams of the tri-color WLED and the PC-WLED are shown in Figure 6(a) and (b) respectively. The tri-stimulus values of these two types of LED are distinguishable from these diagrams. The Tri-color WLED has color rendering index (Ra) about 85 and correlated color temperature (CCT) about 4500°K. The PC-WLED has (Ra) about 75 and CCT about 4000°K. Therefore the PC-WLED exhibits a warmer white color characteristic; it has only two electrical terminals which simplify the design of the transmitter in communication link application. In the following sections, a PC-WLED transceiver characteristics are described.

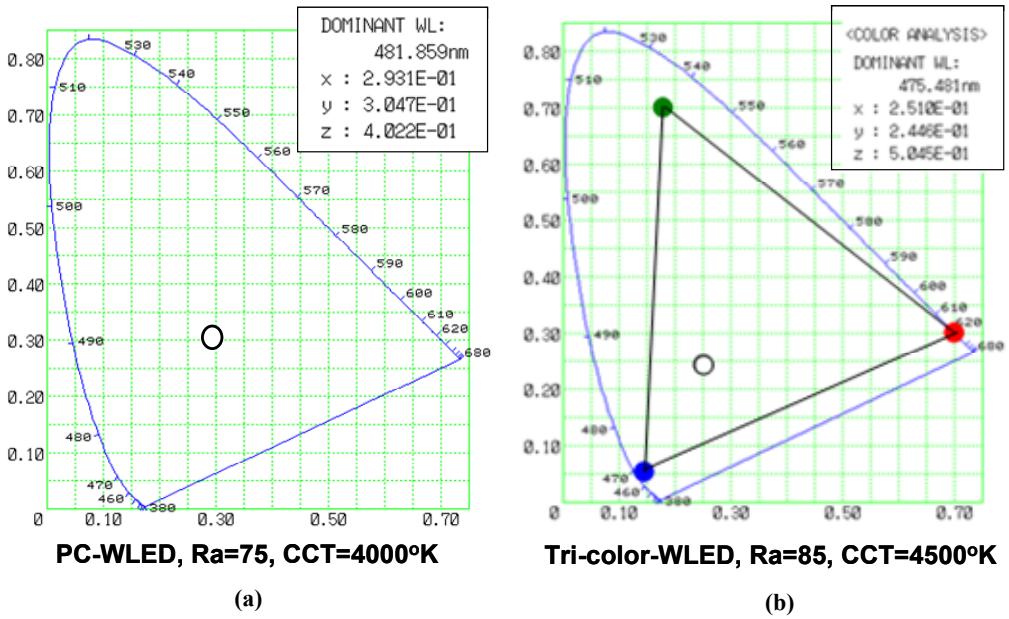


Fig. 6. Chromaticity diagram of (a) a PC-WLED (b) a tri-color WLED.

## 3. THE TRANSCEIVER

The WLED transceiver is fabricated by retrofitting a PC-WLED and a silicon PIN-TIA (p-intrinsic-n detector with trans-impedance amplifier) to a standard 1x9 single-in-line (SIL) Fast Ethernet transceiver with emitter couple logic (ECL) interface. It has a transmitter (Tx) and a receiver (Rx) ASIC on a multi-layer printed wiring board (PWB). The silicon PIN-TIA is a COTS device designed for 1 mm plastic optical fiber (POF) applications. It is housed in a TO-18 header with a semi-spherical lens. The WLED is housed in a molded epoxy header with a dome shape surface to provide a viewing angle typically around 25 degree. Figure 7(a) shows the block diagram of the transceiver design; Figure 7(b) shows a photograph of the PC-WLED transceiver assembled using the low cost chip-on-board (COB) technology.

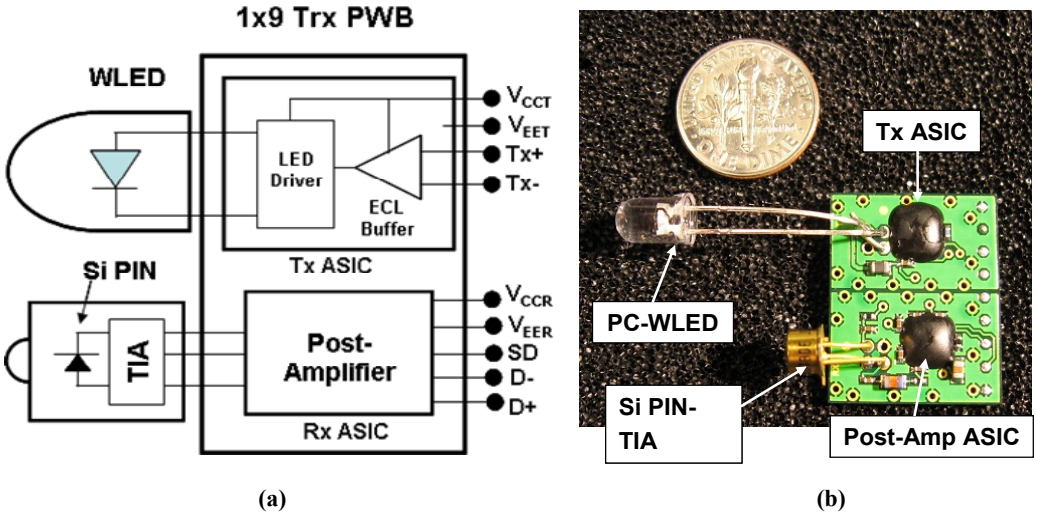


Fig. 7. (a) Schematic block diagram of a PC-WLED transceiver. (b) The transceiver in a chip-on-board 1x9 SIL package.

## 4. TRANSCEIVER TEST SET UP AND RESULTS

Figure 8(a) is a block diagram of the WLED transceiver (trx) test set-up. The transceiver is mounted on a COTS 1x9 ECL transceiver test board. A one meter length of 1-mm diameter plastic optical (POF) is coupled to the WLED on one end, and to the PIN-TIA on the other end. The alignment of the POF to the WLED and the PIN-TIA on both ends of the POF are actively optimized for maximum power coupling. The one meter POF facilitates the loop-back test on the receiver, and it also functions as a variable attenuator by varying the distance D between the POF and the WLED, this allows measurement of the receiver sensitivity at the desired bit-error-rate (BER). Figure 8(b) shows a photograph of the PC-WLED transceiver powered up on a 9-pin transceiver test board.

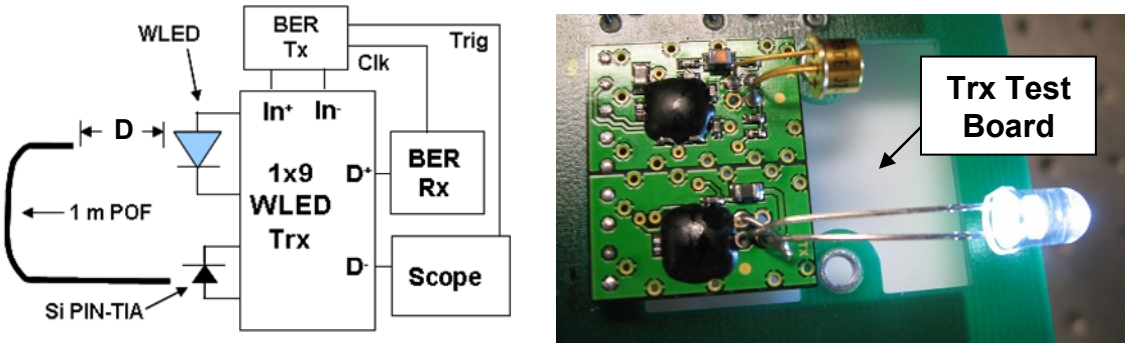


Fig. 8. (a) Block diagram of a PC-WLED transceiver test set up. (b) Photo of the transceiver powered up on the test board.

After the power of the transceiver was turned on, the receiver eye diagrams were measured at various distances, D. Operating the transceiver at 10Mb/s with OOK NRZ modulation, and 2^7-1 Pseudo-random-bit-sequence (PRBS) pattern, error free transmission up to D=4 cm was accomplished. Then the spacing D was kept increasing until BER=1E-6 was observed. At this step, the POF average output power at the receiver end was measured with a power meter; it was around -24.3 dBm at the PC-WLED center wavelength. Figure 9 (a) and (b) show the receiver eye diagrams at D=5 mm and D=4 cm respectively.

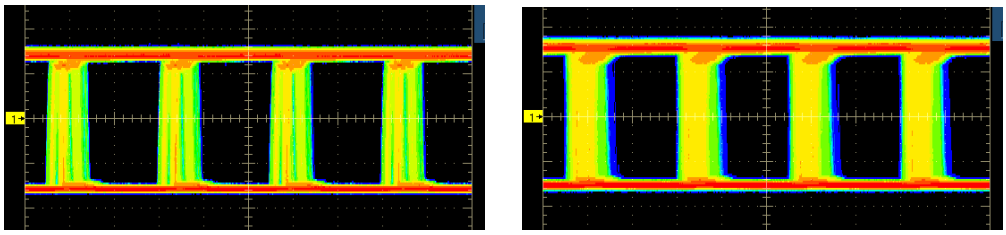


Fig. 9. (a) Eye diagram of the receiver at D=5 mm. (b) Block diagram of the receiver at D=4 cm.

After determining the Rx sensitivity, we have validated the PC-WLED transceiver communication link performance; next we set up a bi-directional free space optical link measurement experiment with two PC-WLED transceivers (labeled as Trx1 and Trx2) at various separation distances (d). The test set up is shown in Figure 10. At d>0.14 m, the bit-error-rate starts to degrade below the desired 1E-6 value. Then we switched to measure the illuminace of the WLED on Trx1 at a few selected distances. Figure 11 shows the set up that is used to perform distance vs. illuminance measurement, a lux meter with a remote sensor head mounted on the x-y-z stage on an optical rail is used to measure the illuminance of the WLED on Trx1 at selected distances, the results are shown in Table 1. These results are used in the WLED array simulation described in Section 5.

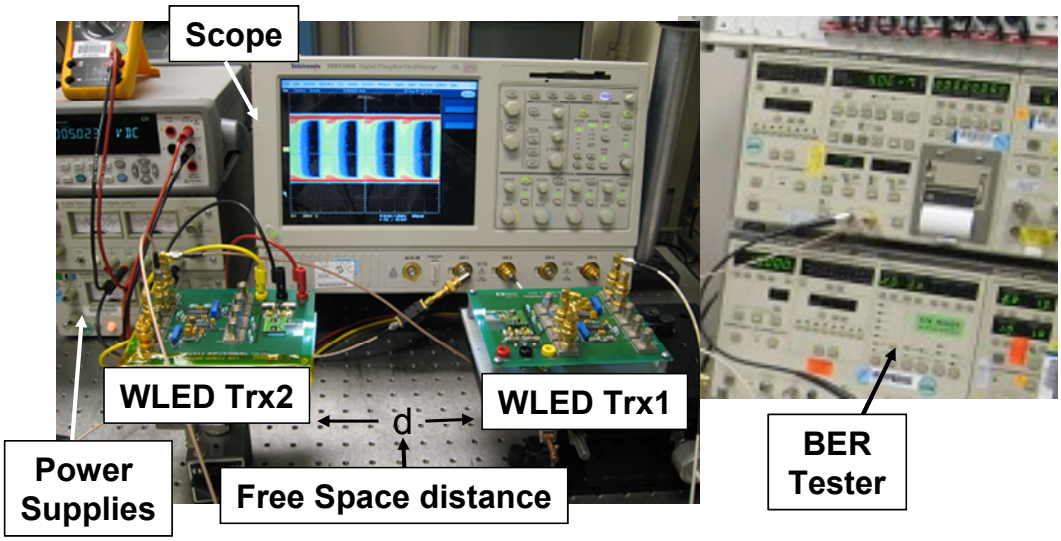


Fig. 10. WLED transceiver free space optical link measurement set up.

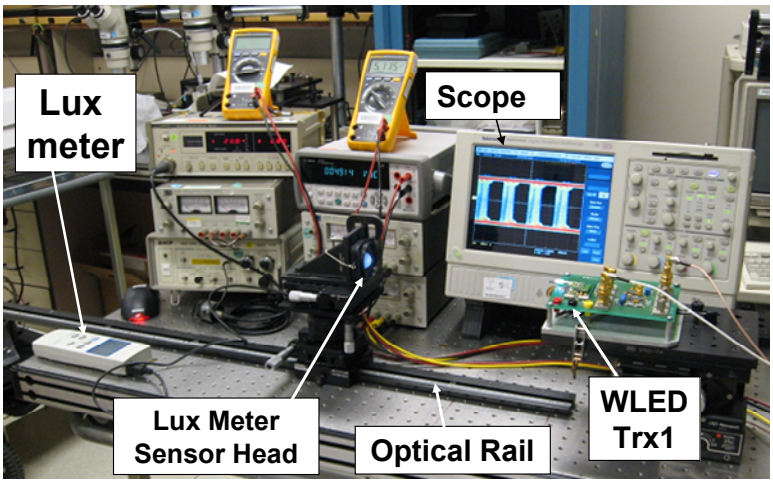


Fig. 11. WLED Distance vs. Illuminant measurement set up.

Table 1 Distance vs. Illuminance

| d (meter) | Lux |
|---|---|
| 0.14 | 390.00 |
| 0.50 | 31.00 |
| 1.00 | 7.80 |
| 2.00 | 2.00 |

## 5. WLED ARRAY APPROACH

The results from the above Sections demonstrated the optical link performance of a single WLED, for a practical optical link operation inside an airplane required the output of an arrays of WLED to meet the requirements of both illumination and communication operation. The results in Table 1 shows a minimum of 390 lux is required for proper optical link operation. We derive the proper WLED array design for application in an airplane using mathematical modeling with a MATLAB simulation program. Using Gaussian approximation, for the WLED array lighting distribution on a flat x-y planner surface is described by Equation (1), where d=WLED array distance from the surface, θ=WLED half power angle, $I_v$=Peak Illuminance, N and M are the number of WLEDs in the array's x and y directions.

$$\sum_{m=1}^{M}\sum_{n=1}^{N} I_v \exp\left[(-\ln(2))\times\left(\frac{(x-x_o(n))^2-(y-y_o(m))^2}{(d\times\tan(\theta))^2}\right)\right] \quad (1)$$

### 5.2. Single WLED array simulation

Figure 12 shows the schematic diagram of a WLED array with length (a) in x-direction and width (b) in y-direction, the illuminated surface has length (L) in the x-direction and width (W) in the y-direction. The WLED array is at distance d above the surface being illuminated. Figure 13 shows the MATLAB simulated results for d=1 meter, L=W=1 meter, a=b=0.2 m, M=N=8, half power angle $\theta=30^{o}$, total number of WLEDs in the array=64. The simulation results show over 75% of the surface area (above the yellow region) has sufficient signal strength for good communication links, and 90% of the surface has sufficient illuminance to meet passenger lighting requirement.

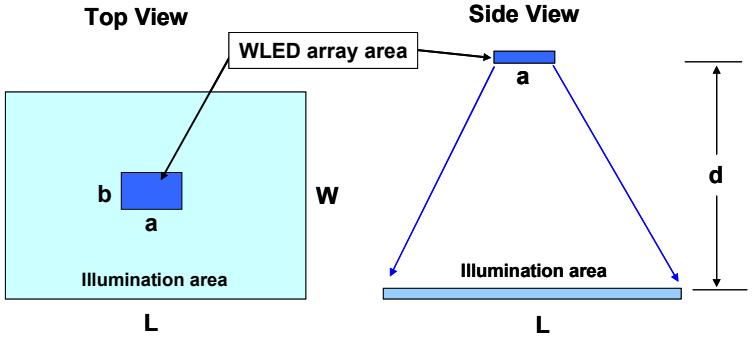


Fig. 12. Schematic diagram of a single WLED array used for simulation.

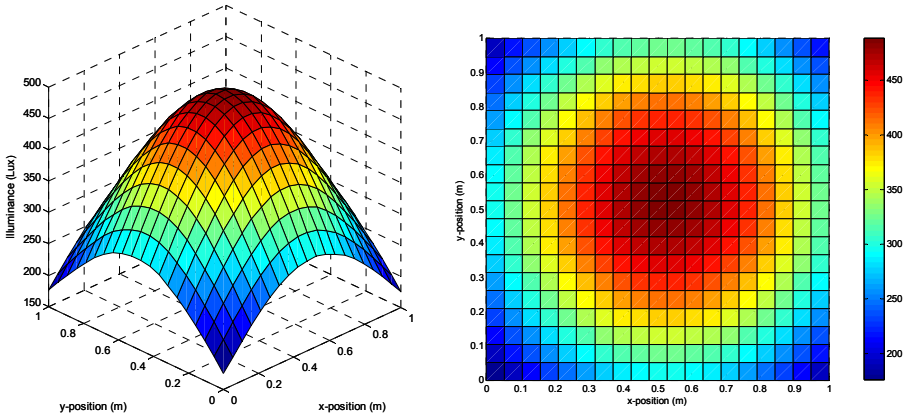


Fig. 13. Simulation result for a single WLED array output on the illuminated surface shown in Figure 12.

### 5.2. Three WLED array simulation

For application with passengers seating side-by-side in a row, three WLED arrays are required. Figure 14 shows the schematic diagram of three LED arrays, each with length (a) in x-direction and width (b) in y direction; each of the illuminated surfaces has length (L) in the x-direction and width (W) in the y-direction. The three WLED arrays are at distance d above the three surfaces being illuminated. Our simulated results show that without changing the half power angle, there will be a large communication signal cross-talk between each passenger. Figure 15 shows the MATLAB simulated results for d=1 meter, L=W=1 meter, a=b=0.2 m, M=N=8, half power angle $\theta=15^{o}$, total number of WLEDs in each array=64. The simulation results show over 50% of each surface area (above the yellow region) has sufficient signal strength for good communication links, and 80% of each surface area has sufficient illuminance to meet passenger

lighting requirement. The WLED signal for each passenger is well confined to the center location of each passenger; the communication signal cross-talk is minimized.

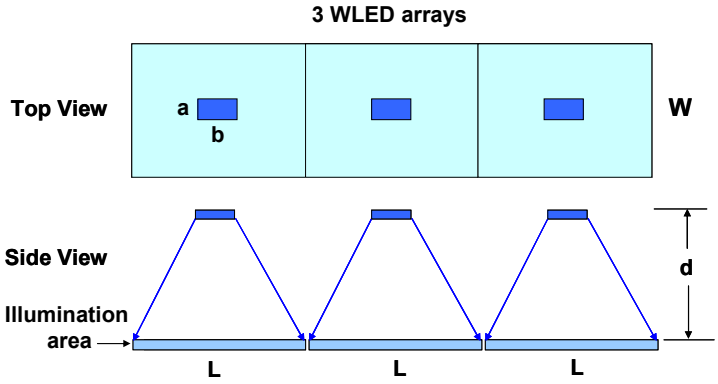


Fig. 14. Schematic diagram of the three side-by-side WLED arrays used for simulation.

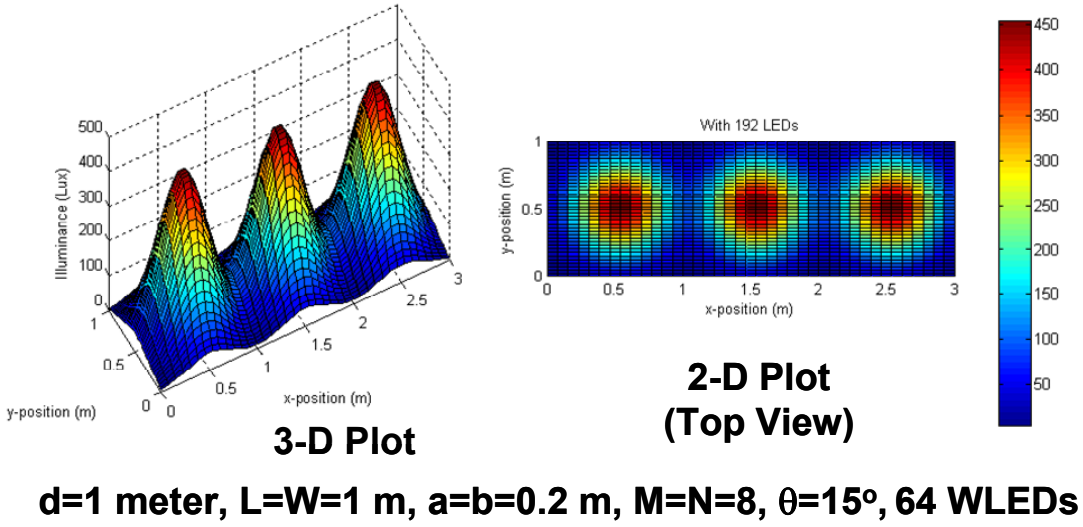


Fig. 15. Simulation result for three WLED arrays' output on the illuminated surface shown in Figure 14.

## 6. CONCLUSIONS

We have described a low cost experimental WLED transceiver implementation which is capable to perform wireless communication at 10 Mb/s in an airplane or a space craft physical environment. From the experimental results, we derived the operational requirements of the WLED transceiver with OOK NRZ modulation. We presented an analytical model to derive the WLED array size and dimensions based on the individual WLED characteristics in the array. These results demonstrate the WLED wireless communication link technology is viable for size, weight, power, cost and EMI reduction in future generation of airplanes and mobile avionics platforms.

## REFERENCES

[1] Mohsen Kavehrad, "Broadband Room Service by Light," Scientific America, pp. 82-87, July 2007.

[2] Yuichi Tanaka, et al, "Indoor Visible Light Data Transmission Utilizing White LED Lights," IEEE Trans. Communication, Vol. E-86-B, No. 8, pp. 2440-2454, August, 2003.

# Space Based Laser Cross-Link Systems used in Satellite Communications

Allen Panahi*
Accro USA LLC, Pasadena, CA91117
&
Alex A. Kazemi
Accro USA LLC, Pasadena, CA91117

## ABSTRACT

Space-based optical communications using satellites in low earth orbit (LEO) and Geo-synchronous orbits (GEO) hold great promise for the proposed Internet in the Sky network of the future. Building high speed communications network using optical links in space has proven to be an extremely complicated task and many such schemes were tried without success in the past. However in the last few years, there has been impressive progress made to bring the concept to fruition in civilian and government-non classified projects. Laser Communications offer a viable alternative to established RF communications for inter-satellite links and other applications where high performance links are a necessity. High data rate, small antenna size, narrow beam divergence, and a narrow field of view are characteristics of laser communications that offer a number of potential advantages for system design. This paper will focus on the requirements of the space-based lasers and optics used for beam forming, as well as receiver antenna gain and detectors used in free space communications. Also discussed are the critical parameters in the transmitter, channel, receiver, and link budget that are employed in successful inter-satellite communications system.

**Key Word:** Space Based Cross Link, Laser Communications, RF, High Data Rate

## 1. INTRODUCTION

Space-based optical communications using satellites in low earth orbit (LEO) and Geo-synchronous orbits (GEO) hold great promise for the proposed Internet in the Sky network of the future. Building high speed communications network using optical links in space has proven to be an extremely complicated task and many such schemes were tried without success in the past. However in the last few years, there has been impressive progress made to bring the concept to fruition in civilian and government-non classified projects. The successful trial tests in space conducted by Japan and the European space agency as well as NASA show the time for successful deployment of this technology is in the realm of reality. The US military has a lot of interest in such systems for building the next generation Transformational Satellite Systems commonly known as (TSAT). To-day's market for space based optical communications is primarily Inter-Satellite Links (ISLs) which are the main focus of this paper. There is also a need for high data rate (Multi-gigabit) space-earth links, although the propagation effects due to atmosphere and weather make it a more difficult link to implement in spite of the many advance made in Adaptive optics technology and Signal Processing algorithms. These orbiting satellites are LEO – LEO or GEO - GEO that cross-link the constellation by communicating amongst each other with additional capability to beam data to ground stations. A picture of the optical cross-link in space is depicted in the figure1. The table1 below Table lists the pros and cons of point to point versus cross-link satellites.

* Corresponding author e-mail address: allen.panahi@verizon.net

Photonics in the Transportation Industry: Auto to Aerospace II, edited by Alex A. Kazemi, Bernard C. Kress
Proc. of SPIE Vol. 7314, 73140K · © 2009 SPIE · CCC code: 0277-786X/09/$18 · doi: 10.1117/12.821346

The usual parameters that systems designers want to optimize drive the desire to utilize optical Communications on board a satellite: size, weight, and power and of course cost. Under ideal assumptions about equal efficiency of signal power generation, detectors, and receiving surfaces, link equations show that optical communications with telescope aperture equivalent to that of the antenna of a radio frequency system could potentially provide tens of dB of link efficiency to improve e.g. data rate, margin, etc. This results strictly from wavelength differences of existing microwave and millimeter wave based ( 60 GHz) systems compared to 0.8 to 1.55 micron based( 200 THz) laser links that have bandwidths that can go even higher when wave division Multiplexing is employed ( WDM). The data rates being carried by optical carriers are at least 200 to 2000 times larger. While this is a theoretical limit, by using WDM technology and tunable wavelength lasers this factor has the potential of being increased by combining data from practical systems employing 4 or more different wavelength lasers. Here again the smaller aperture size of the optical telescopes needed as compared to the microwave telescope (Antennas) used in the transmitter / receiver sections favor the optical domain by a factor of at least 100 to 1000.

While the optical links in space can boast to an incredible number of high technology achievements as is While the optical links in space can boast to an incredible number of high technology achievements as is evidenced in the optical terrestrial networks, however there still remains formidable challenge to test, qualify and successfully integrate in real world full scale deployment. In this paper we will examine the various aspect of the optical crosslink including Transmitter (source), Receiver (detectors), optical telescopes using Adaptive optics and MEMs based agile beam steering, link parameters, channel characteristics and optical noise that ultimately limit the detector sensitivity. A special section will be devoted to ATP (acquisition, tracking, and pointing) in the optical ISL that describe the procedure and algorithm currently proposed for such systems.

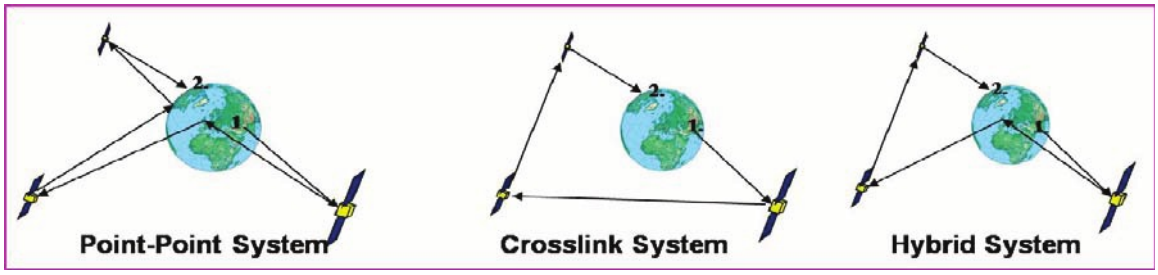


**Figure 1: Various link configurations used in GEO communication satellites**

**Table 1: comparison of point-point with Cross-link systems listing the pros and cons of each configuration**

| | Advantages | Disadvantages | Examples |
|---|---|---|---|
| Point-Point | ▪ Heritage systems<br>▪ Reliability and redundancy<br>▪ Relatively low weight and power requirements | ▪ Reliance on ground stations<br>▪ Frequency management issues<br>▪ Atmospheric losses<br>▪ Additional time delays<br>▪ High probability of interception | DSCS<br>UFO<br>INTELSAT |
| Crosslink | ▪ Very secure channels<br>▪ Reduced propagation delays<br>▪ Reduced or no frequency management issues<br>▪ Coverage flexibility | ▪ Extra spacecraft bus requirements<br>▪ Additional payload complexity<br>▪ Additional ground control requirements | Milstar<br>Iridium<br>TSAT |

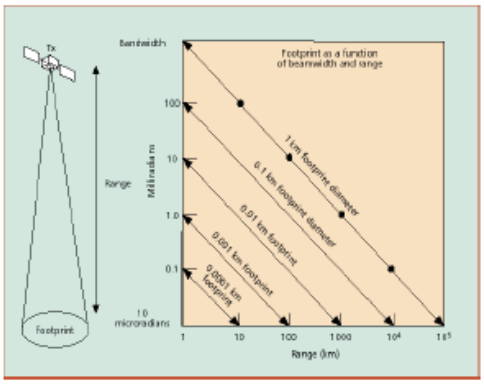


**Figure 2. Footprint as a function of beam width**

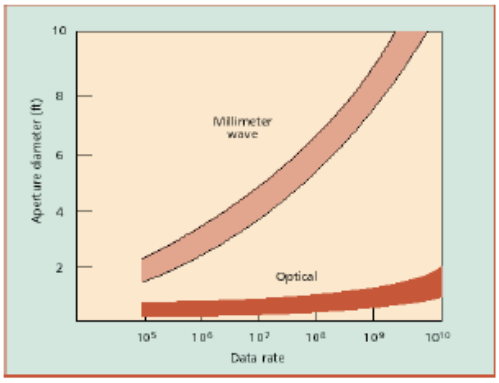


**Figure 3. Aperture diameter and Range comparison of optical and microwave systems versus data**

## 2. ADVANTAGES OF LASER BASED OPTICAL LINKS OVER TRADITIONAL MICROWAVE TRANSMISSION SYSTEMS

In addition to the much increased bandwidth available for high speed communications with data rates in excess of 10 GBPS, another significant factor in this tradeoff is that the optical system will typically have a much narrower beam width than the RF systems. Thanks to the coherent beam that can be focused to spot sizes of the order of the wavelengths of the laser light which approach the diffraction limit. This has both a positive and negative side. On the positive side, a narrower beam width means that the potential for interference to or from adjacent Satellites is greatly reduced. This is particularly important in large LEO constellations. On the negative side, the requirement for much more pointing accuracy, acquisition, and tracking (ATP) and the impact that this may have on the space craft that is moving at 3Km/s for GEO to 7 Km/s for LEO is a formidable task. Accurate APT is critical to the acceptance of optical ISLs. Another key advantage in optical systems is the aperture size of the optical telescopes needed as compared to the microwave (Antennas) used in the transmitter / receiver sections favor the optical domain by a factor of at least 100. For example a communication system operating at 1 GBPS requires an aperture of approximately 15 cm In contrast an RF system with 1 GBPS millimeter wave system would require an antenna with min aperture size of 2.7 m. This parameter alone results in considerable weight and size savings in the satellite payload resulting in reduced disturbance and shaking to the sensitive sensors on board the satellite. These considerations are sufficient to tilt the optical approach in favor of the traditional RF radio used in the last 30 years that have reached a high level of maturity.

A secondary, though not unimportant, fact about the optical communications systems is that unlike the RF spectrum which is regulated by national and international agencies up to 300 GHz, the optical spectrum in space is virgin territory and is currently unregulated. Finally the reliability of optical components, particularly the lasers, has been a concern in the past. This is being overcome by advances made in the optical laser technology of solid state and in particular semiconductor laser technology thanks to the tremendous emphasis and advances made in terrestrial optical networks and communications systems, however this needs documentation for space validation in order to gain wider acceptance.

The figure 4 below compares RF /microwave links with optical links. This graph clearly shows that the microwave link at GEO distance of 40,000 Km can support data rates as high as 10 Mbps while the optical link can provide up to 10Gbps. State of the art microwave links in existence use very efficient QPSK and more recently QAM modulation techniques that can increase the data rate to 25 Mbps per carrier. A 24 Transponder Microwave satellite system using FDM (Frequency division multiplexing) can approach peak data rates of 600 Mbps.

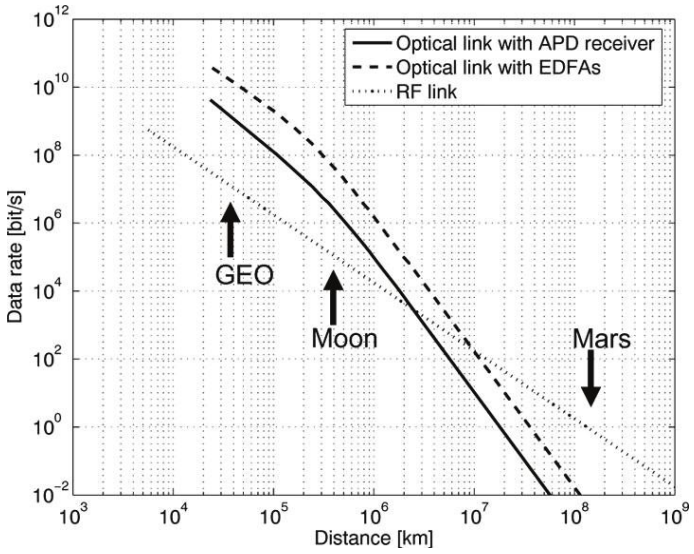


**Figure 4. Comparison of RF links versus Optical for various data rates as a function of link distances. The optical links employ APD detectors in the receiver with and without an optical amplifier.**

## 3. CHALLENGES IN IMPLEMENTING A HIGH SPEED COMMUNICATIONS LINK BETWEEN SATELLITES

An optical ISL is truly a very complex system. One of the key challenges in successful operation of the optical ISL between LEO-LEO and GEO–GEO inter-satellite links is the pointing accuracy and acquisition of the link for successful communication. Note that the narrow beam leads to beam divergence to an illumination area the size of a football field after travelling over 30,000 Km as is shown on graph of figure 2.

Laser beams are coherent in nature but exhibit spreading as they travel in free space with a small divergence angles and beam spreading compared to microwaves that are spherical waves with a much wider angle. The beam width $\theta = 2.28*\lambda/D$ where $\lambda$ wavelength and D is the diameter of the Antenna aperture. For a laser source with 1 um wavelength using a 15 cm aperture the beam width is 22.4 μrad as compared to a 10GHz RF signal where wavelengths is 3 cm and Aperture diameter is 1 m. This results in 67.2 mrad. For this reason the pointing accuracies involved in acquisition of the link, and zeroing and tracking the other space craft becomes a formidable challenge in wake of the enormous speeds involved as well as the jitter and vibration experienced by each space craft used in the constellation while in orbit. This requires an extremely challenging optical/mechanical /thermal system that has eluded some of the best designers in the past. However with the enormous advances made in MEMs based agile beam steering and adaptive optics and micro-optics and on-going research on precision pointing and acquisition using sensitive inertial sensors assisted by accelerometer the challenges are being met with successful test trials in space that prove viable solutions can be implemented to pave the way for coordinated deployment, if all other design and cost targets are met.

The time needed for the light to reach the satellite requires aiming ahead of the target. Many terminals comprise of a combination of coarse and fine pointing as well as an acquisition and tracking CCD sensor system. This exhibits an accuracy of ~ 1 micro-rad, or 30 m at the operating distance in the experiment. The challenge is further exasperated in satellites in orbit experience the 400 to 1000 Hz vibration and shaking that is experienced by the spacecrafts. So the opto/ mechanical APT system need to compensate for this vibration in order to maintain robust and accurate tracking.

As the speed of links increase the noise sources tend to scale with the bandwidth of the electronic circuitry needed in the optical link. At the RF speeds the noise is mostly thermal and excess noise in the amplifiers, however, in the optical links the noise is related to fluctuations of the photon flux being detected that contribute to noise in the detection system. In the optical domain noise in the detectors are dominated by shot noise and excess noise factor from the APD detectors, while the electronics preamplifiers exhibit thermal noise (Johnson noise). As wavelengths get smaller quantum noise increases linearly and become the significant factor in the receiver sensitivity that ultimately dictate the optimum receiver performance. Another major source of optical noise is the irradiance from the sun and bright light sources such as the moonshine etc that the receivers see in the background. With such high data rates, the data pulses approaching 100 ps (10Gbps) exhibit timing uncertainty or jitter that result in Inter Symbol Interference (ISI) that the optical receiver will pass to the clock recovery circuit making it even more difficult to recover the clock for and error free data recovery at the final stage of the receiver.

The figure below is an experimental optical link that was developed by MIT Lincoln Labs and NASA JPL for the US military. It is an example of a 1 GBPS differential Phase shifted Keying test bed that has become the bench mark by which other developments have been measured. It is based on a 1.55 um wavelength laser and a EDFA. An Optical amplifier is used in the Transmit path, while another Optical Pre-amplifier is used in the Receive section.

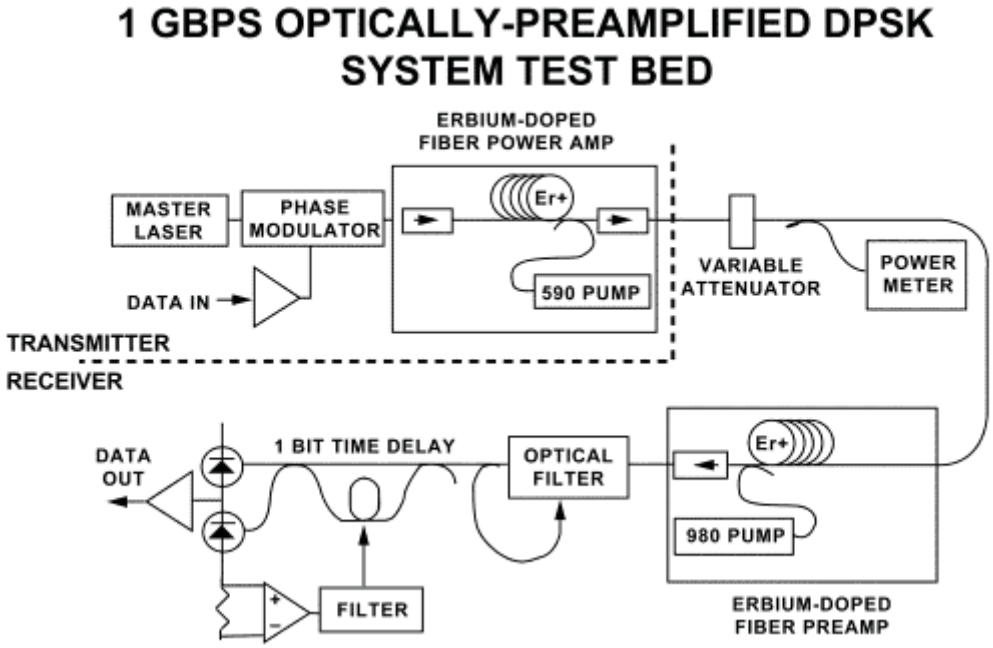


**Figure 5. Experimental test bed of an optical link operating at 1 GBPS developed by JPL/ MIT Lincoln Lab.**

## 4. OPTICAL TRANSMITTERS

Over the years various laser sources have been employed in optical free space communications test trials and demonstrations that covered solid state lasers, as well as semiconductor laser diodes. Earlier optical systems used shortwave semiconductor 0.8 um laser and semiconductor diode pumped ND: YAG 1.064 um Solid state lasers that provided higher power. In an effort to push the technology to achieve even higher data rates the wavelength and laser of choice is the 1.55 um DFB semiconductor laser with extremely narrow line-widths are preferred, especially when they can be followed by optical amplifiers that boost the optical power by as much as 30 dB. The master laser has to have superior amplitude and phase noise characteristics and be extremely stable with frequency. So they operate in cow mode (always ON) with a thermoelectric cooler

to keep them at a constant temperature and are modulated by using a separate external modulator such an electro-optic Lithium Niobate Mach-Zehnder (MZ) interferometer type optical switch or Electro-absorption (EA) modulator being driven by electrical data. External modulation significantly reduces the frequency chirp that accompany the optical spectrum of the resulting optical pulses as compared to traditional intensity modulation techniques, thus allowing higher modulation Bandwidths and lower crosstalk. The current state of–the- art link operates at 10Gbps and by using 4 Channel WDM can reach 40Gbps.

A 1-20 W optical power amplifier can be used to further reduce telescope size reducing the overall weight of the satellite payload. An optical amplifier such as (Erbium doped Fiber amplifier) using a two stage Erbium Amp pumped by 980 nm Laser pump can be used. Double clad Erbium amplifiers have been developed that allows more pumps to be end-coupled into the multimode outer core or better yet coupled with side pumping of the outer core. With this configuration optical powers in excess of 20W have been achieved. Note that optical amplifier at the Transmitter has a noise figure, but is not as crucial and by no means near the quantum limit. With a 20 W amplifier it has been shown that a 40 Gpbs link for 44,000 Km using a 15 cm aperture is feasible. Higher data rates approaching 100Gbps can be achieved by using WDM technology. However, the WDM coupler must be placed after the power amplifier for each wavelength making a low loss (< 1 dB) WDM coupler an essential component.

One of crucial factors in laser space communication is the reliability of the components used including the source, optical pump, and external modulators and so on. The reliability of the optical transmitter is dominated by the reliability of the pump laser. A reliability of 0.9998 over 10 years of operation without degradation in space has been achieved using a pump module with built-in cold and hot redundancy. The light emitted from the laser is guided by a polarization maintaining (PM) Single Mode (SM) fiber to the Phase modulator driving the data electronics. By using a modulator that can operate up to 10Gbps the master laser which is in turn coupled to the optical amplifier by another polarization maintaining SM fiber which amplifies the output power level. A collimator is used to direct the laser beam to a telescope through a system of multiple lenses. The laser sources tend to exhibit a Gaussian intensity distribution in the main lobe. The reduction in the far-field signal strength due to transmitter mispointing is the transmitter pointing losses.

The figure below shows the block diagram of an optical transceiver assembly comprised of a transmit and receive electronics, the ATP assembly using a beacon to acquire and track the satellites. Also show in some detail is the intricate optical assembly and components of lens, beam splitters, optical filters, polarizer etc with a fast steering mirror and telescope.

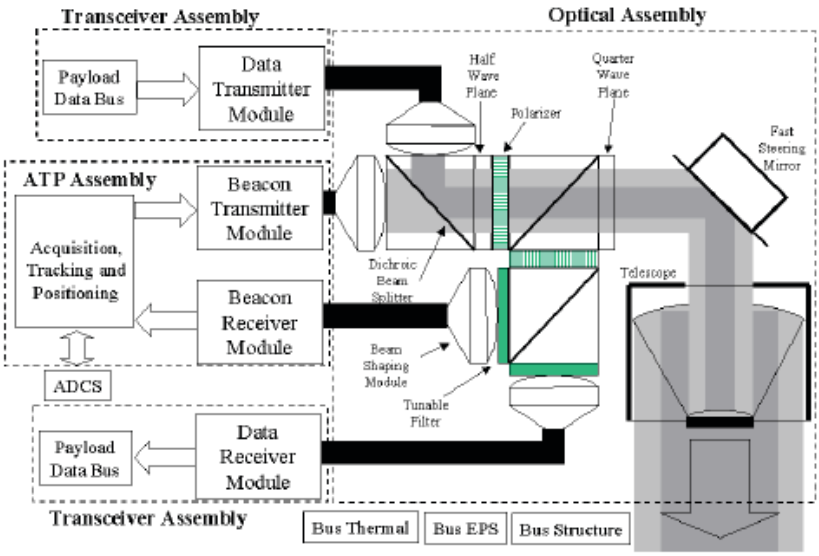


**Figure 6. High Level block diagram of an optical transceiver proposed for ISL.**

## 5. OPTICAL RECEIVERS

The optical receiver consists of sophisticated collection optics that focuses the received optical pulses onto the optical detector, followed by extremely low noise electronic pre-amplifiers, followed by post Amps that convert the received pulse to logical ones and zeros in the electrical domain that are subsequently followed by clock and data recovery circuits. The faint optical fields at the receiving satellite telescopes exhibit significant quantum behavior and hence the optimum receiver is necessarily quantum in nature. However often the quantum optimized receiver is not realizable with known techniques or its implementation is very complicated even if we knew how to make it. Thus simple structured optical receivers are used. For direct detection or incoherent detection receivers are used where the received optical field is energy (square law) detected by means of a photo-detector that usually provides gain.

Examples are APD (avalanche photo-detectors) that typically provide gains of 10 dB, PIN followed by FET preamplifiers or PMT (Photo- multiplier-tubes). Modulation used in Direct detection systems are limited to intensity modulation such as on-off-keying (OOK) and Manchester coding which is self clocking making the clock and data recovery simpler. The ideal form of direct detection is a photon counting receiver, i.e. a receiver with enough gain per photo-electron emitted by the detector surface that individual photo-events are detected and counted by subsequent electronics.

This receiver can achieve a theoretical optimum performance at bit error rate of 1E-12 with 28 detected photons per bit for OOK modulation schemes. Current state of the art APD or PIN-FET receivers are 10 to 15 dB away. The degradation of performance is mostly due to the noisy avalanche process of an APD that produces excess noise or the front-end noise in the electronics preamplifiers after detection. At 10 Gaps in addition to electronic noise, there are the effects of Bandwidth limitations of the electronics and timing system jitter giving rise to inter-symbol interference as well as crosstalk. With a suitable low noise optically pre-amplified detection receiver such as an EDFA, many of the lost dabs can be recovered. This receiver has the same quantum mechanical model and the detection limit of a heterodyne receiver which is considerably more complicated to implement. Essentially one can make the EDFA that has a 3dB quantum limited noise figure.

NASA in an attempt to extend the optical link to space explorations where distance are measured in Astronomical Units (AU), have started experimenting with the next generation of a high efficiency photon counting communications system using semiconductor single photon counting receivers that utilize single photon APDs or (SAPD). A block diagram of the single photon APD receiver used in Geiger counter mode is depicted in the figure 7 below. The link uses a 1550 nm source that is externally modulated. For deep space communication the modulation of choice is the pulse position modulation (PPM). To further enhance the link with additional coding gain a turbo code is being implemented. When high power processors (DSP) on board apply Forward Error Correction (FEC) algorithms an extra 3 dB of coding gain can be obtained in the link. Figure 8 shows the performance of such a link with and without the Turbo coding and clearly show that the BER can be significantly improved in the former case.

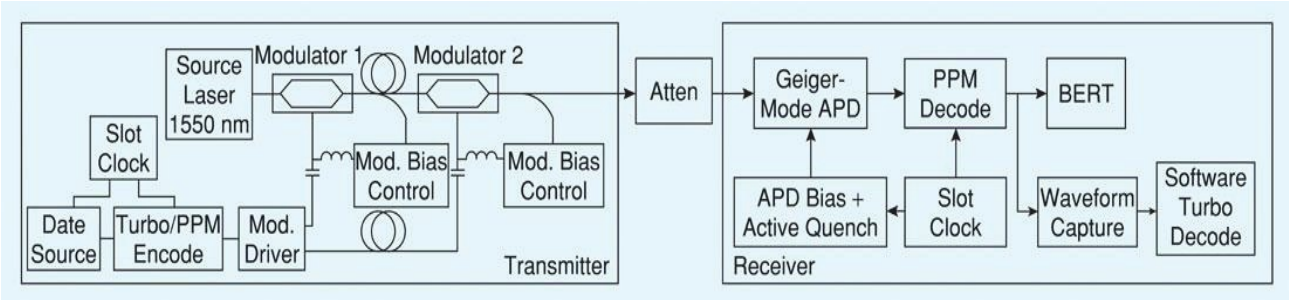


**Figure 7. Experimental setup for demonstration of high-efficiency photon-counting communications using GM-APDs**

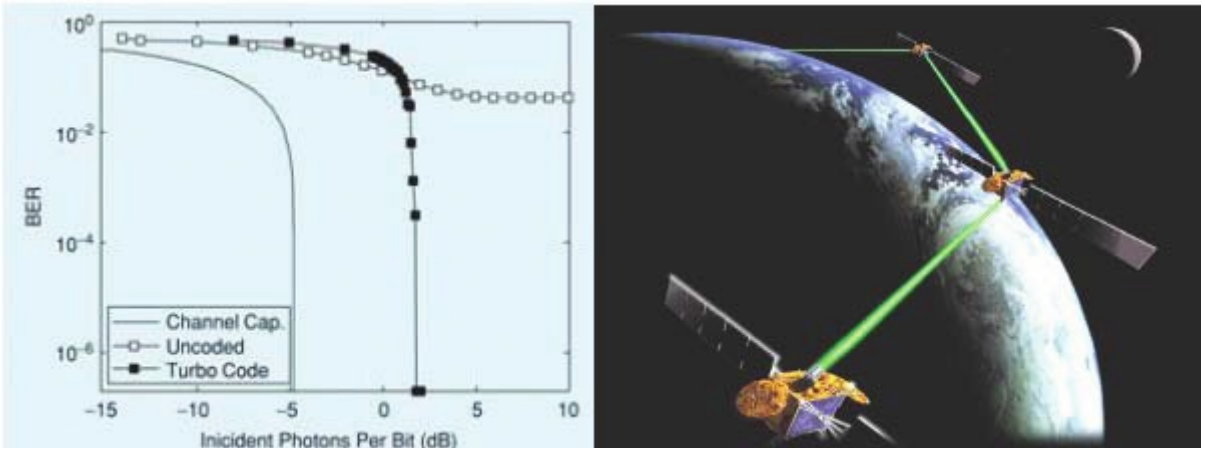


**Figure 8. Measured communications performance**

In the optical receiver the filter bandwidth specifies the spectral width of the narrow–band-pass filter employed in optical ISL. The optical width of the filter must be compatible with the spectral width of the laser source. In addition to source width of the laser, the minimum width will also be determined by the acceptable transmission level of the filter: typically the transmission of the filter decreases with the spectral width. For direct detection systems, narrow field of view spectral filters of 20 Angstroms (2nm) are typical (for 1 mm radiation this corresponds to 600 GHz).

## 6. LINK PARAMETERS

The link parameters consist of the Transmitter optical power, Transmitter/Receiver optical Antenna Gain, Transmit pointing loss and Transmitter and Receiver optical efficiency/coupling (loss) and Receiver sensitivity. The Channel loss for ISL consist mainly of space loss which is roughly equal to (λ/4*π*R)**2, where λ is the laser wavelength and R is the link distance (Range) the Space loss in the optical channel is ~ -290 dB for 40,000 Km distances.

The Optical Antenna gains for TX and RX are given by the formula (π* Dtx/λ) **2 and (π* Drx/λ)**2 respectively where D is the aperture diameter and λ is the wavelength of the Laser source. Typically these optical antenna gains for a 15 cm aperture are of the order of ~ 115 dB each. The TX optical loses including pointing losses are ~ -4dB and Receiver optical loss is estimated at -3 dB. The Receiver sensitivity is 0.48 uW or -33.85 dBm using Manchester coding. Here we used a Quadrant APD detector with 0.8 quantum efficiency, and Multiplication factor of 12 using temperature control of the Bias Voltage followed by a low noise preamplifier preferably a Trans-impedance type.

We are now ready to determine the Laser Transmitter average output power requirements. The total gain in the system is ~ 290 dB (115 +115 + 66 = 296 dB) the total loss in the system is ~ 292 +7 = 299. If we use a 3.35 W (38.25 dBm) 1550 nm DFB laser we should get 3dB of link margin. The master DFB laser is 33.5 mW followed by an optical amplifier with 20 dB gain. Note that by adding turbo coding and FEC to the link we can achieve at least 2dB of coding gain. So now we end up with ~ 5 dB of link margin for BER of 1E-9 which is a good number for a robust optical link The results of the link parameters for a 2.5 Gbps LEO to GEO link for BER< 1E-9 is tabulated in Table 2.

OOK modulation with coding was assumed. Inclusion of the coding will enhance the link margin. The required Average Laser power of 3.35W is well within the reach of EDFA. For higher data rates the transmit channel could be a single Transmitter or could, for example utilize four wavelength coarse WDM to form four 2.5 Gbps Channels. The 1550 nm CWDM technology is very mature and efforts are under way to space qualify all these building block components for 10Gbps applications and higher.

**Table 2. Summary of LEO-GEO Link Budget**

| PARAMETER | VALUE | GAIN / LOSS in dB |
|---|---|---|
| Transmit Power | 3.35 W Avg. | 38.25 dBm |
| Transmit Loss | 64.5% Trans. | 1.90 dB |
| Transmitter Gain | 9.2 urad Beam | 113.51 dB |
| Pointing Loss | | - 2.01 dB |
| Space Loss | | -290.85 dB |
| Atmospheric Loss | none | 0 dB |
| Receiver Gain | | 115.5 dB |
| Receiver Loss | 46% Transmission | -3.36 dB |
| Received Signal | 2570 Photons / Pulse | -30.85 dBm |
| Background Signal | 6.66E-9 Photons/s | 0 dB |
| Required Signal | 1.29E3 Photons/Pulse | -33.85 dBm |
| Link Margin | | 3.00 dB |

The receiver sensitivity for BER of 1E-12 at 2.5 and 10 Gbps is tabulated below in table 3 comparing PINFET, and APD, as well as Optical Amplifier plus FET amplifier. Going from 2.5 to 10Gbps the sensitivity drops by ~ 6 dB. This loss will be compensated for by using a Laser in the 10W range.

**Table 3. Receiver Sensitivity for BER=1D-12 for various detectors. Photo-detector and amplifier noise included.**

| PARAMETER | 2.5 GBPS | 10 GBPS |
|---|---|---|
| Typical rms Noise from Amp | 400 nA | 1.2 uA |
| Input Sensitivity for BER = 1E-12 | 5.6 uA | 16.6 uA |
| Sensitivity for Pin FET | -24.3 dBm | -19.5 dBm |
| Sensitivity for APD | -33.1dBm | -28 dBm |
| Sensitivity for OA + Pin FET | -41.3 dBm | -35.3 dBm |
| Quantum Limit | -53.6 dBm | -47.6 dBm |

## 7. ATP: ACQUISITION, TRACKING, AND POINTING

The optical part of the subsystem design must minimize optical throughput losses (~3dB), and provide high wave front quality under all operation scenarios (~λ/10), and maintain accurate beam pointing and alignment accuracy to within (~1/20 beam width).The pointing and acquisition phase of the optical ISL is one of the most complex and complicated section of the optical Transceiver. This is typically done with a coarse and fine alignment stage in the optical subassembly where a beacon light of usually higher power pulse of low frequency is sent out to scan for the link. This scanning procedure is considered successful when the transceiver Beacon receiver confirms the link. The figure below depicts the block diagram of the various components used for this phase of the communication link. Next is the acquisition phase which can be classified into serial and parallel searches. These strategies can be used for both illuminations by the beacon and search by the acquisition receiver. After acquisition the system will enter the coarse and then fine

tracking phase. Isolators are used to dampen the jitter from the satellite platform as much as possible. The spatial error sensor receives the beacon and derives an estimate of the angle of arrival of the beacon. The signal is fed to a feedback controller and any skew is tracked out by means of a slow outer loop (~ 10 Hz) with the telescope coarse pointing mirror inner loop (~ 1 KHz) with the high speed fine tracking mirror. The transmit beam (~ 10 u-RAD) shares the same optical train as the beacon and thus transmit beam jitter are reciprocally tracked out by the steering mirror. A point a head angle (~ 20-60 u-RAD) is dialed into the outgoing beam to compensate for the finite speed of light and receiver platform movements.

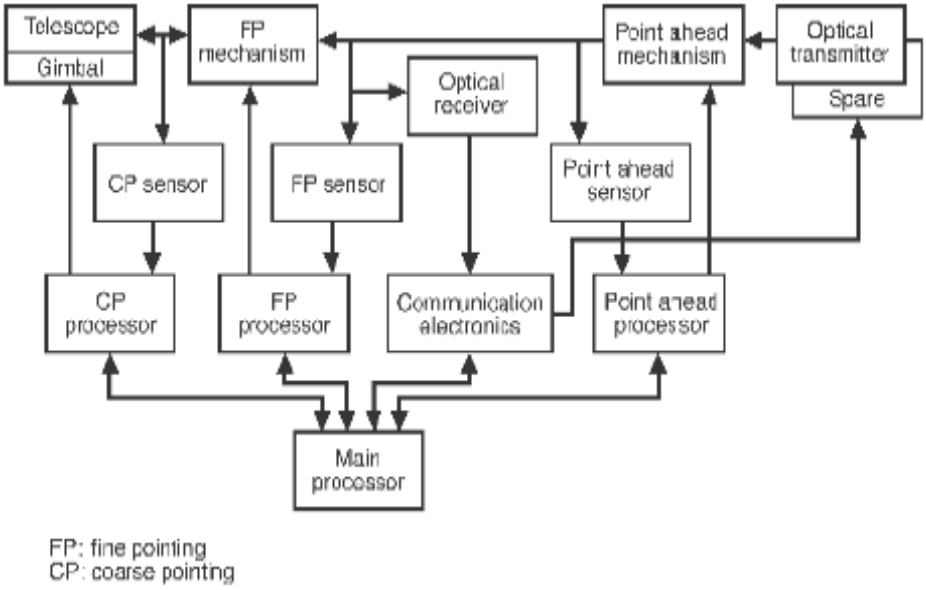


**Figure 9. The block diagram of a proposed pointing and acquisition system, showing the various interconnecting subsystems that are involved in this complex task.**

## 8. CONCLUSION

Optical ISLs are the requisite subsystems of the future optical networks in the sky. There still exist many tough technological and architectural design issues in implementing a cost effective, space qualified high data rate power efficient systems. New research and development point to even higher performance systems with many advantages and substantial gains over what can be achieved today. The success in the bringing the research and development efforts to fruition will depend strongly on six key factors for optimization of the optical link operating at 10 GBPS Duplex at 40,00 Km distance with BER of < 1E-9 . They are as follows:

- Link reliability target of >0.9 for 15 years during lifetime at 100% operation.
- Full immunity to sun, Doppler and satellite mechanical perturbation in any operational mode.
- Power consumption in the area of 100W while weighing less than 100 lbs.
- Low complexity and sensitivity of all optics, still a key issue in production and application acceptance.
- Sufficient margin in the sensitive area of tracking budget.
- Inherent capability of scalability of power.

## 9. REFERENCES

1. Vincent. W.S Chan, ”Optical Space Communications: ”Key Building Blocks for Wide Area Space Networks”, LEOS ’99,San Francisco, CA Nov 1999
2. C.A. Thompson et al,” Free Space Optical Communications utilizing MEMS Adaptive Optics Correction.” Conference # 4821 of SPIE 2002 Annual Meeting in Seattle, Washington, July 7-11, 2002

# Virtual optical interfaces for transportation

**Renaud Kiefer, Bernard Kress (*), Joseph-Joel Fontaine**
Institut National Superieur des Sciences Appliquees INSA.
Boulevard de la Victoire, F-67000 Strasbourg, France
(*) Universite de Strasbourg, 67400 Illkirch, France

## 1. ABSTRACT

Today, the ever increasing number of controls in automobile and aviation cockpits leads to the cluttering of various interfaces (keyboards, switches, panels, etc…). LCD touch screens have proved to be a good alternative to reduce cluttering by reconfiguring in real time different interfaces, appearing on demand as they are needed by the user. However, the underlying screen still remains cumbersome and fragile glass device. We present a novel way to produce virtual consoles and interfaces by projecting diffractive images and sensing the position of the fingers by the use of IR diffractive optics.

**Keywords**: Virtual interfaces and consoles, Automotive consoles, Virtual reality, Diffractive Optics, diffractive projector, position sensing.

Photonics in the Transportation Industry: Auto to Aerospace II, edited by Alex A. Kazemi, Bernard C. Kress
Proc. of SPIE Vol. 7314, 73140L · © 2009 SPIE · CCC code: 0277-786X/09/$18 · doi: 10.1117/12.821375

## 2. INTRODUCTION

Human/machine interfaces have been a vast field of research, especially for applications in automotive and general transportation. We propose here new virtual human/machine interfaces based on diffractive projection and remote optical sensing of finger position in order to increase the control range and reduce the mechanical breakdown linked to traditional interfaces such a screens, switches or other mechanical commands. Such a device has a zero footprint on the projected area (for example the dashboard) since the projection and the sensor are remotely located (in the roof of the vehicle for example).

## 3. CONTROL INTERFACES IN TRANSPORATION TODAY

**- Contact based consoles.**
Contact based switches, sliders and other mechanical circuit breakers are extensively used in industry, both mechanical, electrical and hydraulic. However, these interfaces are relatively simple, very limited in their content, are binary, and have short life times since they are mechanical.

**- Touch screen displays interfaces (including haptics)**
Touch screen interfaces have been introduced in avionics in the late 80s, and transferred into automotive especially with the introduction of the popular GPS system. They rely on a conventional touch screen LCD display and are thus fragile, expensive and bulky (glass). Also, such interfaces are usually lacking mechanical feedback (haptics), although recent efforts are triggered into including haptics in touch screen LCDs.

**- Voice activated controls (voice dialing)**
Voice activated controls have been implemented in automotive as early as the 80s for handicapped drivers, and more recently for voice activated dialing through bluetooth in cars.

**- Wireless gyroscope activated controls.**
These new controls are hand held and can be used to control mobile devices such as phones (i-phone) or video games (Nintendo Wii), They are better adapted to the entertainment sector rather than the transportation sector for obvious safety reasons.

## 4. VIRTUAL INTERFACES IN INDUSTRY TODAY

A virtual interface projection system includes two separate functionality:

- The projection functionality (imaging projectors or far field projectors)
- The 2D or 3D finger position sensing functionality (remote position sensor)

The projection can be performed by a traditional projector in a roof module, or a pico projector based on either traditional imaging, diffractive imaging [1] or laser scanning [2].
The sensing can be done by a variety of techniques developed in industry today [3], [4], [5].

## 5. PROBLEMS WITH CURRENT VIRTUAL OPTICAL INTERFACES

Canesta has introduced in recent years a diffractive keyboard projector based on its proprietary Electronic Perception Chip technology to sense the position of the fingers on the projected keyboard [6]. The keyboard was projected by a diffractive Element designed and fabricated by Heptagon Oy in Finland, based on Fourier optics [7]. The first consumer electronic devices which include this technology are being sold by companies like Celluon and iBiz in Korea (see Fig. 1).

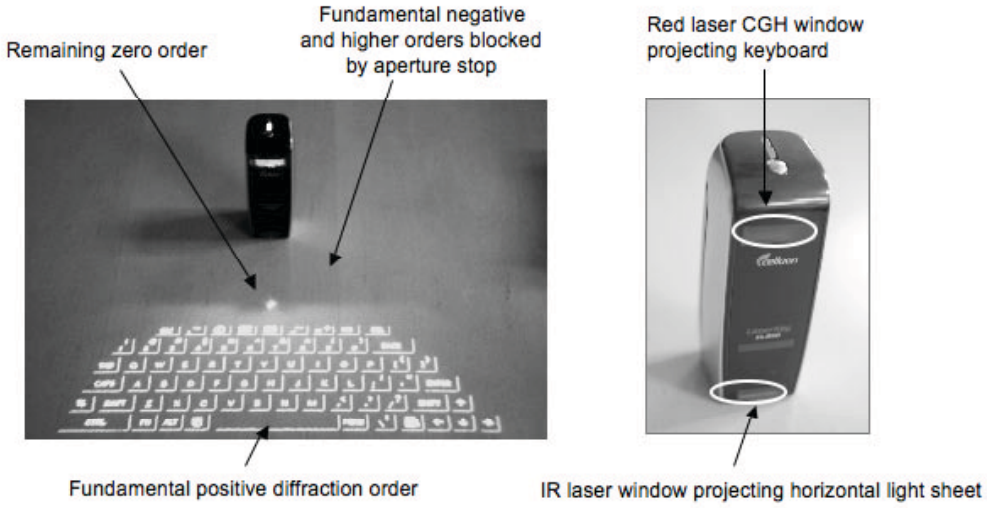


*Fig. 1: Diffractive keyboard projector available today.*

Two laser diodes are included in this device; a red laser at 650nm to project the keyboard and an infrared laser at 780nm to detect the fingers position by triangulation.
An IR light sheet is produced either by a refractive cylindrical lens or a diffractive element, which propagates horizontally 1mm over the table. One a finger is crossing the beam, the reflected light is analyzed by a couple of detectors and the angular direction is sensed. As the keyboard is not symmetric, it is possible to detect which key is to be used. Fig.2 shows the operational principle of the virtual keyboard.

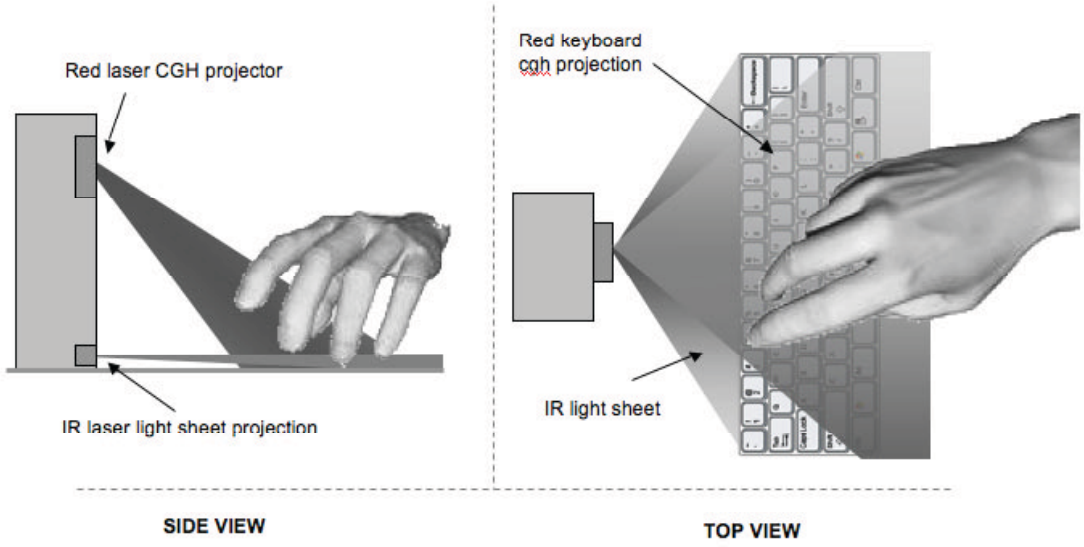


*Fig. 2: Operational principle of the virtual keyboard.*

There are various problems with this technology. One of them is that the sensor only works on perfect planar surfaces, and is thus very difficult to implement on a curved support like a dashboard or a cockpit area. Second, the sensor does not work when it is obstructed by an object (between the fingers and the sensor). Third, it poses safety problems since the projection is launched towards the driver or conductor. Finally, there is no feedback on the strike of a key (no haptics).

## 6. IMPLEMENTATION OF AN ALL DIFFRACTIVE VIRTUAL INTERFACE

***a) Projection system.***
Our projection system is composed of a set of fixed diffractive Fourier pattern projectors etched in quartz, each positioned on top a different visible laser (green or red). These diffractive projectors can be located on a roof module. Several patterns can be lit on at the same time or in a sequential mode as they are required by the user (interface on demand).

***b) Sensor system***
The sensor system is also composed of a set of diffractive Fourier pattern projectors, each projecting a set of linear fringes by the mean of an IR laser (for example a VCSEL laser array) – see Fig.3.

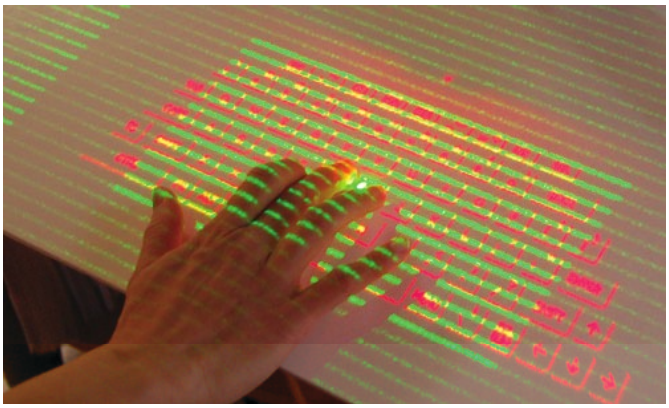

*Fig.3. Diffractive fringe projection on operator's hand.*

The spacing between the fringes tells about the height of the hand on the dashboard, and the deformation of the fringes the position of the hands. One only need to sense the position of the right index, which is used to trigger the i-pod wheel or the other controls projected. The other fingers are not used. Such an illumination will be done in IR, however, to demonstrate the operation, we used a green laser on top of the red virtual keyboard projection.

Fig. 4 shows how we discriminate between the height of the hand on top of the virtual interface. The interface should be active only if the hands (or fingers) are touching the projected pattern. We have therefore developed an algorithm that controls the continuity of the fringes. If the fringes are not continuous over the first deformed fringes (the fingers), these fingers are not touching the interface are meant to do something else (chasing a fly, wiping the windshield, saying hello to someone outside. The only time the interface is actually active is when those fringes are continuous, and only then, the algorithm locating the first deformed fringes (tips of the fingers0 is kicking in.

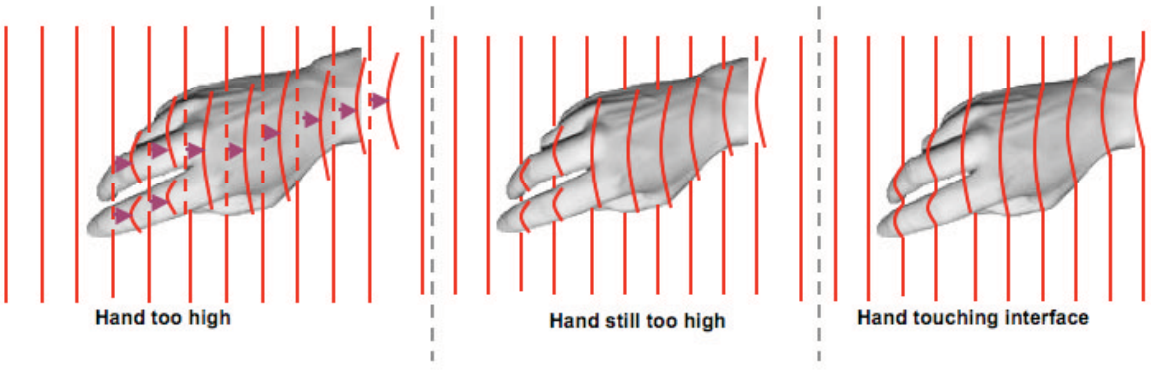


*Fig.4. Discriminating the height of the fingers on top of the virtual interface.*

## 7. DIGITAL DIFFRACTIVE ELEMENTS DESIGN AND FABRICATION

The device is composed of a single diffractive window on which three different optical elements are patterned and pre-aligned:

- The diffractive projectors producing the visible far field patterns (interfaces).
- The diffractive fringe projectors producing the IR fringe patterns used ot sense the position of the fingers
- The camera objective lens used to image both the projected interface and the IR fringes deformed by the hand on top of the CMOS sensor.

Fig. 5 shows a depiction of the final device.

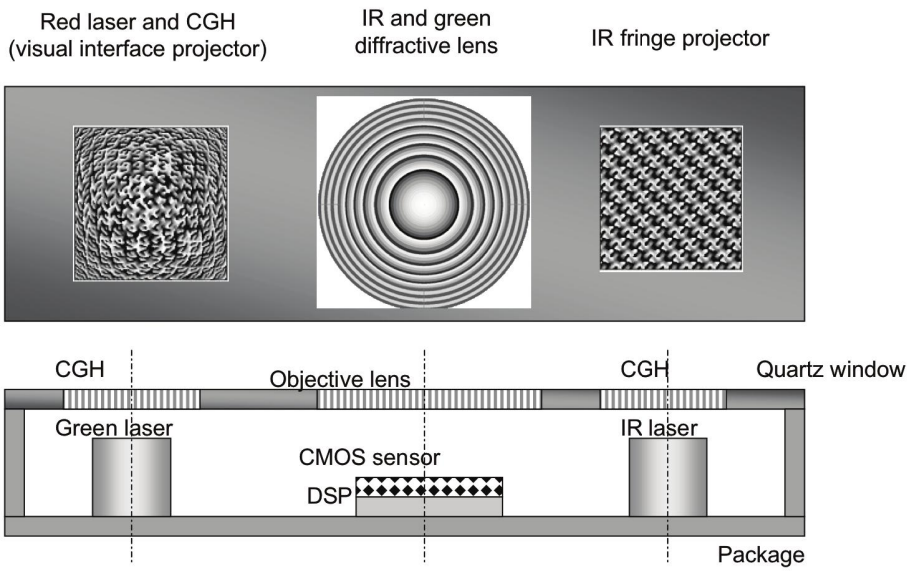


*Fig. 5 The projection and sensing device with a single pre-aligned diffractive window*

The individual dies are diced out from a 4 inch quartz wafer as depicted in figure 6. Many such elements can be integrated in a single wafer. A typical batch of wafers is 20, so a single batch can produce many hundreds of such projectors.

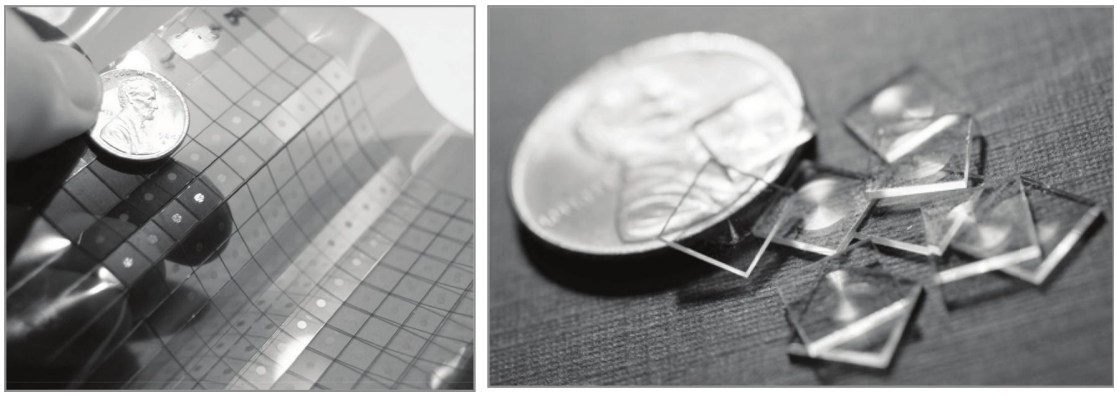

*Fig.6: Individual dicing of the diffractive interface projectors*

## 8. INCREASING THE DIFFRACTION EFFICIENCY

We use in this system two wavelengths: The first one is visible (red 650nm DVD laser diode or green 532nm doubled YAG laser) to project the virtual interface. The second one is infra-red to project the set of fringes (780nm CD laser diode or 850nm VCSEL). The CMOS has to be able to image both wavelengths. A simple diffractive lens would not have enough efficiency over these two separate wavelengths. This is why we have designed our lens as a harmonic lens which has two peak efficiencies in these two spectral regions. We are not interested here in the other wavelengths (full visible spectrum). Fig. 7 shows the diffraction efficiency of such a two wavelength harmonic diffractive lens.

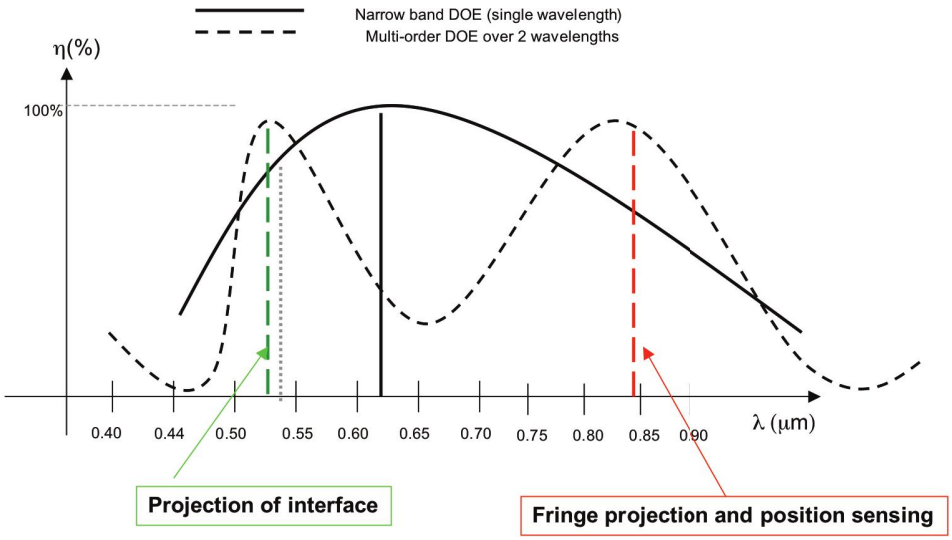


*Fig. 7: Diffraction efficiency of a green/ir diffractive objective lens*

Note that in order to image the IR pattern through the diffractive objective lens onto the CMOS sensor, one needs to take off the IR filter which is usually inserted on top of CMOS sensor.

## 9. INCREASING THE DIFFRACTION ANGLES

One limitation of the projection is the small diffraction angles that can be achieved by the CGHs. These angles are limited both by the fabrication technology available (critical dimension or CD in the optical lithography step) as well as the limit of the validity of scalar diffraction theory used to design the element. In order to increase the diffraction angles, one can use an afocal inverted refractive telescope (a slow positive lens and a fast negative lens) as depicted in Fig. 8.

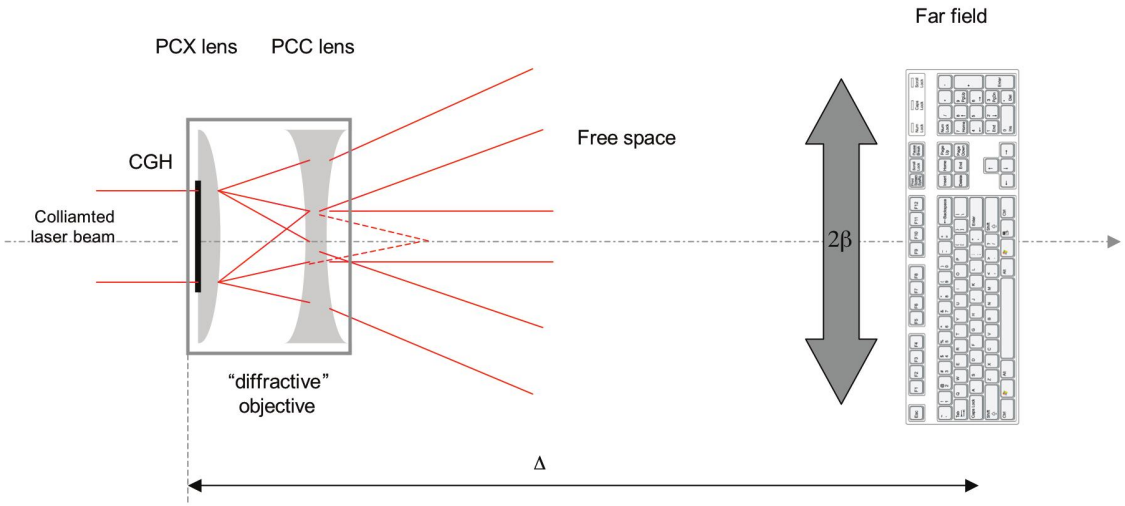


*Fig.8: Increasing the diffraction angles with an afocal inverted telescope system*

## 10. SWITCHING BETWEEN VARIOUS INTERFACES (CONSOLE ON DEMAND)

Many different interfaces can be used with a single projector package. By inserting various interface projectors sitting on top of various lasers (can even be different colors), one can produce the desired interface on demand. The same fringe pattern is projected on the various interfaces in order to sense the finger's positions. Fig. 9 shows such various projected interfaces.

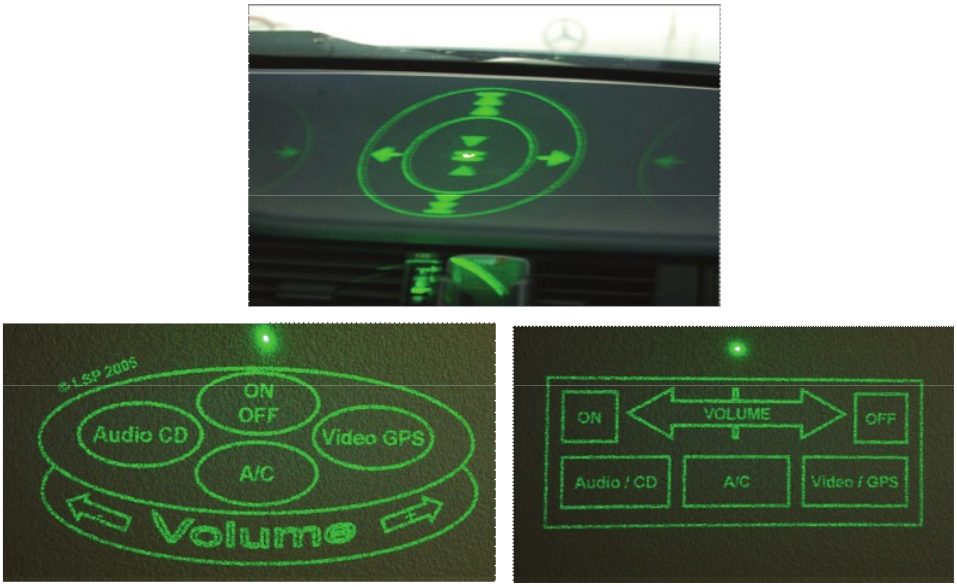


*Fig 9: Example of different virtual interfaces*

## 11. CONCLUSION

We have described and demonstrated a novel approach to virtual interfaces, with emphasis on transportation applications.
The projector/sensor is a micro device and is self contained in a single package in a roof module. It does not require any sensor apparatus to be located near the projection area (dashboard, table, etc…). The device is completely diffractive. The various optical elements are fabricated on a single quartz window and positioned lithographically, therefore reducing dramatically the costs of such a device, since no alignment is necessary during packaging. The sensor can discriminate between fingers in the area of the interface but not touching it, and fingers actually touching the interface to produce the desired command. The finger position sensor is also entirely diffractive, and stealth (uses IR laser light). The CMOS sensor uses a harmonic diffractive lens which has been optimized to yield high efficiency over the projection and sensing wavelengths, and a low efficiency elsewhere on the spectrum.
We have fabricated a first generation device projecting the i-pod interface and several audio-video interfaces on the dashboard. We are now working on integrating the finger sensing algorithm in the device, on a DSP located in the back of the CMOS sensor.

## REFERENCES


[1] www.holoeye.com
[2] www.microvision.com
[3] www.canesta.com
[4] J. Goodman, *Introduction to Fourier Optics*, Mc Graw Hill College Division (1968)
[5] S.B. Gokturk, H. Yalcin, C. Bamji, “A Time-of-Flight Depth Sensor—System Description, Issues, and Solutions," in Proc. IEEE Workshop Real-Time 3D Sensors, 2004
[6] A. Carullo and M. Parvis,An, " Ultrasonic Sensor for Distance Measurement in Automotive Applications", in IEEE Sensors J., Vol. 1, No. 2, (2001)
[7] S Hsu, S. Acharya, A. Rafii and R. New “Performance of a Time-of-Flight Range Camera for Intelligent Vehicle Safety Applications”
[8] B. KRESS & P. MEYRUEIS: "Digital Diffractive Optics, An Introduction to planar diffractive optics and related technology", John Wiley Publisher, September 1999
[9] B. KRESS & R. FISHER “Optical System Design”, chapter on Diffractive Optics, Mac Graw Hill Publisher, February 2008.
[10] B. KRESS & P. MEYRUEIS “Applied Digital Optics, from Micro-Optics to Nano-Photonics”, John Wiley Publisher, January 2009.
[11] G.J.Swanson*, Binary Optics Technology: the theory and design of multi-level diffractive optical elements* ,DARPA Technical report 854 (1989).

# Nanothermites for space and defence applications

Marc COMET*, Denis SPITZER* and Jean-Pierre MOEGLIN

French-German Research Institute of Saint-Louis (ISL)
5 rue du Général Cassagnou, 68301 Saint-Louis - FRANCE
* Laboratoire ISL / CNRS Nanomatériaux pour les Systèmes Sous Sollicitations Extrêmes (NS3E), UMR 3208
comet@isl.eu, spitzer@isl.eu, moeglin@isl.eu

## Abstract

**Thermites** are energetic materials which are made of a **metallic oxide** mixed with a **reducing metal**[1]. The reactivity of classical thermites is moderate but it can be substantially improved when micron-sized particles are replaced by nanoparticles.

In this paper, three examples of **nanothermites** are given in order to illustrate the contribution of these nanomaterials in the future spatial and defence applications:

- the incidence of the size of the metallic oxide particles on the reactivity was illustrated by the case of $WO_3$/Al nanothermites,
- the correlation between the composition/structure of the oxide phase and the reactivity was achieved on $Al_xMo_yO_z$/Al nanothermites,
- the fabrication of Gas Generating Nanothermites was performed by adding military explosives in porous mineral oxides ($Cr_2O_3$; $MnO_2$) used to fabricate nanothermites.

## Introduction

Despite the excellent energetic potential of classical thermites, their use is restricted to anecdotal applications such as industrial welding or incendiary compositions. This underuse can be attributed to their low combustion rates and their high insensitivity. For instance, energetic compositions containing barium peroxide are necessary to ignite most of conventional aluminothermy reactions. Moreover, the slow propagation of the combustion

Photonics in the Transportation Industry: Auto to Aerospace II, edited by Alex A. Kazemi, Bernard C. Kress
Proc. of SPIE Vol. 7314, 73140N · © 2009 SPIE · CCC code: 0277-786X/09/$18 · doi: 10.1117/12.821334

through the thermite composition and the formation of bulky solid or liquid residues strongly limit the field of applications.

The recent advent of nanomaterials in pyrotechnic science has renewed the interest for these materials. Indeed, the decomposition mechanism of thermites involves a transfer of oxygen atoms from the oxide to the reducing metal. The decrease of the particles size which favours this process dramatically increases the reactivity of thermites. The thermites which are made of nanoparticles are called nanothermites or superthermites.

In this paper, several families of nanothermites recently studied at the ISL will be presented:

- The case of tungsten trioxide ($WO_3$) based nanothermites is presented to illustrate the incidence of the size of metallic oxide particles on the reactivity[2]. Moreover, a neat preparation process which consists in the enclosing $WO_3$ nanoparticles by a chemical deposition method will be discussed.
- The second type of nanothermites was formulated from $Al_xMo_yO_z$ phases. These unconventional ceramic materials were prepared by a sol-gel technique in which agar was used as structuring agent[3]. The combustion properties and the extraordinary insensitivity of $Al_xMo_yO_z$ based nanothermites were correlated to the structure of $Al_xMo_yO_z$ phases.
- The last kind of material was obtained by doping at nano-scale porous inorganic oxides ($Cr_2O_3$; $MnO_2$) by military explosives[4,5]. The as-prepared composite materials can be mixed with aluminium nanoparticules to fabricate Gas Generating Nanothermites (GGNT)[6].

## 1. $WO_3$ based nanothermites

Tungsten trioxide ($WO_3$) based nanothermites were prepared by dispersing the oxide with aluminium nanoparticles (50 nm) in diethylether. Two grades of $WO_3$ were used: a micron-sized material (20 μm, 1.2 $m^2.g^{-1}$) and a nanopowder (30 nm, 27.6 $m^2.g^{-1}$).

The microstructure of $WO_3$ / Al nanothermites was observed by Scanning Electron Microscopy (SEM). In the mixtures containing only nanoparticles, it is difficult to discriminate particles according to their chemical nature (**Figure 1A**). Conversely, it appears clearly that aluminium nanoparticles homogeneously cover the surface of $WO_3$ micrometric particles (**Figure 1B**). These micrographs are a good illustration of the fact that the

nanostructuring of each component is necessary to reach a satisfying contact between the reactants.

$WO_3$ / Al nanothermites which contain only nanoparticles have an impressive reactivity. The fireball generated by the deflagration is so hot that a slamming due to overpressure is heard. The combustion rate can reach 7.3 $m.s^{-1}$. This value is extremely high compared to classical energetic materials. For example, a mixture of potassium chlorate and sugar tested in similar experimental conditions exhibits a combustion speed two orders of magnitude lower. The use of nano-sized $WO_3$ allows to shorten the ignition delay time (1/30) and to increase the combustion rate (x 80).

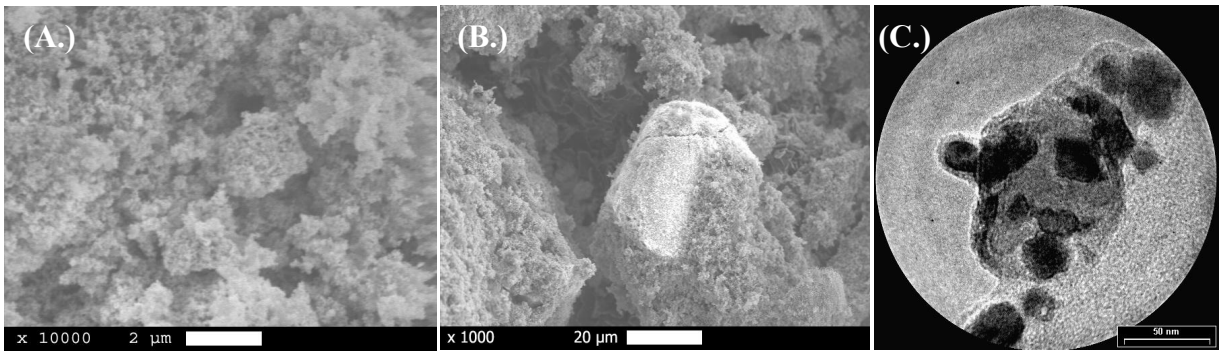


**Figure 1.** Scanning electron micrographs of nanothermites obtained by physical mixing of tungsten trioxide with aluminium. The size of aluminium particle is equal to 50 nm, tungsten trioxide particles have 30 nm **(A.)** and 20 µm **(B.)** mean diameters. Transmission electron micrograph of a $WO_3$/Al composite nanoparticle **(C.)** obtained by a chemical deposition process.

Tungsten trioxide based nanothermites can be significantly desensitized by enclosing the metallic oxide nanoparticles with aluminium[7]. For this purpose, aluminium hydride ($AlH_3$) prepared according to the Schlesinger's reaction is deposited onto the surface of $WO_3$ nanoparticles. The thermolysis of the aluminium hydride is carried out under rigorously anhydrous atmosphere. It leads to a composite material in which $WO_3$ nanoparticles are covered by a layer of amorphous aluminium (**Figure 1C**). These materials have a good reactivity and a reasonable sensitivity level due to the fact that composite particles macroscopically behave as metallic particles.

## 2. $Al_xMo_yO_z$ based nanothermites

Mixed oxides phases ($Al_xMo_yO_z$) were structured at the nano-scale in order to get nanothermites with tuned reactive properties. For this purpose aqueous solutions of ammonium paramolybdate (APM) with various concentrations were gelified by using agar. The resulting hydrated gels were washed with acetone in order to remove water. Water extraction induced the solidification of the inorganic phase (APM) within the organic matrix (agar). These "composite gels" possess a three-dimensional porous structure formed of interlinked strands of average section equal to 45 nm. APM particles are located within the agar strands, in which they define a stringer-like structure. Composite gels are thermally treated in order to burn off the agar and to convert APM into molybdenum oxide. A direct thermal oxidation of composite gels results in a structural collapse, leading to molybdenum trioxide ($MoO_3$) micrometric particles. A chemical treatment was developed to prevent this phenomenon. It consists in treating composite gels powders with an anhydrous aluminium trichloride ($AlCl_3$) solution in diethylether ($Et_2O$). The water adsorbed by the composite gels readily reacts with $AlCl_3$ to give an oxychloride layer at the surface of gel strands. During the thermal treatment, this layer prevents the collapse of the structure by acting as an in-situ nano-sized crucible. Most of the chlorine atoms were removed and several chemical species were formed. The formula $Al_xMo_yO_z$ refers to these species, which mainly consist of amorphous alumina associated to crystallized molybdenum dioxide ($MoO_2$) and aluminium molybdate ($Al_2(MoO_4)_3$). The under-oxygenated $MoO_2$ phase probably forms in the reducing environment of the core of the agar strand. The aluminium molybdate most likely appears at the surface of the agar strand, where the APM particles are in contact with $AlCl_3$ and oxygen from air. The final microstructure of $Al_xMo_yO_z$ phases directly depends on the concentration of the $AlCl_3$ / $Et_2O$ solutions used to impregnate the composite gel. The transition from micro- to nano-scale occurs for alumina weight contents higher than 8.5%. An alumina content of more than 17.0% results in the densification of the material.

Nanothermites were elaborated by the physical mix of $Al_xMo_yO_z$ nano-sized phases with aluminium nanoparticles. From an experimental standpoint, the dispersion was performed by

ultrasonic stirring in hexane. $Al_xMo_yO_z$ nanothermites have ignition delay times (2.8 – 17.8 ms) and combustion rates (1.7 – 103 cm.$s^{-1}$) which can be adjusted through the formulation of $Al_xMo_yO_z$ phases. In other words, the reactivity of these nanothermites is correlated to the structure of the $Al_xMo_yO_z$ phases. Indeed, the higher combustion rate corresponds to the micro to nano transition while the smaller ignition delay time is observed just before the $Al_xMo_yO_z$ densification.

Although they have better energetic performances, $Al_xMo_yO_z$ nanothermites are more insensitive to thermal and friction stresses than a thermite elaborated with pure micron-sized molybdenum trioxide. This insensitivity is probably due to the presence of alumina, which limits the contact between the reactive species.

## 3. Gas generating nanothermites

By definition, thermites are energetic materials which do not release gaseous species when they decompose. However, explosives can be blended in thermites to give them blasting properties. The idea developed at ISL is to solidify military explosives in porous inorganic matrixes ($Cr_2O_3$; $MnO_2$).

Porous chromium (III) oxide was prepared by the combustion of ammonium dichromate. Manganese (IV) oxide was synthesized by reducing potassium permanganate by ethanol in an aqueous acidic medium. These materials have a specific area respectively equal to 44 $m^2.g^{-1}$ and 306 $m^2.g^{-1}$. The observation by scanning electron microscopy (**Figure 2**) reveals that their porosities are very different. $Cr_2O_3$ is made of vermicular particles with a microstructure looking like highly porous pillow lavas (**Figure 2A**). $MnO_2$ exhibits a cauliflower structure in which elementary nanoparticles aggregate in quasi spherical submicron particles (**Figure 2B**) which gather to give larger micron-sized particles.

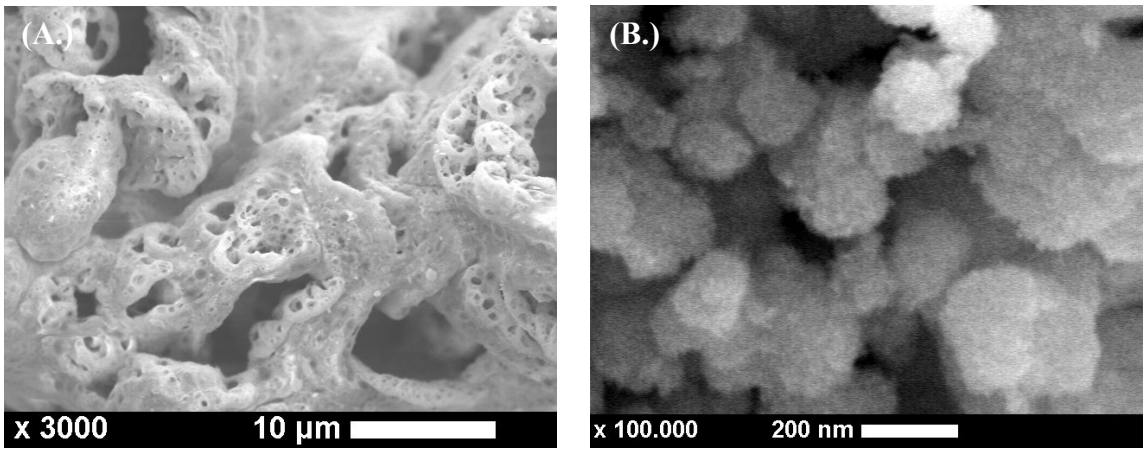


**Figure 2.** Microstructure of porous $Cr_2O_3$ **(A.)** and $MnO_2$ **(B.)** used to prepared gas generating nanothermites.

The impregnation by the explosive phase (RDX) is performed by using solutions of this compound in acetone. When the solvent is evaporated, the explosive solidifies in the porosity and composite nanomaterials are formed. Gas generating nanothermites (GGNT) are prepared by mixing $Cr_2O_3$/RDX and $MnO_2$/RDX materials with aluminium nanoparticles.

The combustion mechanisms of these nanothermites were investigated by atomic force microscopy (AFM), differential scanning calorimetry (DSC) and high speed video. In the case of $Cr_2O_3$ based GGNT, the decomposition of RDX induces the expansion and the fragmentation of the oxide matrix. The resulting $Cr_2O_3$ nanoparticles, which are preheated by the combustion of the explosive, react violently with aluminium nanoparticles. In the case of $MnO_2$ based GGNT, the mechanism of combustion is somewhat different because the decomposition of RDX induces the melting of the oxide particles. The droplets of molten $MnO_2$, which are spread away by the gas formed by the RDX combustion, react with aluminium nanoparticles.

**Conclusions and perspectives of use**

The use of nanoparticles in the thermites formulation improves the reproducibility of their decomposition and significantly increases their combustion rates. Moreover, as the

nanothermites are more sensitive to thermal stress than their micrometric counterparts, they can be easily primed by a laser beam or detonated wire. Nanothermites powders can be easily shaped by pressing due to the surface interactions between the nanoparticles they are made of. The apparent density of the resulting pellets can be adjusted in a large range by varying the pressing level without using any binders. The incorporation of an explosive into the porosity of inorganic oxides permits to obtain gas generating nanothermites with increased performances.

Reactive properties can be defined according to specific needs by controlling the structure of energetic materials at nano-scale. For instance, it becomes possible to tune the density, the combustion rate, the sensitivity or the amount of gas released by the combustion of a material.

Nanothermites can be embedded in numerous devices related to space and defence. Among the most promising perspectives of use the following applications can be quoted:

- Priming devices with a high energetic output and a relative insensitivity to thermal and mechanical stress,
- Enhancement of the power and the density of military explosives,
- Design of thermobaric charges insofar as nanothermites can be used to produce thermal explosions,
- Development of a new generation of powders and propellants, whose properties can be tuned according to industrial needs,
- Separation of the different stages in rockets insofar as the decomposition rates of gas generating nanothermites can be controlled,
- Satellites guidance: due to their densities, nanothermites can provide a high momentum,
- Civilian applications: energetic compositions for security devices (airbags, seat belt pretensioners)[8].

## References

[1] M. Comet, D. Spitzer, Des thermites classiques aux composites interstitiels métastables, *Actualité Chimique*, **2006**, 299, 20-25.

[2] D. Spitzer, M. Comet, J.-P. Moeglin, E. Stechele, U. Werner, Y. Suma, Synthesis and investigation of the reactivity of nano thermite mixtures, *37th International Annual Conference of ICT*, Karlsruhe, Germany, June 27-30, **2006**, 117-1 to 117-10.

[3] M. Comet, D. Spitzer, Elaboration and characterization of nano-sized AlxMoyOz / Al thermites, *33rd International Pyrotechnics Seminar*, Fort Collins, Colorado, USA, July 16-21, **2006**, 93-102.
[4] M. Comet, B. Siegert, V. Pichot, P. Gibot, D. Spitzer, *Nanotechnology*, **2008**, 19, 2-9.
[5] M. Comet, B. Siegert, V. Pichot, D. Spitzer, F. Ciszek, N. Piazzon, P. Gibot, Impressive change of reactive properties of high explosives structured and stabilized at nano-scale in an inert porous matrix, *35th International Pyrotechnics Seminar*, Fort Collins, Colorado, USA, July 13-18, **2008**, 151-158.
[6] M. Comet, V. Pichot, D. Spitzer, B. Siegert, F. Ciszek, N. Piazzon, P. Gibot, Elaboration and characterization of manganese oxide ($MnO_2$) based "green" nanothermites, *39th International Annual Conference of ICT*, Karlsruhe, Germany, June 24-27, **2008**, V 38-1 to V 38-8.
[7] Patent FR 000002905882A1, Production of micro- and-or nano-thermite for use, e.g. in pyrotechnics or weapons, involves coating dispersed oxidant particles with a precursor of a reducing metal and then forming the metal by thermolysis.
[8] M. Comet, V. Pichot, B. Siegert, D. Spitzer, Energetic nanocompositions for automotive safety devices, *International Pyrotechnic Automotive Safety Symposium*, **2007**, 365-374.

# Polarization and mode changes depending on the environmental stress in single mode fibers

Juock Namkung
Naval Air Systems Command, Patuxent River, Maryland
Mike Hoke
Air Force Research laboratory, Hanscom, MA
Gregory Wilkins
Morgan State University, Baltimore, MD
Chris Werniki
New York Institute of Technology, New York, NY

## ABSTRACT

The research discussed below describes experiments and computer simulations involving propagation of polarized radiation in optical fiber cables designed for use in aircraft environments. The main concern of this effort is optical fiber link systems that are installed in military aircraft. Propagation of polarized radiation in a single mode fiber can be theoretically described with electromagnetic field equations for a bounded system. The state of propagation of the radiation polarization will be affected by environmental stress and strain on the fiber, by imperfections within the fiber, cracks or breaks in the fiber across the fiber optical axis, and by a variety of discontinuities at fiber connectors. The transmission, reflection, and scattering of radiation within an optical fiber affected by these various effects results in mode changing of propagating radiation within the fiber. Mode changing effects by imperfection in the fiber link system have been experimentally measured. The experimental results discussed below are preliminary results and applicable to modeling techniques in the future.

Key word: Polarization, Single mode optical fiber, Optical fiber network, Optical fiber wave guide

## 1. INTRODUCTION

There is an evolving need to develop a durable, effective in-situ capability to transport laser radiation through optical fibers for communication between aircraft systems and components. Optical fiber communication cables have several advantages over conventional electrical cables. As a consequence, optical fiber networks for aircraft communication will increasingly become standard structures in military and commercial aircraft. Given this increased interest in optical fiber networks for aircraft systems communications, the mechanisms of radiation transmission in optical fibers and the causes of breakdown of effective radiation transmission, and the resulting system failure will increasingly become important areas of study.

The behavior of propagation of polarized radiation and intensity changes within installed optical fibers that depend on the highly dynamic aircraft environments are currently not well known, with the exception of power loss of the system. Experimental studies are not numerous and computer simulations have not yet reached an appropriate degree of maturity. What needed for numerical simulations are models of optical fiber radiation transport over long fiber lengths undergoing local dynamic changes in stress, strain, and temperature. In principal, fiber imperfections can be modeled numerically, through application of the electromagnetic wave equations and finite element methods. However, experimental investigations are currently the only completely viable means for exploring the effect of fiber imperfections and their resulting effect on system communication capability.

Photonics in the Transportation Industry: Auto to Aerospace II, edited by Alex A. Kazemi, Bernard C. Kress
Proc. of SPIE Vol. 7314, 73140O · © 2009 SPIE · CCC code: 0277-786X/09/$18 · doi: 10.1117/12.834959

Imperfections at junctions cause reflections that alter the intensity and polarization state of the radiation transmitted across the discontinuity.[1,2] Discontinuities including breaks and partial breaks in optical fiber cables that induce scattering that alter the intensity of the radiation transmitted within the fiber. Polarization mode changes due to junctions and connectors, including reflection and scattering, can be modeled with the wave equation and finite element method.[3] Experimental intensity and polarization mode shifts depending on the imperfection of fiber links created by navy environments are the main subject of this effort.

Currently fiber optic cables and fiber optic network are being installed on several aircraft for testing and evaluation. Performance testing, faultfinding and maintenance are also major concerns for these systems. The experimental characterization of radiation transfer into and through the fiber optic network and within single-mode fibers is an important part of this research. The current experimental and modeling efforts should yield benefits in the areas of faultfinding and system maintenance. The first step in the ongoing research is to experimentally explore the dependence of intensity and polarization changes at junctions. From this an immediate benefit is the possibility of recognizing breakage in shielded areas or near connectors, with simple laser faultfinder without using Optical Time Domain Reflectometer (OTDR).

## 2. OPTICAL FIBER WAVEGUIDE

A cross sectional view of an optical fiber, consisting of a core of refractive index $n_1$ and a cladding of refractive index $n_2$, is shown on Figure 1. The general expression of Maxwell's electromagnetic field equations applicable to radiation propagation in optical fibers with no sources or sinks of radiation is the following[4]:

Maxwell's equation:

$\nabla \times E = -\partial B/\partial t$
$\nabla \times H = -\partial D/\partial t$
$\nabla \bullet D = 0$
$\nabla \bullet B = 0$

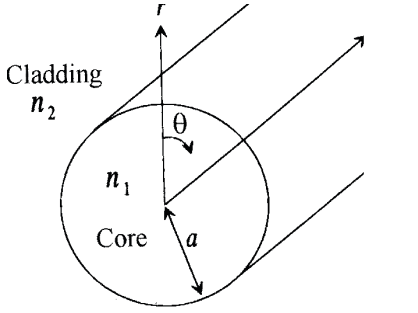


Figure1. Cross sectional view of a fiber

Specialized to the geometry for propagation of radiation within a cylindrical optical fiber, the wave equations are the following.

Helmholtz wave equations:
$\nabla^2 H + k^2 H = 0$
$\nabla^2 E + k^2 E = 0$

Here the k is the wave vector of the radiation propagating in the optical fiber.

The appropriate solutions of the wave equations for radiation propagation in a core of a cylindrical optical fiber are the following[4]:

In the core r < a:

$$E_z = AJ_n\left(\frac{ur}{a}\right)\sin(n\theta+\phi),$$

$$E_r = \left[-A\frac{j\beta}{u/a}J_n'\left(\frac{ur}{a}\right)+B\frac{j\omega\mu_0}{(u/a)^2}\frac{n}{r}J_n\left(\frac{ur}{a}\right)\right]\sin(n\theta+\phi),$$

$$E_\theta = \left[-A\frac{j\beta}{(u/a)^2}\frac{n}{r}J_n\left(\frac{ur}{a}\right)+B\frac{j\omega\mu_0}{u/a}J_n'\left(\frac{ur}{a}\right)\right]\cos(n\theta+\phi),$$

$$H_z = BJ_n\left(\frac{ur}{a}\right)\cos(n\theta+\phi),$$

$$H_r = \left[A\frac{j\omega\varepsilon_1}{(u/a)^2}\frac{n}{r}J_n\left(\frac{ur}{a}\right)-B\frac{j\beta}{u/a}J_n'\left(\frac{ur}{a}\right)\right]\cos(n\theta+\phi),$$

$$H_\theta = \left[-A\frac{j\omega\varepsilon_1}{u/a}J_n'\left(\frac{ur}{a}\right)+B\frac{j\beta}{(u/a)^2}\frac{n}{r}J_n\left(\frac{ur}{a}\right)\right]\sin(n\theta+\phi).$$

Here, $J_n(ur/a)$ is the Bessel function of the first kind, with $u^2 = k_0^2a^2(\varepsilon_{r1}-n_{eff}^2)$.

Three major discontinuities at junctions can be described as misalignment, separation, and tilting. The loss of power for an imperfect junction is well known in the literature, and is shown in Figure 2.

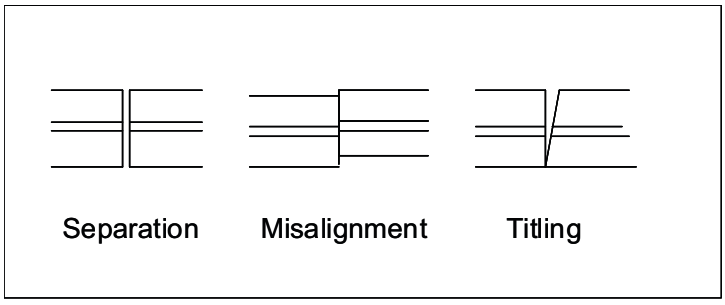


Figure 2. Idealized representation of optical fiber imperfections studied

The relationship between mode changes at imperfect junction is the main concern of this effort. The lowest order solutions to the electromagnetic wave equation are graphically represented[4] in Figure 3.

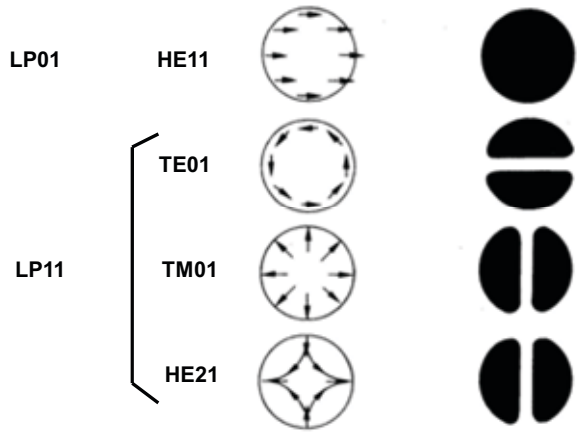


Figure 3. The electric field configuration for the lowest order, LP *l,m* modes

## 3. EXPERIMENTAL SETUP

Laboratory experimental tests for mode changes at imperfect junctions were undertaken using commercially available 9 μm core diameter single mode fibers. Two multi-axis positioning systems with micrometer adjustments were purchased with high-resolution micrometer positioning arms, to position the two portions of the optical fiber (1) bringing the radiation to and (2) taking the radiation away from the junction simulating the discontinuity. See Figure 4.

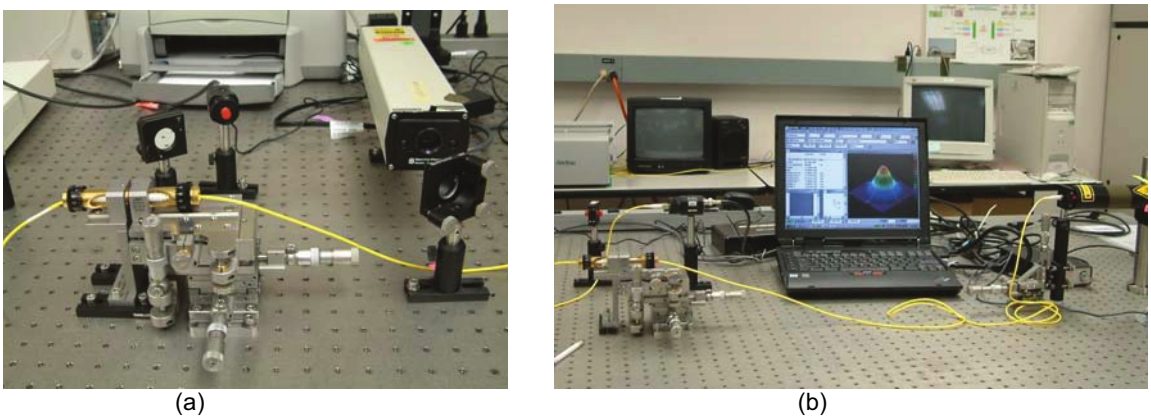

(a) (b)

Figure 4. Experimental setup used to induce and control systematic changes in optical fiber connector junctions: (a) alignment control stage, (b) integrated with CCD camera.

Beam profiler by Spricon with CCD camera was used for checking the intensity and beam shapes. Two CCD cameras, one for HeNe laser and one for 1550nm DFB laser were selected for these experiments. A

HeNe laser was used to insure proper alignment of the fibers at the junctions before the testing of fiber network (See Figure 5).

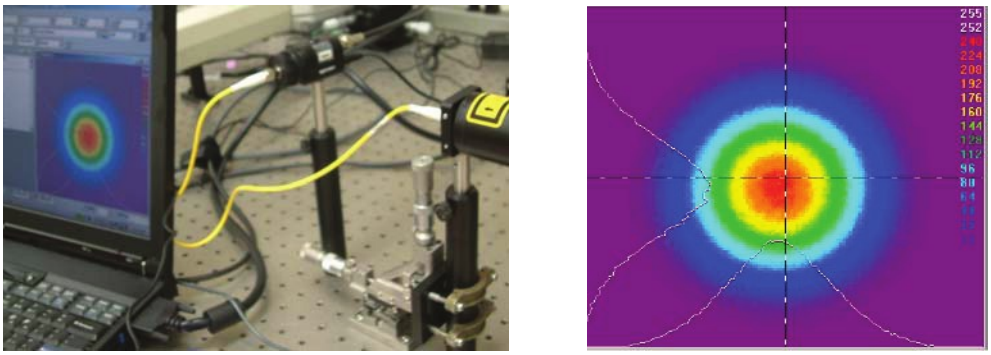

(a) (b)

Figure 5. Experimental setup: (a) HeNe source and CCD camera, (b) output of beam profiler display on monitor

## 4. RESULTS AND DISCUSSION

The theoretical analyses of polarization mode changes at imperfect junctions were thoroughly examined including proper physical characteristics of a single mode fiber. This includes mode coupling at the junction and weakly guided mode changes, since the simulation was not successful with the current setup and software. For the wavelengths being used in the single mode optical fiber (1550nm), the Nyquist Criterion creates an enormous computer memory space problem. In addition, it exceeds the solution capacity of the current version of simulation software available to us.

Attempts were made to test for mode changes at imperfect junctions as outlined above. Radiation of 632.5nm wavelength was transmitted into a single mode fiber at the junction. A simple HeNe laser was used for this test with alignment control. The incident wave was a linearly polarized Gaussian beam and misalignment was introduced to cause mode changes at the junction; see Figure 6. Figure 6(a) shows the output of the end of beam without any gap at the junction and Figure 6(b) shows the output of the end of fiber with the misalignment at the junction. These results demonstrate mode changes, but the control system was not connected to computer. Further investigation is needed to fully understand the details of these results.

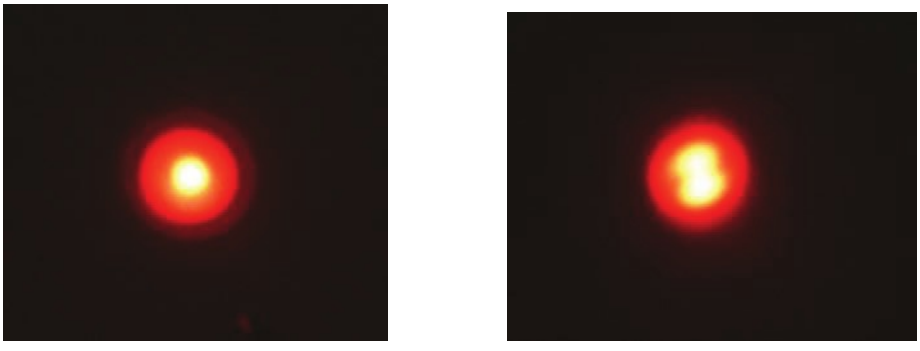

(a) (b)

Figure 6. Output laser radiation at 632.5 nm in (a) with aligned, (b) with imperfect fiber junction.

An experimental setup was prepared as designed, again using 9 μm single mode fibers with 1550nm laser radiation. The 1550nm DFB laser source and infrared beam profiler were connected with 9 μm single mode fiber. A faulty junction was created deliberately to observe the hybrid modes at the end of fiber. Assuming the intensity of laser source was weak, a strong HeNe laser was used as a source for alignment, and switched the source to 1550nm DFB laser after the alignment at the junction. We saturated the intensity in the beginning of the experiment, since the intensity was expected to be weak after the imperfect junction. Then we create discontinuities. The results are shown on the Figure 7. The interference in the Figure7b is unexplained but the two intensity peaks are clearly seen.

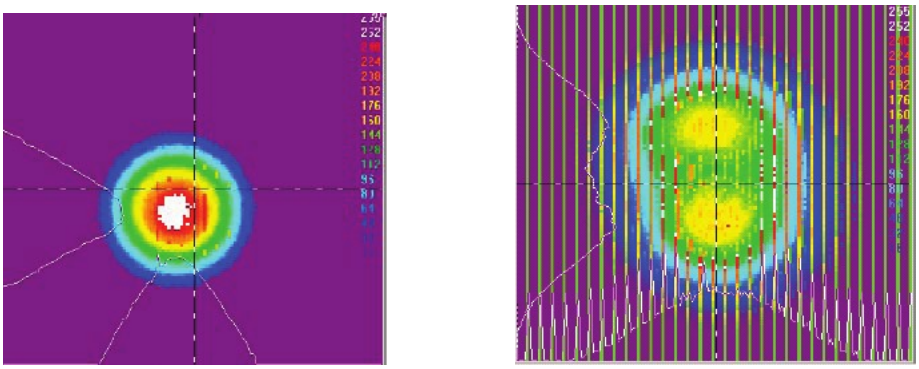

(a) (b)

Figure 7. Output laser radiation at 1550 nm in the LP01 (a) and LP11 (b) transmission modes of the 9 μm

## 5. CONCLUSION AND FUTURE STUDY

Polarization mode changes at junctions have been studied extensively. The electric field configurations for the three lowest modes were identified from the waveguide equations and specific profiles of the selected single mode fiber. The configurations of the fundamental linearly polarized mode and hybrid modes at faulty junctions were studied experimentally. Three cases of discontinuities at junctions in an optical fiber system were selected for study of the electromagnetic field changes and their behaviors, which are governed by Maxwell's equations. The effort to simulate the results using finite element calculation software was tried but exceeded the solution capacity of the current version of the software available to us. An experimental setup, with 1550nm laser and 9 μm single mode fibers produced the result has been shown in Figure 7. The exact extent of misalignment could not be measured with the current setup, yet it may be possible to correlate the mode changes of propagation if all the conditions are met. We will continue this experiment further to investigate the results.

## ACKNOWLEDGEMENTS

This work was supported by ILIR grant from ONR. Gregory Wilkins and Chris Werniki would like to thank NAVAIR for their support and hospitality while their work was done.

## REFERENCES


1. Chung-Hao Tan, Yin-Chieh Lai, and Han-Ping David Shieh, " Polarization analyses of readout signal by a solid immersion lenz in a phase change recording material" *Opt. Eng*, Vol.40 (10), pp. 2285-2292 , 2001

2. Marcuse D. "Reflection losses from imperfectly broken fiber ends" *Applied optics*, Vol. 14, pp 3016-3020

3. Sears F.M. at el "Probability of modal noise in single-mode light guide system" *11th Europ Conf. Opt. Communication* 1985, pp 823-826.

4. Kenji Kawano and Tsutomu Kitoh, " *Introduction to optical wave guide Analysis*", John Wiley & Sons Inc.

# Propagation Loss with Frequency of Ultrasound Guided Waves in a Composite Metal-Honeycomb Structure

Indu F. Saxena[#], Harsh K. Baid*, Narciso Guzman[#], Lothar U. Kempen#
and Ajit Mal*,
[#]Intelligent Optical Systems, 2520 W. 237th St., Torrance, CA, USA 90505
*Mechanical and Aerospace Engineering Department,
University of California Los Angeles, Los Angeles, CA

## ABSTRACT

Non-destructive testing of critical structural components is time consuming, while necessary for maintaining safe operation. Large aerospace structures, such as the vertical stabilizers of aircraft undergo inspection at regular intervals for damage diagnostics. However, conventional techniques for damage detection and identification before repair can be scheduled are conducted off-line and therefore can take weeks. The use of guided ultrasound waves is being investigated to expedite damage detection in composites. We measure the frequency dependent loss of ultrasonic guided waves for a structure comprising a boron-nitride composite skin sandwiching an aluminum honeycomb. A wide range of ultrasound frequencies propagate as measured using PZTs, with the lowest attenuation observed about 200-250 kHz. These measurements are confirmed using optical fiber Bragg grating arrays used as ultrasound transducers.

**Keywords:** large area damage diagnostics, Lamb waves, time-efficient, leaky guided waves

## 1. INTRODUCTION

Aerospace structures develop flaws with use that are caused by fatigue, aging, service loads, or even during handling such as accidental tool drops. Laminated composite materials that are used in many aerospace and aircraft structures, for example, can develop a variety of hidden internal flaws. These flaws can present themselves in a variety of forms: fatigue cracks, corrosion, and dents in metals; delamination, disbonding, and fiber breakage in composites. While a number of techniques are available for detecting and characterizing defects in aircraft and aerospace structures including visual inspection, tap testing, electromagnetics, radiography, thermography, and ultrasonics, they are very time consuming. Currently available methods that can be used to assess structural damage on aircraft components in a non-intrusive and/or non-destructive manner are cumbersome and costly, and must be conducted off-line. One of the industry standards is the ultrasonic (US) scanning system using a water-jet, called the squirter (e.g., Scanmaster-IRT Model DS-2005 (Greensville, SC), other systems from Mortec, Olympus NDT, etc.) are expensive instruments for performing off-line damage diagnostics. As an example, a vertical stabilizer of an F-15 is about 45x120 inches surface area, takes about 3 hours to scan with the squirter. The use of guided ultrasound waves offers the potential to facilitate damage diagnostics with several embedded or surface mounted transducers.[1-7] In addition to ultrasound detection with PZTs, optical fiber Bragg grating (FBG) transducers[7-10] are an emerging, commercially viable detection alternative. We report here the characterization of a section of a vertical stabilizer using guided ultrasound waves. Two sets of measurements are conducted: one with a pair of PZTs as source and receiver, and two, with a PZT source and FBG transducer array. Propagation losses measured on two samples in both ways are found to have increasing losses with frequency.

## 2. EXPERIMENTAL METHODS

### 2.1 Ultrasonic Guided Wave Measurements in Composite Aluminum Honeycombs

The F-15 vertical stabilizer consists of a sandwich of composite with aluminum honeycomb, referred to as CMHC, or composite metal honeycomb. Specimens of F-15 vertical stabilizer section with high stiffness (Youngs Modulus Y = 29.6 E6 psi for the Boron-based composite[11]) were measured. Guided wave propagation loss measurement at different

Photonics in the Transportation Industry: Auto to Aerospace II, edited by Alex A. Kazemi, Bernard C. Kress
Proc. of SPIE Vol. 7314, 73140P · © 2009 SPIE · CCC code: 0277-786X/09/$18 · doi: 10.1117/12.835473

source frequencies was performed using PZTs sources and receivers, as well as FBG receivers at different source-receiver separations while keeping the drive voltage of the source PZT constant. These measurements permit estimating the detection range possible when using a single ultrasound source.

### 2.2 PZTs as source and receiver

PZTs were from PANAMETRICS (Model B1025) with a source PZT drive voltage of 10V and an identical PZT used as receiver. Using a fixed source and multiple points of measurements by receivers in a fixed pattern or grid was used to obtain a discretized/digital ultrasound response. This method has been shown to be capable of imaging the damage based on the amplitude contrast of measured responses along the surface of the specimen.[11] Propagation loss, velocity and dispersion measurements can be obtained from these responses.

A dilatational PZT transducer (B1025 from Digital Wave) driven at frequencies at 150, 250, 350, 500 and 750 kHz provided the ultrasound source. The source was fixed at one location while the receiver was moved along a line from 2 inches to 6 inches, in 1 inch increments. The ultrasound responses were obtained at 2, 3, 4, 5, and 6 inches distances from the source location at varying frequencies. Plots of maximum amplitude of the first guided wave component were obtained.

### 2.3 PZT source and FBG-array receivers

FBGs have been shown to be useful for a variety of static and dynamic strain measurements. As ultrasound transducers, it has been shown that FBG receivers have a maximum ultrasound response to a PZT source when placed radially from it,[12] such that the optical fiber direction is normal to the wavefront originating from the source PZT. An optical fiber with an array of several (15) FBGs spaced equidistantly were placed in this orientation with respect to the PZT source as shown in Fig. 1. A tunable laser was used to interrogate the FBGs sequentially. Tunable lasers offer narrow linewidth and enable high sensitivity for dynamic measurements with FBGs. A Nettest Tunics PLUS laser with narrow linewidth was used and FBG linewidths were 0.3 nm.

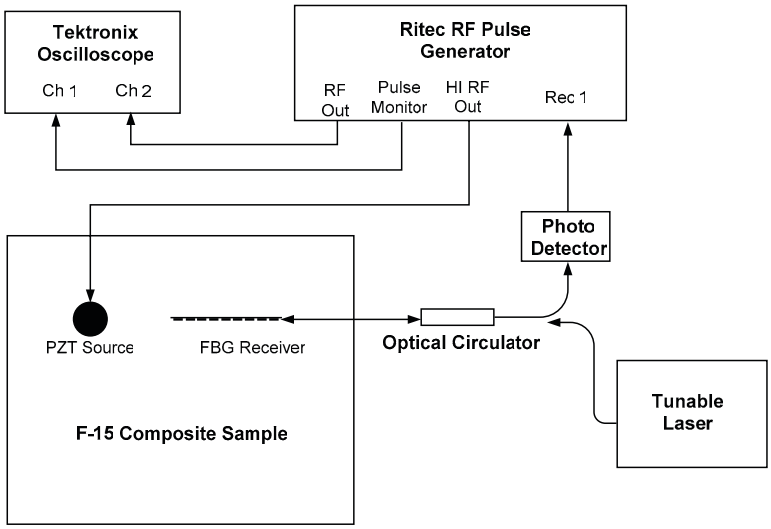


Fig. 1 Experimental schematic for source PZT and FBG receiver detection of guided wave.

## 3. RESULTS AND DISCUSSIONS

The amplitudes of the response obtained with the PZT measures are plotted in Fig. 2 to summarize the attenuation data obtained for all the frequencies.

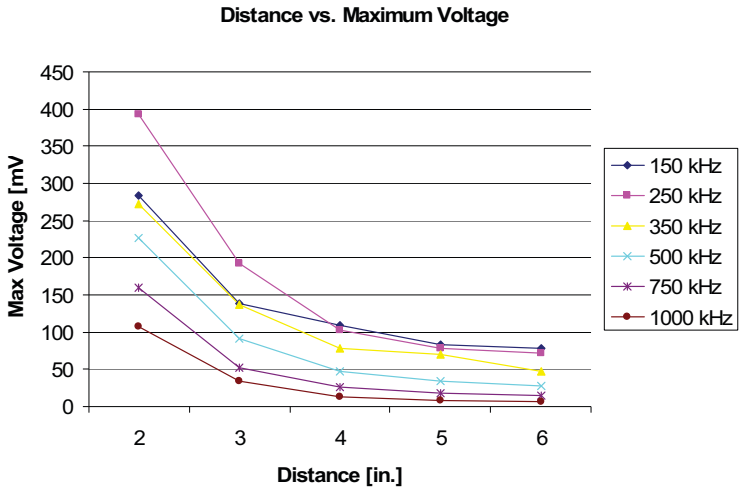


Fig. 2 PZT source and receiver attenuation of guided wave amplitude responses.

The PZT response data at the measured frequencies was assessed as follows. The loss function that was used to compare the rates of decay of the guided waves is the so-called "power function" in Excel, and was used to obtain a curve-fit for the different frequency response data. As the composite thickness of the specimen is non-uniform and tapered (thicker at the base of the vertical stabilizer), the loss properties need to be determined along directions of uniform thickness, and along that of the non-uniform thickness.

| **Guided Wave Frequency** kHz | **Power of 'x'** PZT data | **Amplitude Ratio at 2 inches** (w.r.t. 350kHz) | **Amplitude Ratio at 5 inches** (w.r.t. 350kHz) |
|---|---|---|---|
| 150 | -1.174 | 1.04 | 1.20 |
| 250 | -1.625 | 1.44 | 1.13 |
| 350 | -1.5705 | 1 | 1 |
| 500 | -1.945 | 0.83 | 0.49 |
| 750 | -2.2358 | 0.58 | 0.20 |

The velocity was measured to be 5.2 mm/microsecond at 250 kHz . From the attenuation measured at each frequency f, the amplitude of the response, Vo at x=3" as a function of frequency is obtained and shown in Fig. 3.

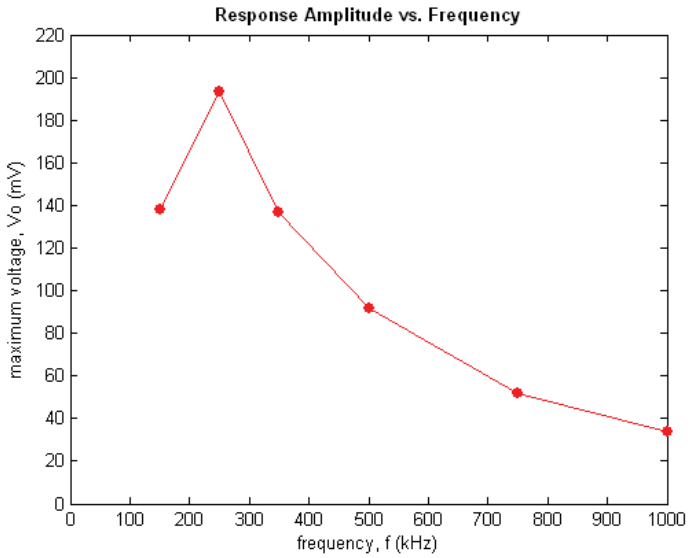


Fig. 3 Amplitudes of guided wave in CMHC structure as a function of source frequency at fixed source-receiver PZTs separation.

### 3.1 Ultrasound measurements with FBG array as receiver

The guided US response was measured by the FBG receivers at varying distances from the PZT source. The following figures (Figs. 4 through 5) show typical US response at a source frequency of 325 kHz and 200 kHz while the PZT to FBG separation was varied up to 15 inches.

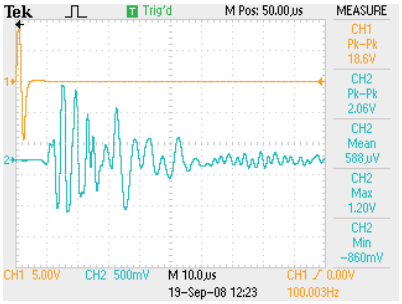


Fig. 4(a) 325 kHz at 2 in.

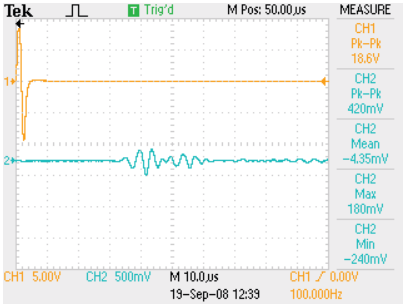


Fig. 4(b) 325 kHz at 7 in.

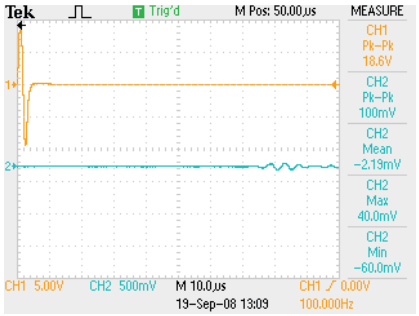


Fig. 4(c) 325 kHz at 15 in.

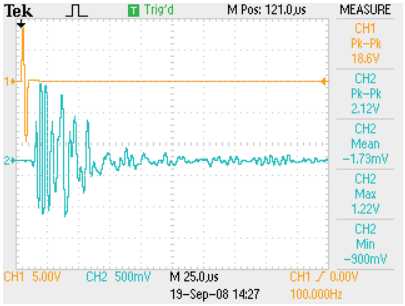


Fig. 5(a) 200 kHz at 2 in.

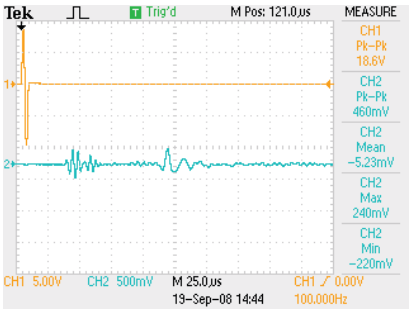


Fig. 5(b) 200 kHz at 7 in.

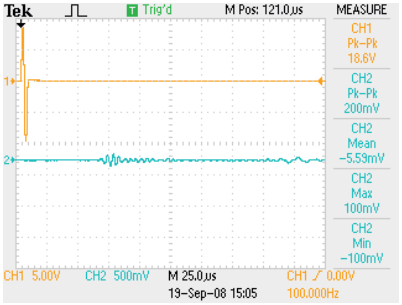


Fig. 5(c) 200 kHz at 13 in.

The FBG response data and the curve fits are summarized in Fig. 6.

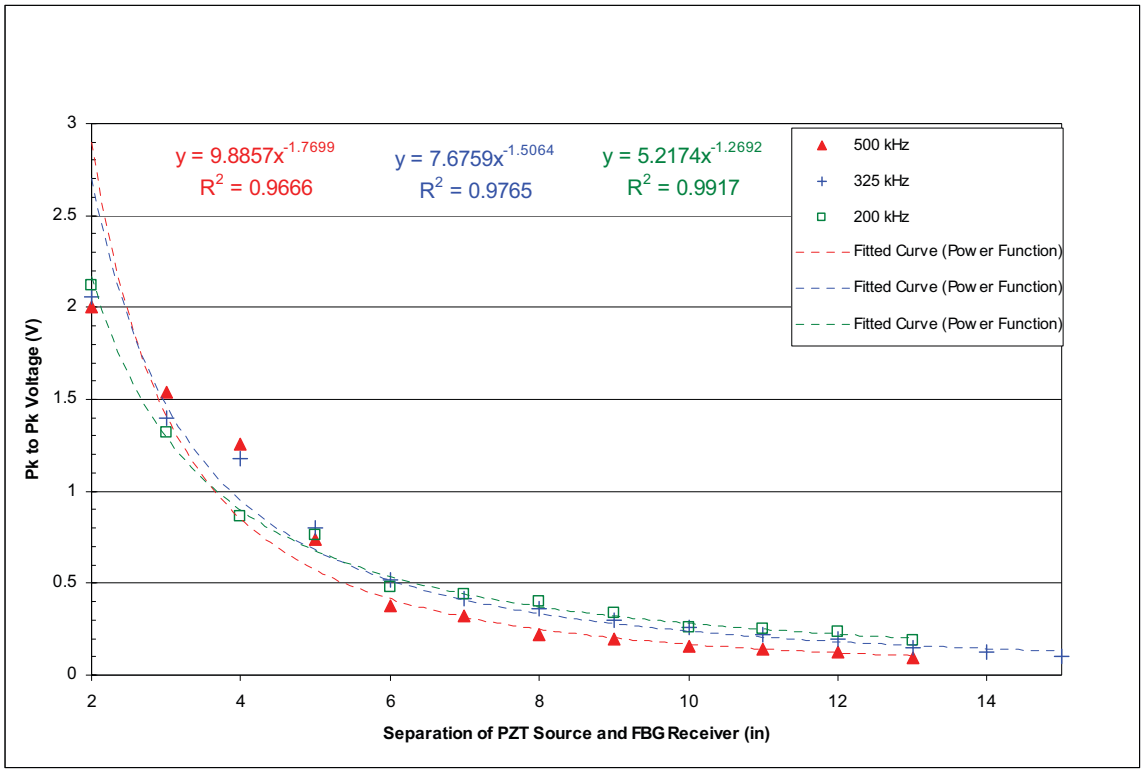


Fig. 6 Peak to peak ultrasound response amplitude vs. source-receiver separation. FBG response at a maximum separation from PZT of up to 15 inches is detected. The peak to peak response falls off at the lowest rate at about 200 kHz.

Curve fit equations (power function) were obtained for 500 kHz, $y = 9.8857x^{-1.7699}$ ($R^2 = 0.9666$); at 325 kHz, $y = 7.6759x^{-1.5064}$ ($R^2 = 0.9765$); and at 200 kHz, $y = 5.2174x^{-1.2692}$ ($R^2 = 0.9917$). Similar to the measured responses with PZT receivers (Fig. 2 and Fig. 3), the lowest rate of attenuation was about 200 kHz. We observed that FBG ultrasound receivers detected guided waves 15 inches away from a source PZT at low ultrasound frequencies.

## 4. CONCLUSIONS

It is observed that for the sample tested, the optimal guided wave ultrasound frequency is about 200 kHz where there is a minimum in ultrasound guided wave attenuation. This enables a large range of single transmitter based diagnostic techniques that employ guided waves. Furthermore, optical fiber FBG transducers can be used to measure these attenuation and ultrasound dispersion characteristics in a time efficient manner. This is especially true for composite materials with anisotropic characteristics. Multiple directions can be efficiently scanned with several individual fiber FBG arrays.

## ACKNOWLEDGEMENTS

We acknowledge the support of the U.S. Air Force through the granting of Contract#FA8501-07-C-0025. We are also grateful to Contract Monitor Mr. Dennis Keene, P.E., for his valuable support and advice, and for providing us with the F-15 sample for evaluation.

## REFERENCES


[1] Y. Bar-Cohen and A.K. Mal, "Ultrasonic inspection," Metals Handbook, 9th Edition, **17**, Nondestructive Evaluation and Quality Control, ASM International, 1989.

[2] S. Banerjee, F. Ricci, E. Monaco, A. Mal, L. Lecce, "Autonomous impact damage monitoring in a stiffened composite panel," Jl. of Intelligent Materials Systems and Structures, 2005.

[3] A.K. Mal, "The role of NDE in structural health monitoring of aircraft and aerospace structures," Proc. SPIE Conf. on NDE of Aging Aircraft, Airports &Aerospace Hardware, Newport Beach, California, **3994**, pp. ix-xiii, 2000.

[4] Y. Bar-Cohen, A.K. Mal, M. Lasser, "NDE of hidden flaws in aging aircraft structures using backscattered ultrasonic signals (OBUS)," SPIE Conf. on NDE of Aging Aircraft, Airports &Aerospace Hardware, Newport Beach, California, **3586**, pp. 347-353, 1999.

[5] J.-H. Shih and A.K. Mal, "Acoustic emission from impact damage in a cross-ply composite," Proc. of the Second Workshop in Structural Health Monitoring, Stanford University, pp. 209-218, Sept. 1999.

[6] Y. Bar-Cohen, A.K. Mal, S.-S. Lih, Z. Chang, "Composite materials stiffness determination and defects characterization using enhanced leaky Lamb wave dispersion data acquisition method," SPIE Conf. on NDE of Aging Aircraft, Airports &Aerospace Hardware, Newport Beach, California, **3586**, pp. 250-255, 1999.

[7] K.O. Hill, Symposium on Physics and Fundamentals of Fiber Bragg Gratings and Applications, 1998 OSA Annual Meeting, Baltimore, MD, October 1998.

[8] K.O. Hill, B. Malo, F. Bilodeau, and D.C. Johnson, "Photosensitivity in optical fibers," Ann. Rev. Mat. Sci., **23**, pp. 125-157, 1993.

[9] P. St. J. Russell, J.L. Archambault, "Fiber gratings," Ch. 2, in Optical Fiber Sensors Components and Subsytems, B. Culshaw and J. Dakin (Eds.), **III**, Artech House Inc., Boston, MA, 1996.

[10] I.F. Saxena, K. Hui, "Optical fiber static strain sensors: reliability issues," SPIE Optics East, Boston, 2007.

[11] A. Mal, I.F. Saxena, H. Baid, and D. Keene, "Detection of disbonds in a honeycomb composite structure using guided waves," IWSHM, Stanford University, 2007.

[12] G. Thursby, D.C. Betz, B. Culshaw, and W. Staszewski, "Versatile fiber Bragg grating arrays for strain mapping and ultrasound Lamb wave detection," Proc. of SPIE, **6379**, 2006.

[13] I. Saxena, "Distributed pressure sensor," NASA Contract NAS5-01054 Final Report, 2002.

[14] D. Keene, private communication, 2007.

# Author Index

Numbers in the index correspond to the last two digits of the six-digit citation identifier (CID) article numbering system used in Proceedings of SPIE. The first four digits reflect the volume number. Base 36 numbering is employed for the last two digits and indicates the order of articles within the volume. Numbers start with 00, 01, 02, 03, 04, 05, 06, 07, 08, 09, 0A, 0B … 0Z, followed by 10-1Z, 20-2Z, etc.